Evaporation of Binary Liquids: Planar Layers and Sessile Drops

Adam Graham Lewis Williams

Thesis submitted for the degree of

Doctor of Philosophy

School of Engineering

The University of Edinburgh

2018

Abstract

This thesis focuses on the dynamics and stability of liquid pools (layers) and droplets comprising of binary mixtures of miscible components, where surface tension induced (Marangoni) flows play a prominent role. Specifically, evaporation of thin horizontally heated liquid layers and thin sessile droplets spreading on heated surfaces are investigated using both modelling and experimental approaches. Below the capillary length gravitational effects weaken and surface tension becomes the prominent driving force in the ensuing flow dynamics. Surface tension gradients arise over the liquid-vapour (LV) interface due to either a variation in temperature (thermal Marangoni stress) or, in the case of binary liquids, concentration (solutal Marangoni stress). In our case, we consider both. Solutal Marangoni stresses can suppress or enhance thermal Marangoni, leading to interesting behaviour.

First, the stability, flow dynamics and evaporation kinetics of bi-component miscible liquid layers subject to a horizontal temperature gradient are investigated by means of two-phase direct numerical simulations (DNS). Both the liquid and gas phases are fully resolved, with the Volume-of-Fluid (VOF) method used to account for the deformable liquid-vapour (LV) interface. Surface tension varies linearly with both temperature and concentration at the interface. In the bulk liquid, thermophoresis (Soret effect) and mixture thermodynamics are accounted for. It is shown that even in absence of evaporation, thermophoresis can drive subtle component separation. Under certain conditions, flow exhibits the so-called hydrothermal wave instabilities with similar concentration fluctuations also propagating at twice their wavelength. Introduction of evaporation over the interface depletes both overall liquid mass and concentration of the more volatile component while the layer remains well mixed due to return flow sustained by thermal Marangoni stress. In the absence of thermal Marangoni, preferential evaporation of the more volatile component from the hot wall combined with solutal Marangoni stress reverses the return flow.

Secondly, the dynamics and stability of thin volatile droplets comprising of binary mixtures deposited on heated substrates are investigated using lubrication theory and linear stability analysis under the quasi-steady-state approximation. Solely the liquid phase is focused on and so a novel one-sided model is developed to predict the spreading and evaporation of a binary axisymmetric drop on a heated substrate with high wettability. A thin drop with a moving contact line is considered, taking into account the variation of liquid properties with concentration as well as the effects of inertia. The parameter space is explored and the resultant effects on wetting and evaporation evaluated. Increasing solutal Marangoni stress enhances spreading rates in all cases, approaching those of superspreading liquids. Preliminary results from the stability analysis indicate that the addition of a second component has a strong destabilising effect on the drop. Quantitative and qualitative agreement is found with experiments.

Thirdly, experiments are conducted with binary ethanol-water droplets spreading on hydrophilic glass slides heated from below. The spreading rate is quantified, revealing that preferential evaporation of the more volatile component (ethanol) at the contact line drives superspreading, leading in some cases to a contact line instability.

Declaration

I declare that this thesis has been composed solely by myself and that it has not been submitted, either in whole or in part, in any previous application for a degree. Except where otherwise acknowledged, the work presented is entirely my own.

Adam Graham Lewis Williams
August, 2018

Acknowledgments

I would like express my sincere gratitude towards my supervisors Dr. P. Valluri and Prof. K. Sefiane for providing me with the opportunity to peruse this work and their continual guidance and support over the past few years. Beyond this, they have provided me with priceless opportunities to visit and work with other researchers from around the world. Of these, I would especially like to thank Dr. P. J. Sáenz, Prof. J. Kim, Dr. G. Karapetsas, Prof. O. K. Matar and Dr. D. Mamalis for their mentorship and valued exchanges. All have taught me an immense amount, not only in their respective fields, but also in how to approach all manner of difficult problems.

Within the the institutes of IMP and IMT, I have met some fantastic and interesting people. To my fellow students, all of whom I have been fortunate to meet, thank you particularly to Stephen, Erich, Jamie, Rohan, James, and Patrick for our often meandering discussions.

I am indebted to my partner Chloe, my mother Nicola, my brother Tristan, and my great friend Louis for their unconditional moral support and continual enrichment of my life. A special thanks goes to my grandparents, Thelma and Keith, who are sadly no longer with us. My grandfather inspired me from a young age and his memory continues to do so today.

Lastly, I would like to thank a former mathematics teacher of mine, Bob Shankland, who had a profound effect on me—more than I think he will ever know. Put simply, without his belief in my ability I could not have pursued engineering at university.

Stay curious.

Contents

List of Figures

List of Tables

Part I

Introduction and literature review

1. Motivation, aims and outline

A novel method for cooling microelectronics is a two-phase system in which an evaporating liquid gives up its latent heat—providing superior cooling over single phase systems [1]. Phase-change cooling is now an important topic to study given the high heat transfer efficiencies required to cool modern electronic processors, with effective cooling increasing both performance and overall lifetime. Picture an array of microchannels bonded to the surface of a heat generating electronic chip over which the coolant liquid flows. As coolant evaporation proceeds, the liquid film within the microchannel reduces in height until the contact line recedes from the vertical walls to the horizontal channel floor. As dry-out is approached, film break-up occurs and sessile droplets of varying sizes will begin to form, following distinct evaporation mechanisms depending on their size and geometry. It is desirable to study both stages of the evaporation system—films and sessile droplets—to understand the flow phenomena at work and hence predict the behaviour of the system.

Typically, coolants used in such systems are miscible liquid mixtures and, as will be shown from the literature review, there is a gap in research investigating the complex interactions between multiphase multi-component fluid-mechanics and phase-change thermodynamics, which this thesis aims to address. The objectives of the thesis are centred towards improving our fundamental understanding of fluid dynamics and phase-change in two-component mixtures by means of advanced numerical modelling and experiments.

The specific objectives of this thesis work are as follows:

1. Understand evaporation of miscible binary mixture liquid layers by developing a new 3D two-phase two-component direct numerical simulation framework.
2. Understand evaporation of a flat (low-contact angle) sessile droplet comprising of two miscible components by developing a transient numerical model under the lubrication approximation.
3. Identify the stability regimes of the evaporating binary mixture sessile droplet by means of a novel quasi-steady stability analysis.

4. Perform experiments on flat sessile droplets (made up of miscible binary mixtures) to validate the numerical modelling and stability analysis.

To aid the reader, this thesis is divided into six parts and subdivided into sixteen chapters. The remainder of this part (Part I) consists of Chapter 2, wherein the literature pertaining to liquid layers is reviewed, and Chapter 3, which summarises the vast body of research conducted on evaporating sessile droplets.

Part II contains the chapters dealing with the numerical modelling of laterally heated liquid layers comprising of miscible binary mixtures. Chapter 4 describes the model and formulates the governing equations while Chapter 5 presents the results for binary layers under both saturated and unsaturated conditions.

Part III considers the numerical modelling of miscible binary mixture sessile droplets deposited on a heated hydrophilic surface. The numerical model is derived in Chapter 6 and the transient results presented in Chapter 7. Chapter 8 examines the stability of the results presented in Chapter 7 by performing a quasi-steady state linear stability analysis.

Part IV, consisting solely of Chapter 9, reports on experiments preformed on binary ethanol-water droplets used to validate our model formulated in Part III.

Part V contains Chapter 10 which draws conclusions and provides suggestions for future research.

Part VI begins with Chapter 11, an appendix containing additional information concerning the lubrication model derived in Chapter 6. Chapter 12 lists all of the acronyms used throughout the text while the final four chapters present a comprehensive list of the symbols used during the formulation of the models developed in Parts II and III. Chapters 13 and 14 list the dimensional and dimensionless symbols from the liquid layer model in Part II while Chapters 15 and 16 do the same for the sessile drop model presented in Part III.

2. Liquid layers subject to heating and evaporation

When a confined pool of liquid is subject to a temperature gradient, interesting behaviour can ensue, the processes behind which are inherently complex. In this chapter we review the literature required to frame the work in Part II concerned with liquid layers consisting of two miscible components subject to a lateral temperature gradient. Particular attention is paid to thin layers where surface tension effects dominate over gravity with both saturated and evaporating cases being considered.

Surface tension driven Marangoni flow is particularly important in the process of crystal growth, the formation of a pure crystal central to several industries. Some of the most common growth processes include the Bridgman, floating-zone and Czochralski methods [2]. Impurities in the crystals can form due to temperature oscillations in the melt—resulting from capillary instabilities [3]. Transparent oxides crystals such as sapphire (Al_2O_3) are used in applications such as solid-state lasers, insulating substrates for semi-conductors and monolithic crystal filters [4]. Conductive transparent oxides are also used as electrodes for liquid crystal displays, light-emitting diodes and solar cells [4]. In addition, surface tension dominated liquid layers in microchannels form the basis of technologies such as diagnostic testing, DNA manipulation and chemical microreactors [5]. With the introduction of phase change, another promising aspect in the advent of rapid technological advancement following Moore's law is the evaporative cooling of microelectronic devices [1]. Using two-phase coolants allows the evaporating liquids to give up substantial amounts of latent heat, providing significantly more cooling that a single phase system.

Now is an appropriate time to introduce the principal driving forces before reviewing the current work in the field. Surface tension over the liquid-vapour (LV) interface plays an important role, particularly for thin liquid layers below the capillary length since the effects of gravity become negligible. Surface tension along the interface arises from the relative strength of the cohesive force between liquid molecules over the weaker adhesive force between the liquid and air. This manifests itself as a net inward force, causing the interface to behave like an elastic membrane under tension. In most fluids, surface tension tends to be a monotonically decreasing function with temperature. In the presence of a temperature gradient, liquid at the interface flows away from hot areas, of low surface tension towards cold areas of high surface tension. This is known as the thermal Marangoni effect.

Above a certain critical temperature gradient between the end walls, surface tension effects can cause the layer flow to depart from its stable equilibrium state into an oscillatory flow regime. Unstable oscillatory flows can take a variety of forms with one of the more discussed being that of HTWs. HTWs take the form of thermal fluctuations travelling along the interface at well-defined angles to the flow. The HTW mechanism is discussed further in Section 2.2.

In a binary liquid mixture comprising miscible components, surface tension variation can also arise from concentration gradients—each component is likely to have a differing surface tension from the other. Concentration gradients can develop under a temperature gradient due to thermodiffusion (also known as the Soret effect) whereby components migrate to hotter or colder areas dependent on their species. This effect is explained further in Section 2.4. Additionally, the introduction of evaporation can produce stronger concentration gradients with the preferential evaporation of the MVC from warmer areas, leaving behind a greater concentration of the less volatile component (LVC). The resultant flow ensuing form these concentration gradients is known as the solutal Marangoni effect.

Most studies so far on phase-change cooling have looked into pure single-component fluids. However, most coolants used are usually mixtures, and as will be seen from the literature review there is a gap in research investigating the complex interactions between multiphase multi-component fluid-mechanics and phase-change thermodynamics, which this thesis is aiming to address.

2.1. Thermocapillarity in liquid layers

The beginnings of research in this field can be traced back to Henri Claude Bénard, a French physicist, who, in 1900 performed experiments on liquid layers subject to a vertical temperature gradient by heating from below. He observed cellular convection patterns within the liquid—the so-called Bénard cells. The Nobel Prize laureate, Lord Rayleigh subsequently examined the problem with linear theory and attributed these cells to buoyancy, arising from density variation with temperature [6]—now known as Rayleigh-Bénard convection. While convection cells can arise from thermal effects, this is not always the principal driving force. Rayleigh's theoretical study ignored thermocapillary effects and it was not until many years later, in 1958, that the surface tension driven convection originally studied by Bénard was explained by Pearson [7].

Pearson noticed that Bénard cells would appear in drying paint films and that inverting the film, effectively reversing the gravity vector, would not suppress the instability. He used linear theory similar to Rayleigh to analyse disturbances, neglecting gravity and considering only a LV surface tension force decreasing linearly with temperature. The stability was quantified by means of a dimensionless number, amounting of the ratio of surface tension to viscous forces—commonly known as the Marangoni number, Ma. Above a critical Marangoni number, Ma_{crit}, Bénard convection cells would form. Pearson concluded that surface tension forces inducing Marangoni flows could provide the driving force to sustain the Bénard cells in the absence of buoyancy—this was the first explanation of Bénard-Marangoni convection.

While both thermocapillary and buoyancy forces are often present, for thin layers in small geometries, such as a film of paint, thermocapillarity is often the dominant force [6]. Thermocapillarity arises from the tendency of LV surface tension, σ, to vary with temperature, T. Typically, a rise in temperature decreases the surface tension whereas a reduction in temperature increases surface tension. The magnitude of this change depends on the temperature coefficient of surface tension, γ, which is particular to the liquid. It is defined as the rate of change of surface tension with respect to temperature ($\partial\sigma/\partial T$). A linear variation in surface tension with surface temperature can be described as [8],

$$\sigma = \sigma_o - \gamma(T - T_o) \tag{2.1}$$

where σ is the surface tension at temperature T and σ_o is a reference surface tension at reference temperature T_o.

Pearson's stability analysis [7] considered a rigid LV interface to the layer, a reasonable assumption but strictly speaking untrue. In 1964, Scriven and Sterling [9] extended his work by accounting for shape deformations of the interface as well as the effects of viscosity. They found that a deformable interface made the layer more unstable while increasing liquid viscosity always had a stabilising effect. Scriven and Sterling [9] also showed that, converse to buoyancy driven Rayleigh-Bénard convection, flow under Bénard-Marangoni convection moves towards the free surface in shallow sections and away from the free surface in deeper sections. This simple criterion could be now used to distinguish between the two and determine the principal driving force sustaining the convection cells.

2.2. Laterally heated layers and hydrothermal waves

While the early work discussed in Section 2.1 focused on layers heated from below, we now switch to liquid pools with a lateral temperature gradient, maintained by heated and cooled vertical end walls at either side. The pool geometry adopted by

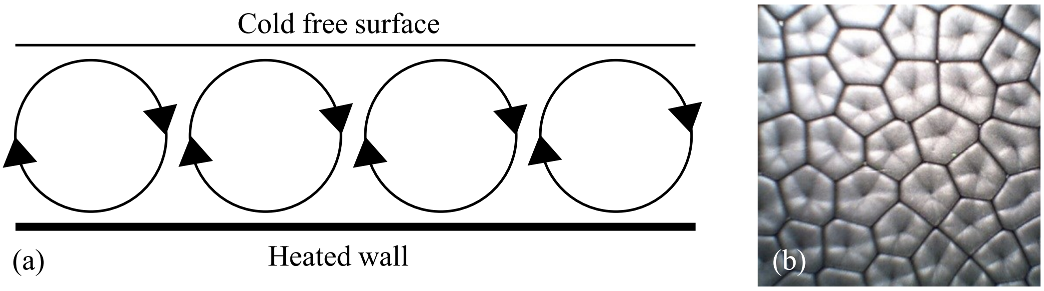

Fig. 2.1 (a) Illustration of Bénard convection caused by either buoyancy and/or Marangoni effects. In both cases warmer fluid from the heated bottom wall is convected towards the cold free surface before being drawn to the lower wall once more to replenish the lost liquid. (b) An experimental image of an interface displaying Bénard-Marangoni cells as viewed from above [10].

researchers tends to be either rectangular or annulus shaped, the temperature driving force maintained by the vertical end walls remaining common to both. As previously mentioned, our focus is centred on thin layers where surface tension tends to dominate over gravity, however, in some cases buoyancy will play a collaborating role. In surface tension dominant flow, the temperature gradient induces a similar gradient in surface tension along the interface in accordance with eq. (2.1). Liquid at the interface is pulled towards the cold wall—where surface tension is at a maximum. The depletion of liquid from the hot side drives a recirculation flow along the bottom wall to replenish the lost liquid, establishing a convective flow driven by surface tension—so-called return flow.

The seminal work on this problem was carried out in two parts by Smith and Davis in 1983 [3, 11]. In Part I, Smith and Davis [3] investigated thermal instabilities, while Part II [11] dealt with the surface-wave instabilities. Like Pearson [7], Smith and Davis [3] conducted stability analysis with a non-deformable interface while ignoring gravity and any dynamics of the gas phase. Heat was transferred across the interface by controlling the Biot number (Bi)—the ratio of conduction resistance within the fluid to convection resistance at the interface, with $Bi = 0$ corresponding to zero heat loss across the interface. Planar layers were considered in two distinct flow regimes. The first corresponding to an infinite layer unbounded by lateral walls—the linear flow solution. The second configuration considered a layer confined in a 2D slot—the return flow solution. Both cases had adiabatic bottom walls. Increasing the temperature gradient between the end walls increased the surface tension gradient along the interface and hence the strength of the thermocapillary Marangoni force. Similar to Pearson [7], stability was quantified in term of a Marangoni number. Above Ma_{crit}, the layer would become unstable and display either steady longitudinal rolls—as observed by Person—or a new mode of instability, known as HTWs. Zero heat loss across the interface ($Bi = 0$) always defined the most unstable mode.

Smith and Davis [3] revealed that thermal instabilities are inherent in these horizontally heated layers with a comprehensive review of instabilities in basic-state and return flow regimes provided by Davis [8]. In the basic-state flow, the entire layer depth flows from the hot to cold side—this corresponds to an unbounded domain and is in contrast with the return flow exhibited in a bounded domain. During return flow, surface liquid sinks upon reaching the cold wall and is recirculated back towards the hot wall where it duly rises to the surface once more. Smith and Davis reported the return flow to always be more stable than the equivalent linear flow, requiring a higher Ma_{crit} to provoke instability [3]. When Ma_{crit} in return flow was reached, steady longitudinal rolls would never emerge, with the preferred instability always being HTWs propagating at well-defined angles. Interestingly, the angle at which these waves propagated was function of the Prandtl number, Pr—the ratio of viscosity to thermal diffusivity. For very high Pr, HTWs would propagate directly upstream as transverse waves, whereas for very small Pr, the waves would prefer to travel in the span-wise direction, resembling longitudinal-type waves. For intermediate Pr, HTWs would propagate upstream at intermediate angles; $\pm\, \psi$ with respect to the reverse direction of surface flow. This mechanism discovered by Smith and Davis [3] offered an explanation to the oscillatory instability observed in experiments with Czochralski crystal growth melts such as those conducted by Schwabe and Scharmann [12].

Following on from this pioneering discovery, in 1986 Smith [13] explained the physical mechanism behind the HTWs. This begins with the surface tension driven return flow inducing a vertical temperature gradient in the layer—the interior being cooler than the interface. The sustaining mechanism then depends on the value of Pr. At small values inertial forces dominate while viscous effects are more prominent at high Pr. In the limit of small Pr, a hot spot develops on the interface causing a surface tension driven outflow to colder areas. This results in mass loss from the hot spot, causing an upward flow from the bulk to replenish the lost liquid. The interface velocity drops, inducing a flow from downstream where the liquid is also cooler towards the hot spot. The cooling flows begin to cancel out the hot spot but inevitably overshoot, causing a cold spot to form. Thermocapillarity now causes surface flow towards the cold spot and continuity from the resultant mass increase produces a downward flow. Consequently, the cold spot is eliminated and temperature overshoots to become a hot spot once more. If the interfacial temperature gradient is large enough and the system is above Ma_{crit}, the energy input to the spot from stream-wise convection outstrips the energy loss from conduction and the process becomes unstable, resulting in HTWs.

For large Pr, the sustaining mechanism is slightly different. Momentum diffusivity becomes greater than thermal diffusivity and viscous effects now dominate the flow [3]. The formation of a hot spot induces a cooling upflow from the bulk but no longer causes a stream-wise flow since inertial effects are negligible at high Pr. When a cold spot forms, the resulting vertical downflow causes heating within the layer—the fluid at the interface is always warmer due to the flow-induced temperature gradient. The comparatively warm fluid drawn down from the interface is displaced upstream by the return flow, causing a relatively intense hot spot within the layer at around mid-depth. The greater the surface temperature gradient—and hence Ma, the more intense the interior hot spot. With high conduction in the liquid at large Pr, the interior hot spot will now heat up the interface downstream of the original hot spot. This new hot spot forces the same upflow as the original one. Similar to the previous mechanism, above Ma_{crit}, the hot spots continue to propagate upstream, sustaining HTWs.

Garr-Peters [14, 15], in 1992, extended the numerical approach of Smith and Davis to account for gravitational effects with the inclusion of a Bond number, Bo—the ratio of buoyancy to surface tension forces, zero corresponding to no gravity. Garr-Peters [14] confirmed the dominance of waves travelling longitudinally for low Pr and transverse waves at high Pr, as reported by Smith and Davis [3]. An increased gravity system ($Bo = 6$) was found to have a stabilising effect when $Pr > 0.56$, increasing the required value of Ma_{crit} for instability to set in. In contrast, $Bo = 6$ was destabilising for $Pr < 0.56$, lowering Ma_{crit} [15]. Parmentier et al. [16] also assessed the linear stability of return flow with buoyancy and again found the behaviour to be heavily dependent on Pr. Buoyancy was introduced by way of the Rayleigh number, Ra—the ratio of buoyancy to viscous forces. First considering solely buoyancy driven flows with no thermocapillary effects; $Pr > 2.6$ rendered the layer unconditionally stable while for $Pr < 2.6$, HTWs emerged. This lead Parmentier et al. [16] to the conclusion that for flows driven by the combined effects of thermocapillarity and buoyancy, surface tension has to be the sustaining force for HTWs when $Pr > 2.6$. Parmentier et al. [16] also reported the stabilising influence of viscosity on the layer.

Mercier and Normand [17] continued work on the stability of horizontally heated layers with the combined effects of buoyancy and thermocapillary by demonstrating that instabilities in return flow could transition from travelling waves to stationary rolls by increasing the fluid depth. This was achieved by way of a Biot number, Bi. Large Bi corresponded to buoyancy being the dominant force—suggesting a deeper layer, whereas a small Bi indicated the dominance of thermocapillary effects. Stationary rolls were not originally predicted by Smith and Davis [3] in return flow. Over a decade later, Chan and Chen [18] examined buoyancy effects in more detail, this time gravity was introduced via a Grashof number, Gr—a derivation of Ra obtained by dividing by Pr. Higher Gr signifies stronger gravitational force. Chan and Chen [18] found that increasing Gr from zero first increases the angle of propagation of HTWs slightly before steadily decreasing to zero when $Gr = 18$. Gr higher than this would cause the HTWs to transition into travelling transverse waves. The mechanism was revealed by an energy budget. Increasing gravity would reduce the kinetic energy available to sustain the HTWs, requiring more energy than the transverse waves. Increasing Gr would therefore gradually suppress the angle of propagation of HTWs before transition to transverse waves. Meanwhile, phase speed, frequency and wavelength all decreased with increasing Gr [18].

The stability analysis of Chan and Chen [18] was originally inspired by experiments performed by in 1998 by Riley and Neitzel [19] who studied layers of 1 cSt silicone oil confined in a rectangular geometry of 30 by 50 mm with $Pr = 13.9$. This marked the first decisive experimental verification of the HTWs predicted by Smith and Davis [3]. Nine layer depths were investigated, the thickest being 2.50 mm decreasing in 0.25 mm increments to the thinnest at 0.75 mm. Below 1.25 mm, HTWs were discovered propagating at angles well predicted by Smith and Davis [3]. At greater depths, the instability transitioned to a steady multicellular structure and this was also observed experimentally by Villers and Platten [20] and Schwabe et al. [21]. Riley and Neitzel [19] could not conclude at the time if the transition from HTWs to the multicellular structure was due to buoyancy or geometry confinement effects—Chan and Chen [18] later confirmed the role of buoyancy.

Riley and Neitzel's experimental work was continued by Burguete et al. [22] who extended to a wider cavity of up to 250 mm. A slightly less viscous silicone oil was used (0.65 cSt) which resulted in HTWs prevailing up to depths of 4.0 mm for the same width as Riley and Neitzel [19] (30 mm). For depths below 1.8 mm, HTWs were well predicted by the theory of Smith and Davis [3], with the critical Marangoni number matching particularly well. Between depths of 1.8 mm–4.0 mm, vertical temperature gradients amplified buoyancy effects and the propagation angle and phase speed of the HTWs resembled those predicted by Mercier and Normand [17]. For depths greater than 4.0 mm, flow transitioned away from HTWs into stationary rolls.

HTWs have also been observed experimentally in annular geometries, having the advantage of avoiding any side-wall effects and resembling the conditions found in Czochralski method of crystal growth melts [21, 23, 24, 25]. In 2002, Schwabe and Benz [23] reported their experiments in an annular gap containing 0.65 cSt silicon oil ($Pr = 6.7$) conducted under microgravity aboard the Russian satellite FOTON-12. Removing the effects of gravity in space, they observed well defined HTWs which then transitioned into more complicated temperature oscillations at higher Ma. By conducting similar experiments back on Earth, Schwabe and Benz [23] reported the significant stabilisation of gravity on thermocapillary flow, with much higher Ma_{crit} required for instability under normal gravity. Peng et al. [26] followed several years later with a series of three-dimensional numerical simulations based on Schwabe and Benz's [23] experiments, specifically examining the characteristics of the thermocapillary-buoyancy driven flow under gravity. Their simulation results showed that in a shallow pool 1 mm in depth, HTWs characterised by curved spoke-like patterns are dominant. For intermediate depths between 2 mm and 4 mm, HTWs coexist with a three-dimensional oscillatory flow with both traveling around the annulus in the same azimuthal direction with the same angular velocity. For deep pools of depths greater that 5 mm, the flow transitions to stationary rolls with the flow pattern corresponding to Rayleigh-Bénard convection—driven by buoyancy rather than surface tension. However, Kuhlmann and Albensoeder [27] later showed using an energy budget from their stability analysis that the production of kinetic energy from buoyancy is relatively weak, even in deep layers. This would seem to rule out buoyancy as the direct cause for stationary rolls observed by Peng et al. [26] but Kuhlmann and Albensoeder [27] argued that buoyancy may be important to the instability indirectly as it influences the basic flow state and temperature fields.

With improvements in computing performance accelerating into the 21st century, more complex modelling approaches could also be adopted. Xu and Zebib [28] conducted numerical simulations on thermocapillary driven layers in two and three-dimensions using a finite-volume solver. In two-dimensions, Prandtl numbers ($Pr = \nu/\mu$) between 1 and 10 where investigated while varying the Reynolds number ($Re = \gamma_T \Delta T H/\mu\nu$) and the length to height aspect ratio of the layer. Note here that ν and μ are the kinematic and dynamic viscosities respectively, ΔT is the temperature difference between the hot and cold end walls, and H is the height of the layer. Xu and Zebib [28] found that unsteady flow develops when the aspect ratio exceeds a critical value, the size of which increases with decreasing Pr. Increasing Re also destabilised the layer, critical Re for instability (Re_{crit}) also increased with decreasing Pr. In three-dimensions, Xu and Zebib [28] investigated the influence of the front and back side walls on instability, specifically for $Pr = 4.4$ and $Pr = 13.9$. In both cases, side walls had an increasingly damping effect on oscillations the closer together they were, with larger Pr exhibiting greater damping for the same distance. In 2003, Sim et al. [29] also used a finite-volume approach for a model to complement their experiments in annuli under microgravity [24]. They too found Re_{crit} to depend on the aspect ratio. In accordance with previous studies, Sim et al. [29] also saw the increasing Bi increases the interface heat transfer and stabilises the flow. Around the same time, Bucchignani [30] used direct numerical simulations (DNS) to model the experiments conducted by Riley and Neitzel [19] in three-dimensions with the effects both of buoyancy and thermocapillary included. These simulations focused on a silicon oil depth of 1 mm with $Pr = 13.9$. HTWs were observed consistent with the observations of Riley and Neitzel [19] and the theoretical predictions by Smith and Davis [3]. In 2013, Sáenz et al. [31] took this a step further by fully modelling both the liquid and gas phases with DNS, while accounting for the deformable liquid-gas interface. They too observed HTWs consistent with Smith and Davis [3] but in addition reported interface deformations enslaved to the HTWs which were also found to affect the local interface heat fluxes. Recently, Lappa [4] examined by way for two-dimensional simulations, the effect a sudden change of cavity cross-sectional area—such as a backward facing step—on HTWs in high Pr layers. Interestingly, HTWs in high Pr layers could be completely suppressed with a step of sufficiently large thickness due to decreasing the available liquid depth.

2.3. Evaporating layers

In all of the works discussed previously, both numerical and experimental, measures were taken to suppress evaporation of the liquid while the temperature gradient was maintained artificially by external heating. Upon introducing evaporation, however, we have quite a different problem. To explain this, let us first consider a case with no external heating with evaporation present. When a liquid evaporates at an interface, it must consume latent heat from the system to liberate to a vapour. In a layer of liquid, a sufficiently high evaporation rate—consuming large amounts of latent heat—will cause the interface to cool, resulting in a vertical temperature gradient between the interface and the bulk. This is analogous to the layers heated from below such as those studied by Bénard and Pearson [7], the key difference being that the temperature gradient now arises naturally from evaporative cooling.

Merkt and Bestehorn [32] showed numerically that, similar to heated configurations, evaporation in liquid layers could cool the interface sufficiently to destabilise the layer—resulting in Bénard convection cells. The buoyancy term was omitted from their analysis, meaning Marangoni stresses had to be the cause of the instabilities. With liquid mass loss from evaporation causing the layer height to decrease over time, the magnitude of the vertical temperature gradient would constantly increase. This altered the mode of the instabilities, transforming the convective patterns from squares to hexagons and eventually, a non-convective state at small thicknesses. Already in collaboration with Merkt and Bestehorn [32], Mancini and Maza [33] subsequently released complementary experimental results with thin layers of volatile hexamethyldisiloxane (HMDSO) evaporating into a regulated atmosphere. Using shadowgraphy techniques, the expected convection cells predicted by Merkt and Bestehorn [32] were experimentally observed. Mancini and Maza [33] found that shrinking layer depth decreased the size of the convection cells while simultaneously increasing their number. Square cells, observed below depths of 0.8 mm transitioned to hexagonal cells at a depth of 0.5 mm, as predicted by Merkt and Bestehorn [32]. At thicknesses below this dryout occurred, characterised by destruction of the film [33].

Introducing heating back into the problem while retaining evaporation, Burelbach et al. [34] used linear theory to analyse the instabilities in evaporating and condensing liquid films residing on heated and cooled planes respectively. They reported the destabilising effect of the vapour recoil force exerted on the interface when liquid molecules are liberated to vapour—a theory previously proposed by Palmer [35]. Considering first the heated plane, the thinning film became more unstable over time from increased evaporation while the film residing on the cooled plane became thicker due to condensation, increasing its stability. Sultan et al. [36] extended the model of Burelbach et al. [34] to account for the dynamics of the vapour phase. As expected, they found Marangoni flow to be the main driver of instability while evaporation of the heated layer interestingly had a stabilising effect. Guo and Narayanan [37] explained the stabilising effect of evaporation being due to the reduction in temperature of local hot spots from increased local evaporation rate. Guo and Narayanan [37] also showed that the vapour flow field plays a stabilising role due to always flowing from cold (low pressure) regions to hot (high pressure) regions. Stabilising effect of the vapour flow was also documented by Ozen and Narayanan [38]. Additionally, McFadden et al. [39] demonstrated that the entropy differences between the vapour and liquid impacts stability in both heated and non-heated evaporating layers.

Researchers began to look further into the effects of the vapour phase. Kanatani and Oron [40] examined, using linear stability analysis, the impact of varying vapour pressure—which naturally changes with temperature. Variations in interface vapour pressure could therefore arise in locations where interface temperature fluctuates—for example due to the presence of HTWs. The mechanism is simple: vapour pressure increases around areas of heated liquid, pushing on the interface from the vapour side; vapour pressure decreases around areas of cooled liquid, pulling on the interface from the vapour side. Kanatani and Oron [40] concluded that vapour pressure is destabilising when the liquid side is heated, acting against the stabilising effects of gravity. Recently, Sáenz et al. [41] extended their two-phase DNS model used to study saturated layers [31] to include the effects of phase change, subsequently examining the resultant effects this has on HTWs. Sáenz et al. [41] found that the latent heat consumed from evaporation tended to suppress the HTW instabilities while the level reduction of the layer as it evaporated had an amplifying effect on the physical waves at the interface. This was attributed to the suppression of gravitational effects with reduced layer mass. Convective patterns in the gas phase induced by the HTWs were also revealed. There impacted the local evaporation flux and vapour concentration at the interface, with the highest vapour concentration found above hot spots—as previously predicted by Kanatani and Oron [40].

All of the above work dealt with single-component fluids. This work will present a novel three-dimensional, two-phase, two-component direct numerical simulation framework to resolve the instabilities and to capture phase-segregation in binary liquid layers.

2.4. Binary component layers

Marangoni flows in pure liquid layers arise solely due to thermocapillary effects (thermal Marangoni stresses). With the addition of a second miscible component, solutocapillary effects (solutal Marangoni stresses) now also influence the flow. Solutocapillary works on the premise that each component in a miscible binary mixture possess a different surface tension to the other. This means that local concentration gradients arising on the interface (from evaporation or by other means) will also cause surface tension gradients, giving rise to solutally induced Marangoni flow. This new form of Marangoni flow has the potential to enhance or suppress thermally induced Marangoni flow, depending on the component properties. Assuming a an ideal mixing law, which often not the case (e.g., the self-rewetting liquids), the surface tension variation with temperature given in eq. (2.1) can be extended to a binary mixture via [42],

$$\sigma = \sigma_o - \gamma_T(T - T_o) - \gamma_C(C - C_o) \tag{2.2}$$

where $\gamma_T = (\partial\sigma/\partial T)_C$ is the temperature coefficient of surface tension at constant concentration and $\gamma_C = (\partial\sigma/\partial C)_T$ is the concentration coefficient of surface tension at constant temperature. The change in concentration from the reference state of surface tension, σ_o, is given by, $(C - C_o)$, and is usually measured in (dimensionless) mole or mass fraction.

In addition to complicated surface effects, binary layers subject to imposed or maintained temperature gradients can exhibit spontaneous fluid motion due to thermophoresis (also known as the Soret effect). The Soret effect describes the preferential migration of components in a mixture under a temperature gradient, leading to mass separation. Each species in the mixture reacts in a unique way to the force from the temperature gradient. For example, the denser species tends to migrate to colder areas and vice versa for the less dense species [43]. The effect was first discovered by the Swiss scientist Charles Soret in 1879 [44] by noticing that a sealed tube of salt solution did not remain uniform in composition when a temperature gradient was applied over its length. The strength of the thermally induced diffusion is commonly described by way of the Soret coefficient (S_T), simply being the ratio of the thermodiffusion coefficient ($\mathcal{D}_T$) over the molecular (isothermal) diffusion coefficient ($\mathcal{D}$) associated with Fick's Law. In mathematical terms, $S_T = \mathcal{D}_T/\mathcal{D}$ [45]. S_T has units of K^{-1} and the sign (positive or negative) indicates the direction of migration—with or against the temperature gradient. Typically, S_T has a magnitude of 10^{-3}–10^{-2} K^{-1}, and although small, can have significant implications. Notable examples include the microstructure of the ocean and convection in stars [45].

One of the first experimental studies into the combined effects of a lateral temperature and concentration gradient in a liquid test cell was carried out by Kamotani et al. [46] in 1985. Using a copper sulphate electrolyte, the application of a voltage through a pair of electrodes caused copper to dissolve into solution at the anode and be deposited at the cathode, hence creating a lateral concentration gradient. The test-cell remained enclosed meaning there was no surface tension effects, rather, Kamotani et al. [46] demonstrated that convection patterns were influenced by the competition between thermal and solutal buoyancy. The year later, Bergman [47] considered numerically a binary liquid layer in a rectangular cavity with a liquid-vapour interface and only Marangoni induced convection, removing any complications from buoyancy. Bergman [47] went on to focused specifically on the situation where thermal Marangoni stress equally opposes solutal Marangoni stress, resulting in an overall Marangoni number (the sum of the opposing forces) equal to zero. Even the layer was expected to be motionless, Bergman [47] found that convective motion still occurred. This was due to double-diffusive Marangoni convection—analogous to double-diffusive convection driven by density gradients, however, in this case due to surface tension.

In 2004, Bergeon and Knobloch [48] performed three-dimensional simulations on binary layers with *non-deformable* (flat) interfaces with the inclusion of the Soret effect. The interface was heated and the bottom wall maintained at a constant temperature, inducing a vertical temperature gradient. Surface tension varied linearly with temperature and concentration as in eq. (2.2), while buoyancy was discounted. Interface oscillations were observed, resulting directly from concentration induced changes in surface tension from component migration driven by the Soret effect.

In 2015, Yu et al. [42] presented a series of experiments on alkane mixtures confined in a laterally heated annular geometry. Pure hexane was used as a reference case while the mixtures investigated included decane-hexane, toluene-hexane and benzene-heptane in various concentrations corresponding to $5.52 \leq Pr \leq 8.03$. A plexiglass shroud covered the annulus to suppress liquid evaporation and air convection, achieving a motionless and saturated gas phase. Focusing on a 50 wt.% decane-hexane mixture of depth 2.2 mm, Yu et al. [42] observed HTWs using infrared thermography at wall-to-wall temperature gradients from as low as 1.9 K to as high as 11 K. They reported the temperature for the critical onset of HTWs to be lower in all binary mixtures than for pure hexane, suggesting that the Soret effect played a destabilising role in the flow. It was suggested that this could be due to the migration of decane to the cold side of the annulus under the Soret effect. Since decane has higher surface tension than hexane, the higher concentration would raise the surface tension gradient beyond the purely thermally induced gradient, lowering Ma_{crit}. They also reported that increasing layer depth in both the pure and binary cases resulted in a lower Ma_{crit}, leading to HTWs taking hold at lower temperature gradients. This casts some doubt of the role of the Soret effect since it is possible that buoyancy is destabilising the flow in deeper layers.

What is not clear is the authors criteria for defining HTWs—as layer depth increases so does the effects of buoyancy, meaning Rayleigh-Bénard instability will take over from the Rayleigh-Marangoni instability at greater depths [26]. This means it is not possible to determine the exact mechanism driving the observed thermal disturbances and whether or not the Soret effect played any role in the instability as the layer depth increased.

Yu et al. [49] subsequently released a second paper modelling a similar problem numerically in three-dimensions with a moderate Pr of 9.08. A single phase approach was taken with a rigid, non-deformable LV interface and no vapour phase. The Soret effect was accounted for in the advection-diffusion equation along with Fick's law. The model replicated the experimental results in their previous study [42], with a thicker layer destabilising the flow due to buoyancy. In addition, Yu et al. [49] noted the lateral concentration gradient depended strongly on the temperature gradient—due to the increased strength of Soret diffusion. The denser component (decane) would gather in colder areas near the inner cylinder, as was surmised from their experiments. A later publication by the same authors [50] confirmed that increasing the initial concentration also destabilised the layer since the Soret induced concentration gradient at a given temperature is larger. As well as surface temperature oscillations, small magnitude fluctuations in surface mass fraction in the order of $\pm\ 10^{-5}$–10^{-4} were also observed. There was a phase lag between the temperature and concentration oscillations. Chen et al. [51] and Yu et al. [52] used the same model to investigate the special case when the solutocapillary and thermocapillary forces are equal and opposite—similar to Bergman [47]. The strength of thermocapillary force was quantified by Re_T and solutocapillary force by Re_C, with equal and opposite forces defined by a capillary ratio, R_σ, of -1:

$$R_\sigma = \frac{Re_C}{Re_T} = -1 \tag{2.3}$$

Keeping R_σ constant and increasing the opposing capillary forces, the oscillatory flow bifurcates through several modes. From travelling waves, to stationary waves, to vibrating spoke patterns [51]. In 2017, Yu et al. [53] release another study using the same model again but this time examining an extremely low Pr fluid of 1.37×10^{-3} By decreasing R_σ from 0.2 to -2, Yu et al. [53] reported the decrease in the critical Re_T required for the onset of oscillatory flow. Seven oscillatory flow patterns were observed with patterns at $R_\sigma < -0.8$ being more distinct than patterns at $R_\sigma > -0.8$ [53].

The numerical model of Yu and co-workers [49, 50, 51, 52, 53] provide a valuable insight into the flow dynamics and stability of binary liquid layers. However, there are some major simplifications in their model such as only considering the liquid phase, neglecting the flow features of the deformable interface and additionally the gas phase dynamics which have previously been shown to be important in single component layers [31, 54]. Additionally, the added effect of evaporation has yet to be examined in any great detail in binary layers, aside from a recent model by Rieks and Kenig [55].

As seen above, most work concerning binary mixtures either assume a non-deformable and adiabatic interface or assume a one-sided approximation (i.e. the vapour phase has no role to play). Each of these assumptions are far away from reality and therefore, render their results valid for very limited conditions. In reality, the interface is always wavy (as shown by Sáenz et al. [31] and references therein) and there is strong interaction between the vapour and liquid phases during phase-change as shown by Sáenz et al. [41]. The work described in this thesis will present a novel three-dimensional, two-phase, two-component direct numerical simulation framework to resolve both the interface fluctuations, thermocapillary and solutocapillary instabilities, strong vapour phase interaction, and capture phase-segregation in binary fluids.

3. Sessile droplets: pinned and dynamic conditions

A sessile drop evaporating from a solid substrate is central to a wide variety of processes. Examples range from spray cooling of microelectronics [1, 56, 57] to inkjet printing [58, 59], pesticide deposition [60, 61] and even disease diagnosis [62, 63, 64]. At first glance an evaporating drop may seem like a simple scenario. However, a closer look reveals rich and complex phenomena which, despite significant research interest, remains poorly understood.

Complexity arises from the sheer number of factors governing sessile drop dynamics. Behaviour is heavily influenced by properties of the solid substrate, including substrate roughness [65, 66, 67] and conductivity [68, 69]; the liquid, including surface tension and volatility [70, 71]; and the surrounding gas, including atmospheric pressure [72], humidity [73] and vapour properties [74]. In addition, the dynamics are strongly dependent on the temperature of each phase [75, 76, 77], drop shape [78], and gravity has increasing impacts as volume increases [79, 80]. Further complications emerge with the suspension of polymers or nanoparticles [81, 82, 83], the dissolution of surfactants [84, 85] or salts [86, 87], and the introduction of additional miscible and/or immiscible liquids [88, 89, 90]. Finally, there are even examples of electric fields having significant impacts [91].

A sessile drop is rarely at true equilibrium due to persistent evaporation. Evaporation in non-volatile drops tends to be limited by the diffusion of vapour away from the interface [92, 93] whereas more volatile liquids can be modelled using kinetic theory and interface non-equilibrium effects [94, 95]. Depending on wettability, drops can either spread and completely over the substrate, forming a pancake with a zero contact angle, or they can become pinned at the triple contact line (where the three phases meet), settling at an equilibrium contact angle. In both cases, once spreading is finished, evaporation soon takes over and drop profile changes, making the non-equilibrium nature of the problem clear.

The work in this thesis (contained in Parts III and IV) is concerned with the non-isothermal evaporation of thin volatile drops consisting of miscible binary mixtures

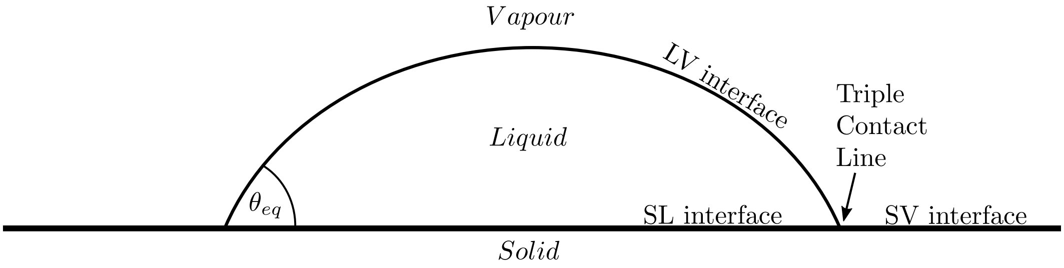

Fig. 3.1 Two-dimensional illustration of a pinned drop with equilibrium contact angle θ_{eq} resting on a solid substrate bounded above by vapour.

achieving complete wetting or a very low contact angle. This bears a direct resemblance to the later stages of a two-phase cooling mechanism, e.g. for microelectronics, where the cooling liquid film approaches dry-out and drops begin to form. Binary drops display distinctly different behaviours from the single component equivalent.

3.1. Basic physics and fundamentals

When a drop comes into contact with a surface, it seeks to minimise its surface energy and reach equilibrium. This manifests as the triple contact line (TCL), the meeting point of solid, liquid and vapour, where a finite contact angle between the solid-liquid (SL) and LV interfaces forms. This behaviour was first explained by British polymath Thomas Young and this in turn lead to the concept of surface tension. In 1805 Young released his work “An essay on the cohesion of fluids” [96] where he detailed various experimental observations between a solid, liquid, and vapour. Young posed that the interface between a liquid and vapour behaves like a membrane under tension, adhering to the contacting solid surface. He observed the reproducibility of a constant contact angle between liquids and solids, the value being dependent on the substances used. The Young equation describes his observations mathematically, giving the interfacial force balance between the three phases, resulting in the prediction of the contact angle at equilibrium [97]:

$$\sigma_{SV} - \sigma_{SL} - \sigma_{LV} \cos\theta_{eq} = 0 \tag{3.1}$$

Here, σ signifies the free energy per unit surface, or surface tension, of an interface and the subscript refers to the interface in question; solid-vapour (SV) being the only one not previously defined. σ_{LV} is the only interface tension that can be experimentally measured and is what is typically referred to as “surface tension”. θ_{eq} is the equilibrium contact angle formed between the SL and LV interfaces. It is clear that there is a delicate interplay between the adhesive and cohesive forces. Explained by energy minimisation, SV energy is minimised by the spreading of the liquid over the solid, minimising the area of the SV interface exposed. Areas of both the SL and LV interface are minimised by the liquid being drawn toward the drop centre, resulting in the drop contracting inwards. This leads to the understanding of σ_{SL} and σ_{LV} as cohesive forces and σ_{SV} and an adhesive force.

The year following Young's publication, the French scholar Pierre-Simon Laplace released his fourth volume of "Traité de Mécanique Céleste" [98] where he expanded on Young's observations. Laplace provided the mathematical derivation of what is now known as the Young-Laplace equation, giving an expression for the pressure discontinuity sustained over an interface, causing it be become curved:

$$\Delta p = \sigma\left(\frac{1}{R_1} + \frac{1}{R_2}\right) = 2\sigma\kappa \tag{3.2}$$

The excess in pressure, Δp, is known as the capillary pressure, σ denotes the surface tension of the LV interface, R_1 and R_2 are the principle radii of curvature of the interface, and κ is the mean curvature. At any defined point on the interface, R_1 and R_2 are orthogonal to each other and so for a perfect sphere, for example, both are equal to the sphere radius. κ is then the mean curvature of the interface resulting the radii of curvature. An important aside is that eq. (3.2) only begins to dominate the physics when hydrostatic pressure (caused by gravity) becomes negligible, allowing surface tension to become the most significant force. Comparing the relative strength of capillary to hydrostatic pressure leads to the capillary length, $L_c = \sqrt{\sigma/\rho g}$, below which gravitational forces are assumed negligible [99]. Here, ρ and g are the liquid density and gravitational acceleration respectively.

As we already know from Chapter 2, when the effects of gravity dwindle and surface tension dominates, variations in temperature will invariably cause Marangoni flows to arise. These flows have a strong influence on small drops, dictating much of their behaviour. Defined simply as the flow of liquid from low to high surface tension, the effect was named after Italian physicist Carlo Marangoni who was the first to propose a clear model for the phenomenon, identifying that surface tension gradients can be due to variations of temperature and composition [100]. The dependence of surface tension on composition was actually explained a decade earlier by James Thompson, who, in 1855 was studying the tears of wine problem. He correctly identified that the tendency of alcoholic beverages to climb the sides of the glass was due to an uneven alcohol concentration, increasing the surface tension and pulling the liquid upwards [101]. This has come to be known as solutal Marangoni flow. Solutal Marangoni will only arise in liquids with multiple components or interfacial impurities such as surfactants [83] and can either enhance or suppress thermally induced Marangoni, depending on the conditions.

Due to the breadth and depth of the field, we cannot expect to cover all areas of drop research in this review. We will restrict ourselves to the most relevant topics required to frame the work in this thesis. For comprehensive reviews spanning the field, the reader is directed to [97, 102, 103, 104, 105, 106, 107, 108].

3.2. Droplet evaporation

A sessile drop is rarely at true equilibrium due to persistent evaporation. For relatively non-volatile drops evaporating close to ambient pressure and temperature, the evaporation time is slow and generally accepted to follow the diffusion-limited evaporation model [92, 93]. The mechanism is explained as follows; as vapour molecules are liberated from the liquid, the gas in the immediate vicinity of the drop becomes saturated with its vapour. Once saturation vapour pressure is reached, the rate limiting step becomes the diffusion of vapour away from the drop to a far field value. For more volatile liquids, diffusion can cease to be the rate limiting step and kinetic theory using interface non-equilibrium effects can be employed [94, 95].

The well-known paper by Picknett and Bexton [109], now over 40 years old, was a landmark development. The authors studied pinned drops of methyl acetoacetate evaporating from polytetrafluoroethylene (PTFE) substrates. They identified two distinct behaviours during evaporation. Drops would either evaporate with a constant contact angle (CCA), where the contact line recedes with the original contact angle being retained, or with a constant contact radius (CCR), where the contact line remains fixed and the drop height decreases with evaporation. In addition, they formulated a theoretical model to explain drop evaporation. They proposed that as evaporation occurs, the atmosphere just above the LV interface will rapidly become saturated with liquid vapour. For evaporation to proceed further, vapour at the interface would have to diffusive through the atmosphere to a far field value. This is comparative slow compared with the liberation of molecules from liquid to vapour and so is the rate limiting step in evaporation. This is hence known as diffusion-limited evaporation and Picknett and Bexton's model to describe it has become known as the "basic model". The use of this model in the isothermal case has been verified by other researchers such as Poulard et al. [110].

When evaporation is diffusion limited, it is intuitive to see that the rate can be increased by raising the temperature—increasing the saturation vapour pressure, or by increasing the rate of diffusion in the surrounding atmosphere. Sefiane et al. [72] investigated the effects of pressure with three different atmospheres; helium, nitrogen, and carbon dioxide, on the evaporation rate of water drops. Water vapour has a unique diffusion coefficient in each gas and so Sefiane et al. [72] predictably saw faster evaporation for higher diffusion coefficients. In addition, each gas was run at a range of reduced pressures. For all cases measured, the lower the gas pressure, the faster evaporation took place, suggesting that the diffusion coefficient increases with decreasing pressure.

Diffusion-limited evaporation in the basic model works under the assumption of a motionless gas phase with no convective effects. In 2006, Shahidzadeh-Bonn et al. [74] suggested that while the basic model may accurately predict evaporation of organic drops, it is not sufficient for water drops. They suggested that since water vapour is lighter than the surrounding air, buoyancy effects act in compliment to diffusion and transport vapour away from the interface, increasing the evaporation rate. Additionally, it has been seen that for organic drops such as alkanes, the dense vapour sinks, compressing the vapour concentration gradient and inducing a convective flow away from the drop [111]. Convective gas flows can also be caused by sufficiently strong evaporation due to the sudden change in gas phase density as vapour is rapidly liberated from the liquid [112]. Moreover, if the substrate is heated, thermal convection of the gas phase results—caused by the gas temperature gradient near and far from the substrate [113]. The basic model also fails to consider the effects of evaporative cooling whereby the interface is cooled by the evaporating liquid giving up its latent heat, the effect becoming more profound if volatility increases [114]. In 2008, Dunn et al. [115] published amendments to the basic model to account for evaporative cooling which produced good qualitative agreement with experiments. Dunn's model was however limited to small contact angles but this has been addressed recently by Tran et al. [116]. Thermal conductivity of the substrate has also been shown to have a great influence [117] with an amended model for this also being provided by Dunn et al. [69]. The influence of the substrate is discussed further in Section 3.4.

As eluded to above, for drops evaporating into air under isothermal conditions, the diffusion-limited basic model tends to accurately describe the behaviour. Modifications have been made to account for evaporative cooling and substrate conductivity, however there are cases where an altogether different model is appropriate. When drops are heated or particularly volatile [118], in purely vapour atmospheres [119, 120, 104], unstable [121], or very small [122, 123], diffusion can cease to be the rate limiting process and non-equilibrium effects at the interface begin to play a more prominent role. In 1988, Burelbach et al. [34] derived a model to study horizontal liquid layers using kinetic theory from Palmer [35]. This was a so-called "one-sided" model where the vapour density, viscosity and thermal conductivity are assumed negligible, avoiding the need to model the gas phase. An advantage of this is that the position of the LV interface can be determined without the need to model the actual vapour flow. This was subsequently extended by Ajaev [95] and others [94, 119, 120] to model thin volatile drops evaporating from heated substrates. The variety of approaches used to model drops will be covered further in Section 3.7.

Most work considered above is concerned with sessile drops solely of pure fluids. In this thesis, we focus on sessile drops made up of binary mixtures—with components having contrasting volatilities, latent heats and other properties.

3.3. Contact line pinning and spreading

When a drop is deposited on a flat solid surface (the substrate), it can adopt one of two equilibrium regimes; partial wetting, where the contact line is pinned to the substrate with a finite contact angle; or complete wetting, where a flat macroscopic film wets the entire surface giving a contact angle of zero [97]. Each regime can be described by revisiting Young's eq. (3.1). For a partial wetting drop with a non-zero equilibrium contact angle, the cohesive forces of σ_{SL} and σ_{LV} are larger than the adhesive force of σ_{SV}, i.e., $\sigma_{SV} \leq \sigma_{SL} + \sigma_{LV}$. Therefore, the surface energy is minimised by inward motion of the drop, resulting a finite contact angle. For a completely wetting drop with zero contact angle ($\theta_{eq} = 0$), a special case arises from the fact that $\cos\theta_{eq} = 1$, yielding; $\sigma_{SV} = \sigma_{SL} + \sigma_{LV}$. This means cohesive and adhesive forces are perfectly balanced. We will review the work on partially wetting pinned drops first before moving on to wetting drops with moving contact lines.

The pioneering work of Picknett and Bexton [109] in 1977 identified that pinned drops (those with a non-freely moving contact line) could evaporate in CCA or CCR modes. They reported that drop mass decreases in a power law with the contact radius during the CCA mode and linearly with contact angle during the CCR mode. Evaporation in the CCR mode would always result in shorter lifetimes. Birdi et al. [124] reported that in the CCR mode, overall evaporation rate is higher for larger drop radii, meaning that larger drops evaporate more rapidly, losing volume faster than smaller ones. Rowan et al. [125] then examined the height of pinned drops evaporating in the CCR mode and uncovered a power law dependence of mass loss with height.

In 1995, Bourges-Monnier and Shanahan [92], conducted experiments on pinned drops of either n-decane or water on various smooth and rough substrates. They reported the impact of substrate roughness, showing that drops tended to evaporate in four distinct stages, mixing the CCA and CCR modes with pinning/de-pinning behaviour of the contact line. This has come to be known as the stick-slip (SS) model. Subject to numerous investigations, Sefiane and Tadrist [126] studied the effects of pressure, temperature and surfactants on the SS behaviour while Moffat et al. [127] along with Orejon et al. [82] explored fluids with added nanoparticles and changing substrate hydrophobicity. In the absence of large surface tension gradients, the pinning/de-pinning behaviour can be explained by an unbalanced Young's force—see eq. (3.1). Pinning and de-pinning forces are balanced at equilibrium, the contact line held by chemical and surface heterogeneities dictating the drop profile. Mass loss from evaporation alters the drop profile, deviating the drop from equilibrium and causing the contact line to de-pin and recede before settling pinned again where forces are balanced once more.

1997 saw another leap in understanding as Deegan et al. [128] explained the tendency for a drop containing dispersed solids to arrange the particles in a ring visible after evaporation—the so-called "coffee-stain" problem. They proposed that a pinned contact line induces an outward radial flow, due to fluid rushing from the bulk to the drop edge as it replenishes liquid evaporating from the contact line. This was verified with a theoretical model from the same authors in 2000 [129] where they also reported that if the contact line was not pinned, there would be no radial flow and the contact line would recede inward as evaporation occurs. In 2005, Hu and Larson looked more closely at the interior flow using a finite-element model both with [130] and without [131] thermal Marangoni effects. Popov [132] also investigated the spatial deposition of solute particles by employing an analytical model while assuming a finite volume was occupied by the solute particles. Hu and Larson saw that for pinned drops in the absence of thermal Marangoni stress, flow was always directed radially outwards. However, upon the introduction of thermocapillarity, Marangoni flows would drive fluid recirculation against the outward radial flow. The effect was profound in drops with large contact angles while having negligible impact for small contact angles. This was due to evaporative cooling at the contact line, where the evaporation rate is highest. The cooler, higher surface tension liquid draws flow along the interface from the drop apex to the contact line, acting against the outward radial flow from the bulk. In 2006, Hu and Larson [133] verified this with experiments and showed that Marangoni flow, if strong enough, can reverse the flow and suppress ring formation in pinned drops. Therefore, in order for the ring-stain explained by Deegan et al. [128] to form, the contact line must be pinned and Marangoni-induced flows weak.

The works covered up to this point assume a perfectly hemispherical drop, a reasonable assumption but rarely found in nature. In 2015, Sáenz et al. [78] used DNS to model a pinned drop with a non-spherical contact area. They discovered the emergence of azimuthal currents and pairs of counter-rotating vortices in the bulk flow, induced by the irregular geometry. The non-circular contact area changed the local interface curvature which in turn affected the local evaporation rate, causing powerful Marangoni induced bulk flows not present in axis-symmetric drops.

In contrast to the coffee-stain problem, the contact line of a completely wetting drop (provided it is deposited on a smooth surface) is free to move throughout its lifetime. Such surfaces are of high energy compared to the liquid [97] and are described as having high wettability. Drop behaviour on a high wettability surface typically consists of fast initial spreading of the contact line with the drop quickly achieving a maximum radius greatly exceeding its height. Depending on liquid volatility, the contact line then oscillates weakly around that position (duration increasing with decreasing volatility) before retracting as evaporation takes over and the drop recedes until disappearance [134]. An explanation of this behaviour can again be obtained by revisiting Young's eq. (3.1). Assuming θ_{eq} is equal to zero and rearranging eq. (3.1), we arrive at an expression for the equilibrium spreading parameter, S_{eq} [102]:

$$S_{eq} = \sigma_{SV} - (\sigma_{SL} + \sigma_{LV}) \tag{3.3}$$

This difference in surface tensions measures the free energy of the SV interface relative to its complete wetting value. It is easy to see that for a partial wetting scenario, such as the coffee-stain problem, S_{eq} must be negative since the cohesive effects of σ_{SL} and σ_{LV} will dominate over the adhesive σ_{SV}. For the complete wetting case, ($S_{eq} = 0$), adhesion perfectly balances cohesion, meaning liquid will spread to form a layer of macroscopic thickness covering the surface at equilibrium, effectively eliminating the LV interface [135]. However, for a drop spreading on a dry surface, equilibrium is rarely achieved—taking up to several days for a strictly non-volatile drop such as silicon oil [136]. This leads us to the case of a positive wetting parameter, representing the strictly non-equilibrium regime before complete wetting is achieved. Eq. (3.3) can be re-defined in terms of an initial spreading parameter, S_i, made more appropriate for a drop spreading on a dry substrate [102]:

$$S_i = \sigma_{SO} - (\sigma_{SL} + \sigma_{LV}) \tag{3.4}$$

Here σ_{SO} is the surface tension of the dry substrate rather than the SV interface. Rather than an equilibrium value, S_i gives the initial driving force for a deposited drop to spread, with non-negative values establishing a wetting scenario.

An important property as films spread and become increasingly thin is the disjoining pressure, introduced by Derjaguin in 1940 [137]. Considering a microscopically thin nonpolar film, molecular forces between the liquid and solid become important. For a film of molecular thickness, all of the liquid molecules are attracted to the solid substrate by way of van der Waals interactions [138]. This is in contrast to a thick film consisting of multiple layer of liquid molecules where only the bottom layer adjacent to the solid is attracted by van der Waals—leaving the vast majority unattractive. If the molecular attraction between the liquid and solid is strong enough, the system will attempt to lower its free energy by compressing the film [102]. This decreases the distance between the SL and LV interfaces leading to overlap in these transition zones [139]. The overlap causes a repulsive force between the two interfaces and it is this repulsive force that is referred to as the disjoining pressure, $\mathit{\Pi}$. For a film of thickness, h, the disjoining pressure resulting from van der Waals interactions is defined by [140],

$$\Pi(h) = \frac{\mathscr{A}}{6\pi h^3} \tag{3.5}$$

where $\mathscr{A}$ is the Hamaker constant.

The viscous spreading rate of small non-volatile wetting drops is generally accepted to obey Tanner's law [141]. This states that the increase drop in radius is proportional to the spreading time to the power of an exponent—one tenth for capillary-driven spreading ($R \propto t^{1/10}$) [134]. This power law was verified experimentally by researchers such as Cazabat and Cohen Stuart [65], Chen [142], and Chen and Wada [136]. Tanner's law is independent of the substrate surface chemistry and so the spreading coefficient (providing the substrate is smooth). This due to the formation of a microscopically thin film ahead of the perceived contact line, stabilised and supressed from evaporation by the disjoining pressure—known as the precursor layer [97]. First noticed by Hardy [143] a century ago and subsequently detected experimentally years later [144, 145]. Recently, the precursor layer has been detected advancing ahead of partial wetting drops using atomic force microscopy (AFM) [146]. It is important to note that in the very early initial stages after drop deposition, spreading is significantly faster. This is due to the sudden availability of capillary energy when the drop touches the solid and is known as the inertial spreading phase. For low-viscosity liquids such as water, the radius growth rate is proportional to time to the square root of time; $R \propto t^{1/2}$ [147].

When a wetting liquid becomes volatile, the non-equilibrium contact angle can be non-zero [102]. Elbaum and Lipson experimentally studied a volatile water film completely wetting a mica substrate [148]. They noticed that while the condensing film completely wetted surface, when evaporation was introduced, a de-wetting effect occurred, leaving apparent dry patches. They later concluded that evaporation causes a wetting film to become effectively non-wetting, taking form as a stable drop on top of a thin film [149]. They noted the size of the non-zero contact angle to be a function of LV surface tension and partial pressure, demonstrating its inherent non-equilibrium nature.

Cachile and co-workers [134, 150] investigated, both experimentally and theoretically, completely wetting alkane drops on isothermal surfaces of silicon and mica. By selecting alkanes, evaporation was firmly in the diffusion limited regime. A film advancing ahead of a hexane drop was clearly captured [134], however they concluded that for this to be a precursor film immune from evaporation, the depth was required to be in the region of 1 nm, making it not visible to the camera [150]. Cachile et al. [134] reported initial radial spreading exponents up to the power of 0.16 with time (0.1 for Tanner's) due to temperature induced Marangoni flows driving the drop outwards. Considering the receding contact line and assuming, $R \propto (t - t_0)^n$, where R is the drop radius and

t_0 is the time of vanishing, they found that the exponent n was close to 0.5 for all alkanes tested. Although very small, ($\sim 0.01°$), non-zero contact angles resulting from evaporation were also observed, the angles decreasing with time. Poulard et al. [151] subsequently found n to be larger for receding water on mica at $n = 0.6$, resulting from an increase in evaporation rate Shahidzadeh-Bonn et al. [74] attributed to the effects of water vapour buoyancy. In 2005, Poulard et al. [152] proposed a model generalising Tanner's law for evaporating drops. Recently, Jambon-Puillet et al. [153] found the non-equilibrium receding contact angle in alkane wetting drops on clean glass surfaces to be proportional to one third of the evaporation rate.

Guéna et al. [154] extended the research on wetting alkanes to various alkane mixtures and found remarkable behaviour in that binary mixture drops tended to spread and evaporate faster than either of their single component counterparts. Spreading would deviate from Tanner's law, with the spreading exponent rising to $n = 0.3$ ($R \propto t^n$). This behaviour was owing to the solutal Marangoni effect. Mixtures were carefully selected so that the LVC had a higher surface tension than the MVC. The preferential evaporation of MVC at the contact line would leave a higher concentration of LVC and hence a higher surface tension compared to the bulk. The surface tension gradient would induce Marangoni flows towards the contact line, enhancing the capillary force and, as a result, the spreading rate. Drops would spread to minimum thickness more quickly than their single components counterparts and reach dry-out faster due to enhanced evaporation from the reduced interface thickness. Depending on the initial concentration, interesting drying profiles were observed, such as the drop centre drying out before the contact line, leaving a torus shaped ring. Further works on multicomponent drops are reviewed in Section 3.6.

The topic of enhanced drop spreading leads us on to the effects of surfactants. It has long been know that drop spreading can be improved by adding a surface-active agent (or surfactant) to the liquid [102]. Structurally, surfactant molecules tend to have a hydrophilic part—attracted to the liquid, and another part with a higher affinity for another phase. Surfactants are therefore adsorbed at interfaces, altering the interface free energy (SL and/or LV interfacial tensions) [155]. Some surfactants, such as trisiloxanes, can increase spreaded drop area to 25 times larger than a pure water drop with a generic surfactant [155]. Trisiloxanes are classed as superspreaders, meaning that the exponent, n, takes larger values in the ranges of $n = 0.16$–1 [156]. The dynamics behind surfactant superspreading remained elusive for some time [102], with Karapetsas et al. [85], in 2011, suggesting a plausible mechanism for trisiloxane enhanced spreading. For a surfactant-laden particle deposited on a hydrophilic substrate, the adsorption of trisiloxane molecules from the LV interface contact line directly to the substrate initiates the spreading. As the drop spreads, the continuously depleted surfactant from the LV interface is replenished from the bulk, inducing high Marangoni stresses close to the drop edge and driving fast spreading. They reported spreading exponent of $n = 1$ or higher and additionally saw the formation of a contact line ridge while the drop spread outwards, forming an outer rim of thicker liquid. This has been observed experimentally with trisiloxane-laden drops [156] as well as bearing remarkable resemblance to selected drops in the study of Guéna et al. [154].

A final point worth mentioning about wetting drops is that their thin profile and low contact angle lends them particularly well to modelling with lubrication theory. The lubrication approximation exploits the disparity in length scale between the height and width of the drop to formulate simplified governing equations in terms of thickness—see [157]. This method was first used for modelling drops by Ehrhard and Davis [158] who studied the role of thermocapillarity in wetting drops on heated substrates. Subsequently extended to include evaporation by Anderson and Davis [94], the later the inclusion of a precursor layer was made by Ajaev [95]. Karapetsas et al. [85] also used a lubrication -based model with precursor layer to elucidate the surfactant superspreading mechanism described above. While suited perfectly to liquid films, lubrication theory has been shown to be acceptably accurate for drops with contact angles up to 40° [130, 131]. Further discussion of the typical modelling approaches used for drops will be discussed further in Section 3.7 with the effects of substrate temperature being covered next in Section 3.4.

As seen above, a vast amount of previous work is dedicated to the study of pure sessile drops or the ones with surfactants (such as trisiloxanes) adsorbed on the interface. This thesis demonstrates the spreading of evaporating binary mixture drops through modelling and experiments.

3.4. Substrate influences

As far back as 1986, Cazabat and Cohen Stuart [65] noticed the effect substrate roughness could have on wetting drops. For smooth surfaces, Tanner's Law is obeyed and radius expansion is proportional to one-tenth of the spreading time. However, when surface roughness is introduced, they noted a deviation from the conventional behaviour. After initial spreading, the drop edges spread rapidly with an exponent, $n = 0.25$–0.5, appearing to fill the roughness of the substrate. The drops formed a thin film with a spherical cap retained in the centre which gradually flattened as the drops spread again at a reduced rate.

Continuing with wetting drops, Ehrhard and Davis [158] proved theoretically and then Ehrhard [159] experimentally that cooled substrates enhance spreading while heated substrates suppress it. This effect can be explained by thermocapillarity. A cool substrate will cause the contact line region, where the liquid is thinnest, to become colder than the bulk. A higher surface tension at the contact line results and Marangoni flow towards the contact line is enhanced, complementing capillary forces and driving spreading. A heated substrate will have the opposite effect, causing Marangoni flow away from the contact line which acts against the capillary spreading force. Ajaev [95] also drew similar conclusions with a lubrication-based model including the precursor layer, noting the delicate interplay between evaporation and capillary spreading. At large values of substrate superheat, Ajaev [95] reported that high evaporation would prevent initial spreading, causing the drop to remain thick. The system would then reach a quasi-steady regime characterised by slow evaporation and weak fluid flow.

Substrate temperature also affects the behaviour of partially wetting drops. In 2004, Mollaret et al. [160] reported the influence of substrate temperature on the pinning/de-pinning behaviour of water drops on PTFE and aluminium, verifying their experiments with a numerical model. They found that increasing temperature suppressed contact line de-pinning, with drops remaining pinned for substrate temperatures above 80 °C. This can be explained by the Young's force balance at the triple line—eq. (3.1). Increasing temperature weakens the LV surface tension, σ_{LV}, meaning a weaker Young's unbalanced force pulling on the triple line along the LV interface. Beyond a critical temperature, σ_{LV} becomes so low that it is not strong enough to overcome the adhesion forces of the substrate, resulting in the drop remaining pinned. Sefiane and Tadrist [126] reported similar findings and noted the sensitivity of this effect to surface roughness. Girard et al. [161] investigated pinned drops on heated substrates numerically, showing that the increased substrate temperature created Marangoni stresses that went on to induce strong convective flows within the drops. In a later paper, Girard et al. [162] confirmed that this convective flow added a significant contribution to the evaporation rate. The mode of evaporation a drop follows can have a profound impact on the overall evaporation rate. Sáenz et al. [78] numerically modelled pinned and receding drops on heated substrates by way of DNS. They found that average interface temperature remains constant for drops evaporating in the CCA mode and increases with decreasing thickness for drops evaporating in the CCR mode. It was therefore concluded that for increasing substrate temperatures, drops would evaporate more rapidly in the CCR mode than in the CCA mode.

High temperature substrates also affect the flow of the gas phase surrounding the drop, causing thermal convection and buoyancy effects to become more prominent. Sobac and Brutin [76] conducted experiments with pinned water drops on both heated hydrophilic and heated hydrophobic substrates. They demonstrated the inadequacy of the basic model of Picknett and Bexton [109] to predict evaporation rates in these heated cases, becoming more inaccurate as the temperature increased. Sobac and Brutin [76] postulated that this is due to buoyancy effects of the water vapour in air, evaporative cooling, and thermal conductivity between the drop and the substrate. In addition, as will be discussed in Section 3.5, evaporation of drops with instabilities on the LV interface cannot be predicted with the basic diffusion model.

Thermal conductivity of the substrate can also have profound effects on drop evaporation. Inspired by the work of Kavehpour et al. [117], in 2007, David et al. [163] reported their experimental investigation into the effects of substrate thermal conductivity on the evaporation of water drops. Substrates included PTFE, macor, titanium, and aluminium, all coated with an aluminium layer—giving all substrates equal surface energies and constant wettability. They saw that for higher substrate conductivities, evaporation was enhanced over the insulated substrates due to additional energy available for evaporation being thermally conducted through the through the solid. Ristenpart et al. [68] then demonstrated the ability of substrate conductivity to enhance thermal Marangoni in pinned water drops and reverse the radial outward flow. In 2009, over a series of papers, Dunn and co-workers [115, 69, 164] developed and validated a numerical model to predict conductivity effects. In 2011, Sefiane and Bennacer [165] proposed amendments to extend the validity of the basic model by accounting for the effects of evaporative cooling and thermal resistances of both the substrate and liquid.

The shape of the pinned contact line as the drop resides on the substrate has recently been shown to be of great importance to its dynamics. Sáenz et al. [166] studied drops with well-defined non-spherical geometries. Contact lines were artificially pinned in shapes ranging from triangles to kidney-shaped. The irregular shapes introduced variations in curvature over the LV interface. Sáenz et al. [166] proved both experimentally and numerically that higher interface curvature enhances evaporation flux. A scaling law was derived, taking into account overall surface curvature to predict the evaporation rate of any shape. The authors went on to assess the impact this had on binary ethanol-water mixtures—see Section 3.6 for more on multiple component drops.

Whilst undoubtedly important, an in-depth study of the influence of substrate is outwith the scope of this work and so we only focus on a single substrate.

3.5. Thermocapillary instabilities

Since being confirmed by Pearson in liquid layers subject to a vertical temperature gradient [7], surface tension driven instabilities have also been found to be prevalent in volatile drops. In contrast to the liquid layer problem, temperature gradients arise naturally in drops due to evaporation, leading in some cases to “self-excited” thermocapillary instabilities—or HTWs. It was Sefiane et al. [70] who, in 2008, reported the presence of HTWs in evaporating sessile drops. Aerial thermal imaging, capturing the whole LV interface, was used with drops of water and the more volatile liquids ethanol, methanol, and refrigerant FC-72. In addition to volatility, the effects of thermal conductivity were investigated using a range of non-heated substrates, specifically PTFE, macor, titanium and copper. No instabilities were found in water drops but as the volatility increased, interesting temperature profiles on the LV interface of the drops emerged. For ethanol and methanol, surface instabilities took the form of wave-trains circling around the drop in the azimuthal direction, the number of waves decreasing linearly with volume as they evaporated. The number of waves were also lessened by decreasing substrate conductivity, as was the angle at which they propagated. A later study by Sefiane et al. [167] found that heating of the substrate also increased the wavenumber. Increasing the volatility by using FC-72, the instabilities took on an entirely different form. Instead of waves, they now resembled Bérnard-like convection cells. This study inspired Karapetsas et al. [168] to devise a model to numerically assess the stability of similarly volatile drops. Using a simple "one-sided" model (discussed in Section 3.7), a clear temperature gradient developed with evaporation. Performing a stability analysis using the quasi-steady-state approximation (QSSA)—assuming the growth rate of disturbances is much faster than the rate of evaporation, a series of unstable regimes were identified over the drop lifetime. This analysis suggested the presence of HTWs under certain conditions and demonstrated their strong dependence on thermocapillarity.

The same volatile liquids studied by Sefiane and co-workers [70, 167] have also been investigated by Brutin et al. [169] and Sobac and Brutin [170] on temperature controlled PTFE substrates. They found similar results to Sefiane and co-workers [70, 167], with HTWs spontaneously appearing on the LV interface. In contrast to Sefiane et al. [70], Brutin and co-workers [169, 170] found the wavenumber decreasing as a power law with volume, rather than linearly. This was attributed to differences in thermal conductivity and wettability of the substrates used by the two researchers. This again highlights the powerful influence substrates can have on drop dynamics. In 2012, Carle et al. [171] confirmed thermocapillarity as the driving force of HTWs by performing experiments in parabolic flight. The gravitational force present in terrestrial experiments had a negligible effect when compared to the reduced gravity in parabolic flight, and so it was concluded that the instabilities were purely surface tension driven. Revisiting the problem in 2013, Sefiane et al. [121] measured the temperature and heat-flux at the SL interface of FC-72 drops on a heated surface while simultaneously measuring the drop profile. Their results indicated that if HTWs are present, the evaporation rate cannot be explained by the vapour diffusion mechanism alone, suggesting that HTWs contribute to energy transport and evaporation. Evaporation was not concentrated at the contact line and was not proportional to the base radius, as is the case in stable drops.

Thermocapillary driven instabilities have also been reported in spreading volatile drops.

In 2006, Gotkis et al. [172] found a novel contact-line instability when a drop of isopropyl alcohol (IPA) was released onto a monocrystalline silicon wafer. The instability took form by ejecting smaller drops just ahead of the expanding contact line as the drop continued to spread to a pancake shape. This followed with the resultant formation of a regular but dynamic ring of drops along the contact line, earning the nickname "octopi" from its appearance. Gotkis et al. [172] reported that a less volatile liquid or a more conductive substrate suppressed the instability. By using a model similar to Sultan et al. [36] they confirmed the instability was due to thermocapillary effects induced from evaporation. A thermocapillary induced fingering-type instability was observed earlier in thin films by Cazabat et al. [173]. Surfactant laden drops have also show similar contact line fingering instabilities, as shown by Matar and Craster [174]. Festoon like instabilities at the contact line of spreading drops have also been reported [175, 151]. Others have observed Marangoni driven instabilities on liquid substrates, recently Wodlei et al. [176] saw similar drop ejection to Gotkis et al. [172] in a dichloromethane drop spreading on an aqueous substrate. Also spreading on a liquid but this time immiscible oil, Keiser et al. [177] saw the same drop ejection when depositing ethanol-water mixture drops. These were still driven by surface tension gradients from evaporation, but with solutocapillary effects playing the dominant role. Multiple component drops are discussed further in Section 3.6.

In the current thesis work, we focus on thermocapillary instabilities resulting during the evaporation of sessile drops made up of binary mixtures. Both theoretical and experimental approaches are presented.

3.6. Droplets with multiple components

In real world applications such as ink-jet printing, the fluid is a mixture of solvents, sparking the interest to investigate drops consisting of multiple components. In 2000, Rowan et al. [178] studied the evolution of contact angle in small drops of 1-propanol and water deposited on poly(methyl methacrylate) (PMMA) substrates. 1-propanol-water develops an azeotrope at 0.39 mole fraction 1-propanol. Mixtures on either side of the azeotrope were considered, with contrasting behaviours found. 1-propanol in excess displayed typical behaviour, evaporating in the CCR mode until de-pinning for the final third of the evaporation. However, when water was in excess, the drop became unstable and virtually disappeared before subsequently forming a new drop. This instability was attributed to the competing effects of local surface tension minima—caused by preferential adsorption of 1-propanol to the LV interface, and maxima—caused by evaporative cooling. This early study made it abundantly obvious that by the combined effects of thermal and solutal Marangoni, the dynamics of binary mixtures are significantly complicated over those of pure drops.

Another early study by Sefiane et al. [179] in 2003 found that unlike pure drops, displaying a monotonous evolution of evaporation rate and interface profile in time, binary drops of ethanol-water mixtures displayed non-monotonous behaviour, heavily influenced by the initial concentration. A PTFE substrate was used, partially wet by both water and ethanol. Due to the lower surface tension of ethanol, the higher the ethanol concentration, the greater the wetted area and the lower the initial contact angle. Sefiane et al. [179] postulated that evaporation occurred in three distinct stages (I–III). In the first stage, the contact line remained pinned and evaporation reduced only the contact angle—this is the CCR mode. The volume of liquid evaporated in Stage I increased with ethanol concentration, leading to the conclusion that the vast majority of ethanol had evaporated by the end of the stage. Sefiane et al. [179] also speculated that some residual ethanol remained entrapped within the drop at the end of Stage I. Stage II is a transition phase whereby the drop de-pins, decreasing the base area and increasing contact angle. The length of Stage III corresponded to the initial concentration of water—higher water concentration resulting in longer duration where the drop evaporates in the CCA mode until disappearing. Essentially, Stage I corresponded to the behaviour of the MVC (ethanol) and Stage III to that of the LVC (water). The same behaviour was found on other substrates by separate researchers [180, 181, 182]. Sefiane et al. [183] revisited the problem in 2008, this time with methanol-water drops evaporating in both unsaturated ambient and saturated water atmospheres. For all concentrations investigated, they reported that the contact angle at the start of Stage III (where only the LVC should be present) was always higher for the saturated case. Interestingly, this suggested that in an unsaturated atmosphere, some residual methanol remained in the drop. It was proposed that this is due to the diffusion of methanol molecules in water being much slower than their evaporation from the LV interface. Since methanol near the surface evaporates rapidly, small amounts of residual methanol in the bulk will not have time to diffuse to the interface before the drop evaporates completely. Liu et al. [184] found similar hints to residual amounts of ethanol entrapped in ethanol-water drops.

Shedding more light on the internal flow of each regime, Christy et al. [185] used particle image velocimetry (PIV) to experimentally visualise the flow velocity near the SL interface within ethanol-water drops. Small volumes of 0.1 µl with immersed fluorescent particles were deposited onto transparent glass cover slides and viewed from below. They noticed that at the azeotropic concentration of ethanol (96 wt.%) in water, the velocity distribution was quite different from the outward radial flow in pure water drops. The velocity would start off chaotic (Stage I) before decaying into a pattern of three or four recirculating zones (Stage II) and then subsequently settling at a solely radial flow (Stage III). The latter stage was identical to pure water, suggesting that

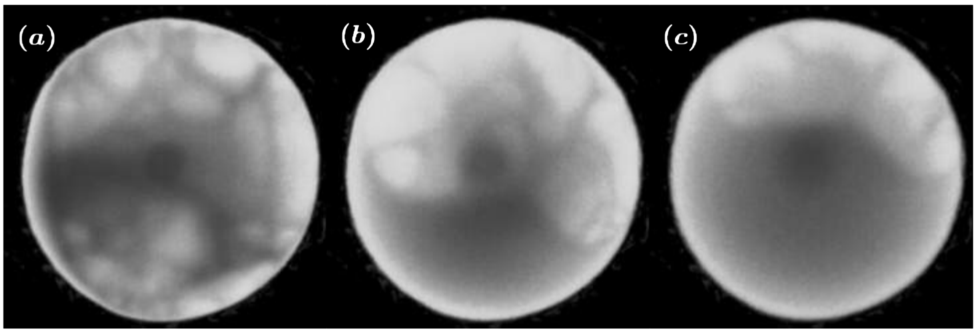

Fig. 3.2 Infrared thermography snapshots taken from and aerial view point of an experiment where a pinned 25 vol.% ethanol-water drop is evaporating into a nitrogen atmosphere from a 40 °C aluminium substrate. Lighter areas indicate higher temperature. (*a*) = 5s, (*b*) = 65s, and (*c*) = 110s after deposition. Thermal disturbances on the interface, decaying as time proceeds from (*a*) to (*c*) are clear to see. The calming of the surface flow is directly correlated with the depletion of ethanol as it preferentially evaporates over water. A smooth temperature profile is obtained when negligible amounts of ethanol remain—Similar to a pure water drop. Unpublished experiments conducted by the author.

ethanol evaporates off preferentially. Investigating further, Christy et al. [88] then used an initial ethanol concentration of 5 vol.%. They deduced that the chaotic flow in Stage I was due to surface tension differences arising from the uneven concentration as a result of preferential ethanol evaporation. Stage II, so-called transition regime, was characterised by an exponential decay in vorticity as remaining vortices migrated towards the contact line. Interestingly, the end of Stage II was accompanied by a spike in radial velocity along the base of the drop. Christy et al. [88] postulated that this could be due to a "zero-concentration" wave caused by the total depletion of ethanol at the LV interface, resulting in a surface tension instability.

Bennacer and Sefiane [89] expanded the study to include drops of 25 vol.% and 50 vol.% initial ethanol. They showed that for both concentrations, the transition away from chaotic Stage I occurred when the concentration of ethanol was almost depleted and unable to sustain solutal Marangoni flow. The subsequent decay of vortices in Stage II was therefore explained by viscous dissipation and the velocity spike due to the final traces of ethanol evaporating from the surface. They also speculated on the connection between the decreasing number of vortices in Stage I (despite the average vorticity remaining constant) and the decreasing concentration of ethanol—resulting in increasingly weaker solutal Marangoni flows. Recently, Zhong and Duan [186] conducted similar experiments depositing concentrations of 10, 20, 40, and 50 vol.% initial ethanol onto silicon wafers. They characterised the flow into three slightly different regimes. Regime I was similar to the beginning of Stage I proposed by Bennacer and Sefiane [89]—chaotic flow with strong vortices. The vortices then disappeared to reveal

Regime II, characterised by a slower, more regular flow travelling radially inwards, the strength of which decreases with evaporation. Zhong and Duan [186] explained this in terms of solutal Marangoni, with preferential ethanol evaporation from the contact line increasing the local surface tension and pulling fluid from the apex along the LV interface. To replenish the lost liquid from the bulk, an inward flow along the base from the contact line is established. They found that the length of Regimes I and II was prolonged with greater initial ethanol concentration, providing further evidence to the flow being solutally driven. The final regime (III) corresponds to Stage III of Bennacer and Sefiane [89]—when ethanol reaches total depletion and the base flow reverses to radially outwards.

With all prior studies being concerned only with spherically symmetrical drops, Sáenz et al. [166] took a different approach by investigating well defined non-spherical geometries. Covered previously in Section 3.4, they proved that interface curvature enhances evaporation rate in pure drops. Expanding to binary ethanol-water mixtures, they saw that by controlling curvature they could segregate the two component within the drop. Seemingly chaotic behaviour on the interface was captured using infrared thermography and the subsequent thermal fluctuations, similar to those seen by Sefiane et al. [70], indicated the presence of ethanol. Similar to the base velocity examined by Christy and co-workers [185, 88], Sáenz et al. [166] observed chaotic motion decaying with time in all geometries. The location of final thermal fluctuations, and hence the last vortices and last traces of ethanol were always found at the areas of lowest interface curvature. With evaporation proceeding slowest at areas of minimum curvature, ethanol would linger in these areas for the longest times. The findings of Sáenz et al. [166] demonstrated that drop geometry is viable option for controlling internal flow and segregating components, if desired.

With the additional effect of solutal Marangoni, introduction of a second component can also have profound impacts on the spreading behaviour of wetting and partially wetting drops. As first mentioned in Section 3.3, an early study by Guéna et al. [154] identified the enhanced spreading effect for alkane mixture drops due to the preferential evaporation of the lower surface tension component at the contact line, duly exerting an outward force. Alkanes, along with most mixtures, adopt the convenient property of a linear surface tension profile, meaning that surface tension decreases linearly with temperature. However, some mixtures in specific concentrations can adopt a non-linear parabolic profile in temperature—the so-called self-rewetting fluids [187]. Recently, Mamalis et al. [188] investigated the spreading dynamics of drops of self-rewetting mixtures, namely 5 vol.% 1-butanol in water and 2 vol.% 1-pentanol in water, deposited on heated substrates. A clear dependence on temperature was seen for the very first stages of spreading—the inertial regime. The spreading exponent rose from $n = 0.48$ at 20 °C to $n = 0.71$ at 60 °C. The authors explained this in terms of the spontaneous segregation of the more volatile alcohol, particularly from the contact line, as the drop touches the heated surface. Similar to observations by Guéna et al. [154], this enhanced capillary spreading in the early stages before the last traces of alcohols left the drop. Furthermore, through infrared thermography of the interface, "flowery" thermal patterns, also dependent on the substrate temperature, were additionally observed at these early times. Chen et al. [189] investigated evaporation of 5 vol.% 1-butanol-water drops at longer times, reporting thermal patterns at the interface, subsequently disappearing with 1-butanol depletion. Chen et al. [189] also reported the absence of thermal patterns in either the pure 1-butanol or water drops, pointing—along with the former—to the importance of solutal influences in the mixture.

Recently, Cira et al. [190] demonstrated that binary drops of food colouring (propylene glycol (PG)) and water exhibit a non-zero contact angle on glass despite a spreading coefficient, S, larger than zero (see eq. (3.4)) and drops of the respective pure component both achieving complete wetting. Note that water is the MVC in this case and has a higher surface tension than PG. As water evaporates preferentially from the contact line, the increased concentration of PG decreases the local surface tension. Solutal Marangoni stress then pulls liquid along the interface towards the apex with higher surface tension. This slows down spreading until the drop is stabilised at an equilibrium contact angle. This effect was also reported earlier by Pesach and Marmur [191] who in addition showed the possibility of spreading enhancement if the MVC has the lower surface tension of the pair—similar to the findings of Guéna et al. [154]. Perhaps more interestingly, Cira et al. [190] also saw that when a drop was deposited near another drop with the same or different concentration of PG-water, the pair would move together due to the emitted vapour. The explanation for this lies in the relative vapour pressures, the vapour pressure of water being $O(2)$ larger than that of PG. For two neighbouring drops, evaporation will cause a local increase in relative humidity between them. The evaporation of the thin films in this region are therefore suppressed from the increased humidity, leading to an increased water concentration (the MVC) relative to the rest of the thin film surrounding the drop—any remaining film not sandwiched between the two drops and hence not under the higher humidity vapour cloud. Greater water concentration in the film area between the adjacent drops results in a higher local surface tension in the film, causing a net force that drives the drops together.

Modelling of binary drops is particularly valuable as it enables measurement of the local concentration within the drop, not possible with experiment. The first complete model to simulate the evaporation of a multicomponent drop was provided in 2017 by Diddens et al. [192] using a finite element method under lubrication approximation. They considered partially wetting binary drops of ethanol-water and water-glycerol evaporating from an isothermal substrate at contact angles 6.6°–40° using a Navier-slip condition at the contact line. For ethanol-water drops, [192] saw that at large times ethanol had almost entirely evaporated but a strong thermal Marangoni flow was still present—validating the hypothesis of Christy et al. [88]. They noted that when the drop becomes flat, the surface tension gradient leads to shape deformation with a depression in the drop centre—similar to the observations of Guéna et al. [154]. Entrapped residual ethanol, previously predicted [183, 184], could not be noticed, which the authors argues was due to strong convective mixing resulting from the fast Marangoni flow. However, residual amounts of water in glycerol-water drops (where diffusive transport is slower) was found to remain in the later stages. By then extending the model to non-isothermal heated substrates, Diddens et al. [192] was able to reproduce the flow regimes and transitions reported experimentally by Zhong and Duan [186]. Diddens [193] quickly followed up with another finite element model to tackle larger contact angles above 90°, this time not invoking the lubrication approximation. Thermal convection was also added, accounting for the effects of substrate thickness and evaporative cooling. Here the results showed that the evaporation of the MVC can drastically decrease the interface temperature, causing the ambient vapour of the LVC to condense onto the drop. The approach used here by Diddens [193] was compared with the previous lubrication-based model by Diddens et al. [192]. While the volume evolutions agreed well, even at low contact angles, the lubrication approach over predicted the regular Marangoni velocities and under predicted the chaotic velocities in the case of an instability.

In 2016, Tan et al. [90] for the first time looked into the evaporation of ternary mixtures. Specifically, partially wetting 1 µl drops of the Greek aperitif, Ozuo—a mixture of water, ethanol and anise oil. The addition of anise oil adds a further complication of mutual solubility, with the oil being miscible in ethanol but immiscible in water. The evaporation phenomena was revealed to be extremely rich, with evaporation induced phase separation being observed. The process can be broken down into four stages (I–IV). Stage I is characterised by the newly deposited Ouzo drop being a transparent spherical cap. Here ethanol is evaporating preferentially at the contact line, leading to a local decrease (increase) in ethanol (water) concentration. Stage II begins with the nucleation of oil microdrops at the contact line due to their decreased solubility in water, quickly spreading to the rest of the drop, causing it to become cloudy. As ethanol totally evaporates, the drop becomes clear once more, leaving a predominately water bulk circled by a ring of oil around the rim—this is Stage III. In Stage IV, only a tiny spherical cap of anise oil is left after all water evaporates. Tan et al. [90] then used a generalisation of the model presented by Diddens et al. [192] to reproduce Ouzo drop evaporation. The model demonstrated the ability to predict the onset of oil-nucleation, as seen in the experiments. The following year, Tan et al. [194] extended their study to superamphiphobic surfaces, with low wettability to all components giving very large initial contact angles of 150°. Here they saw the oil ring surrounding the drop in Stage III climb the LV interface towards the top of the drop, eventually cloaking it in entirety. Interestingly, Li et al. [195] have recently observed component segregation in binary drops. In their case this was driven by evaporation from the rim being faster than the induced Marangoni flow, resulting in the convection usually caused by Marangoni flows not being strong enough to maintain perfect mixing.

In this work, we consider ethanol-water mixtures far away from azeotropic concentrations and focus on flat/thin drops specifically looking at the spreading behaviour using both experiments and modelling.

3.7. Modelling approaches

As we know by now, the evaporating drop problem is complex. With three phase, flow in both the liquid and gas as well as a moving contact line to contend with, modelling in complete detail would be extremely intensive. The same common models arise again and again, and so it would apt to cover these briefly. The fundamental differences between all models tends to be two very important considerations—the manner in which evaporation is introduced and how the motion of the contact line is dealt with [196]. We will discuss evaporation models first before moving on to contact line considerations.

With evaporation being a two-phase process, it seems logical when modelling the phenomena to consider both the gas and the liquid phases. Full resolution of both phases will require Navier-Stokes, energy, and possibly (depending on the problem), species equations in both the liquid and gas. Models of this type are dubbed “two-sided”. They have the potential to be highly accurate—providing other possible effects such as substrate conductivity, evaporative cooling, and vapour buoyancy are also accounted for. The disadvantages come with two-sided being inherently complex and computationally expensive. An example of a two-sided model used for drops is the work of Sáenz et al. [78].

The two-sided problem is commonly simplified by assuming that no convection takes place in the gas phase. This is justified by accepting that vapour viscosity and thermal conductivity are much smaller than the equivalent liquid properties. Note that diffusion of the vapour is still retained for the time being. The liquid phase is still fully resolved but the gas phase is reduced to only being solved for diffusion, with boundary conditions introduced along the LV interface for the liberation of the liquid to vapour. By reducing the number of equations in the gas phase significantly but not completely, models of this type are commonly referred to as “1.5-sided” models. Further simplifications can be made while still retaining the 1.5-sided classification by assuming diffusion of the vapour is a steady state process. This results in the transient term in the diffusion equation being dropped, leaving only Laplace's equation. This particular variation is often referred to as the "lens" model, interestingly because the mixed-boundary method for determining vapour concentration is analogous to finding the electric potential around a lens-shaped conductor [197]. Lens models have been used extensively for both pinned and unpinned drops and the type adopted in the works of Deegan [128, 129], Mollaret [160], Girard [161, 162] Dunn [115, 164, 69], Cazabat [104] and Diddens [192], mentioned previously.

The next simplification is to ignore the vapour phase altogether and move to the so-called "one-sided" model. Properties of the gas phase are neglected completely, assuming that vapour diffuses rapidly away from the LV interface and that it is far from a saturated state. One-sided models are therefore suited to modelling volatile and non-isothermal heated drops. By circumventing the need to model the gas, the continuum equations are only retained in the liquid phase. Evaporative flux is then generally handled with a non-equilibrium relation based on kinetic theory of gases, such as the Hertz-Knudsen expression [198]. Sometimes referred to as a non-equilibrium one-sided (NEOS) model, this is the approach used by Burelbach [34], Anderson and Davis [94], Ajaev [95], and Karapetsas [168, 83]. The one-sided model has the draw of simplicity, allowing for fast computation with modest resources.

Regardless of the evaporation model, in all cases the dynamics at the contact line need to be dealt with. Generally, contact lines must be specified as either moving—like in works such as Ajaev [95], or pinned—as used by Sáenz et al. [78]. The obvious disadvantage with a pinned contact line is that evaporation is restricted to the CCR mode. De-pinning events and contact line movement cannot be predicted. For this reason, many pinned contact line models are pseudo-transient in nature—meaning the transient evolution of the drop is a sum of several stead-state solutions over the drop lifetime. In order to do this, the geometry of the drop must be imposed a priori. The models used by Hu and Larson [93, 130, 131, 133] and Girard [161, 162] take this approach.

Inconveniently, when modelling moving contact lines, a non-physical singularity can arise at the contact line due to the incompatibility of the boundary conditions applied where the three phases meet. If the traditional no-slip condition is applied on the substrate along with the moving free surface of the LV interface, a singularity in the viscous shear-stress will result [199, 122]. Several methods have been proposed to work around this with only two covered here—see [102] for a full discussion. The first solution is to introduce a "slip length" by relaxing the no-slip condition at the contact line and allowing some "slip" (i.e. contact line movement) along the solid surface. This can be particularly useful when modelling rough surfaces as they can be approximated as a smooth surface with slip, with the slip length taken as the corrugation wavelength of the rough surface desired to be modelled [200]. Using this method, the physical presence of the contact on the substrate is retained. Models by Anderson [94] and Karapetsas [85] take this approach. However, the value given to the slip length is always subject to question—a given slip length for motion of drops is typically of the order of non-continuum scales. The second option is to introduce a precursor layer ahead of the contact line, taking the form of an ultra-thin film. The drop is no longer directly residing on the substrate but rather on the thin film. This effectively removes the SL contact line and also, conveniently, the shear stress singularity. First used for sessile drops by Ajaev [95] who was inspired by the works of Potash [201] and Moosman [202], both using the approach to study steady contact lines on heated surfaces. More than purely a modelling aid, the presence of a precursor layer has been detected experimentally [143, 144, 145], as discussed previously in Section 3.3. The thin-film exists due to its evaporation being suppressed by attractive van der Waals forces. A precursor layer is also adopted in other works from Karapetsas [83, 203].

Overall, it can be seen that drop evaporation demonstrates strong instabilities that are intermittent and dynamic. With the introduction of a second component, Marangoni flows can arise from both solutal effects in addition to already present thermal gradients. In this thesis, a novel numerical model is presented for the evaporation of flat drops comprised of miscible binary mixtures. A one-sided approach is used under the lubrication approximation for the dynamic model while the stability at a discrete time instance is assessed by evoking the quasi-steady state approximation.

Part II

DNS model for laterally heated binary liquid layers

4. Formulation of the DNS model

The model we present is novel in its capability to consider a liquid layer with two miscible components while accounting for the deformable interface, effects of thermodiffusion and fully resolving both phases by use of DNS. Phase is modelled for one evaporating component which can be suppressed in cases where a saturated layer with no evaporation wished to be investigated.

Before we begin, the notation convention will be explained to avoid confusion. The use of a capital delta symbol, $\mathit{\Delta}$, before a scalar quantity (e.g. $\mathit{\Delta}T$) indicates the change in that quantity over the domain. The nabla symbol (∇) is used as a shorthand for the gradient, or "del" operator, meaning, $\nabla = \big(\partial/\partial x,\ \partial/\partial y,\ \partial/\partial z\big)$. A further important distinction is the crowning of a "cap" ($\hat{}$) over a symbol which signifies a dimensional quantity while its absence signifies a dimensionless quantity. We go on to define the model in dimensional terms before introducing scaling variables and presenting the dimensionless equations.

4.1. Description of the problem

Our model is inspired by the experiments conducted in annular geometries by Yu et al. [42]. Consider a horizontal liquid layer consisting of a liquid mixture of 50 % hexane and 50 % decane bounded above by air. In contrast from the experiments in [42], the layer is confined in a rectangular geometry subject to a horizontal temperature gradient by heating and cooling the end walls. We first consider the saturated case in the absence of phase change, as studied by Yu et al. [42] and then later introduce the effects of evaporation.

Consider a thin liquid layer of depth $\hat{d}$, confined in a rectangular geometry in co-ordinate frame $\hat{\boldsymbol{x}} = (\hat{x}, \hat{y}, \hat{z})$ of height $\hat{H}$, length $\hat{L}$, and width $\hat{W}$. A temperature gradient is induced by maintaining lateral end walls temperatures $\hat{T}_h$ and $\hat{T}_c$ respectively. Both phases are assumed to be incompressible and viscous with the two components of the liquid phase, A and B, being fully miscible together. Key fluid properties of the liquid phase are density $\hat{\rho}_l$, viscosity $\hat{\mu}_l$, thermal conductivity $\hat{k}_l$, specific heat capacity, $\hat{c}_{p,l}$,

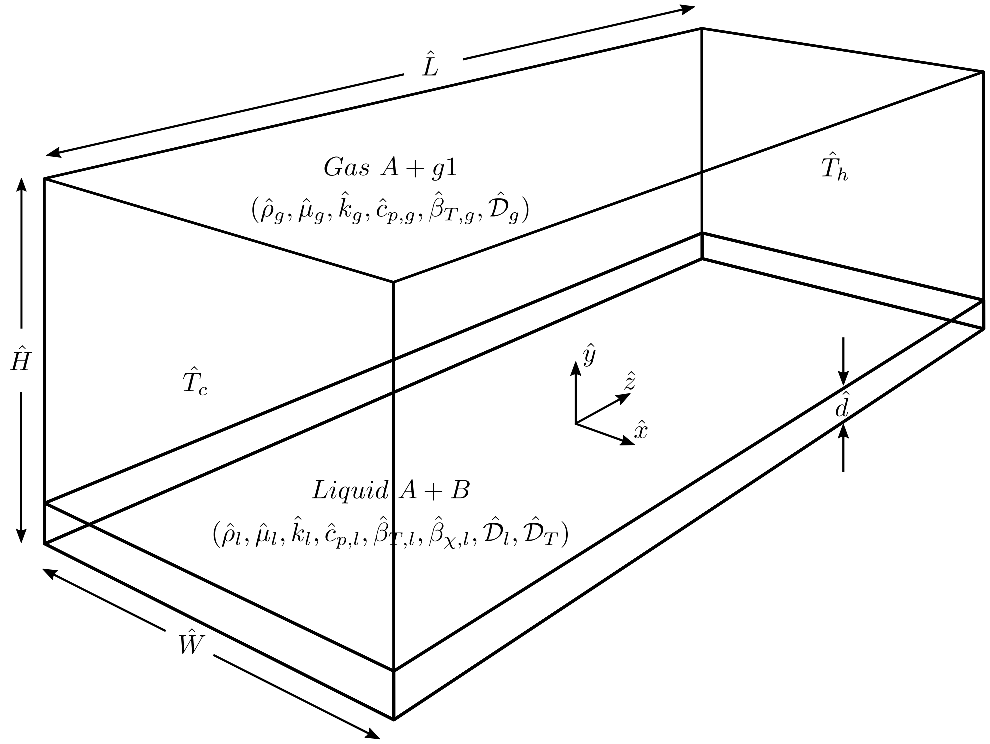

Fig. 4.1 A planar pool of depth $\hat{d}$ consisting of miscible liquids A and B bounded above by vapour A and non-condensable inter gas $g1$. Both fluids are confined in a cuboid of length $\hat{L}$, width $\hat{W}$, and height $\hat{H}$ with an open upper boundary. A temperature gradient across the layer is imposed by maintaining the lateral end wall at hot and cold temperatures $\hat{T}_h$ and $\hat{T}_c$ respectively.

coefficient of thermal expansion $\hat{\beta}_{T,l}$ and coefficient of solutal expansion $\beta_{\chi,l}$. Since the gas phase consists of one component, there is no solutal expansion. Using the same convention, key gas properties are $\hat{\rho}_g$, $\hat{\mu}_g$, $\hat{k}_g$, $\hat{c}_{p,g}$, $\hat{\beta}_{T,l}$.

The surface tension between the liquid and gas varies linearly with both temperature and component concentration [42],

$$\hat{\sigma} = \hat{\sigma}_r - \hat{\gamma}_T(\hat{T} - \hat{T}_r) - \hat{\gamma}_\chi(\chi_A - \chi_{A,0}) \tag{4.1}$$

where $\hat{\sigma}_r$ is the mixture surface tension at the reference temperature $\hat{T}_r$ and initial mixture concentration $\chi_{A,0}$. $\hat{\gamma}_T = -\partial\hat{\sigma}/\partial\hat{T}$ is the temperature coefficient of surface tension, describing the change in surface tension with temperature. χ_A is the local mass fraction of component A (the MVC) in the liquid, with $\chi_{A,0}$ being its initial value. $\hat{\gamma}_\chi = -\partial\hat{\sigma}/\partial\chi_A$ is the solutal (mass fraction) coefficient of surface tension, describing the rate of change with concentration.

The density of the liquid mixture is also assumed to vary linearly with temperature and concentration,

$$\hat{\rho}_l = \hat{\rho}_{r,l}\big(1 - \hat{\beta}_{T,l}(\hat{T} - \hat{T}_r) - \beta_{\chi,l}(\chi_A - \chi_{A,0})\big) \tag{4.2}$$

where $\hat{\rho}_{r,l}$ is the reference liquid density ambient temperature and initial mixture concentration and $\hat{\beta}_{T,l} = -(\partial\hat{\rho}_l/\partial\hat{T})/\hat{\rho}_{r,l}$ and $\hat{\beta}_{\chi,l} = -(\partial\hat{\rho}_l/\partial\chi_A)/\hat{\rho}_{r,l}$ are the liquid coefficients of thermal and solutal expansion respectively.

The bounding gas phase above is a mixture of an inert gas and vapour of the MVC. The evaporation rate of the LVC is assumed to be sufficiently slow that it is negligible on the timescales considered—this assumption will be justified later. Since the inert gas is always present in larger concentration, only the inert gas thermal expansion is considered and solutal expansion effects are ignored. The total gas density therefore varies only with temperature,

$$\hat{\rho}_g = \hat{\rho}_{r,g}\big(1 - \hat{\beta}_{T,g1}(\hat{T} - \hat{T}_r)\big) \tag{4.3}$$

with $\hat{\rho}_{r,g}$ being the reference gas mixture density at ambient temperature and $\hat{\beta}_{T,g1}$ $= -(\partial\hat{\rho}_{g1}/\partial\hat{T})/\hat{\rho}_{r,g1}$ is the coefficient of thermal expansion for the inert gas in the mixture. Let us use Υ_A to denote the mass fraction of MVC vapour in the gas phase. Assuming both inert gas and vapour are incompressible, the total gas phase density at reference temperature is approximated as [204],

$$\hat{\rho}_{r,g} = \left[\frac{(1-\Upsilon_A)}{\hat{\rho}_{r,g1}} + \frac{\Upsilon_A}{\hat{\rho}_{r,gA}}\right]^{-1} \tag{4.4}$$

Here the reference density of the inert gas is given by $\hat{\rho}_{r,g1}$ and the reference density of A vapour by $\hat{\rho}_{r,gA}$.

We use the volume of fluid (VOF) method to account for the deformable interface. The VOF method is a volume based interface tracking technique. Fluids on each side of the interface are given a value or either 0 or 1 with a value between the two indicating the interface region. The scalar function used to distinguish between phases is essentially the volume fraction known as the colour function, c, defined as,

$$\begin{aligned} c &= 1, \quad \text{cells filled with liquid} \\ c &= 0, \quad \text{cells filled with gas} \end{aligned}$$

The VOF method treats both the liquid and gas as a single phase, with c giving their spatial volume over the domain. We can therefore define the problem by a single set of governing equations along with the colour function conservation equation. This is known as the one-fluid formulation and has the advantage of saving on computational resources since other methods may require separate transport equations for each phase.

If we then combine eq. (4.2) and (4.3), we arrive at the one-fluid form of the expression for density,

$$\hat{\rho} = \hat{\rho}_r \big(1 - (1-c)\hat{\beta}_{T,g1}(\hat{T} - \hat{T}_r) - c\hat{\beta}_{T,l}(\hat{T} - \hat{T}_r) - c\hat{\beta}_{\chi,l}(\chi_A - \chi_{A,0})\big) \tag{4.5}$$

4.1.1 Soret flux

For a liquid consisting of miscible binary fluids subject to a temperature gradient, there are two main phenomena governing the mass flux. Like most mixtures, molecular diffusion is primarily governed by Fick's law, however, there is also an additional mechanism at work—the Soret effect, also known as thermodiffusion [45]. We can write the mass flux of component A in the liquid exclusively in the x-direction, $\hat{\mathcal{J}}_{A,x}$ as follows,

$$\hat{\mathcal{J}}_{A,x} = -\hat{\rho}\hat{\mathcal{D}}_l \frac{\partial \chi_A}{\partial \hat{x}} - \hat{\rho}\hat{\mathcal{D}}_T \chi_{A,0}(1 - \chi_{A,0}) \frac{\partial \hat{T}}{\partial \hat{x}} \tag{4.6}$$

The first term on the RHS gives the Fick's law component and describes the homogenisation along x due to normal diffusion, the second term on the RHS is the Soret flux which gives the mass separation, driven by and proportional to the temperature gradient in the x-direction. $\hat{\mathcal{D}}_l$ is the binary molecular diffusion coefficient of component A in B and $\hat{\mathcal{D}}_T$ is the thermal diffusion coefficient of the subject species in the equation.

Let us assume that component A has a lower molecular mass than B and so A is the lighter component (LC) and B is the heavier component (HC). Considering only Fick's law, $\partial \chi_A / \partial \hat{x}$ gives the change in χ_A along x. $\hat{\mathcal{D}}_l$ is always positive, hence we can see from eq. (4.6) that χ_A will decrease with x, meaning mass flux will act in the opposite direction from the concentration gradient, homogenising the mixture. Considering now the second term on the RHS of eq. (4.6) describing the Soret flux, $\partial \hat{T} / \partial \hat{x}$ gives the temperature gradient along x. In this case, component A is the LC and will migrate to warmer regions [43]. Therefore, $\hat{\mathcal{D}}_T$ is negative with the net term being positive, causing the flux of A to act in the same direction as the temperature gradient. This causes the LC to migrate towards warmer regions and the HC to migrate towards colder regions [43].

To summarise, Fick's diffusion increases the homogenisation of the mixture whereas Soret diffusion decreases the homogenisation, driving component segregation.

4.1.2 The Soret coefficient

To quantify the strength of Soret (thermal) diffusion over Fick's (molecular) diffusion, we introduce the Soret coefficient, $\hat{S}_T$. This is derived from eq. (4.6) when $\hat{\mathcal{J}}_A = 0$, meaning the two opposing fluxes are of equal intensity and in steady state. The steady state concentration gradient is therefore given by [45],

$$\frac{\partial \chi_A}{\partial \hat{x}} = -\frac{\hat{\mathcal{D}}_T}{\hat{\mathcal{D}}_l} \chi_{A,0}(1-\chi_{A,0}) \frac{\partial \hat{T}}{\partial \hat{x}} \tag{4.7}$$

where the Soret coefficient is then defined as $\hat{S}_T = \hat{\mathcal{D}}_T/\hat{\mathcal{D}}_l$. This can then be written as the expression for the concentration difference between the hottest and coldest regions at steady state,

$$\varDelta \chi_A = -\hat{S}_T \chi_{A,0}(1-\chi_{A,0}) \varDelta \hat{T} \tag{4.8}$$

$\hat{S}_T$ will be positive if component A moves to the hot side and negative if it moves to the hot side. The magnitude of $\hat{S}_T$ is generally in the region of 1×10^{-3} to $1 \times 10^{-2}\,\mathrm{K}^{-1}$ for most mixtures. When $\chi_{A,0} = 0.5$, $\chi_{A,0}(1-\chi_{A,0}) = 0.25$. Therefore, imposing a temperature difference of $4\,\mathrm{K}$ could induce a concentration difference equal to the $\hat{S}_T$ [45].

4.2. Introducing evaporation

Before introducing the governing equations for the layer, we first describe the phase change model used in the cases where evaporation is "switched on". This is a diffusion limited model originally employed by Sáenz et al. [41]. Obviously, in a binary liquid mixture we have two vapours which can be evolved into the gas phase. This leads to 3 components in the gas phase. We simplify this by considering the evaporation of only the MVC. We now justify this approximation for our specific case of a hexane-decane mixture.

As mentioned, a diffusion limited model is employed and so we assume that the vapour-liquid interface is saturated with liquid vapour. The rate-limiting step for evaporation is therefore the rate of diffusion of vapour in the gas mixture. As vapour diffuses away from the interface, the partial vapour pressure decreases and more vapour is evolved from the liquid to maintain the saturation condition. Temperature also affects the rate of evaporation since an increase in temperature will increase the vapour pressure (and hence the amount of fluid evaporated) and a decrease in temperature will have the opposite effect.

The rate at which component A evaporates with respect to component B (A being

Tab. 4.1 Saturated vapour pressures at 298.15 K and relative volatility ratios. Calculated using Antoine relations with data taken from [205, 206, 207, 208].

$\frac{mvc}{lvc}$	p_{sat} (Pa)	$p_{sat,R}\left(\frac{mvc}{lvc}\right)$
ethanol	7858	
water	3170	2.48
hexane	20 192	
decane	182	110.95

the MVC) depends on the relative saturated vapour pressure of each component. A liquid with a high vapour pressure will evaporate relatively quickly whereas one with a low vapour pressure will evaporate at a slower rate. Consider the binary mixtures ethanol-water and hexane-decane. The vapour pressures of each component along with their relative ratios are given in Tab. 4.1. The higher the ratio, the faster the MVC evaporates with respect to the LVC. We can see that ethanol is over twice as volatile as water while the volatility of hexane is 3 orders of magnitude larger than decane. In both cases the lower volatility LVC does evaporate, but on a larger timescale. In the case presented here, where we consider a hexane-decane mixture, we therefore assume that the LVC does not evaporate w.r.t. the MVC in the timescale considered.

4.2.1 Phase change model

We use the phase change model of Sáenz et al. [41] and assume that diffusion of away from the interface into the gas phase is the rate limiting mechanism for phase change. We start by considering an infinitesimal control volume within the domain, $\hat{V}_C$. This can contain some mass of liquid $\hat{m}_l$, gas $\hat{m}_g$, or a combination in the case of the interfacial region. Analogous is the combination of gas and liquid volumes in the control volume: $\hat{V}_C = \hat{V}_l + \hat{V}_g$, given by the volume fraction, c. The total gas phase constitutes a combination of inert gas and component A vapour, with the total gas density being given by eq. (4.4). Therefore by Dalton's law, the total gas pressure, which we assume is atmospheric, is given by,

$$\hat{p}_g = \hat{p}_{g1} + \hat{p}_A \tag{4.9}$$

where $\hat{p}_{g1}$ and $\hat{p}_A$ are the partial pressures of inert gas as component A vapour in the mixture respectively. Recall that c indicates the level to which $\hat{V}_C$ is filled with liquid. With $c = 1$ corresponding to pure liquid, $c = 0$ to the total gas phase and $0 < c < 1$ indicating $\hat{V}_C$ is partially filled—this is the interface region. Within this interfacial region, we can calculate the mass of vapour contained in $\hat{V}_C$ per unit volume of the

Tab. 4.2 Empirical coefficients for hexane for the Antoine equation given in eq. (4.13) with $\hat{p}_{sat}$ in bar and $\hat{T}$ in K. Valid between 286.18 K–342.69 K. Data taken from Willingham et al. [207].

$\hat{A}$	$\hat{B}$	$\hat{C}$
4.00	1171.53	-48.78

total gas phase ($\hat{\mathcal{C}}$) using,

$$\hat{\mathcal{C}} = \frac{\hat{m}_{gA}}{\hat{V}_g} = \hat{\rho}_g \Upsilon_A \tag{4.10}$$

This then expressed as the amount of vapour within the interface control volume per unit total volume (both gas and liquid combined) by multiplying eq. (4.10) by $(1-c)$ to give,

$$\hat{\mathcal{C}}(1-c) = \hat{\mathcal{C}}\left(\frac{\hat{V}_g}{\hat{V}_C}\right) = \frac{\hat{m}_{gA}}{\hat{V}_C} = (1-c)\hat{\rho}_g \Upsilon_A \tag{4.11}$$

Employing Raoult's Law and Dalton's law of partial pressures, we assume that the partial vapour pressure of component A in the gas phase is equal to the pressure of the gas phase multiplied by the mole fraction of component A in the mixture. As such, we find the saturation mole fraction of the component A in the gas phase, $X_{A,sat}$, at temperature $\hat{T}$,

$$X_{A,sat} = \frac{\hat{p}_{sat,A}}{\hat{p}_g} \tag{4.12}$$

where $\hat{p}_{sat,A}$ is the saturation pressure of component A at temperature $\hat{T}$. As a function of temperature, $\hat{p}_{sat,A}$ is assumed to vary following the Antoine equation,

$$\log_{10}(\hat{p}_{sat,A}) = \hat{A} - \frac{\hat{B}}{\hat{C}+\hat{T}} \tag{4.13}$$

where $\hat{A}$, $\hat{B}$, $\hat{C}$ are component-specific constants given in Tab. 4.2. Using the Antoine relation to calculate $\hat{p}_{sat,A}$, over the valid temperature range of 286.18 K–342.69 K, Fig. 4.2 shows the corresponding saturated mole fraction of component A in the gas phase under atmospheric conditions, as calculated by eq. (4.12).

We have used mass fractions exclusively up to this point and so continue to do so, we convert eq. (4.12) from mole to saturated mass fraction $\Upsilon_{A,sat}$ via,

$$\Upsilon_{A,sat} = \frac{X_{A,sat}}{X_{A,sat} + \dfrac{(1-X_{A,sat})}{\mathcal{M}}} \tag{4.14}$$

Where $\mathcal{M} = \hat{M}_A/\hat{M}_{g1}$ is the ratio of the molecular weight of the component A, $\hat{M}_A$ to that of the inert gas, $\hat{M}_{g1}$. We now obtain the mass of vapour per unit total volume contained in $\hat{V}_C$ at saturation conditions by multiplying eq. (4.14) by $(1-c)\hat{\rho}_g$

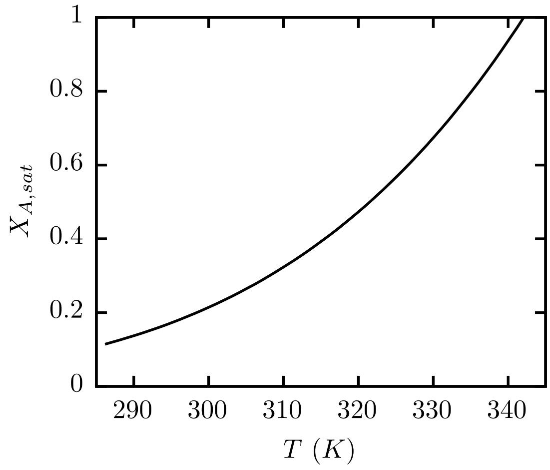

Fig. 4.2 Saturated mole fraction of component A in the gas phase, $X_{A,sat}$, at atmospheric pressure against local temperature, T.

yielding,

$$\frac{\hat{m}_{gA,sat}}{\hat{V}_C} = (1-c)\hat{\rho}_g \Upsilon_{A,sat} \tag{4.15}$$

$\hat{m}_{gA,sat}$ is the mass of component A vapour at saturation conditions. Using eq. (4.11) and eq. (4.15) we can construct an expression of the volumetric mass transfer across the interface, $\hat{S}$, of the form [41],

$$\hat{S} = (1-c)\hat{\rho}_g(\Upsilon_{A,sat} - \Upsilon_A) \tag{4.16}$$

where the computation of $\hat{S}$ is restricted to the interface region only, computed as $0 < c < 1$. Under saturated conditions across the interface, $\Upsilon_A = \Upsilon_{A,sat}$, and hence $\hat{S} = 0$ and there is no net mass transfer across the interface. If $\hat{S} > 0$, liquid evaporates from the interface while if $\hat{S} < 0$, vapour condenses back into the liquid phase.

One further point to consider is the rate of this process—this is not accounted for in eq. (4.16). As stated above, the rate limiting step is assumed to be the vapour diffusion. For this to be valid we must ensure a saturated interface is maintained. If we divide the RHS of eq. (4.16) by the marching time step of the system $\hat{t}_s$, we arrive at a rate based equation that will maintain a saturated interface providing $\hat{t}_s$ is smaller than the smallest relevant timescales in the system.

$$\hat{\mathscr{S}} = \frac{(1-c)\hat{\rho}_g(\Upsilon_{A,sat} - \Upsilon_A)}{\hat{t}_s} \tag{4.17}$$

Where $\hat{\mathscr{S}} = \hat{S}/\hat{t}_s$. Using eq. (4.14), eq. (4.17) can be re-written in terms of pressure [41],

$$\hat{\mathscr{S}} = \frac{(1-c)\hat{\rho}_g}{\hat{t}_s}\left(\frac{X_{A,sat}}{X_{A,sat} + \dfrac{(1-X_{A,sat})}{\mathcal{M}}} - \Upsilon_A\right) \tag{4.18}$$

where saturated mole fraction $X_{A,sat}$ is given by eq. (4.12).

4.3. Dimensional governing equations

The physical properties of the liquid vary linearly with concentration,

$$
\begin{aligned}
\hat{\rho}_l &= \chi_A \hat{\rho}_{lA} + (1-\chi_A)\hat{\rho}_{lB}, \\
\hat{\mu}_l &= \chi_A \hat{\mu}_{lA} + (1-\chi_A)\hat{\mu}_{lB}, \\
\hat{k}_l &= \chi_A \hat{k}_{lA} + (1-\chi_A)\hat{k}_{lB}, \\
\hat{\beta}_{T,l} &= \chi_A \hat{\beta}_{T,lA} + (1-\chi_A)\hat{\beta}_{T,lB}, \\
\hat{\beta}_{\chi_A} &= \chi_A \hat{\beta}_{\chi,lA} + (1-\chi_A)\hat{\beta}_{\chi,lB}, \\
\hat{c}_{p,l} &= \chi_A \hat{c}_{p,lA} + (1-\chi_A)\hat{c}_{p,lB}.
\end{aligned}
\tag{4.19}
$$

where subscript lA denotes component A in the liquid phase and lB similarly denotes liquid component B. Note that the mass fraction of component B in the liquid is given by $(1-\chi_A)=\chi_B$. A similar definition is used for the gas phase properties, where the mass fraction of the inert gas $g1$ is given by $(1-\Upsilon_A)=\Upsilon_{g1}$.

$$
\begin{aligned}
\hat{\rho}_g &= \left[\frac{\Upsilon_A}{\hat{\rho}_{gA}} + \frac{(1-\Upsilon_A)}{\hat{\rho}_{g1}}\right]^{-1}, \\
\hat{\mu}_g &= \Upsilon_A \hat{\mu}_{gA} + (1-\Upsilon_A)\hat{\mu}_{g1}, \\
\hat{k}_g &= \Upsilon_A \hat{k}_{gA} + (1-\Upsilon_A)\hat{k}_{g1}, \\
\hat{\beta}_{T,g} &= \hat{\beta}_{T,g1}, \\
\hat{c}_{p,g} &= \Upsilon_A \hat{c}_{p,gA} + (1-\Upsilon_A)\hat{c}_{p,g1}.
\end{aligned}
\tag{4.20}
$$

In line with the VOF approach, the physical properties for each phase are combined to give the one-fluid form. With density, viscosity, thermal conductivity, and coefficient of thermal expansion averaged by volume, the coefficient of solutal expansion only present in the liquid and the specific heat capacity is averaged by mass.

$$
\begin{aligned}
\hat{\rho} &= c\hat{\rho}_l + (1-c)\hat{\rho}_g, \\
\hat{\mu} &= c\hat{\mu}_l + (1-c)\hat{\mu}_g, \\
\hat{k} &= c\hat{k}_l + (1-c)\hat{k}_g, \\
\hat{\beta}_T &= c\hat{\beta}_{T,l} + (1-c)\hat{\beta}_{T,g}, \\
\hat{\beta}_\omega &= c\hat{\beta}_{\omega,l}, \\
\hat{c}_p &= \frac{c\hat{\rho}_l\hat{c}_{p,l} + (1-c)\hat{\rho}_g\hat{c}_{p,g}}{c\hat{c}_{p,l} + (1-c)\hat{c}_{p,g}}.
\end{aligned}
\tag{4.21}
$$

The dimensional one-fluid form of the conservation of colour, mass, momentum and energy equations along with the advection-diffusion equations for both liquid and gas phases are defined as follows,

$$\frac{\partial c}{\partial \hat{t}} + \hat{\nabla} \cdot c\hat{\boldsymbol{u}} = -\frac{\hat{\mathscr{S}}}{\hat{\rho}_l} \tag{4.22}$$

$$\hat{\nabla} \cdot \hat{\boldsymbol{u}} = -\frac{\hat{\mathscr{S}}}{\hat{\rho}_l}\Big(1 - \frac{\hat{\rho}_l}{\hat{\rho}_{gA}}\Big) \tag{4.23}$$

$$\frac{\partial(\hat{\rho}\hat{\boldsymbol{u}})}{\partial \hat{t}} + \hat{\nabla} \cdot (\hat{\rho}\hat{\boldsymbol{u}}\hat{\boldsymbol{u}}) = -\hat{\nabla}\hat{p} + \hat{\nabla} \cdot \hat{\mu}(\hat{\nabla}\hat{\boldsymbol{u}} + \hat{\nabla}\hat{\boldsymbol{u}}^T) + \hat{\boldsymbol{f}}_{\boldsymbol{b}} + \hat{\boldsymbol{f}}_{\boldsymbol{sv}} \tag{4.24}$$

$$\frac{\partial(\hat{\rho}\hat{c}_p\hat{T})}{\partial \hat{t}} + \hat{\nabla} \cdot (\hat{\rho}\hat{c}_p\hat{T}\hat{\boldsymbol{u}}) = \hat{\nabla} \cdot (\hat{k}\hat{\nabla}\hat{T}) - \frac{\hat{L}_v\hat{\mathscr{S}}}{\hat{c}_{p,l}\mathit{\Delta}\hat{T}} \tag{4.25}$$

$$\frac{\partial(\hat{\rho}c\chi_A)}{\partial \hat{t}} + \hat{\nabla} \cdot (\hat{\rho}c\chi_A\hat{\boldsymbol{u}}) = \hat{\nabla} \cdot (\hat{\rho}c\hat{\mathcal{D}}_l\hat{\nabla}\chi_A) + \big(\hat{\nabla} \cdot \hat{\rho}c\hat{\mathcal{D}}_T\big(\chi_{A,0}(1-\chi_{A,0})\big)\hat{\nabla}\hat{T}\big) - \hat{\mathscr{S}} \tag{4.26}$$

$$\frac{\partial\big(\hat{\rho}(1-c)\mathit{\Upsilon}_A\big)}{\partial \hat{t}} + \hat{\nabla} \cdot \big(\hat{\rho}(1-c)\mathit{\Upsilon}_A\hat{\boldsymbol{u}}\big) = \hat{\nabla} \cdot \big(\hat{\rho}c\hat{\mathcal{D}}_g\hat{\nabla}\mathit{\Upsilon}_A\big) + \hat{\mathscr{S}} \tag{4.27}$$

Where $\hat{\nabla}$ is the dimensional gradient operator, $\hat{\boldsymbol{u}} = (\hat{u}, \hat{v}, \hat{w})$ is the velocity vector and $\hat{p}$ the total pressure. $\hat{L}_v$ in eq. (4.25) the specific latent heat of vaporisation and $\hat{\mathcal{D}}_g$ in eq. (4.27) is the molecular diffusion coefficient of component A in the gas phase. Turning attention to eq. (4.24), $\hat{\boldsymbol{f}}_{\boldsymbol{b}}$ is the buoyancy force and $\hat{\boldsymbol{f}}_{\boldsymbol{sv}}$ is the surface force per unit volume resulting from surface tension. Before non-dimensionalising the problem, we expand these addition terms on the RHS of the momentum equation, given by eq. (4.24). The buoyancy force is defined by combining the one-fluid form of the density, given in eq. (4.5), and the acceleration due to gravity, $\hat{g}$.

$$\hat{\boldsymbol{f}}_{\mathbf{b}} = -\big(\hat{\rho} + \hat{\rho}\hat{\beta}_T(\hat{T} - \hat{T}_a) + c\hat{\rho}\hat{\beta}_\omega(\hat{\omega} - \hat{\omega}_0)\big)\hat{g}\boldsymbol{e}_{\boldsymbol{z}} \tag{4.28}$$

Where $\boldsymbol{e}_z$ is the unit vector in the vertical direction. Surface tension is incorporated via the continuum surface force (CSF) model by Brackbill et al. [209]. The CSF model exploits the colour function, c, (defined above) to identify the interface transition region between phases ($0 < c < 1$), within which surface tension acts. The interfacial transition region has a finite thickness with contours of constant c and curvatures that subtly vary between them. At any point within the transition region, a force density is computed—defined as proportional to the curvature of the surface with constant c at that point. When the local ratio of transition region thickness over the radius of curvature approaches zero, the conventional definition of surface tension on a discontinuous interface is recovered [209]. Under the CSF model, the surface force per unit volume resulting from surface tension, $\hat{\mathbf{f}}_{\mathbf{sv}}$, is given by,

$$\hat{\boldsymbol{f}}_{\boldsymbol{sv}} = \big(\hat{\sigma}\hat{\kappa}\boldsymbol{n} + \hat{\nabla}_s\hat{\sigma}\big)|\hat{\nabla}c| \tag{4.29}$$

Here, $\hat{\kappa} = -(\hat{\nabla}_s \cdot \boldsymbol{n})$ denotes the interface curvature, $\boldsymbol{n} = \hat{\nabla} c/|\hat{\nabla} c|$ is the unit vector normal to the transition region (interface) pointing from gas ($c = 0$) to liquid ($c = 1$) and $\hat{\nabla}_s = \hat{\nabla} - \boldsymbol{n}(\boldsymbol{n} \cdot \hat{\nabla})$ is the gradient operator tangent to the interface. $\hat{\boldsymbol{f}}_{\boldsymbol{sv}}$ is expressed in full by inserting the definition of linearly varying surface tension defined in eq. (4.1) to give,

$$\hat{\boldsymbol{f}}_{\boldsymbol{sv}} = \Big(\hat{\sigma}\kappa\boldsymbol{n} + \hat{\nabla}_s\big(\hat{\sigma}_r - \hat{\gamma}_T(\hat{T} - \hat{T}_a) - \hat{\gamma}_\chi(\chi_A - \chi_{A,0})\big)\Big)|\hat{\nabla} c| \tag{4.30}$$

We now scale the governing equations into their dimensionless forms before applying the relevant boundary and initial conditions.

4.4. Scaling and resulting dimensionless equations

We begin by scaling the one-fluid forms of the physical properties by the liquid phase value,

$$\hat{\rho} = \hat{\rho}_l \rho, \quad \hat{\mu} = \hat{\mu}_l \mu, \quad \hat{k} = \hat{k}_l k, \quad \hat{\beta}_T = \hat{\beta}_{T,l} \beta_T, \quad \hat{\beta}_\chi = \hat{\beta}_{\chi,l} \beta_\chi, \quad \hat{c}_p = \hat{c}_{p,l} c_p. \tag{4.31}$$

Dealing first with the gas phase, the ratio of liquid to component A vapour properties of generic property ϑ is defined as $\varPsi_\vartheta = \hat{\vartheta}_l/\hat{\vartheta}_{gA}$. Similarly, $\varOmega_\vartheta = \hat{\vartheta}_l/\hat{\vartheta}_{g1}$ is the ratio of the liquid to inert gas $g1$ properties. All gas phase property ratios are defined as,

$$\begin{gathered}
\varPsi_\rho = \frac{\hat{\rho}_{lA}}{\hat{\rho}_{gA}}, \quad \varPsi_\mu = \frac{\hat{\mu}_{lA}}{\hat{\mu}_{gA}}, \quad \varPsi_k = \frac{\hat{k}_{lA}}{\hat{k}_{gA}}, \quad \varPsi_{\beta T} = \frac{\hat{\beta}_{T,lA}}{\hat{\beta}_{T,gA}}, \quad \varPsi_{cp} = \frac{\hat{c}_{p,lA}}{\hat{c}_{p,gA}}, \\
\varOmega_\rho = \frac{\hat{\rho}_{lA}}{\hat{\rho}_{g1}}, \quad \varOmega_\mu = \frac{\hat{\mu}_{lA}}{\hat{\mu}_{g1}}, \quad \varOmega_k = \frac{\hat{k}_{lA}}{\hat{k}_{g1}}, \quad \varOmega_{\beta T} = \frac{\hat{\beta}_{T,lA}}{\hat{\beta}_{T,g1}}, \quad \varOmega_{cp} = \frac{\hat{c}_{p,lA}}{\hat{c}_{p,g1}}.
\end{gathered} \tag{4.32}$$

Given the dimensional definition in eq. (4.4), we define the combined dimensionless properties of the gas phase,

$$\begin{aligned}
\rho_g &= \Big[\varUpsilon_A \varPsi_\rho + (1 - \varUpsilon_A)\varOmega_\rho\Big]^{-1}, \\
\mu_g &= \varUpsilon_A/\varPsi_\mu + (1 - \varUpsilon_A)/\varOmega_\mu, \\
k_g &= \varUpsilon_A/\varPsi_k + (1 - \varUpsilon_A)/\varOmega_k, \\
\beta_{T,g} &= \varUpsilon_A/\varPsi_{\beta T} + (1 - \varUpsilon_A)/\varOmega_{\beta T}, \\
c_{p,g} &= \varUpsilon_A/\varPsi_{cp} + (1 - \varUpsilon_A)/\varOmega_{cp}.
\end{aligned} \tag{4.33}$$

Moving on to the liquid phase, the dimensional physical properties given in crefdimensional liquid properties are scaled by the corresponding component A property, giving,

$$\begin{aligned}
\hat{\rho}_l &= \chi_A + (1-\chi_A)\hat{\rho}_{lR},\\
\hat{\mu}_l &= \chi_A + (1-\chi_A)\hat{\mu}_{lR},\\
\hat{k}_l &= \chi_A + (1-\chi_A)\hat{k}_{lR},\\
\hat{\beta}_{T,l} &= \chi_A + (1-\chi_A)\hat{\beta}_{T,lR},\\
\hat{\beta}_{\chi_A} &= \chi_A + (1-\chi_A)\hat{\beta}_{\chi,lR},\\
\hat{c}_{p,l} &= \chi_A + (1-\chi_A)\hat{c}_{p,lR}.
\end{aligned} \tag{4.34}$$

Where subscript lR denotes the property ratio of liquid component B to A. For some generic property, ϑ, it is defined as $\vartheta_R = vart\hat{h}eta_B/vartheta_A$. Turning our attention now to the total property expression in one-fluid form introduced in eq. (4.21). To convert this to dimensionless form, we define the following ratios of dimensionless liquid to gas properties,

$$\mathit{\Gamma}_\rho = \frac{\rho_l}{\rho_g}, \quad \mathit{\Gamma}_\mu = \frac{\mu_l}{\mu_g}, \quad \mathit{\Gamma}_k = \frac{\hat{k}_l}{k_g}, \quad \mathit{\Gamma}_{\beta T} = \frac{\beta_{T,l}}{\beta_{T,g}}, \quad \mathit{\Gamma}_{\beta\chi} = \frac{\beta_{\chi,l}}{\beta_{\chi,l}} \quad \mathit{\Gamma}_{cp} = \frac{c_{p,l}}{c_g}. \tag{4.35}$$

Note that since β_χ is special case being solely a property of the liquid and so, $\beta_{\chi,l}$ is scaled by itself to give a value of unity. Eq. (4.21) are non-dimensionalised to give dimensionless of the one-fluid form properties.

$$\begin{aligned}
\rho &= c + (1-c)/\mathit{\Gamma}_\rho,\\
\mu &= c + (1-c)/\mathit{\Gamma}_\mu,\\
k &= c + (1-c)/\mathit{\Gamma}_k,\\
\beta_T &= c + (1-c)/\mathit{\Gamma}_{\beta T},\\
\beta_\chi &= c\mathit{\Gamma}_{\beta\chi},\\
c_p &= \frac{c + (1-c)/(\mathit{\Gamma}_\rho \mathit{\Gamma}_{cp})}{c + (1-c)/\mathit{\Gamma}_{cp}}.
\end{aligned} \tag{4.36}$$

We use the thermocapillary velocity as our velocity scale, $\hat{U}^* = \hat{\gamma}_{T,lA}\mathit{\Delta}\hat{T}/\hat{\mu}_{lA}$, where $\mathit{\Delta}\hat{T}$ is the difference it temperature between the hot and cold walls. The following scaling quantities are defined,

$$\begin{aligned}
\hat{\boldsymbol{x}} &= \hat{d}\boldsymbol{x}, & \hat{\boldsymbol{u}} &= \frac{\hat{\gamma}_{T,lA}\mathit{\Delta}\hat{T}}{\hat{\mu}_{lA}}\boldsymbol{u}, \quad \hat{p} = \frac{\hat{\gamma}_{T,lA}\mathit{\Delta}\hat{T}}{\hat{d}}p,\\
\hat{t} &= \frac{\hat{\mu}_{lA}\hat{d}}{\hat{\gamma}_{T,lA}\mathit{\Delta}\hat{T}}t, & \hat{T} &= T\mathit{\Delta}\hat{T} + \hat{T}_r, \quad \hat{\sigma} = \hat{\sigma}_r\sigma.
\end{aligned} \tag{4.37}$$

Scaling the dimensions of the domain are by the initial liquid depth, $\hat{d}$,

$$L = \frac{\hat{L}}{\hat{d}}, \qquad H = \frac{\hat{H}}{\hat{d}}, \qquad W = \frac{\hat{W}}{\hat{d}}. \tag{4.38}$$

The dimensionless form of the tension introduced in eq. (4.1) simplifies to,

$$\sigma = 1 - Ca_T T - Ca_\chi \chi_A \tag{4.39}$$

where $Ca_T = \hat{\gamma}_{T,lA}\mathit{\Delta}\hat{T}/\hat{\sigma}_r$ is the thermal capillary number and $Ca_\chi = \hat{\gamma}_{\chi,lA}\mathit{\Delta}\chi_A/\hat{\sigma}_r$ is the solutal capillary number. $\mathit{\Delta}\chi_A = (\chi_A - \chi_{A,0})/\chi_A$ is the mass fraction gradient of component A. Incorporating this new expression into eq. (4.30) yields the dimensionless surface force per unit volume.

$$\boldsymbol{f_{sv}} = \Big(\frac{1}{We}(\sigma\kappa\boldsymbol{n}) - \frac{1}{Re_T}(\nabla_s T) - \frac{R_\sigma}{Re_T}(\nabla_s \chi_A)\Big)|\nabla c| \tag{4.40}$$

The arising dimensionless numbers begin with $We = \hat{\gamma}^2_{T,lA}\mathit{\Delta}\hat{T}^2\hat{d}/\hat{\mu}_{lA}\hat{\nu}_{lA}\hat{\sigma}_r$, the Weber number which quantifies the strength of inertia to interface surface tension. $Re_T = \hat{\gamma}_{T,lA}\mathit{\Delta}\hat{T}\hat{d}/\hat{\nu}_{lA}\hat{\mu}_{lA}$ is the thermocapillary Reynolds number, indicating the strength of forces arising from thermal Marangoni stress. $R_\sigma = \hat{\gamma}_\chi\mathit{\Delta}\chi_A/\hat{\gamma}_{T,lA}\mathit{\Delta}\hat{T}$ is the capillary ratio, giving the strength of solutal over thermal Marangoni forces. The previously defined capillary numbers can be constructed from We, Re_T, and R_σ such that $Ca_T = We/Re_T$ and $Ca_\chi = R_\sigma We/Re_T$. Another dependent dimensionless number we define is the Reynolds number arising from solutal Marangoni forces; $Re_\chi = R_\sigma Re_T$.

Non-dimensionalisation of eq. (4.28) results in the dimensionless buoyancy,

$$\boldsymbol{f_b} = \rho g\Big(\frac{1}{Fr} - \frac{Gr_T}{Re_T^2}(\beta_T T) - \frac{Gr_\chi}{Re_T^2}(c\beta_\chi\chi_A)\Big)\boldsymbol{e_z} \tag{4.41}$$

where $Fr = \hat{\gamma}^2_{T,lA}\mathit{\Delta}\hat{T}^2/\hat{g}\hat{d}\hat{\mu}^2_{lA}$ is the Froude number, quantifying the strength of inertial over gravitational forces. $Gr_T = \hat{g}\hat{\beta}_{T,lA}\mathit{\Delta}\hat{T}\hat{d}^3/\hat{\nu}^2_{lA}$ and $Gr_\chi = \hat{g}\hat{\beta}_{\chi,l}\mathit{\Delta}\chi_A\hat{d}^3/\hat{\nu}^2_{lA}$ are the thermal and solutal Grashof numbers respectively and give the ratios of buoyancy to viscous forces. The dynamic bond number can also be derived as $Bo_d = Gr_T/Re_T$

The volumetric mass flux across the interface introduced in eq. (4.18) is scaled by $\hat{\gamma}_{T,lA}\mathit{\Delta}\hat{T}/\hat{\rho}_{lA}\hat{\mu}_{lA}\hat{d}$ giving the dimensionless form as,

$$\mathscr{S} = \frac{(1-c)\rho_g}{t_s}\left(\frac{X_{A,sat}}{X_{A,sat} + \dfrac{(1-X_{A,sat})}{\mathcal{M}}} - \mathit{\Upsilon}_A\right) \tag{4.42}$$

The dimensionless governing eqs. (4.22) to (4.27) take the following forms,

$$\frac{\partial c}{\partial t} + \nabla\cdot c\boldsymbol{u} = -\mathscr{S} \tag{4.43}$$

$$\nabla\cdot\boldsymbol{u} = -\mathscr{S}(1 - \mathit{\Psi}_\rho) \tag{4.44}$$

$$\begin{aligned}\frac{\partial(\rho\boldsymbol{u})}{\partial t}+\nabla\cdot(\rho\boldsymbol{u}\boldsymbol{u})=\frac{1}{Re_T}&\Big(-\nabla p+\nabla\cdot\mu(\nabla\boldsymbol{u}+\nabla\boldsymbol{u}^T)\Big)\\ &-\rho g\Big(\frac{1}{Fr}-\frac{Gr_T}{Re_T^2}(\beta_T T)-\frac{Gr_\chi}{Re_T^2}(c\beta_\chi\chi_A)\Big)\boldsymbol{e_z}\\ &+\Big(\frac{1}{We}(\sigma\kappa\boldsymbol{n})-\frac{1}{Re_T}(\nabla_s T)-\frac{R_\sigma}{Re_T}(\nabla_s\chi_A)\Big)|\hat{\nabla}c|\end{aligned}\tag{4.45}$$

$$\frac{\partial(\rho c_p T)}{\partial t}+\nabla\cdot(\rho c_p T\boldsymbol{u})=\frac{1}{Re_T Pr}\Big(\nabla\cdot(k\nabla T)\Big)-\frac{\mathscr{S}}{Ja}\tag{4.46}$$

$$\frac{\partial(\rho c\chi_A)}{\partial t}+\nabla\cdot(\rho c\chi_A\boldsymbol{u})=\frac{1}{Re_T Sc_l}\Big(\nabla\cdot(\rho c\nabla\chi_A)+\nabla\cdot(\rho c S_T\nabla T)\Big)-\mathscr{S}\tag{4.47}$$

$$\frac{\partial\big(\rho(1-c)\mathit{\Upsilon}_A\big)}{\partial t}+\nabla\cdot\big(\rho(1-c)\mathit{\Upsilon}_A\boldsymbol{u}\big)=\frac{1}{Re_T Sc_g}\Big(\nabla\cdot\big(\rho(1-c)\nabla\chi_A\big)\Big)+\mathscr{S}\tag{4.48}$$

Dimensionless groups first arising in the energy equation include the Prandtl number $Pr = \hat{\nu}_{lA}/\hat{\alpha}_{lA}$, giving the ratio of momentum to thermal diffusivity and the Jacob number $Ja = \hat{c}_{p,lA}\mathit{\Delta}\hat{T}/\hat{L}_v$, representing the ratio of sensible heat to latent heat absorbed during phase change. $Sc_l = \hat{\nu}_{lA}/\hat{\mathcal{D}}_l$ and $Sc_g = \hat{\nu}_{lA}/\hat{\mathcal{D}}_g$ appearing in advection-diffusion equations eq. (4.47) and eq. (4.48) are the Schmidt numbers of the liquid and gas phase respectively, indicating the importance of momentum diffusivity over mass diffusivity. The dimensionless Soret coefficient in eq. (4.47) is defined as $S_T = \hat{S}_T\mathit{\Delta}\hat{T}\chi_{A,0}(1-\chi_{A,0})$. A further dependent number derived from the product of Re_T and Pr is the thermal Marangoni number (Ma_L),

$$Ma_L = Re_T Pr = \frac{\hat{\gamma}_{T,lA}\mathit{\Delta}\hat{T}\hat{d}}{\hat{\mu}_{lA}\hat{\alpha}_{lA}}\tag{4.49}$$

Note that the liquid thermal diffusivity, $\hat{\alpha}_l$, can be calculated as; $\hat{\alpha}_l = \hat{k}_l/\hat{\rho}_l\hat{c}_{p,l}$. The independent dimensionless groups are summarised as follows,

$$\begin{array}{llll}Re_T=\dfrac{\hat{\gamma}_{T,lA}\mathit{\Delta}\hat{T}\hat{d}}{\hat{\nu}_{lA}\hat{\mu}_{lA}}, & R_\sigma=\dfrac{\hat{\gamma}_\chi\mathit{\Delta}\chi_A}{\hat{\gamma}_{T,lA}\mathit{\Delta}\hat{T}}, & Fr=\dfrac{\hat{\gamma}_{T,lA}^2\mathit{\Delta}\hat{T}^2}{\hat{g}\hat{d}\hat{\mu}_{lA}^2}, & We=\dfrac{\hat{\gamma}_{T,lA}^2\mathit{\Delta}\hat{T}^2\hat{d}}{\hat{\mu}_{lA}\hat{\nu}_{lA}\hat{\sigma}_r},\\[2ex] Gr_T=\dfrac{\hat{g}\hat{\beta}_{T,lA}\mathit{\Delta}\hat{T}\hat{d}^3}{\hat{\nu}_{lA}^2}, & Gr_\chi=\dfrac{\hat{g}\hat{\beta}_\chi\mathit{\Delta}\chi_A\hat{d}^3}{\hat{\nu}_{lA}^2}, & Pr=\dfrac{\hat{\nu}_{lA}}{\hat{\alpha}_{lA}}, & S_T=\hat{S}_T\mathit{\Delta}\hat{T}\chi_{A,0}(1-\chi_{A,0}),\\[2ex] Sc_l=\dfrac{\hat{\nu}_{lA}}{\hat{\mathcal{D}}_l}, & Sc_g=\dfrac{\hat{\nu}_{lA}}{\hat{\mathcal{D}}_g}, & Ja=\dfrac{\hat{c}_{p,lA}\mathit{\Delta}\hat{T}}{\hat{L}_v}. & \end{array}$$

4.5. Boundary and initial conditions

The layer resides on an impermeable horizontal no-slip adiabatic wall bounded by equally impermeable vertical walls. The domain centre is situated on the bottom

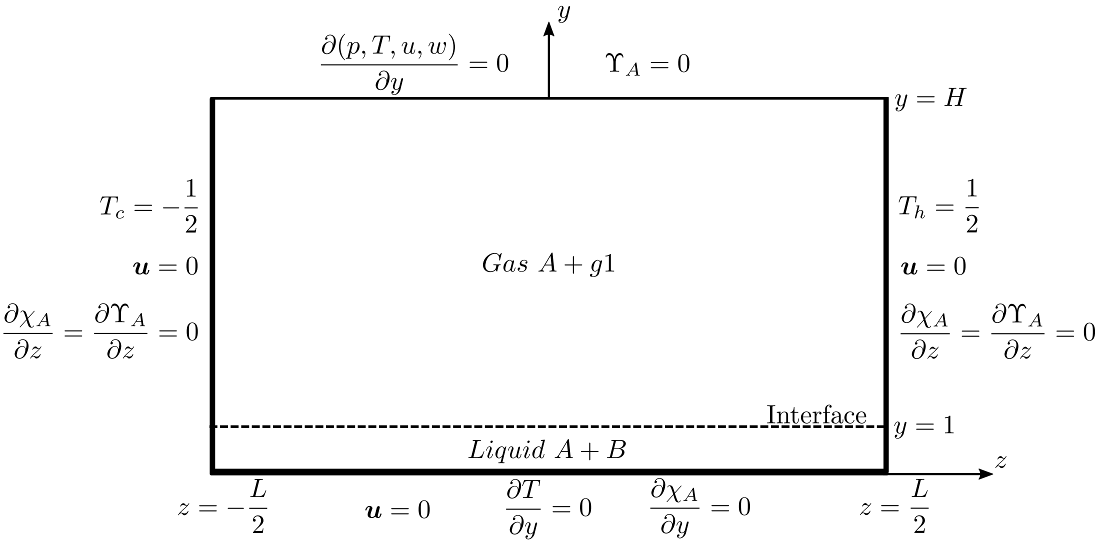

Fig. 4.3 Illustration of boundary conditions applied over the domain in a two-dimensional y-z view.

wall, centred between the four vertical walls. Streamwise walls are maintained at fixed temperatures with periodic boundaries being imposed on the spanwise walls. The horizontal upper wall is modelled as an open boundary with vertical (y-direction) gradients of pressure, temperature and velocities tangential to the boundary set to zero. Additionally, the top boundary is positioned sufficiently far from the LV interface that concentration of the component A vapour is zero. Boundary conditions as functions of (x, y, z, t) therefore are summarised in mathematical form as follows, as well as in Fig. 4.3,

$$\boldsymbol{u}(x,0,z,t)=0, \qquad \frac{\partial T}{\partial y}(x,0,z,t)=0, \qquad \frac{\partial \chi_A}{\partial y}(x,0,z,t)=0. \tag{4.50}$$

$$\boldsymbol{u}(x,y,\pm L/2,t)=0, \quad T(x,y,\pm L/2,t)=\mp\frac{1}{2}, \quad \left[\frac{\partial\chi_A}{\partial z}=\frac{\partial\Upsilon_A}{\partial z}\right](x,y,\pm L/2,t)=0. \tag{4.51}$$

$$\Upsilon_A(x,H,z,t)=0, \qquad \frac{\partial(p,T,u,w)}{\partial y}(x,H,z,t)=0. \tag{4.52}$$

Regarding the initial conditions, the initial layer depth is set to unity with equal concentrations of each component distributed uniformly throughout the liquid phase. Return flow velocity and pressure fields as applied as used by Sáenz et al. [31, 41] to approximate the return flow solution of Smith and Davis [3]. The initial temperature gradient in both phases is imposed as linear, dictated by the boundary conditions at the streamwise walls. The gas phase is initially stagnant at zero pressure with the vapour mass fraction being initialised as a concentration gradient approximating isothermal steady-state diffusion [41]. Initial conditions are summarised in the following mathematical forms,

$$\begin{aligned} &\boldsymbol{u} = \frac{c}{L}\Big(0, 0, \frac{2y^2 - 2y}{4}\Big), && T = -\frac{z}{L}, && p = \frac{3z}{2L}c, \\ &\chi_A = 0.5c, && \varUpsilon_A = 1 - (1 - \varUpsilon_{A,sat})^{\frac{H-y}{H-1}}. && \end{aligned} \tag{4.53}$$

4.6. Numerical method

The equations laid out in eq. (4.43) to eq. (4.48) form a set of eight PDEs with eight unknowns—$(c, u, v, w, p, T, \chi_A, \varUpsilon_A)$. These are solved over a discretised domain using the commercial CFD software ANSYS CFX [210] which makes use of a finite-volume method with a centred scheme used for the diffusion derivatives and a second-order upwind scheme for the advective terms. Time is advanced with a second-order backward Euler method with target root mean squared (RMS) residuals below 1×10^{-5} and the time step, t_s, always below the thermal Marangoni timescale. Double-precision floating-point accuracy is used in all simulations, meaning 16 decimal digits are retained in all variables.

In the special case of no phase change, the interface is continuously saturated, meaning $S = 0$, and the governing equations are reduced accordingly. For simplicity, the component A vapour is removed from the gas phase leaving only inert gas. This means that the advection-diffusion in the gas phase—eq. (4.48)—is also removed. In this case a set of seven PDEs with seven unknowns $(c, u, v, w, p, T, \chi_A)$ are formed. The independent dimensionless groups for the saturated case are hence the same as those laid out in eq. (4.50) with the absence of Sc_g and Ja.

The domain is discretised into a hexahedral mesh using a staggered grid. The scalar variables are stored at the centres of the discretised cells while the velocity is stored at their faces. The areas around the heated end wall are subject to additional mesh refinement in order to effectively recreate the thermal boundary layers (TBLs) in the liquid phase—discussed further in Section 5.1.2. Furthermore, the domain size is altered accorded to the case considered—either saturated or unsaturated, chiefly for the saving of computational time and resources. This is done by reducing the depth of the gas phase in the saturated case to approximately two times that of the layer. While in case inclusive of evaporation, the gas phase is twenty times the layer depth, allowing diffusion of the vapour through the inert gas to the upper boundary.

After application of the boundary and initial conditions, every simulation begins with the time-stepping of the solution towards a stable base state. This has deemed to be achieved once the TBLs have completely formed and the return flow velocity within the layer is remains constant and stable. In order to observe HTWs, we then perturb this quasi-steady base state and continue to evolve the solution in time, allowing the instability either to take hold or for the perturbations to decay.

4.7. Perturbing the base state

We introduce perturbations to the base state that will travel along the horizontal LV interface at well-defined angles to the bulk flow. Note that in-line with the work of Smith and Davis [3], we assume the resulting disturbance to be a wave travelling in a direction amalgamating the streamwise (z) and spanwise (x) directions, and hence we do not introduce a perturbing function in the vertical (y) direction. The form of perturbation presented here is also used by Sáenz et al. [31, 41] in their DNS model for single component layers. The process of introducing the interfacial disturbances is outlined as follows. Let us define the general form of the perturbation, ϑ_1, of generic variable, ϑ, as,

$$\vartheta_1 = \tilde{\vartheta} e^{i(k_z z + k_x x - \omega t)} \tag{4.54}$$

where $\tilde{\vartheta}$ is the amplitude of the perturbation in the vertical y-direction—chosen as a small number. k_z and k_x are the disturbance wavenumbers in the z and x directions respectively, and $\omega = \omega_R + i\omega_I$ is the complex eigenvalue. Expansion of eq. (4.54) yields,

$$\vartheta_1 = \tilde{\vartheta} e^{(i(k_z z + k_x x - \omega_R t) + \omega_I t)} = \tilde{\vartheta}(e^{i(k_z z + k_x x - \omega_R t)} e^{\omega_I t}) \tag{4.55}$$

with application of Euler's' theorem and subsequent expansion, we obtain the real (physical) part of the perturbation to be applied to the interface,

$$R(\vartheta_1) = \tilde{\vartheta} \cos(k_z z + k_x x) \tag{4.56}$$

The stability analysis of Smith and Davis [3] revealed that the stability of the return flow layer is enslaved to the Prandtl number. Fig. 4.4(a) shows the critical Marangoni number above which the layer is unstable and HTWs take hold. Note that line (i) in Fig. 4.4(a) corresponds to HTWs travelling obliquely to the flow as such is considered here. Larger Pr has a stabilising effect on the layer, requiring a greater Marangoni number for instability to ensue. HTWs are then expected to travel at distinct angles of propagation also dictated by Prandtl number, as shown in Fig. 4.4(b), with larger Pr broadly resulting in a smaller propagation angle to the flow. The wavenumber of the HTWs broadly increases with Pr which is illustrated in Fig. 4.4(c). Phase speed has a more complex dependency—see Fig. 4.4(d)—with maximum at $Pr \approx 10^{-2}$ and minimum at $Pr \approx 1$.

Returning to eq. (4.56), we obtain values of k_z and k_x to apply our perturbations for a given Pr from the results of Smith and Davis [3] in Fig. 4.4. Specifically, k_z and

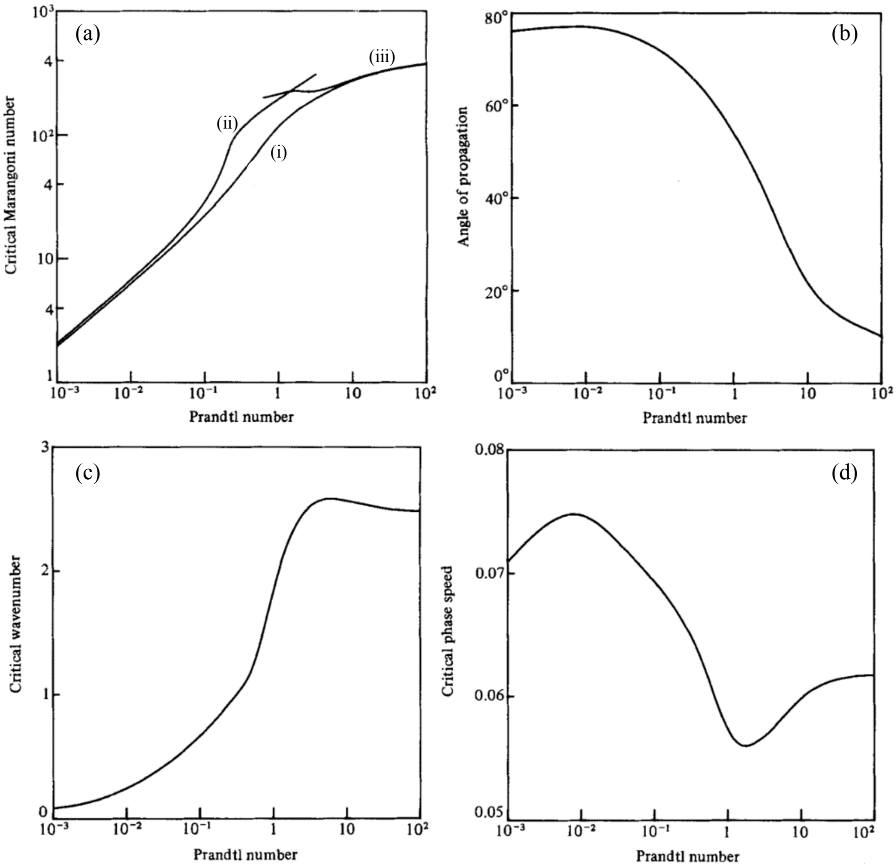

Fig. 4.4 Results from the stability analysis of Smith and Davis [3] showing the nature of the most dangerous modes according to Prandtl number. (*a*) the critical Marangoni number at each Prandtl number marking the onset of HTWs (line (*a*) pertaining to oblique HTWs), (*b*) the corresponding angle of propagation of the oblique HTWs (ψ_{SD}), (*c*) the corresponding critical wavenumber (K_{SD}), and (*d*) the critical phase speed.

k_x are obtained from the overall wavenumber (K_{SD}), in Fig. 4.4(c), and the travelling direction of the waves (ψ_{SD}), in Fig. 4.4(b), according to the following expressions [3],

$$K_{SD} = \sqrt{{k_z}^2 + {k_x}^2} \qquad \Psi_{SD} = \tan^{-1}\left(\frac{k_x}{k_z}\right) \tag{4.57}$$

5. Behaviour of binary layers

5.1. Saturated binary layers

Previous detailed investigations into the behaviour of saturated binary liquid layers have considered only a rigid interface and have not accounted for the gas phase [49, 50, 51, 52, 53], which has been shown to have a measurable effect in single component layers [31].

Since our detailed model captures the deformable interface and fully resolves the gaseous flow field, we begin first by suppressing evaporation and examine the saturated case. Areas of particular interest are:

1. The effect of the thermodiffusion (Soret effect) on component segregation within the layer.
2. The effect of solutal Marangoni stress on the formation of HTWs.

5.1.1 Driving force and layer physical properties

Physical properties

Our analysis is based on a liquid layer consisting of equal concentration of hexane (component A) and decane (component B), hence $\chi_A = 0.50$. With no evaporation considered in the following cases, the average concentration in the liquid phase remains constant over time. Physical properties of liquid hexane, decane and the inert gas (air) constituting the gas phase above are given in Tab. 5.1. The corresponding dimensionless properties are given in Tab. 5.2. The fluids we consider here are same as the mixtures used in the experiments and simulations of Yu and co-workers [42, 49]. To aid our modelling approach, we lower the viscosity slightly while increasing the thermal conductivity. This has the effect of reducing Pr from 9.08 to 0.746. Since Pr is the ratio of a fluids ability to transport momentum over its ability to transport energy, a high Pr means that a small amount of heat is conducted while heat transfer

Tab. 5.1 Physical properties of air and hexane/decane mixture for at $\hat{T} = 25\,°\mathrm{C}$ and $\hat{p} = 1\,\mathrm{atm}$.

		Air	Liquid mixture
$\hat{\rho}$	$(\mathrm{kg\,m^{-3}})$	1.18	690
$\hat{\mu}$	$(\mathrm{Pa\,s})$	1.83×10^{-5}	4.70×10^{-4}
$\hat{k}$	$(\mathrm{W\,s^{-1}\,K^{-1}})$	0.01	0.115
$\hat{c}_p$	$(\mathrm{J\,kg^{-1}\,K^{-1}})$	1004	2222
$\hat{\beta}_T$	$(\mathrm{K^{-1}})$	3.36×10^{-3}	1.2×10^{-3}
β_ω			-0.103
$\hat{\sigma}$	$(\mathrm{N\,m^{-1}})$		2.10×10^{-2}
$\hat{\gamma}_T$	$(\mathrm{N\,m^{-1}\,K^{-1}})$		6.98×10^{-5}
$\hat{\gamma}_\chi$	$(\mathrm{N\,m^{-1}})$		-5.19×10^{-3}
$\hat{S}_T$	$(\mathrm{K^{-1}})$		2.42×10^{-3}
$\hat{M}$	$(\mathrm{g\,mol^{-1}})$	28.96	114.23

by natural convection is significant. For a low Pr, the opposite is true—heat is conducted effectively while convection plays a smaller roll. Practically, this means that for high Pr there is a "sharp" TBL region at the end walls which significantly lowers the effective thermal gradient, $\hat{b}_i$, once the boundary layers have established. $\hat{b}_i$ is therefore computed as the temperature gradient between the hot and cold walls outside of the established TBLs—see Fig. 5.1 overleaf. We now introduce a "posterior" effective Marangoni number,

$$Ma_E = \frac{\hat{\gamma}_T \hat{d}^2 \hat{b}_i}{\hat{\mu}_l \hat{\alpha}_l} \tag{5.1}$$

which is analogous to the one used by Smith and Davis [3] in their pioneering stability analysis. This allows us to predict the stability of the layer, however approximate since only the effects of thermal Marangoni are considered in this equation. For any given Pr, the system is unstable if Ma_E is above a critical Marangoni number, Ma_{crit}. Reducing $\hat{b}_i$ therefore lowers effective Marangoni number, lowering the driving force for thermal instabilities (such as HTWs)and moving the flow out of a critical region. To maximise the effective temperature gradient and chance of observing HTWs, we lower the value of Pr to "soften" the TBLs and retain a larger effective thermal gradient between the heated and cooled end walls.

Tab. 5.2 Corresponding dimensionless properties for those given in Tab. 5.1.

Re_T	12 206
R_σ	0.045–0.45
Fr	1763
We	567
Gr_T	1420
Gr_χ	74
Pr	0.746
S_T	8.47×10^{-3}
Sc_l	127
Bo_d	0.116

Capillary ratio

With no evaporation from the interface under saturated conditions, concentration differences in the liquid therefore arise solely from the Soret effect causing component migration under the applied temperature gradient. Whilst this driving force is weak, it must still be investigated before phase change is introduced. Using eq. (4.8), the maximum difference in mass fraction present within the layer at steady state is predicted to be 8.47×10^{-3}. The relative strength of solutal to thermal Marangoni stress is measured using the capillary ratio, R_σ, introduced in Chapter 4:

$$R_\sigma = \frac{Re_\chi}{Re_T} = \frac{\hat{\gamma}_\chi \Delta \hat{\chi}}{\hat{\gamma}_T \Delta \hat{T}} \tag{5.2}$$

By controlling the magnitude of the concentration coefficient of surface tension ($\hat{\gamma}_\chi$), we consider the effect R_σ has on the layer flow. We investigate two values of R_σ, the first arises naturally from the dimensional properties given in Tab. 5.1—$R_\sigma = 4.5 \times 10^{-2}$, while for the second we increase this by $O(1)$ to give $R_\sigma = 4.5 \times 10^{-1}$.

5.1.2 2D Quasi-stable base state

Before we can introduce HTWs and monitor the transient behaviour, we must first achieve a quasi-stable base state upon which to initiate the disturbances. We do this by imposing initial conditions similar to the return flow solution obtained by Smith and Davis [3]. The initial conditions are given in Section 4.5 with an initial layer depth of $d = 1$. We solve the base state transiently by time stepping the solution towards larger times, allowing the flow to equilibrate. For efficient computation, the base state

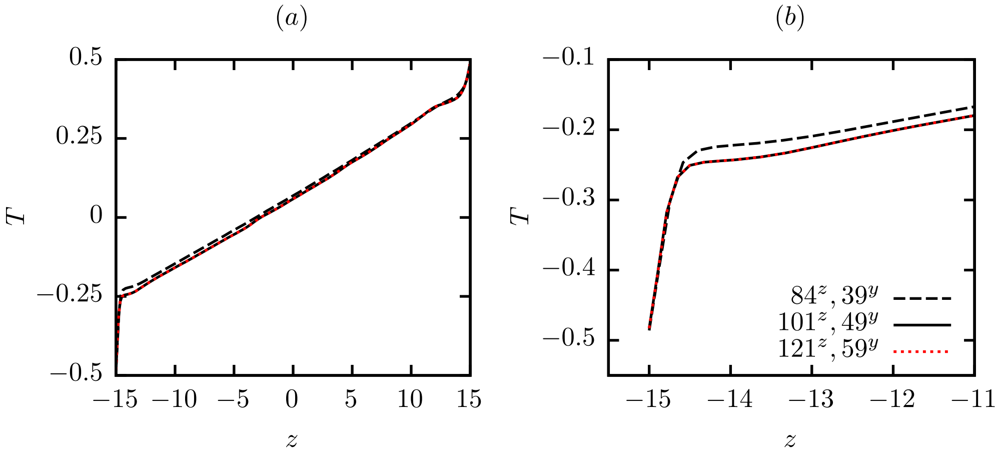

Fig. 5.1 Temperature profiles along the horizontal liquid-vapour interface for $R_\sigma = 4.5 \times 10^{-2}$ at $t = 7.00 \times 10^5$, showing increasing mesh refinements. The remaining dimensionless properties are given in Tab. 5.2. (a) shows complete profile between hot and cold end walls. (b) presents the same data but as a close-up of the thermal boundary layer at the cold wall.

is restricted to 2D. To characterise the base state flow, we limit ourselves to examining profiles over the horizontal LV interface and profiles in the liquid phase from a vertical slice (i.e. in the y-direction) taken at the centre of the domain.

Thermal boundary layers

Let us consider the base state case for $R_\sigma = 4.5 \times 10^{-2}$. The layer is deemed to be at thermal steady state when the TBLs are fully formed and horizontal thermal profile between the heated and cooled walls remains unchanged with time. Steady state appears to be achieved by $t \approx 4.00 \times 10^5$ and the solution is then time-stepped well beyond this time to $t = 7.00 \times 10^5$ before introducing perturbations. $t = 7.00 \times 10^5$ corresponds to $\hat{t} = 140\,\text{s}$ which is achieved in approximately 6 weeks of simulation time at 101^zx49^y grid density. Fig. 5.1 shows the effective temperature gradient formed along the interface at $t = 7.00 \times 10^5$ for increasing mesh refinement. In all cases, the grid is refined at the hot and cold end walls where formation of TBLs are clearly visible. With negligible difference between grids 101^zx49^y and 121^zx59^y, we use the former to proceed in our analysis. The TBLs observed here are analogous to those in pure liquid as seen by Sáenz et al [31], shown in Fig. 5.2. Note that the bulk fluid properties differ from our binary mixture, leading to a steeper thermal gradient between the heated and cooled walls in our case. Using eq. (5.1) and the results from Smith and Davis [3], we obtain $Ma_E = 182$. For solely themocapillary-driven layers at $Pr = 0.746$, Smith and Davis [3] predict $Ma_{crit} \approx 100$—see Fig. 4.4(a). It then follows that our base state should be positioned well within the critical regime, based on thermal Marangoni alone.

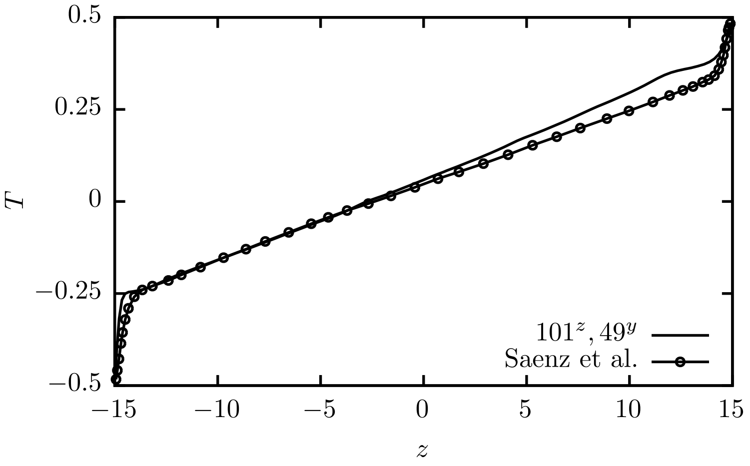

Fig. 5.2 Temperature profiles along the horizontal liquid-vapour interface for $R_\sigma = 4.5 \times 10^{-2}$ at $t = 7.00 \times 10^5$ and mesh refinements compared to the results from Sáenz et al. [31] for a single component mixture with similar (but not identical) bulk properties to the binary mixture studied here. Formation of thermal boundary layers at the hot and cold walls are clear in both cases.

Return flow and induced vertical temperature gradient

We now consider a vertical slice taken at the centre of the domain ($z = 0$), equidistant from the heated and cooled end walls. Fig. 5.3 shows the vertical variation in temperature and streamwise velocity in the liquid phase for both capillary ratios. In both cases there is a strong return flow profile where liquid at the LV interface is drawn towards the cold wall due to the higher surface tension present there. Upon reaching the cold wall, liquid sinks and is convected back towards the hot wall within the lower portion of the layer interior. Note that the dynamic Bond number is well below 1 at $Bo_d = 0.116$ (see Tab. 5.2), indicating that surface tension dominates over buoyant-driven convection in driving the return flow. The velocity profile in Fig. 5.3(b) reflects this process. Coupled to this is a vertical temperature profile, whereby at any discrete point on the interface, the liquid directly below that point is cooler—see Fig. 5.3(a). This return flow profile is a well know phenomena in laterally heated layers [3, 31], being driven by thermal Marangoni effects. We see, however, that increasing R_σ (and hence the magnitude of solutal Marangoni stress) marginally enhances the return flow profile. The interfacial velocity towards the cold wall is marginally enhanced, as is the return flow towards the hot wall in the opposite direction. This also has an effect on the vertical temperature profile, increasing the induced gradient. This effect is in line with the experimental predictions and modelling of Yu and co-workers [42, 50] who document the Soret-induced migration of decane to cooler regions, lowering Ma_{crit} required for the onset of instability.

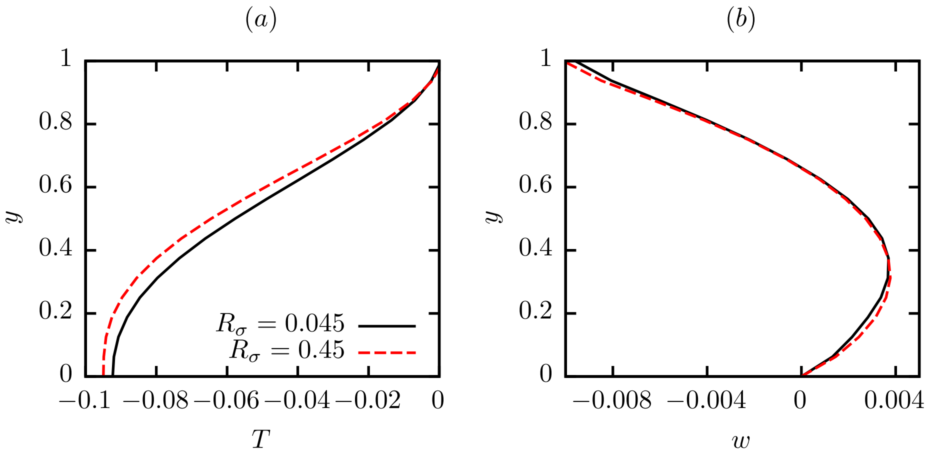

Fig. 5.3 Vertical temperature (a) and w-velocity profiles (b) in the liquid phase in the centre of the domain at $z = 0$. Solid line shows $R_\sigma = 4.5 \times 10^{-2}$ while dashed red line shows $R_\sigma = 4.5 \times 10^{-1}$. $t = 7.00 \times 10^5$ will all other dimensionless properties given in Tab. 5.2.

Component segregation

Fig. 5.4 presents 2D slices in the yz-plane of the layer at $t = 7.00 \times 10^5$, with Fig. 5.4(a) showing the volume fraction and streamlines, revealing the return flow profile first shown in Fig. 5.3(b). The 2D temperature field in both phases corresponding to Fig. 5.3(a) is then displayed in Fig. 5.4(b). Fig. 5.4(c) shows the difference in mass fraction between heavier component B, decane, and lighter component A, hexane, within in the liquid phase. As previously mentioned, in the current saturated environment, component segregation is driven by Soret diffusion. We see a subtle concentration gradient developing within the layer with the maximum difference in mass fraction being of $O(10^{-6})$. Component separation is of course still a transient process with extension to larger times resulting in further segregation from thermodiffusion. Although there is negligible component segregation along the interface, within the layer interior the largest mass fractions of decane are found in comparatively cooler areas—these being the LHS cooled wall and the bottom horizontal wall. Although concentration gradients are subtle, this is the expected behaviour of decane molecules in a hexane-decane mixture [43, 50]. It is also clear from comparing Fig. 5.4(c) to (a) that return flow within the liquid influences the distribution of components A and B, appearing to facilitating mixing, particularly along the bottom wall.

We now continue our analysis by applying a perturbation to the numerically generated base states for each capillary ratio, frozen at $t = 7.00 \times 10^5$. The perturbation will stimulate the formation of HTWs which we then monitor as they evolve over time.

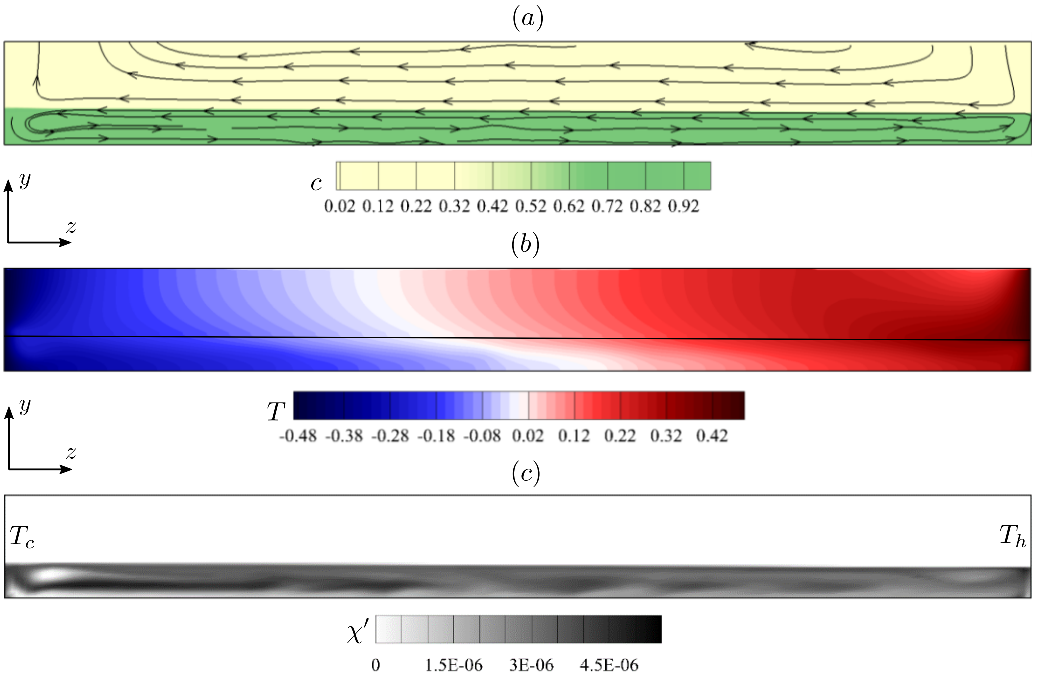

Fig. 5.4 Slice of the zy-plane for $R_\sigma = 4.5 \times 10^{-2}$ at $t = 7.00 \times 10^5$ showing (a) the colour function, c, along with the streamlines in both phases, (b) the temperature of both phases, and (c) the difference in mass fraction between components B and A, χ' ($= \chi_B - \chi_A$). All other dimensionless properties are given in Tab. 5.2.

5.1.3 Transient results

The procedure used to introduce perturbations to the flow along with the form of the perturbing function is introduced in Section 4.7. To initiate HTWs in 3D, we first take the numerical base state previously obtained in 2D and apply the profile uniformly to a new 3D domain. This 3D mesh has a width, $W = 15$, in the x-direction and a grid resolution of 101^zx49^yx73^z. The non-heated vertical walls bounding the yz-plane are again treated as periodic—we expect HTWs to travel at angles perpendicular to the z-axis, as per the predictions of Smith and Davis [3] and the DNS results of Sáenz et al. [31]. With the numerical base state frozen at $t = 7.00 \times 10^5$ applied as initial conditions in 3D, we then add the perturbing function—eq. (4.56)—to the initial values of (T, p, χ_A, u, v and w). The perturbation amplitude is chosen to be one-thousandth the size of the field variable being perturbed, i.e. $\tilde{\vartheta} = \vartheta/1000$. Note that we do not perturb the vapour-liquid interface directly because this tends to result in it becoming more diffuse. We then proceed as before, stepping the solution forward in time from $t = 7.00 \times 10^5$, allowing any interface disturbances caused by the perturbing function to either take hold or decay with time. Note that identical perturbing functions are applied both cases; $R_\sigma = 4.5 \times 10^{-2}$ and $R_\sigma = 4.5 \times 10^{-1}$ at the same instance in time.

After applying the perturbing function, HTWs emerge on the interface with time for both capillary ratios. These are observed as temperature fluctuations from the base state travelling along the interface. The local deviation from the base state of generic variable, ϑ', is computed as [31];

$$\vartheta' = \vartheta - \frac{1}{W}\int_{-W/2}^{+W/2} \vartheta dx \tag{5.3}$$

Fig. 5.5 shows the spatial growth of the interfacial temperature fluctuations for both capillary ratios at $t = 8.00 \times 10^5$, $t = 8.25 \times 10^5$, and $t = 9.00 \times 10^5$ respectively. Starting first with $R_\sigma = 4.5 \times 10^{-2}$ (shown in Fig. 5.5(a)–(c)) at $t = 8.00 \times 10^5$, HTWs begin to propagate from left to right in the spanwise direction (along the x-axis), propagating at angles of 50° with respect to the reverse flow direction (negative z-axis)—Fig. 5.5(a). By $t = 8.25 \times 10^5$, this first HTW mode is disrupted by a second mode propagating now at angles of 54° with respect to the positive z-axis. This second mode eventually completely overwhelms the first mode to become the prevailing mode seen in Fig. 5.5(c). This same behaviour was seen by Sáenz et al. [31] in single component layers. Note that HTWs travelling in the prevailing mode in our case remain restrained to near the hot wall ($z = 15$), terminating at $z \approx 5$ as the interface becomes cooler. Sáenz et al. [31] observed similar HTWs in single component layers engulfing the entire domain. The reason for this apparent difference is likely due to the reduced effective Marangoni number in our case (182 versus 211 for Sáenz et al. [31]), making our binary layer slightly more stable to the introduced perturbations.

Turning attention now to the increased capillary ratio, $R_\sigma = 4.5 \times 10^{-1}$ shown in Fig. 5.5(d)–(f). At $t = 8.00 \times 10^5$ in Fig. 5.5(d), we see HTWs propagating in a similar way to those observed at the same time instance for $R_\sigma = 4.5 \times 10^{-2}$, the waves travelling at angles of 50° with respect to the negative z-axis. As time proceeds, however, rather than being taken over by a second prevailing mode, the HTWs retain the same form while growing in the streamwise direction towards the cold wall—see Fig. 5.5(e) and (f). It is clear, therefore, that increasing the capillary ratio (and hence the strength of solutal Marangoni stress) impacts the HTW instability and suppresses the onset of the prevailing mode. The angle of wave propagation (ψ) along with the overall wavenumber K for the HTWs at $t = 9.00 \times 10^5$ for both capillary ratios are compared to the predictions of Smith and Davis [3] and the DNS results of Sáenz et al. [31] in Tab. 5.3. The overall wavenumber in the final prevailing mode both in capillary ratios are comparable to those obtained by Sáenz et al. [31].

Similar to previous finding [31, 41], we find that the thermal interfacial disturbances caused by HTWs induce subsequent fluctuations in the bulk liquid and gas flow fields. Fig. 5.6 shows slices of the spanwise flow fields in temperature, velocity and hexane mass fraction for both phases, taken at $z = 10$. Convective rolls in both phases, coupled to the interfacial HTWs are observed, evidenced in Fig. 5.6(b). Subtle fluctuations in

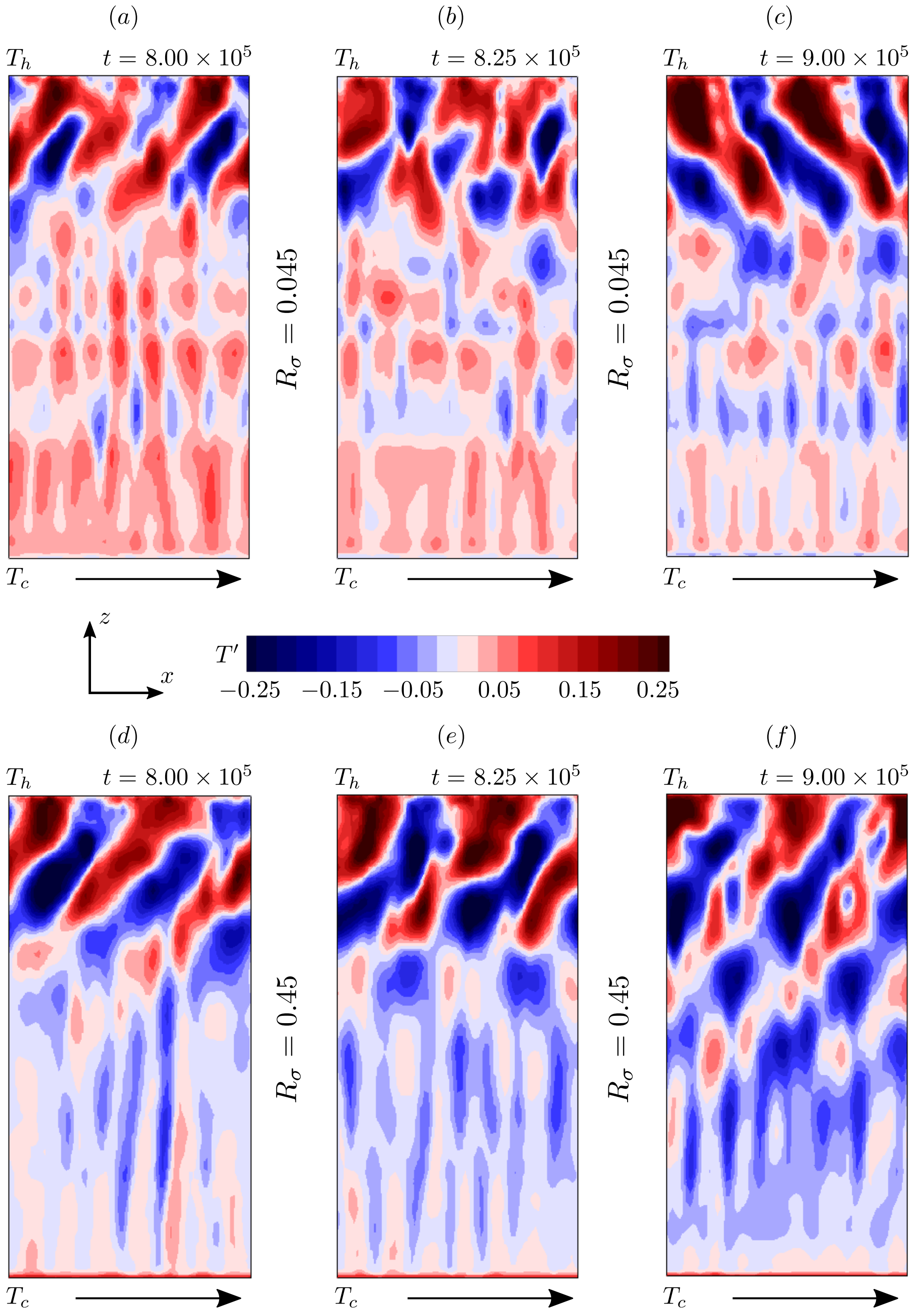

Fig. 5.5 Snapshots in the xz-plane showing the temperature fluctuation of the liquid-vapour interface. (a)–(c) show the interface for $R_\sigma = 4.5 \times 10^{-2}$ at $t = 8.00 \times 10^5$–9.00×10^5 while (d)–(f) show the same for $R_\sigma = 4.5 \times 10^{-1}$. All other properties are given in Tab. 5.2. Arrows at the foot of each snapshot show the direction of travel of the prevailing waves (left to right).

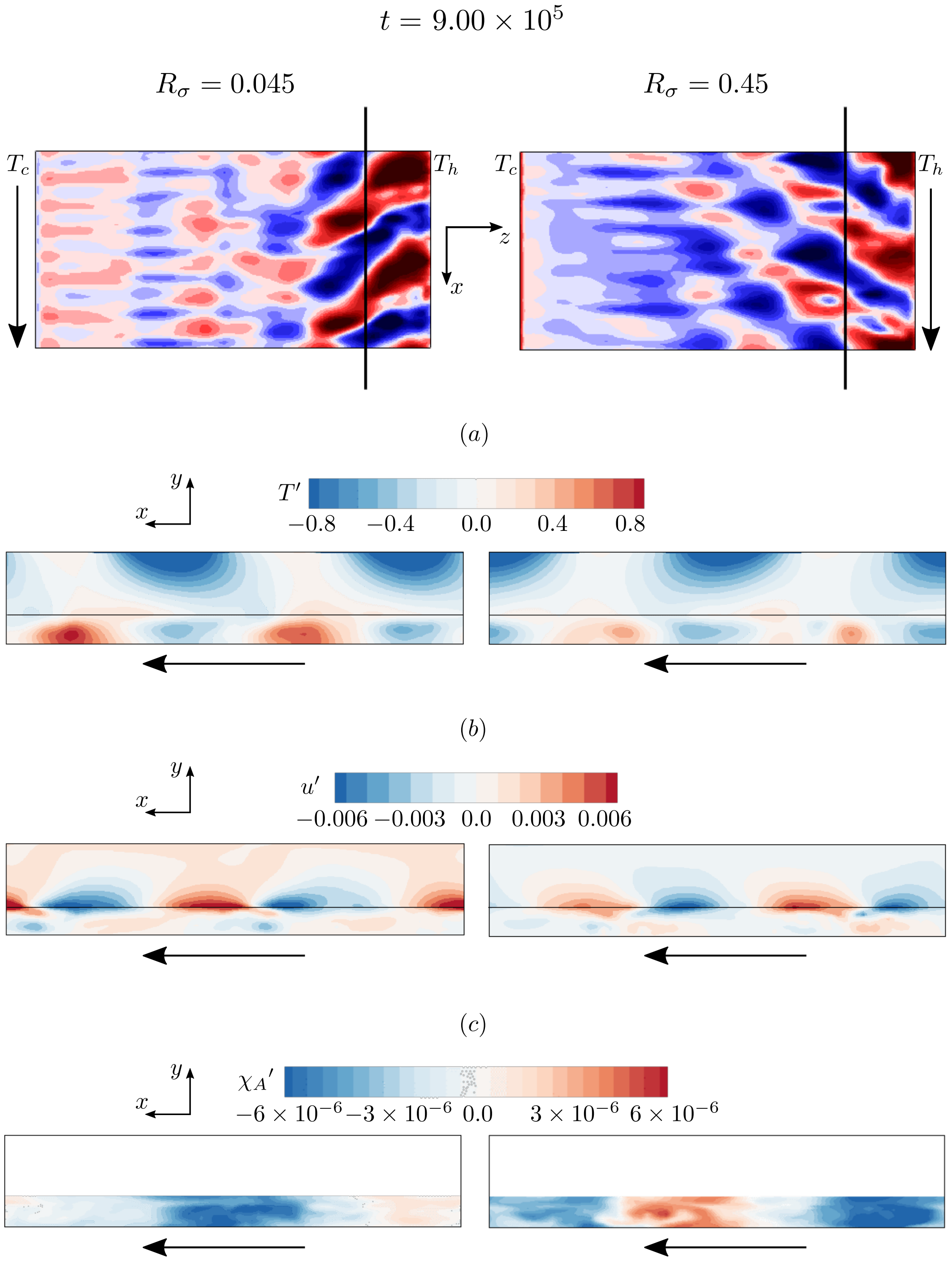

Fig. 5.6 Flow field in the spanwise direction (xz-plane) at $z = 10$ and $t = 9.00 \times 10^5$. $R_\sigma = 4.5 \times 10^{-2}$ is shown on the LHS while $R_\sigma = 4.5 \times 10^{-1}$ is on the RHS. Remaining dimensionless properties are given in Tab. 5.2. (a) shows temperature fluctuations in both liquid and gas phase, (b) shows the corresponding velocity fluctuation in both liquid and gas, (c) shows the fluctuation in MVC (hexane) mass fraction in the liquid. All other properties are given in Tab. 5.2. Arrows show the direction of travel of the prevailing waves.

Tab. 5.3 Angle of propagation (ψ) and overall wavenumber (K) for the final HTW modes at $t = 9.00 \times 10^5$ for both capillary ratios compared to the results obtained by Smith and Davis [3] and Sáenz et al.[31].

	ψ	K
Smith & Davis [3]	57°	1.52
Sáenz et al. [31]	55°	1.04
$R_\sigma = 0.045$	54°	1.01
$R_\sigma = 0.45$	−50°	1.01

hexane mass fraction from the base state value of $O(10^{-6})$ persist throughout the depth of the layer—see Fig. 5.6(c). Similar concentration fluctuations were also observed by Yu et al. [50] but at around two orders of magnitude lager than we obtain for a similar thermocapillary Reynolds number.

Figs. 5.7 and 5.8 then plot the spanwise temperature disturbance along the interface (T') compared to the spanwise interface velocity, height and component A (hexane) mass fraction fluctuation (u', d', χ'_A) for $R_\sigma = 4.5 \times 10^{-2}$ and $R_\sigma = 4.5 \times 10^{-1}$ respectively. For both capillary ratios, the profiles of velocity and interface height fluctuation in the x-direction are similar to the temperature fluctuation, with a wavenumber of 1.04 in all cases (shown by (a) and (b) in Figs. 5.7 and 5.8). With $T' \approx \pm 0.2$ for both values of R_σ, $u' \approx \pm 0.01$ and $d' \approx 0.002$ in both cases. Concentration disturbances take on a slightly different form ((c) in Figs. 5.7 and 5.8), with the wavenumber in the x-direction being reduced to 0.50—the wavelength being approximately twice that of the temperature and spanwise velocity fluctuations. While the magnitude of the concentration fluctuation is subtle at $O(10^{-6})$, this is the same order of magnitude as Soret-induced concentration difference presented in Fig. 5.4(c). Yu et al. [50] observed similar surface concentration fluctuations in an annular geometry using a one-sided model with a non-deformable rigid LV interface.

The flow field fluctuations for each capillary ratio are then compared directly in Fig. 5.9. It is clear from Fig. 5.9(a) that increasing R_σ causes a delay of approximately 0.1 times the wavelength of the temperature fluctuation with the interface deformation enslaved to the temperature field (Fig. 5.9(c)). Sáenz et al. [31] was the first to reveal this dependency is single component layers. The fluctuation in velocity and mass fraction exhibits an even greater delay of 0.5 times the wavelength between $R_\sigma = 0.045$ and $R_\sigma = 0.045$—see Fig. 5.9, graphs (b) and (d).

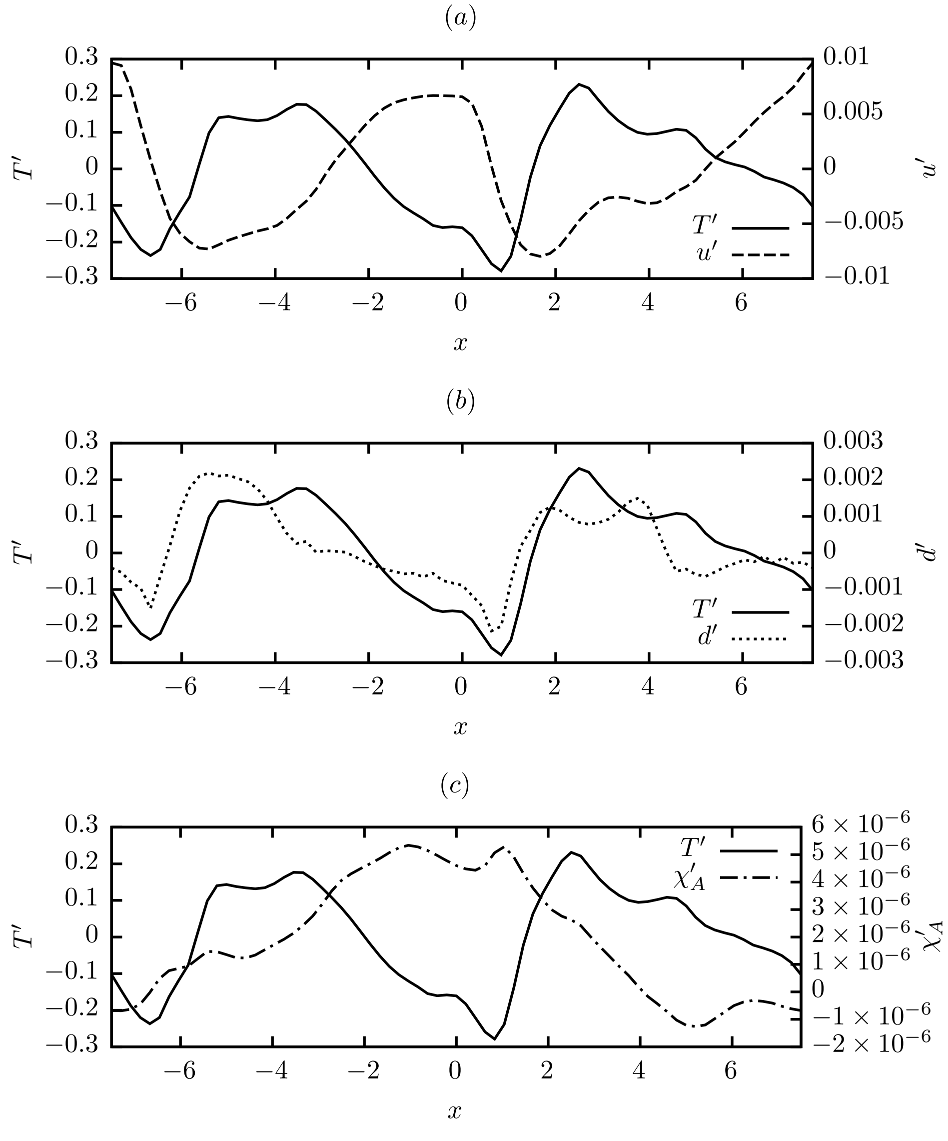

Fig. 5.7 Interface ($y = d$) profiles at $z = 10$ along the spanwise (x) direction at $t = 9.00 \times 10^5$ for $R_\sigma = 4.5 \times 10^{-2}$ (black). Temperature fluctuations are shown on all plots with (a) showing comparison with velocity fluctuation, u', (b) comparison with liquid depth (interface height) fluctuation, d', and (c) comparison with MVC (hexane) mass fraction fluctuation, χ'_A. Remaining properties are given in Tab. 5.2.

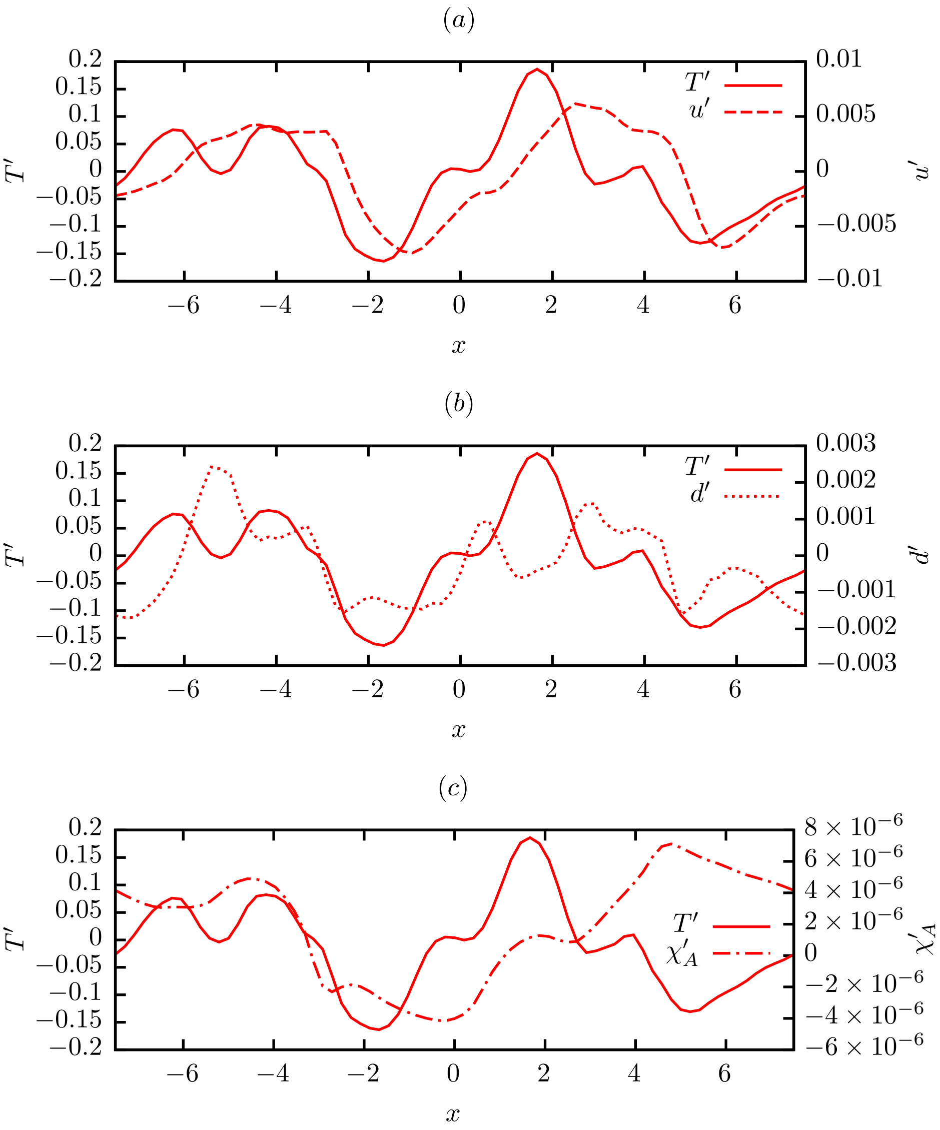

Fig. 5.8 Interface ($y = d$) profiles at $z = 10$ along the spanwise (x) direction at $t = 9.00 \times 10^5$ for $R_\sigma = 4.5 \times 10^{-1}$. Temperature fluctuations are shown on all plots with (a) showing comparison with velocity fluctuation, u', (b) comparison with liquid depth (interface height) fluctuation, d', and (c) comparison with MVC (hexane) mass fraction fluctuation, χ'_A. Remaining properties are given in Tab. 5.2.

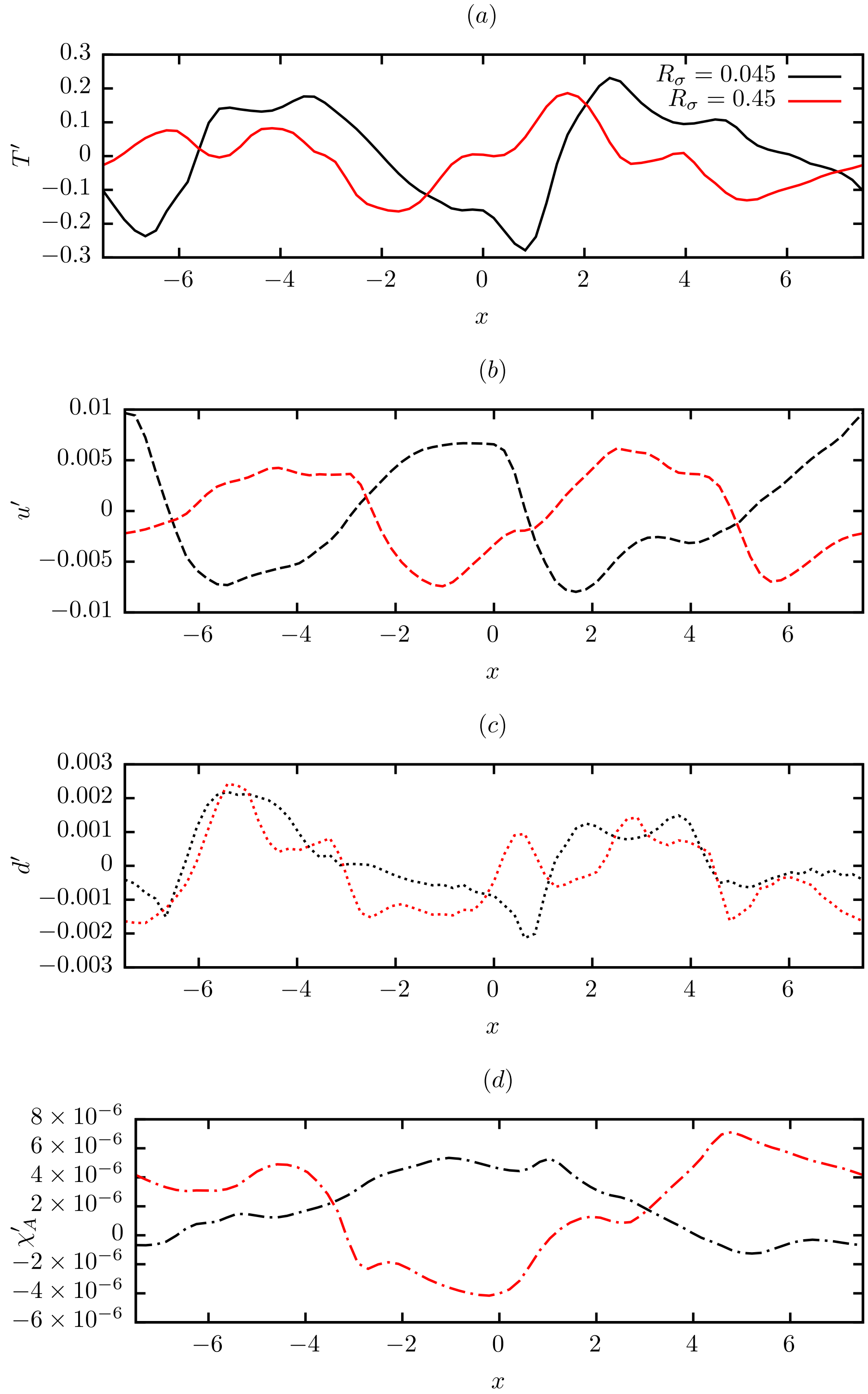

Fig. 5.9 Comparison of interface ($y = d$) fluctuations between $\sigma = 4.5 \times 10^{-2}$ (black) and $\sigma = 4.5 \times 10^{-1}$ (red) at $z = 10$ and $t = 9.00 \times 10^5$. (a) shows temperature fluctuation, (b) velocity fluctuation, and (c) MVC mass fraction fluctuation. Remaining properties are given in Tab. 5.2.

5.2. 2D Binary layers with evaporation

Prior to the current investigation, Sáenz et al. [41] used a similarly detailed model to examine the behaviour of unsaturated liquid layers of silicone oil, revealing the following:

1. Evaporative cooling inhibits HTWs and delays the onset of the instability.
2. Evaporation reduces liquid depth and this amplifies the interfacial disturbance due to the reduced effects of gravity, which stabilises the liquid as depth increases.
3. The interfacial instabilities generate oscillatory features in the temperature, local evaporation flux, and hence vapour concentration above the gas-liquid interface.
4. Comparison to a case where $\gamma_T = 0$, it was demonstrated that thermal Marangoni alters the evaporation flux along the interface which in turn caused condensation of the vapour phase.

We will build on this knowledge by investigating the behaviour of an evaporating binary layer consisting, as before, of equal parts of hexane and decane. We focus on phenomena that arises from the introduction of a second liquid component and investigate the role played by the Soret effect and solutal Marangoni flow with the added complication of evaporation. Specifically, the following aspects are investigated:

1. Varying the saturation pressure of the MVC (hexane) to investigate the effects of evaporation rate.
2. Removing γ_T, the temperature coefficient of surface tension (and hence the influence of temperature on surface tension), meaning capillary action is driven solely by solutal Marangoni flow.

In this work, our analysis is restricted to the 2D base state only and transient instabilities such as HTWs are not considered.

5.2.1 Vapour physical properties

As previously discussed in Section 4.2, upon introducing phase change, we consider the case where only hexane evaporates and so the gas phase consists of a mixture of inert air and hexane vapour. The updated dimensional physical properties of the problem, accounting for hexane vapour, are given in Tab. 5.4 with the corresponding dimensionless properties given in Tab. 5.5. Note the addition of gas phase Schmidt

Tab. 5.4 Physical properties of air, hexane vapour, and hexane/decane mixture for at $\hat{T} = 25\,^{\circ}\mathrm{C}$ and $\hat{p} = 1\,\mathrm{atm}$.

		Air	Hexane vapour	Liquid mixture
$\hat{\rho}$	$(\mathrm{kg\,m^{-3}})$	1.18	3.54	690
$\hat{\mu}$	$(\mathrm{Pa\,s})$	1.83×10^{-5}	6.47×10^{-6}	4.70×10^{-4}
$\hat{k}$	$(\mathrm{W\,s^{-1}\,K^{-1}})$	0.01	1.27×10^{-2}	0.115
$\hat{c}_p$	$(\mathrm{J\,kg^{-1}\,K^{-1}})$	1004	1695	2222
$\hat{\beta}_T$	$(\mathrm{K^{-1}})$	3.36×10^{-3}	3.36×10^{-3}	1.2×10^{-3}
β_ω				-0.103
$\hat{\sigma}$	$(\mathrm{N\,m^{-1}})$			2.10×10^{-2}
$\hat{\gamma}_T$	$(\mathrm{N\,m^{-1}\,K^{-1}})$			6.98×10^{-5}
$\hat{\gamma}_\chi$	$(\mathrm{N\,m^{-1}})$			-5.19×10^{-3}
$\hat{S}_T$	$(\mathrm{K^{-1}})$			2.42×10^{-3}
$\hat{M}$	$(\mathrm{g\,mol^{-1}})$	28.96	86.18	114.23

number, Sc_g, the Jakob number, Ja, and the dimensionless vapour pressure of hexane, p_{sat,χ_A}.

The addition of phase change complicates our already parametrically rich problem. In this initial investigation, we focus on two specific scenarios; first, we assess the influence of evaporation rate by varying the volatility of hexane; second, we remove thermal Marangoni effects altogether and consider an evaporating binary layer driven only by solutal Marangoni stress. Similar to the saturated cases in Section 5.1, the initial concentration of hexane is always 50 wt.% in the liquid phase—$\chi_A = 0.50$.

5.2.2 Influence of evaporation rate

The evaporation of hexane (component A) from the liquid phase will decrease both the remaining liquid volume of the layer along with the interior mass fraction. Evaporation will be stronger at the heated end wall. When coupled with the return flow of the layer and the effects of Soret diffusion, uneven evaporation over the interface poses an interesting problem. We consider three cases where the volatility is altered by way of changing the saturation vapour pressure of hexane, p_{sat,χ_A}. The first ($p_{sat,\chi_A} = 2.07 \times 10^4$), corresponds to the naturally arising vapour pressure from dimensional properties. The second and third ($p_{sat,\chi_A} = 5.17 \times 10^3$ and $p_{sat,\chi_A} = 2.07 \times 10^3$), decrease the original by a factor of 4 and 10 respectively. For the results presented here, we consider only the transient base state frozen at $t = 1.00 \times 10^6$.

Tab. 5.5 Dimensionless properties for the evaporating liquid layer, corresponding to those given in Tab. 5.4.

Re_T	0–12 206
R_σ	0.045
Fr	1763
We	567
Gr_T	1420
Gr_χ	74
Pr	0.746
S_T	8.47×10^{-3}
Sc_l	127
Bo_d	0.116
Sc_g	0.173
Ja	0.065
p_{sat,χ_A}	2.07×10^{2}–2.07×10^{4}

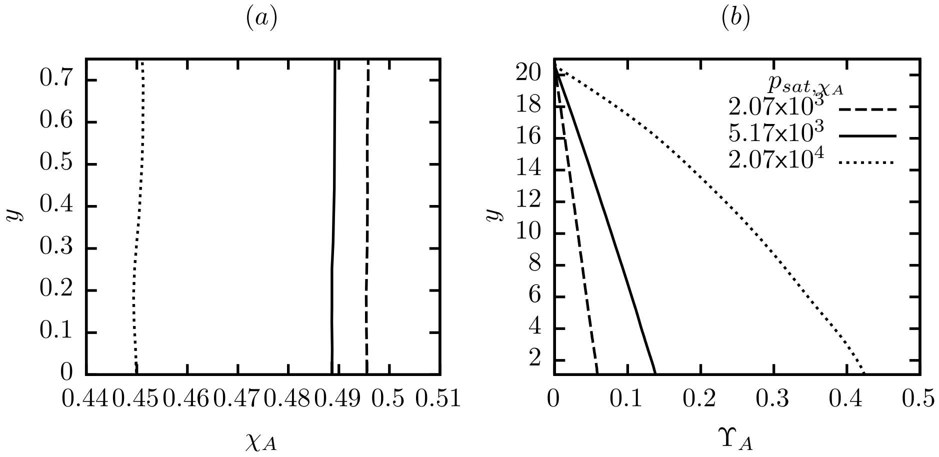

Fig. 5.10 Vertical distribution of hexane in (a) the liquid phase (χ_A), and (b) the gas phase (Υ_A) at the centre of the domain at $t = 1.00 \times 10^6$. Remaining dimensionless properties are found in Tab. 5.5.

To illustrate the impact of evaporation on the layer, Fig. 5.10 shows the vertical concentration of hexane in both phases along a vertical slice (y-direction) taken at the centre of the domain. As we expected, greater volatility from increased vapour pressure increases the mass fraction of hexane in the gas phase while decreasing the corresponding mass fraction in the liquid as non-evaporating decane remains.

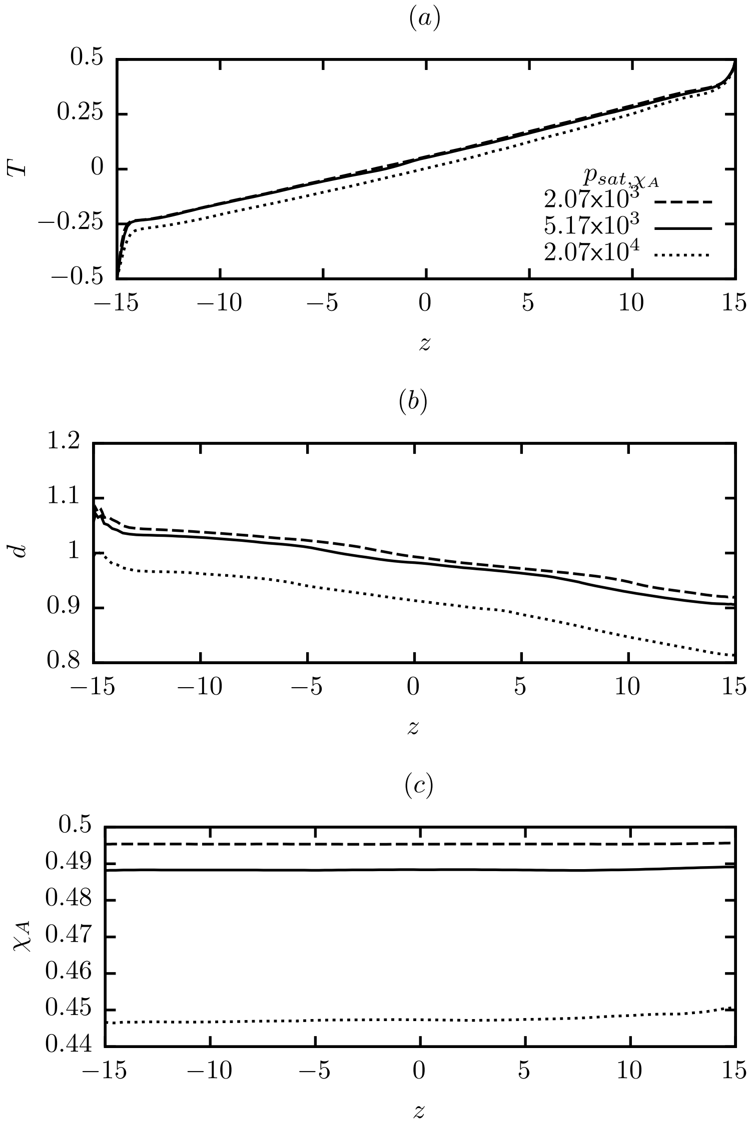

Fig. 5.11 Horizontal interface profiles for increasing hexane (χ_A) volatility at $t = 1.00 \times 10^6$. Remaining dimensionless properties are given in Tab. 5.5. (a) shows the temperature profile and thermal boundary layers, (b) the liquid depth, and (c) the hexane mass fraction in the liquid phase along the interface.

Fig. 5.11 shows the profiles in temperature (T), liquid depth (d), and hexane mass fraction (χ_A) along the LV interface for each saturation pressure at $t = 1.00 \times 10^6$. As we would expect, d and χ_A both decrease with increasing volatility as more hexane is liberated from liquid to vapour over the same time period. It is clear from Fig. 5.11(b) that in all cases the liquid is significantly deeper at the cold wall—due to Marangoni stresses pulling the interface in this direction towards higher surface tension. Greater volatility also increases the effective temperature gradient at the interface and reduces the size of the TBLs—see Fig. 5.11(a). Note that an increased temperature gradient will not only enhance thermal Marangoni flow but also Soret diffusion, strengthening the

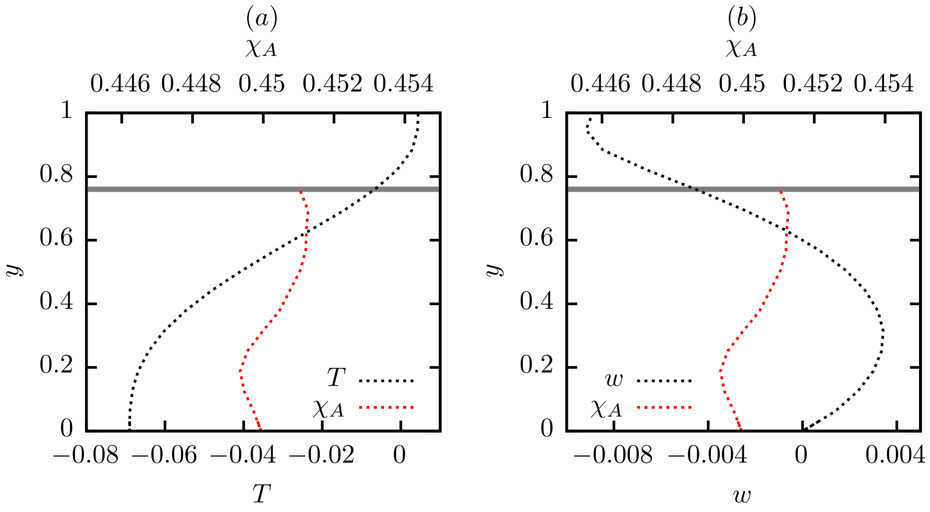

Fig. 5.12 Vertical (a) temperature and (b) streamwise velocity profiles compared to vertical distribution of liquid hexane, χ_A (red line) for the most volatile case (p_{sat,χ_A}) in the centre of the domain at $t = 1.00 \times 10^6$. Horizontal grey line indicated position of the liquid-vapour interface. For remaining dimensionless properties, see Tab. 5.5.

migration of decane to the cold wall and vice versa for hexane. The most interesting result, however, is revealed in Fig. 5.11(c), where χ_A is observed to be marginally greater at the hot wall. Evaporation rate is largest at the hot wall due to temperature elevating the saturated vapour pressure. We would expect this region to be depleted in hexane and instead to be rich in decane, the non-evaporating component. This will ultimately mean that the surface tension at the hot wall is lowered, while surface tension at the cold wall is increased—raising the surface tension gradient and therefore the critical Marangoni number. This makes the binary layer more unstable than a pure liquid layer. The proposed mechanism for this is the strong return flow maintaining component mixing within the layer combined with the Soret effect driving component separation to the hot and cold end walls.

To further examine this, Fig. 5.12 plots the return flow induced temperature profile (T) and streamwise velocity (w) for the most volatile case ($p_{sat,\chi_A} = 2.07 \times 10^4$) compared to the vertical distribution of hexane mass fraction in the liquid (χ_A). Like previous cases, we see a clear return flow profile with liquid on the interface drawn towards the cold wall before being re-circulated back towards the hot wall within the layer interior—Fig. 5.12(b). This causes the liquid in the vertical (y-direction) to become cooler with depth, as seen in Fig. 5.12(a). Both figures show that although both components are well mixed owing to the strong return flow, there is a subtle vertical mass concentration gradient in χ_A accompanying these profiles—the maximum mass fraction difference being approximately 0.001. The greatest mass fraction of hexane is found at the interface and the smallest within the interior, coinciding roughly with the maximum return flow velocity flowing back towards the hot wall on the RHS. Under the Soret effect, decane will preferentially migrate along the temperature gradient towards cooler parts—towards the bottom left in Fig. 5.12(a). At the same time, the return flow is near the bottom wall is transporting the liquid mixture to the RHS. It is clear that these two effects are in competition with each other, the return flow pulling decane to the RHS and Soret diffusion causing preferential migration to the LHS. Over time, the Soret induced migration leads to a subtle decane depletion (hexane enrichment) within the layer interior when compared to the interface concentration. The hexane enriched interior is circulated back towards the hot wall, and upon reaching, rises to the surface and duly evaporates. This offers as plausible explanation for the increased hexane concentration observed at the hot wall in Fig. 5.11(c), despite enhanced evaporation rate. Therefore, in laterally heated evaporating layers, the Soret effect (where the LVC migrates to colder regions) drives a mild replenishing effect of the MVC at the hot wall.

5.2.3 Removal of thermal Marangoni stress

It is clear from the previous case that the layer is predominantly driven by thermal Marangoni stresses maintained by the lateral temperature gradient, sustaining the return flow profile and in turn facilitating mixing. We now consider a different scenario entirely, removing thermal Marangoni flows by setting $Re_T = 0$ while retaining solutal Marangoni stress at the same strength considered previously by way of the solutal Reynolds number, $Re_\chi = 550$. We also examine the influence of the Soret effect on the flow by increasing S_T several orders of magnitude over its base value. Again, we examine only the base state frozen at only $t = 1.00 \times 10^6$.

Fig. 5.13 shows the profiles of T, d, and χ_A along the LV interface for three test cases, all at $t = 1.00 \times 10^6$ with the remaining base properties given in Tab. 5.5. The first case (solid black line in Fig. 5.13) is the standard case with $Re_T = 1.22 \times 10^4$ and $S_T = 8.87 \times 10^{-3}$. The second case (blue dotted line) retains the thermocapillary driving force of the first but increased the Soret coefficient by $O(10^2)$ to $S_T = 8.87 \times 10^{-1}$, meaning component diffusion driven by temperature differences is one hundred times larger than the standard case. The third configuration (black dashed-dot line) retains the Soret coefficient of the first standard case but thermal Marangoni stress is completely removed, meaning $Re_T = 0$ and $S_T = 8.87 \times 10^{-3}$.

We can see from Fig. 5.13(a) that upon the removal of thermal Marangoni stress, TBLs clearly present in cases one and two no longer form leading to a larger effective temperature gradient between the heated and cooled end walls. With no surface tension dependence on temperature, liquid at the interface ceases to be strongly drawn to the cold wall (LHS). Closer inspection of Fig. 5.13(b) shows that the liquid is now slightly deeper at the hot wall (RHS). The distribution of hexane mass fraction along the interface—shown in Fig. 5.13(c)—reveals the reason for this: hexane is substantially depleted at the hot wall compared to cases one and two where $Re_T = 1.22 \times 10^4$—confirming the role of thermal Marangoni in liquid mixing. Since solutal Marangoni is retained in case three, and decane possesses the higher surface tension of the pair, liquid is now drawn to the RHS towards the now decane-rich hot wall.

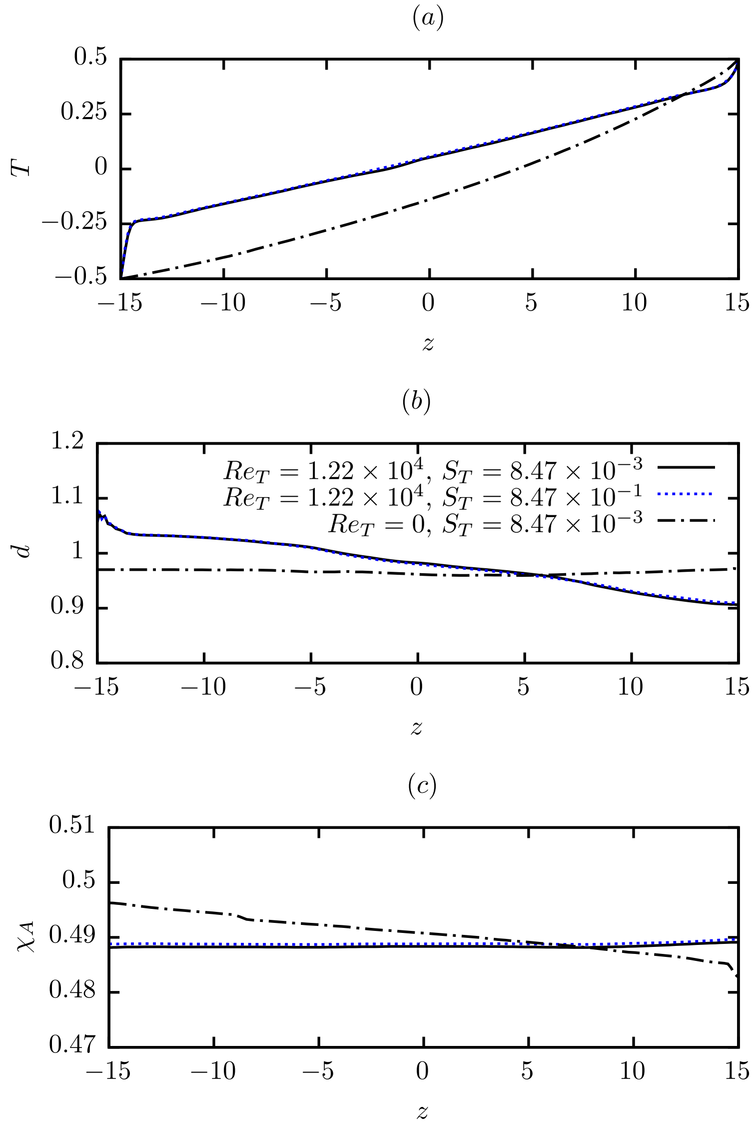

Fig. 5.13 Horizontal interface profiles for $Re_T = 1.22 \times 10^4$ and $S_T = 8.87 \times 10^{-3}$ (solid black), $Re_T = 1.22 \times 10^4$ and $S_T = 8.87 \times 10^{-1}$ (dotted blue), $Re_T = 0.00$ $S_T = 8.87 \times 10^{-3}$ (dash dot black) at $t = 1.00 \times 10^6$. $Re_\chi = 550$ in all three cases with remaining dimensionless properties given in Tab. 5.5. (a) shows the temperature profile and thermal boundary layers, (b) the liquid depth, and (c) the hexane mass fraction in the liquid phase along the interface.

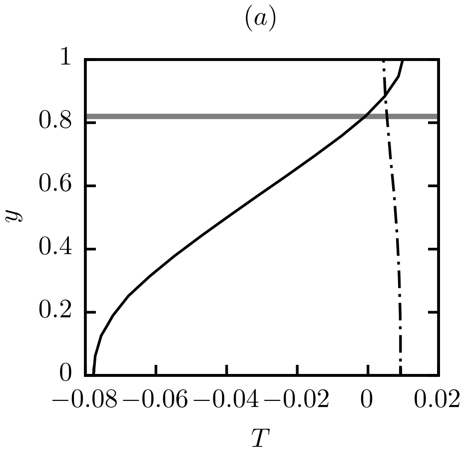

Fig. 5.14 Vertical (a) temperature, and (b) streamwise velocity profiles at the centre of the domain for case one ($Re_T = 1.22 \times 10^4$) and case three ($Re_T = 0.00$) at $t = 1.00 \times 10^6$. Horizontal grey line indicated position of the liquid-vapour interface. $Re_\chi = 550$ and $S_T = 8.87 \times 10^{-3}$ in both cases with remaining dimensionless properties given in Tab. 5.5.

Comparing cases one and two in Fig. 5.13, it is clear that increasing S_T—and hence the strength of thermodiffusion—has a negligible effect on the thermocapillary driven return flow. The thermal boundary layers, liquid depth, and mass fraction profiles along the interface, shown in Fig. 5.13(a), (b), and (c) respectively, remain largely unchanged. This leads us to the conclusion that the differences observed between cases one and three are independent of thermodiffusion. Instead, the reversed concentration gradient arises due to preferential hexane evaporation from the hot side coupled with stagnation of the layer flow upon the removal of thermal Marangoni stress.

Fig. 5.14 compares the vertical temperature and streamwise velocity profiles for cases one ($Re_T = 1.22 \times 10^4$, $S_T = 8.87 \times 10^{-3}$) and three ($Re_T = 0$, $S_T = 8.87 \times 10^{-3}$) at the centre of the domain. The return flow profile that dominates when $Re_T = 1.22 \times 10^4$ is reversed when $Re_T = 0$ while being significantly reduced in magnitude. With the flow reversed in case three, liquid at the interface now flows weakly towards the hot wall with a similarly weak return flow towards the cold wall—see Fig. 5.14(b). With the reversed return flow, liquid in the layer interior is now warmer than the interface directly above—as shown in Fig. 5.14(a).

Examining the corresponding vertical hexane mass fraction (χ_A) at the centre of the domain for case three ($Re_T = 0$)—shown in Fig. 5.15—we see that maximum χ_A is located at the interface. This χ_A profile is more segregated than when thermal Marangoni is present—see Fig. 5.12. With Soret diffusion remaining unchanged from case one, being $S_T = 8.87 \times 10^{-3}$ in both cases, the likely explanation for the pronounced profile again lies with the reversal of the return flow. With hexane evaporating preferentially

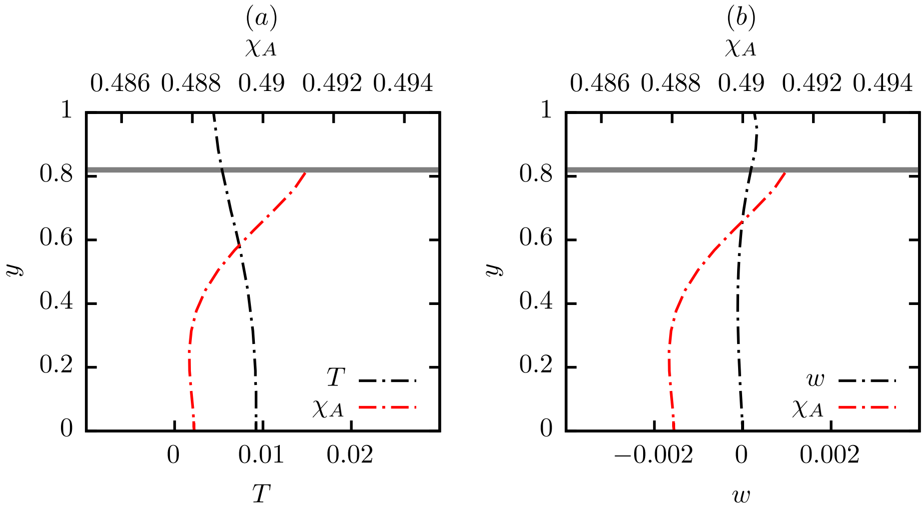

Fig. 5.15 Vertical (a) temperature and (b) streamwise velocity profiles compared to vertical distribution of liquid hexane, χ_A (red line) in the centre of the domain at $t = 1.00 \times 10^6$ for case three ($Re_T = 0.00$). Horizontal grey line indicated position of the liquid-vapour interface. $Re_\chi = 550$ and $S_T = 8.87 \times 10^{-3}$ with remaining dimensionless properties given in Tab. 5.5.

from the hot side and interfacial flow now travelling from the cold (LHS) to hot (RHS) wall, interfacial hexane-rich liquid from the cold side replenishes hexane-depleted liquid as it travels towards the hot side. At the hot well where hexane evaporation is highest and χ_A is lowest, interface liquid sinks and travels back leftwards towards the cold wall, explaining χ_A depletion toward the bottom wall at the centre of the domain as shown in Fig. 5.15. Soret diffusion may play a contributory role, with this requiring further investigation.

5.3. Conclusions

We have developed a numerical model to investigate the behaviour of laterally heated liquid layers consisting of miscible binary liquids, both with and without the effects of evaporation. We account for the deformable interface, fluid flow in both phases, thermal and solutal Marangoni stress, and Soret diffusion in the liquid phase. With the dynamic Bond number well below one in all cases, buoyancy effects in the liquid are deemed negligible, the flow driven by surface tension effects (Marangoni stress). We have shown that in the absence of evaporation, Soret induced component migration is able to enhance the return flow profile and alter the nature of propagating HTWs. Increasing the magnitude of solutal Marangoni stress combined with Soret diffusion active suppresses the onset of a second HTW mode while causing HTWs to spread over a larger portion of the domain. Additionally, the addition of a second component introduces subtle concentration waves propagating in the same direction as HTWs at double their wavelength. Introducing evaporation of the MVC (hexane) causes both overall mass and mass fraction (χ_A) depletion in the layer while both components remain well mixed, owing to the strong return flow driven by thermal Marangoni stress. Increasing the strength of Soret diffusion by two orders of magnitude appears to have negligible effects on the thermally driven layer, with flow profiles remaining unchanged. Upon the removal of thermal Marangoni stress, preferential evaporation of the more volatile component form the hot wall combined with the resulting solutal Marangoni stress reverses the return flow. Interfacial liquid now flows towards the hot wall before being re-circulated to the cold wall within the layer interior. Reversal of the return flow in this solutal Marangoni driven case increases the vertical concentration gradient in the liquid over the well mixed thermal Marangoni driven case.

Part III

Lubrication model for volatile binary sessile droplets

6. Formulation of the lubrication model

The one-sided model developed here is capable of modelling a volatile drop comprised of a miscible binary mixture deposited onto a heated surface with high wettability. No prior imposition of drop shape from experiment or theory is required and the contact line is permitted to move freely over the total life time. The use of a one-sided model invoking the lubrication approximation allows for fast and efficient computation with results obtainable using only modest resources. Any pair of miscible liquids can be considered in the model.

Continuing notation from Chapter 4, the crowning of a "cap" ($\hat{}$) over a symbol signifies a dimensional quantity, while its absence signifies a dimensionless one. As before, we first define the model using dimensional equations before scaling the problem for computation.

6.1. Description of the problem

We study the behaviour of a small and thin sessile droplet consisting of a mixture of two volatile, miscible, liquids; A and B. Liquid A is the MVC in the mixture and liquid B the LVC. The mixture is assumed to be ideal and the drop is considered Newtonian with density $\hat{\rho}$, specific heat capacity $\hat{c}_p$, thermal conductivity $\hat{k}$ and viscosity $\hat{\mu}$. For simplicity, we assume the liquid to be incompressible and the density of components A and B to be equal, $\hat{\rho}_A = \hat{\rho}_B = \hat{\rho}$. This assumption will have a minor impact since we also assume that the drop is sufficiently small as to neglect gravitational effects. With the exception of density, the remaining properties vary locally with concentration and are accounted for using the following rule of mixtures,

$$\begin{aligned} \hat{\mu} &= \chi_A \hat{\mu}_A + (1-\chi_A)\hat{\mu}_B \\ \hat{k} &= \chi_A \hat{k}_A + (1-\chi_A)\hat{k}_B \\ \hat{c}_p &= \chi_A \hat{c}_{p,A} + (1-\chi_A)\hat{c}_{p,B} \end{aligned} \tag{6.1}$$

All symbols retain the same meaning as previously defined in Chapter 4. For mass transport in the liquid, we consider only Fick's Law, with the effects of thermodiffusion

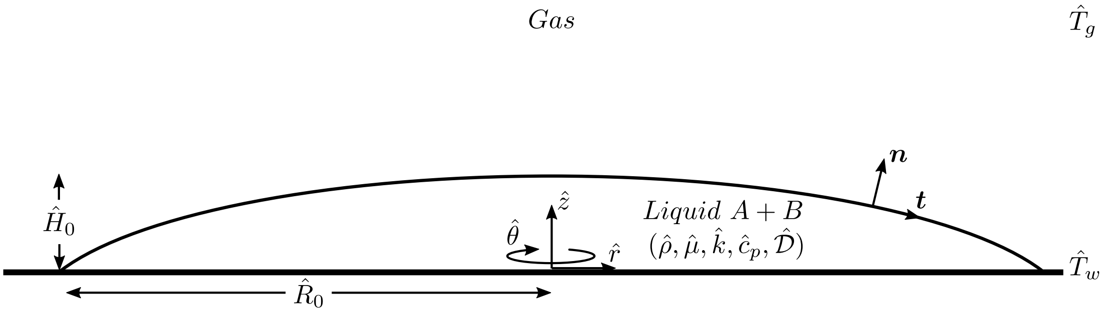

Fig. 6.1 Drop geometry of initial height $\hat{H}_0$ and radius $\hat{R}_0$ in the cylindrical coordinate frame consisting of miscible components A and B. The drop resides on a heated substrate at temperature $\hat{T}_w$ and is sufficiently thin such that the aspect ratio is much less than one, $\hat{H}_0/\hat{R}_0 \ll 1$. Gas temperature is kept constant at $\hat{T}_g$. $\boldsymbol{n}$ and $\boldsymbol{t}$ denote the outward units vectors acting in normal and tangential directions to the interface respectively.

arising from the Soret effect neglected. The surface tension, $\hat{\sigma}$, of the binary liquid mixture again depends on both the local concentration of each component and the local temperature, $\hat{T}$, but this time takes the form,

$$\hat{\sigma} = \chi_A(\hat{\sigma}_{A,r} + \hat{\gamma}_{T,A}(\hat{T} - \hat{T}_r)) + (1 - \chi_A)(\hat{\sigma}_{B,r} + \hat{\gamma}_{T,B}(\hat{T} - \hat{T}_r)) \tag{6.2}$$

where $\hat{\gamma}_{T,i} = \partial\hat{\sigma}_{T,i}/\partial\hat{T}$ is the temperature coefficient of surface tension of component i $(i = A, B).\hat{\sigma}_{i,r}$ is the surface tension of component i at reference temperature $\hat{T}_r$, which we assume to be the temperature of the vapour phase, $\hat{T}_r = \hat{T}_g$.

The drop resides on a solid, impermeable, and perfectly horizontal substrate heated to a constant temperature $\hat{T}_w$ and is released into a thin precursor film which consists solely of the LVC. Evaporation in the precursor film is stabilised by the disjoining pressure which accounts for the attractive van der Waals interactions. The inclusion of the precursor film removes the stress singularity that can arise at the moving contact line if the usual no-slip boundary condition is used. This is due to the no-slip boundary condition applied at the TCL being incompatible with the kinematic boundary condition applied at the LV interface [200]. Rather than a purely artificial tool, the precursor film is also a physical effect with experimental verification [97], as discussed in Section 3.3. The precursor film is always formed on the solid surface if the droplet is surrounded by its vapour, from which it is adsorbed. The precursor film is sufficiently thin that the liquid molecules are attracted to the substrate by van der Waals interactions, stabilising the film and suppressing evaporation [138].

6.2. Main assumptions and limitations

The drop is in contact with the gas phase which has a bulk temperature of $\hat{T}_g$. The velocity of the gas and vapour particles are assumed sufficiently low so that they are negligible. The gas phase has density $\hat{\rho}_g$, viscosity $\hat{\mu}_g$, and thermal conductivity $\hat{k}_g$. These gas phase properties are assumed to be significantly smaller than that of their liquid counterparts, such that, $\hat{\rho}_g \ll \hat{\rho}$, $\hat{\mu}_g \ll \hat{\mu}$, $\hat{k}_g \ll \hat{k}$ [34], with the same assumption similarly being applied to vapour properties. In addition, we assume that the total gas phase pressure is sufficiently large that it remains constant with evaporation and changing vapour pressure. Given these assumptions, we adopt the so-called one-sided model and focus solely on the liquid phase. This approach provides some distinct advantages along with several limitations.

By eliminating the gas phase, our model is efficient and can be solved with modest resources in short timescales. Obviously a limitation of this is that we are forced to assume evaporation is not vapour diffusion limited and is rather controlled by the transfer of molecules across the liquid-vapour (LV) interface. The model is expected to be valid in the regime where convection is important (e.g. for a well ventilated environment) and therefore the phase-transition process (i.e., the transfer of molecules across the interface) is the rate limiting step. It is well known that the vapour diffusion from the interface to a far-field value is several orders of magnitude slower than the liberation of liquid molecules to the vapour phase. In practice, this means while our model will qualitatively simulate evaporation, a quantitative comparison with evaporation fluxes against diffusion-limited experiments cannot be possible. However, as demonstrated in the following sections, a full quantitative comparison against the interfacial dynamics such as spreading and retraction is fully possible. One-sided models such as ours have also proved powerful in the prediction of qualitative behaviour for evaporating drops in the past, an example being the prediction of hydrothermal waves in evaporating pure component drops [168].

More complex 1.5-sided models such as Sultan et al. [36] or two-sided models such as Sáenz et al. [78] could be implemented. However, simulation of both phases comes with the disadvantage of added complexity and computational expense. In particular, non-trivial extensions such as addition of the full 3D species equation in the gas phase and the thermodynamic coupling between phases—including the individual liquid and vapour components—must be implemented. Experimental studies comparing pure droplet evaporation on heated substrates with predictions made from a 1.5-sided model with a diffusion limited gas phase have revealed that even this is not sufficient for a quantitative match [76]. Two-sided models, such as those of Sáenz et al. [78], therefore offer the best means to simulate evaporation fluxes observed in experiments.

Additionally, two-sided models have the advantage of accounting for complex drop shapes that reveal azimuthal flow phenomena. Given the complexities of the equations (described above), this is not the subject of this thesis.

Particularly when a heated substrate is involved, drop evaporation is more complex than diffusion limitation alone. First, the density of the vapour with respect to air is important, with dense vapour tending to sink and shroud the LV interface. If the vapour is less dense than air, buoyancy in the gas phase begins to play a role with vapour being convected away from the LV interface of the drop in addition to the diffusion already present [74]. Note that the vapours considered here (water and ethanol vapour) are both less dense than air. Second, there is the presence of evaporative cooling, with a more volatile liquid being subjected to more significant the evaporative cooling effects [114]. Evaporative cooling decreases the temperature of the interface and slows the evaporation rate. The final consideration not accounted for in this work is the thermal conductivity of the substrate. The temperature of a highly conductive substrate with remain unchanged by any evaporative cooling around the drop. A less conductive substrate, however, can be significantly cooled as the drop evaporates and this in turn has the effect of slowing the evaporation further [69].

To summarise, we adopt a one-sided approach with the goal to derive a simple model that contains the most important parts of physics necessary to reproduce, at least qualitatively, the behaviour seen in the experiments.

Initially, we assume that the drop has maximal thickness $\hat{H}_0$ and radius $\hat{R}_0$. We consider the drop to be very thin and therefore $\hat{R}_0$ greatly exceeds $\hat{H}_0$, such that the drop aspect ratio (ε) is much less than one, $\varepsilon = \hat{H}_0/\hat{R}_0 \ll 1$. This assumption permits the use of lubrication theory which we will employ to derive the evolution equations. Additionally, we assume the drop is sufficiently small as to neglect gravitational effects. This means a Bond number of much less than one, $Bo \ll 1$, requiring the radius of the drop to be below the capillary length.

A working mixture of ethanol and water is considered. Both liquids are sufficiently volatile on a heated substrate, with ethanol being the MVC and possessing a lower surface tension than water. The selection of an ethanol-water mixture also avoids any self-rewetting properties present in other alcohol-water mixtures at certain concentrations, a common example being butanol-water. The pure component properties of each liquid used to calculate those of the mixture are given in Tab. 6.1.

We now go on to introduce the dimensional equations describing the flow field in Section 6.3, explaining any assumptions made in the physics. Section 6.4 then introduces the scaling parameters and derives the dimensionless equations used in the model while also explaining any methods used to circumvent modelling limitations.

Tab. 6.1 Physical properties of ethanol (MVC) and water (LVC) at 20°C and 1 atm.

	Ethanol	Water
$\hat{\rho}$ (kg m^{-3})	800	999
$\hat{\mu}$ (Pa s)	1.198×10^{-3}	6.513×10^{-4}
$\hat{k}$ (W m^{-1} K^{-1})	0.183	0.602
$\hat{c}_p$ (kJ kg^{-1} K^{-1})	2.400	4.182
$\hat{L}_v$ (kJ kg^{-1})	1030.0	2453.8
$\hat{\sigma}_R$ (N m^{-1})	2.28×10^{-2}	7.29×10^{-3}
$\hat{\gamma}_T$ (N m^{-1} K^{-1})	8.32×10^{-5}	1.51×10^{-4}
$\hat{M}$ (kg mol^{-1})	4.61×10^{-2}	1.80×10^{-2}
$\hat{p}^o$ (N m^{-2})	5.80×10^{3}	7.37×10^{3}
$\hat{\mathcal{D}}$ (m^2 s^{-1})	1.23×10^{-9}	

6.3. Dimensional governing equations

For this model we used a cylindrical coordinate system, $(\hat{r}, \hat{\theta}, \hat{z})$ and solve for the velocity field, $\hat{\boldsymbol{u}} = (\hat{u}, \hat{v}, \hat{w})$, where $\hat{u}$, $\hat{v}$, and $\hat{w}$ correspond to the horizontal, azimuthal, and vertical components of velocity respectively. The LV interface is located at $\hat{z} = \hat{h}(\hat{r}, \hat{t})$ with the SL and SV interfaces both being located at $\hat{z} = 0$.

The liquid phase is governed by the incompressible momentum, mass, energy and concentration equations,

$$\hat{\rho}\left(\frac{\partial \hat{\boldsymbol{u}}}{\partial \hat{t}} + \hat{\boldsymbol{u}} \cdot \hat{\nabla} \hat{\boldsymbol{u}}\right) = \hat{\nabla} \cdot \hat{\boldsymbol{\tau}} \tag{6.3}$$

$$\frac{\partial \hat{\rho}}{\partial \hat{t}} + \hat{\nabla} \cdot (\hat{\rho} \hat{\boldsymbol{u}}) = 0 \tag{6.4}$$

$$\hat{\rho}\left(\frac{\partial (\hat{c}_p \hat{T})}{\partial \hat{t}} + \hat{\boldsymbol{u}} \cdot \hat{\nabla}(\hat{c}_p \hat{T})\right) = \hat{\nabla} \cdot (\hat{k} \hat{\nabla} \hat{T}) \tag{6.5}$$

$$\frac{\partial \chi_A}{\partial \hat{t}} + \hat{\nabla} \cdot \hat{\boldsymbol{u}} \chi_A = \hat{\mathcal{D}}_A \hat{\nabla}^2 \chi_A \tag{6.6}$$

$\hat{\mathcal{D}}_A$ denotes the mass diffusion coefficient of component A. As previously mentioned, we consider only Fick's diffusion, with the Soret and Dufour effects neglected. $\hat{\boldsymbol{\tau}}$ is the total stress tensor in the liquid, defined as,

$$\hat{\boldsymbol{\tau}} = -\hat{p}\mathbf{I} + \hat{\mu}\left(\hat{\nabla} \hat{\boldsymbol{u}} + \hat{\nabla} \hat{\boldsymbol{u}}^T\right) \tag{6.7}$$

where $\mathbf{I}$ denotes the identity tensor. We now apply boundary conditions in order to obtain solutions to the above conservation equations. First, let us define the outward unit vectors, one normal and the other tangential to the interface, with notation $\boldsymbol{n}$ and

$\boldsymbol{t}$ respectively [34],

$$\boldsymbol{n} = \left(-\frac{\partial \hat{h}}{\partial \hat{r}}, 1 \right) \left(1 + \left(\frac{\partial \hat{h}}{\partial \hat{r}} \right)^2 \right)^{-\frac{1}{2}} \tag{6.8}$$

$$\boldsymbol{t} = \left(1, \frac{\partial \hat{h}}{\partial \hat{r}} \right) \left(1 + \left(\frac{\partial \hat{h}}{\partial \hat{r}} \right)^2 \right)^{-\frac{1}{2}} \tag{6.9}$$

Along the interface, $\hat{z} = \hat{h}(\hat{r}, \hat{t})$, it is necessary to distinguish between the liquid mixture velocity, $\hat{\boldsymbol{u}}$ and the velocity of the interface, $\hat{\boldsymbol{u}}_s = (\hat{u}_s, \hat{w}_s)$. The relationship between $\hat{\boldsymbol{u}}$ and $\hat{\boldsymbol{u}}_s$ is then given by the evaporative flux boundary condition [211],

$$\hat{\boldsymbol{u}} = \hat{\boldsymbol{u}}_s + \frac{\hat{J}}{\hat{\rho}} \boldsymbol{n} \tag{6.10}$$

$\hat{J}$ denotes the total evaporative flux, constituent of the individual evaporative fluxes of A and B; $\hat{J} = \hat{J}_A + \hat{J}_B$. The tangential components of both velocities are the same; $\hat{\boldsymbol{u}}_\tau = \hat{\boldsymbol{u}} - (\hat{\boldsymbol{u}} \cdot \boldsymbol{n})\boldsymbol{n} = \hat{\boldsymbol{u}}_s - (\hat{\boldsymbol{u}}_s \cdot \boldsymbol{n})\boldsymbol{n}$. The liquid is assumed to evaporate normal to the interface, leading to the liquid-vapour jump conditions given by the jump mass balance and jump energy balance respectively,

$$\hat{J} = \hat{\rho}(\hat{\boldsymbol{u}} - \hat{\boldsymbol{u}}_s) \cdot \boldsymbol{n} = \hat{\rho}_g(\hat{\boldsymbol{u}}_g - \hat{\boldsymbol{u}}_s) \cdot \boldsymbol{n} \tag{6.11}$$

$$\hat{J}_A \hat{L}_{v,A} + \hat{J}_B \hat{L}_{v,B} + \hat{k} \hat{\nabla} \hat{T} \cdot \boldsymbol{n} = \hat{k}_g \hat{\nabla} \hat{T}_g \cdot \boldsymbol{n} \tag{6.12}$$

Subscript g denotes the vapour phase, and so $\hat{\rho}_g$, $\hat{k}_g$, $\hat{\boldsymbol{u}}_g$, $\hat{T}_g$ is the gas phase density, thermal conductivity, velocity and temperature respectively. $\hat{J}_i$ and $\hat{L}_{v,i}$ are the evaporative flux and latent heat of vaporisation of component i, where $i = A, B$. To balance the jump in normal stress with the surface tension, mean curvature and van der Waals interactions, we define the normal stress boundary at the interface [34, 211],

$$\boldsymbol{n} \cdot (\hat{\boldsymbol{\tau}} - \hat{\boldsymbol{\tau}}_g) \cdot \boldsymbol{n} = 2\hat{\kappa}\hat{\sigma} + \hat{\Pi} \tag{6.13}$$

Here $\hat{\boldsymbol{\tau}}$ is the liquid phase stress tensor given in eq. (6.7) and $\hat{\boldsymbol{\tau}}_g$ is the stress tensor in the gas phase. $2\hat{\kappa} = -\hat{\nabla}_s \cdot \boldsymbol{n}$ is twice the mean curvature of the free surface and $\hat{\nabla}_s = (\mathbf{I} - \boldsymbol{n}\boldsymbol{n}) \cdot \hat{\nabla}$ is the surface gradient operator. Surface tension of the liquid, $\hat{\sigma}$, is given by eq. (6.2). $\hat{\Pi}$ denotes the disjoining pressure accounting for intermolecular interactions near the contact line,

$$\hat{\Pi} = \frac{\hat{\mathscr{A}}}{6\pi \hat{h}^3} \tag{6.14}$$

with $\hat{\mathscr{A}}$ being the dimensional Hamaker constant [34, 211]. Since we consider a small drop where surface tension is the dominating force, we ignore the effect of vapour recoil from the normal stress boundary condition (NSBC) [212]. Vapour recoil is an inward normal force exerted on the drop as evaporation occurs at the LV interface. Vapour molecules liberated from the interface are accelerated away from the liquid due the significantly smaller density of the gas phase, with this kick back force causing vapour recoil [94]. The end effect would a contraction of the drop as the interface recoils, but practically, the recoil force will be relatively weak and resisted by surface tension. Therefore, ignoring vapour recoil and disregarding stress from the vapour side (since the gas viscosity is considered to be negligible), eq. (6.13) becomes,

$$-\hat{p} + \boldsymbol{n} \cdot \hat{\boldsymbol{\tau}} \cdot \boldsymbol{n} = 2\hat{\kappa}\hat{\sigma} + \hat{\mathit{\Pi}} - \hat{p}_g \tag{6.15}$$

where $\hat{p}_v$ is the total pressure of the gas phase. The tangential stress boundary condition then balances the shear stress jump with the surface tension gradient [34], yielding,

$$\boldsymbol{n} \cdot (\hat{\boldsymbol{\tau}} - \hat{\boldsymbol{\tau}}_g) \cdot \boldsymbol{t} = \hat{\nabla}_s \hat{\sigma} \cdot \boldsymbol{t} \tag{6.16}$$

Then by adopting one-sided methodology, we assume shear stress of the gas phase is negligible, meaning eq. (6.16) simplifies to,

$$\boldsymbol{n} \cdot \boldsymbol{\tau} \cdot \boldsymbol{t} = \hat{\nabla}_s \hat{\sigma} \cdot \boldsymbol{t} \tag{6.17}$$

The concentration balance for component i over the interface is defined as,

$$\chi_i(\hat{\boldsymbol{u}} - \hat{\boldsymbol{u}}_s) \cdot \boldsymbol{n} = \hat{\mathcal{D}}_i(\boldsymbol{n} \cdot \hat{\nabla}\chi_i)_{\hat{z}=\hat{h}} = \frac{\hat{J}_i}{\hat{\rho}} \tag{6.18}$$

Interface motion is then related to the fluid velocities by imposing the kinematic boundary condition,

$$\frac{\partial \hat{h}}{\partial \hat{t}} + \hat{u}_s \frac{\partial \hat{h}}{\partial \hat{r}} + \hat{v}_s \frac{\partial \hat{h}}{\partial \hat{\theta}} = \hat{w}_s \tag{6.19}$$

Along the heated liquid-solid interface ($\hat{z} = 0$), we impose the no-slip and zero vertical concentration flux meaning,

$$\hat{u} = 0, \qquad \hat{v} = 0, \qquad \hat{w} = 0, \qquad \frac{\partial \chi_A}{\partial \hat{z}} = 0 \qquad \hat{T} = \hat{T}_w. \tag{6.20}$$

To complete the model description we need employ a constitutive equation for the evaporative flux of each component, $\hat{J}_i$ $(i = A, B)$. Based on the well known Hertz-Knudsen equation from kinetic theory, we write the following non-equilibrium interfacial condition for the evaporative flux for each i component [202, 213],

$$\hat{J}_i = \frac{\hat{p}_{v,i}\hat{M}_i}{\hat{R}_g\hat{T}|_h} \left(\frac{\hat{R}_g\hat{T}|_h}{2\pi\hat{M}_i}\right)^{\frac{1}{2}} \left(\alpha_{v,i}\frac{\hat{p}_{v,e,i}}{\hat{p}_{v,i}} - \beta_{v,i}\right) \tag{6.21}$$

where $\hat{p}_{v,i}$ is the partial vapour pressure of component i and $\hat{T}|_h$ is the interfacial temperature of the liquid. The more volatile the species, the larger its partial vapour pressure and the greater its evaporative flux. Note that the specific gas constant will vary with mixture composition in our case, hence $\hat{R}_g$ denotes the universal gas constant and $\hat{M}$ is the molecular weight of component i. $\hat{p}_{v,e,i}$ is the equilibrium vapour pressure of component i. This corresponds to the dynamic equilibrium in which molecules crossing the interface from the vapour to liquid sides (and vice versa) are in balance with each other. In other words there is no net mass transfer between phases. $\hat{p}_{v,e,i}$ is therefore a constant defined for a given interface temperature and pressure. This differs from the local partial vapour pressure of component i, $\hat{p}_{v,i}$, since during evaporation or condensation there is a net mass transfer across the interface.

Accommodation coefficients for evaporation and condensation have notation $\alpha_{v,i}$ and $\beta_{v,i}$ respectively in eq. (6.21). These coefficients are defined as the probability of a molecule impinging on the interface crossing over to the other phase [214]. An alternative definition for $\beta_{v,i}$ is the probability that a vapour molecule striking the liquid surface sticks to the surface [213]. The precise values of both accommodation coefficients are not well known. At equilibrium, evaporation and condensation will be balanced and the accommodation coefficients will be equal. With no barrier to phase change in either direction, the value of both accommodation coefficients will be equal to 1. Note that $\alpha_{v,i} < 1$ would indicate the presence of a barrier impeding evaporation. Using Raman thermometry, Smith et al. [215], determined the evaporation accommodation coefficient of liquid water (α_{v,H_2O}) to be 0.62 ± 0.09 while reporting no discernible effect of temperature. This led to their conclusion of there being a rate-limiting energetic or entropic barrier to evaporation. Prior to this, Li et al. [216] suggested a negative temperature dependence on the evaporation accommodation coefficient. Later measurements by Drisdell et al. [217] and Duffey et al. [218] found similar values to Smith et al. [215] for ammonium sulfate solution and aqueous acetic acid at $\alpha_{v,(NH_4)_2SO_4(aq)} = 0.58 \pm 0.05$ and $\alpha_{v,CH_3COOH(aq)} = 0.53 \pm 0.12$. Using molecular simulations, Julin et al. [219] found the evaporation accommodation coefficient of water to be unity ($\alpha_{v,H_2O} = 1$) at $T = 273.15$ K while Davies et al. [220] concluded experimentally that $\alpha_{v,H_2O} = 0.5 - 1$ at $T = 248 - 298$ K. Note that in the works above, the evaporation and condensation coefficients are assumed equal to each other and constant [198]. Needless to say, although both $\alpha_{v,i}$ and $\beta_{v,i}$ are likely between 0.5 and 1, the exact values of the accommodation coefficients is still an open research question with the dependence on temperature also not known. For simplicity, and in line with other similar models [202, 118], we assume the system is always near equilibrium and that each molecule of vapour or liquid striking the interface changes to the opposite phase [198], hence we set $\alpha_{v,i} = \beta_{v,i} = 1$.

The local partial vapour pressure can be evaluated from equilibrium thermodynamics

[95, 202, 221, 222, 223],

$$\frac{\hat{p}_{v,e,i}}{\hat{p}_{v,i}} - 1 = \frac{\hat{v}_i}{\hat{R}_g\hat{T}_g}(\hat{p} - \hat{p}_{sat,i}) + \frac{\hat{M}_i\hat{L}_{v,i}}{\hat{R}_g\hat{T}_g}\left(\frac{\hat{T}|_h}{\hat{T}_g} - 1\right) \tag{6.22}$$

where $\hat{v}_i = \hat{M}_i/\hat{\rho}_i$ is the liquid molar volume of pure component i, with $\hat{T}|_h$ and $\hat{T}_g$ being the temperature of the interface and gas respectively. Since we assume that the system is not very far from equilibrium, these temperatures are approximately equal; $\hat{T}|_h \approx \hat{T}_g$. $\hat{p}_{sat,i}$ is the saturation pressure of component i at the reference temperature, T_r. This is the pressure at which the vapour in equilibrium with pure liquid i is completely saturated with i vapour. For simplicity, we assume $\hat{p}_{sat,i}$ to be constant at this stage. Finally, to close the model, we define the local vapour pressure for each component by applying Raoult's law,

$$\hat{p}_{v,A} = \chi_A\hat{p}_{sat,A} \tag{6.23}$$

$$\hat{p}_{v,B} = (1 - \chi_A)\hat{p}_{sat,B} \tag{6.24}$$

The final expression for the constitutive relation of total evaporation flux is obtained by substituting eqs. (6.22) to (6.24) into eq. (6.21),

$$\begin{aligned}\hat{J} = \chi_A\hat{p}_{sat,A}\left(\frac{\hat{M}_A}{2\pi\hat{R}_g\hat{T}_g}\right)^{1/2}\left[\frac{\hat{M}_A}{\hat{\rho}_A\hat{R}_g\hat{T}_g}(\hat{p} - \hat{p}_{sat,A}) + \frac{\hat{M}_A\hat{L}_{v,A}}{\hat{R}_g\hat{T}_g}\left(\frac{\hat{T}|_h}{\hat{T}_g} - 1\right)\right] + \\ (1 - \chi_A)\hat{p}_{sat,B}\left(\frac{\hat{M}_B}{2\pi\hat{R}_g\hat{T}_g}\right)^{1/2}\left[\frac{\hat{M}_B}{\hat{\rho}_B\hat{R}_g\hat{T}_g}(\hat{p} - \hat{p}_{sat,B}) + \frac{\hat{M}_B\hat{L}_{v,B}}{\hat{R}_g\hat{T}_g}\left(\frac{\hat{T}|_h}{\hat{T}_g} - 1\right)\right]\end{aligned} \tag{6.25}$$

6.4. Scaling and resulting dimensionless equations

We now introduce the following scaling quantities in order to formulate the dimensionless governing equations and boundary conditions required for the model. Where appropriate, mixture properties are scaled by the value for the MVC—component A (ethanol). Again, the crowning of a "cap" (ˆ) over a symbol signifies a dimensional quantity while the absence signifies a dimensionless quantity. The equations presented in Section 6.3 are scaled according to the following,

$$\begin{aligned}
&\hat{r} = \hat{R}_0 r, && \hat{z} = \hat{H}_0 z, && (\hat{u}, \hat{v}, \hat{w}) = \left(\hat{U}^* u, \hat{U}^* v, \frac{\hat{H}_0}{\hat{R}_0} \hat{U}^* w\right), \\
&\hat{p} = \hat{p}_{ig} + \frac{\hat{\mu}_A \hat{U}^* \hat{R}_0}{\hat{H}_0^2} p, && \hat{t} = \frac{\hat{R}_0}{\hat{U}^*} t, && \hat{T} = \hat{T}_0 + T \mathit{\Delta} \hat{T}, \\
&\hat{J}_i = \frac{\hat{k}_A \mathit{\Delta} \hat{T}}{\hat{H}_0 \hat{L}_{v,A}} J_i, && \hat{\sigma}_i = \hat{\sigma}_{A,0} \sigma_i, && \hat{\mu} = \hat{\mu}_A \mu, \\
&\hat{k} = \hat{k}_A k, && \hat{c}_p = \hat{c}_{p,A} c_p.
\end{aligned} \tag{6.26}$$

where $\hat{U}^*$ is a characteristic velocity of the system, which here we choose to be the thermocapillary velocity—defined as $\hat{U}^* = \varepsilon \hat{\gamma}_A \mathit{\Delta} \hat{T} / \hat{\mu}_A$. Applying these scalings to the mixed liquid properties defined in eq. (6.1) yields,

$$\begin{aligned}
\mu &= \chi_A + (1 - \chi_A) \mu_R \\
k &= \chi_A + (1 - \chi_A) k_R \\
c_p &= \chi_A + (1 - \chi_A) c_{pR}
\end{aligned} \tag{6.27}$$

where $\mu_R = \hat{\mu}_B / \hat{\mu}_A$ is the viscosity ratio of component B to A, $k_R = \hat{k}_B / \hat{k}_A$ is the ratio of thermal conductivities, and $c_{pR} = \hat{c}_{p,B} / \hat{c}_{p,A}$ is the ratio of specific heats. The dimensionless equation of state for surface tension derived from eq. (6.2) takes the following form,

$$\sigma = \chi_A (1 - MaT) + (1 - \chi_A) \sigma_R \left(1 - \frac{\gamma_R Ma}{\sigma_R} T\right) \tag{6.28}$$

with $Ma = \hat{\gamma}_A \mathit{\Delta} \hat{T} / \hat{\sigma}_{A,r}$ being the Marangoni number, $\sigma_R = \hat{\sigma}_{B,r} / \hat{\sigma}_{A,r}$ the ratio of surface tensions, and $\gamma_R = \hat{\gamma}_{T,B} / \hat{\gamma}_{T,A}$ the ratio of temperature coefficients of surface tension. When scaling the governing equations, we apply the lubrication approximation and assume the drop is much wider than it is tall, hence $\varepsilon \ll 1$. In doing this, we are therefore able to discount any terms multiplied by ε^2—due to being $O(10^{-2})$ and will hence having negligible effects. By scaling eqs. (6.3) to (6.5), the dimensionless forms of the governing equations for mass, (r,θ,z)-momentum, and energy are defined as follows,

$$\frac{1}{r} \frac{\partial (ru)}{\partial r} + \frac{1}{r} \frac{\partial v}{\partial \theta} + \frac{\partial w}{\partial z} = 0 \tag{6.29}$$

$$\varepsilon Re\left(\frac{\partial u}{\partial t}+u\frac{\partial u}{\partial r}+\frac{v}{r}\frac{\partial u}{\partial \theta}-\frac{v^2}{r}+w\frac{\partial u}{\partial z}\right)=-\frac{\partial p}{\partial r}+\frac{\partial \tau_{zr}}{\partial z} \tag{6.30}$$

$$\varepsilon Re\left(\frac{\partial v}{\partial t}+u\frac{\partial v}{\partial r}+\frac{v}{r}\frac{\partial v}{\partial \theta}+\frac{uv}{r}+w\frac{\partial v}{\partial z}\right)=-\frac{1}{r}\frac{\partial p}{\partial \theta}+\frac{\partial \tau_{z\theta}}{\partial z} \tag{6.31}$$

$$\frac{\partial P}{\partial z}=0 \tag{6.32}$$

$$\varepsilon RePr\left(\frac{\partial (c_pT)}{\partial t}+u\frac{\partial (c_pT)}{\partial r}+\frac{v}{r}\frac{\partial (c_pT)}{\partial \theta}+w\frac{\partial (c_pT)}{\partial z}\right)=\frac{\partial}{\partial z}\left(k\frac{\partial T}{\partial z}\right) \tag{6.33}$$

Where $\tau_{zr} = \tau_{rz} = \mu(\partial u/\partial z)$ is the stress component in the r direction on a unit area perpendicular to the z direction and $\tau_{z\theta} = \tau_{\theta z} = \mu(\partial v/\partial z)$ is the stress component in the θ direction on the same unit area in z. The dimensionless groups arising are the Reynolds number, $Re = \hat{\rho}_A\hat{U}^*\hat{H}_o/\varepsilon\hat{\mu}_A$, and the Prandtl number, $Pr = \hat{\mu}_A\hat{C}_{p,A}/\hat{k}_A$.

Similarly, scaling the dimensional concentration eq. (6.6) yields,

$$\begin{gathered}\frac{\hat{U}^*}{\hat{R}_o}\left(\frac{\partial \chi_A}{\partial t}+u\frac{\partial \chi_A}{\partial r}+\frac{v}{r}\frac{\partial \chi_A}{\partial \theta}+w\frac{\partial \chi_A}{\partial z}\right)=\frac{\hat{\mathcal{D}}_A}{\hat{R}_o^2}\left(\frac{1}{r}\frac{\partial}{\partial r}\left(r\frac{\partial \chi_A}{\partial r}\right)\right.\\ \left.+\frac{1}{r}\frac{\partial}{\partial \theta}\left(\frac{1}{r}\frac{\partial \chi_A}{\partial \theta}\right)+\frac{\hat{R}_o^2}{\hat{H}_o^2}\left(\frac{\partial^2 \chi_A}{\partial z^2}\right)\right)\end{gathered} \tag{6.34}$$

Upon simplification, we arrive and the general form of the dimensionless concentration equation,

$$\begin{gathered}\frac{\partial \chi_A}{\partial t}+u\frac{\partial \chi_A}{\partial r}+\frac{v}{r}\frac{\partial \chi_A}{\partial \theta}+w\frac{\partial \chi_A}{\partial z}=\frac{1}{Pe}\left(\frac{1}{r}\frac{\partial}{\partial r}\left(r\frac{\partial \chi_A}{\partial r}\right)\right.\\ \left.+\frac{1}{r}\frac{\partial}{\partial \theta}\left(\frac{1}{r}\frac{\partial \chi_A}{\partial \theta}\right)+\frac{1}{\varepsilon^2}\left(\frac{\partial^2 \chi_A}{\partial z^2}\right)\right)\end{gathered} \tag{6.35}$$

where $Pe = \hat{U}^*\hat{R}_o/\hat{\mathcal{D}}_A$ is the Péclet number. We then simplify the dimensionless concentration equation further by applying either the rapid vertical diffusion approximation, where we assume $\varepsilon^2 Pe \ll 1$, or, imposing the limit of weak diffusion, where $Pe \approx O(\varepsilon^{-2})$ is assumed. The method used depends on the value of Pe we wish to investigate. With $\varepsilon \approx O(0.1)$, rapid vertical diffusion allows for $Pe \approx 1 - 10$ and weak diffusion allows for $Pe \approx 100$.

6.4.1 Rapid vertical diffusion

Rapid vertical diffusion assumes that vertical diffusion (in our case this is the z-direction) acts rapidly to smooth out concentration gradients in this plane. The dimensionless time scale of which is $O(\varepsilon^2 Pe)$. To apply the rapid vertical diffusion approximation, we assume that the total concentration of component A consists of a mean concentration independent of z plus a rapidly diffusing component[224, 225],

$$\chi_A(r,\theta,z,t) = \chi_{A0}(r,\theta,t) + \varepsilon^2 Pe\chi_{A1}(r,\theta,z,t) \tag{6.36}$$

The first term on the RHS (χ_{A0}) is the averaged component A mass fraction independent of z while the second term, containing χ_{A1}, represents a small perturbation accounting for z dependence assuming that $\varepsilon^2 Pe \ll 1$. Substitution of eq. (6.36) into eq. (6.35) then yields,

$$\begin{gathered}\frac{\partial\chi_{A0}}{\partial t} + u\frac{\partial\chi_{A0}}{\partial r} + \frac{v}{r}\frac{\partial\chi_{A0}}{\partial\theta} + \varepsilon^2 Pe\left(\frac{\partial\chi_{A1}}{\partial t} + u\frac{\partial\chi_{A1}}{\partial r} + \frac{v}{r}\frac{\partial\chi_{A1}}{\partial\theta} + w\frac{\partial\chi_{A1}}{\partial z}\right) = \\ \frac{1}{Pe}\left(\frac{1}{r}\frac{\partial}{\partial r}\left(r\frac{\partial\chi_{A0}}{\partial r}\right) + \frac{1}{r}\frac{\partial}{\partial\theta}\left(\frac{1}{r}\frac{\partial\chi_{A0}}{\partial\theta}\right)\right) + \varepsilon^2\left(\frac{1}{r}\frac{\partial}{\partial r}\left(r\frac{\partial\chi_{A1}}{\partial r}\right) + \frac{1}{r}\frac{\partial}{\partial\theta}\left(\frac{1}{r}\frac{\partial\chi_{A1}}{\partial\theta}\right)\right) \\ + \frac{\partial^2\chi_{A1}}{\partial z^2}\end{gathered} \tag{6.37}$$

Discounting terms multiplied by ε^2 as negligible, we arrive at the governing equation for concentration assuming rapid diffusion in the vertical direction,

$$\frac{\partial\chi_{A0}}{\partial t} + u\frac{\partial\chi_{A0}}{\partial r} + \frac{v}{r}\frac{\partial\chi_{A0}}{\partial\theta} = \frac{1}{Pe}\left(\frac{1}{r}\frac{\partial}{\partial r}\left(r\frac{\partial\chi_{A0}}{\partial r}\right) + \frac{1}{r}\frac{\partial}{\partial\theta}\left(\frac{1}{r}\frac{\partial\chi_{A0}}{\partial\theta}\right)\right) + \frac{\partial^2\chi_{A1}}{\partial z^2} \tag{6.38}$$

6.4.2 Weak diffusion

In the limit of weak diffusion it is assumed that $Pe \approx O(\varepsilon^{-2})$ [226]. We substitute $Pe = Pe'\varepsilon^{-2}$ into eq. (6.35), giving,

$$\frac{\partial\chi_A}{\partial t} + u\frac{\partial\chi_A}{\partial r} + \frac{v}{r}\frac{\partial\chi_A}{\partial\theta} + w\frac{\partial\chi_A}{\partial z} = \frac{\varepsilon^2}{r}\left(\frac{\partial}{\partial r}\left(r\frac{\partial\chi_A}{\partial r}\right) + \frac{\partial}{\partial\theta}\left(\frac{1}{r}\frac{\partial\chi_A}{\partial\theta}\right)\right) + \frac{1}{Pe'}\left(\frac{\partial^2\chi_A}{\partial z^2}\right) \tag{6.39}$$

with Pe' being a new modified form of the Péclet number, where $Pe' \approx O(1)$. Since diffusion is no longer assumed rapid in the vertical (z) direction, we cannot instantly simplify the concentration equation as we did when applying rapid diffusion in Section 6.4.1. Instead, we make use of an approximate Galerkin expansion for χ_A, seeking solution of the following form [226],

$$\chi_A(r,\theta,z,t) = \chi_{A0}(r,\theta,t) + \chi_{A2}(r,\theta,t)\left(\frac{z^2}{h^2} - \frac{1}{3}\right) \tag{6.40}$$

Where the χ_{A0} again corresponds to a mean concentration independent of z, while the second term on the RHS containing χ_{A2} represents a zero-mean quadratic fluctuating component. Substituting eq. (6.40) into the LHS of eq. (6.39), we obtain an intermediate form of the concentration equation in the limit of weak diffusion,

$$\frac{\partial \chi_{A0}}{\partial t}+u\frac{\partial \chi_{A0}}{\partial r}+\frac{v}{r}\frac{\partial \chi_{A0}}{\partial \theta}+\left(\frac{\partial \chi_{A2}}{\partial t}+u\frac{\partial \chi_{A2}}{\partial r}+\frac{v}{r}\frac{\partial \chi_{A2}}{\partial \theta}\right)\left(\frac{z^2}{h^2}-\frac{1}{3}\right)=\frac{\varepsilon^2}{r}\frac{\partial}{\partial r}\left(r\frac{\partial \chi_{A0}}{\partial r}\right)+$$
$$\frac{\varepsilon^2}{r}\frac{\partial}{\partial \theta}\left(\frac{1}{r}\frac{\partial \chi_{A0}}{\partial \theta}\right)+\frac{\varepsilon^2}{r}\left(\frac{\partial}{\partial r}\left(r\frac{\partial \chi_{A2}}{\partial r}\right)+\frac{\partial}{\partial \theta}\left(\frac{1}{r}\frac{\partial \chi_{A2}}{\partial \theta}\right)\right)\left(\frac{z^2}{h^2}-\frac{1}{3}\right)+\frac{1}{Pe'}\left(\frac{\partial^2 \chi_A}{\partial z^2}\right) \tag{6.41}$$

This will be simplified further in Section 6.4.3 where we also derive an expression for the zero-mean quadratic fluctuation component, χ_{A2}.

6.4.3 Boundary conditions

Turning our attention to the interfacial boundary conditions at $z = h(r,t)$, the scaled outward unit vector normal to the interface and the outward tangential unit vector components in r and θ ($\boldsymbol{t}_r$ and $\boldsymbol{t}_\theta$) are non-dimensionalised as follows,

$$\boldsymbol{n}=\frac{-\varepsilon r\dfrac{\partial h}{\partial r}\boldsymbol{e}_r-\dfrac{\partial h}{\partial \theta}\boldsymbol{e}_\theta+r\boldsymbol{e}_z}{\sqrt{\varepsilon^2 r^2\dfrac{\partial^2 h}{\partial r^2}+\dfrac{\partial^2 h}{\partial \theta^2}+r^2}} \tag{6.42}$$

$$\boldsymbol{t}_r=\frac{\boldsymbol{e}_r+\varepsilon\dfrac{\partial h}{\partial r}\boldsymbol{e}_z}{\sqrt{1+\varepsilon^2\boldsymbol{e}_r^2}},\qquad \boldsymbol{t}_\theta=\frac{r\boldsymbol{e}_\theta+\varepsilon\dfrac{\partial h}{\partial \theta}\boldsymbol{e}_z}{\sqrt{r^2+\varepsilon^2\boldsymbol{e}_\theta^2}} \tag{6.43}$$

Here, $\boldsymbol{e}_r$, $\boldsymbol{e}_\theta$, and $\boldsymbol{e}_z$ are unit vectors in the r, θ and z direction respectively. Scaling eq. (6.10) gives the dimensionless evaporative flux boundary condition,

$$EJ=-(u-u_s)\frac{\partial h}{\partial r}-(v-v_s)\frac{1}{r}\frac{\partial h}{\partial \theta}+(w-w_s) \tag{6.44}$$

with the dimensionless evaporation number, $E=\hat{k}_A \varDelta \hat{T}\hat{R}_o/\hat{H}_o^2\hat{L}_{v,A}\hat{U}^*\hat{\rho}$, arising.

Let us now consider briefly the gas phase (g), consisting of inert gas, ig, and the vapour, v, of both components A and B. Therefore, the total gas pressure is given by,

$$\hat{p}_g=\hat{p}_{ig}+\hat{p}_{v,A}+\hat{p}_{v,B} \tag{6.45}$$

We assume that the surrounding gas phase consists mainly of inert gas rather than vapour, meaning $\hat{p}_{ig} \gg \hat{p}_{v,A}$ and $\hat{p}_{ig} \gg \hat{p}_{v,B}$. This leads to the simplification that the total gas phase pressure is approximately equal to the pressure of the inert gas,

$$\hat{p}_{ig}\approx\hat{p}_g\approx(\hat{p}_g-\hat{p}_{v,A})\approx(\hat{p}_g-\hat{p}_{v,B}) \tag{6.46}$$

Substitution of eq. (6.46) into eq. (6.15) and application of the appropriate scaling yields the dimensionless form of the NSBC,

$$p = -\frac{\sigma\varepsilon^2}{Ma}\left(\frac{1}{r}\frac{\partial}{\partial r}\left(r\frac{\partial h}{\partial r}\right) + \frac{1}{r^2}\frac{\partial^2 h}{\partial\theta^2}\right) - \frac{\mathscr{A}}{h^3} \tag{6.47}$$

where $\mathscr{A} = \hat{\mathscr{A}}/6\pi\hat{\mu}_A\hat{U}^*\hat{R}_0\hat{H}_0$ is the dimensionless Hamaker constant. Following this, eq. (6.25) is scaled to give the dimensionless constitutive equation for the total combined evaporative flux of both liquid components A and B,

$$J = \frac{1}{K}\left[\chi_A\left(\delta p + T|_h\right) + (1-\chi_A)\alpha M_R^{3/2}\left(\delta p + \Lambda T|_h\right)\right] \tag{6.48}$$

Where $K = \hat{k}_A(2\pi\hat{R}_g^3\hat{T}_g^5)^{\frac{1}{2}}/\hat{H}_o\hat{L}_{v,A}^2\hat{p}_{sat,A}\hat{M}_A^{\frac{3}{2}}$ is the Knudsen number, measuring the importance of kinetic effects at the interface. K can be thought of as analogous to inverse of the Biot number, controlling the heat loss across the interface [168]. $\delta = \hat{\mu}_A\hat{U}^*\hat{R}_o\hat{T}_g/\hat{\rho}_l\hat{H}_o^2\hat{L}_{v,A}\Delta\hat{T}$ accounts for the effects of changes in liquid pressure on the local phase change temperature at the interface [95]. The relative volatility of the mixture is given by $\alpha = \hat{p}_{sat,B}/\hat{p}_{sat,A}$, and $M_R = \hat{M}_B/\hat{M}_A$ is the ratio of molar weights. We partition eq. (6.48) into two separate expressions, yielding the evaporative fluxes of components A and B respectively,

$$J_A = \frac{\chi_A}{K}\left(\delta p + T|_h\right) \tag{6.49}$$

$$J_B = \frac{(1-\chi_A)\alpha M_R^{3/2}}{K}\left(\delta p + \Lambda T|_h\right) \tag{6.50}$$

The dimensionless jump energy and tangential stress balances are obtained by scaling eqs. (6.12) and (6.17),

$$J_A + J_B\Lambda + k\frac{\partial T}{\partial z} = 0 \tag{6.51}$$

$$\tau_{zr} = \frac{1}{Ma}\frac{\partial\sigma}{\partial r}, \qquad \tau_{z\theta} = \frac{1}{Ma}\frac{\partial\sigma}{\partial\theta} \tag{6.52}$$

where $\Lambda = \hat{L}_{v,B}/\hat{L}_{v,A}$ is the ratio of latent heats. The kinematic boundary condition is re-written in dimensionless form as,

$$\frac{\partial h}{\partial t} + u\frac{\partial h}{\partial r} + \frac{v}{r}\frac{\partial h}{\partial\theta} - w + EJ = 0 \tag{6.53}$$

Dimensionless forms of the boundary conditions at the SL interface ($z = 0$) given in eq. (6.20), excluding the concentration boundary condition are given as,

$$u = 0, \qquad v = 0, \qquad w = 0, \qquad T = T_w. \tag{6.54}$$

The concentration boundary conditions at $z = h$ and $z = 0$, first introduced in eq. (6.18) and then eq. (6.20) are scaled to give their general dimensionless forms,

$$\left[\frac{\partial \chi_A}{\partial z}\right]_{z=0} = 0 \tag{6.55}$$

$$\frac{1}{Pe}\left[\frac{1}{r}\left(-r\frac{\partial h}{\partial r}\frac{\partial \chi_A}{\partial r} - \frac{1}{r}\frac{\partial h}{\partial \theta}\frac{\partial \chi_A}{\partial \theta} + \frac{1}{\varepsilon^2}r\frac{\partial \chi_A}{\partial z}\right)\right]_{z=h} = E(\chi_A J - J_A) \tag{6.56}$$

Similarly with the general form of the concentration equation (eq. (6.35)), we now utilise either the rapid or weak diffusion approximations to simplify eq. (6.55) and eq. (6.56).

Rapid diffusion

Substituting eq. (6.36) into eqs. (6.55) and (6.56) and then discounting terms multiplied by $\varepsilon^2 Pe$ yields the concentration balance at $z = 0$ and $z = h$ assuming rapid vertical diffusion,

$$\left[\frac{\partial \chi_{A1}}{\partial z}\right]_{z=0} = 0 \tag{6.57}$$

$$\left[\frac{\partial \chi_{A1}}{\partial z}\right]_{z=h} = E(\chi_{A0} J - J_A) + \frac{1}{Pe}\left[\frac{\partial h}{\partial r}\frac{\partial \chi_{A0}}{\partial r} + \frac{1}{r^2}\frac{\partial h}{\partial \theta}\frac{\partial \chi_{A0}}{\partial \theta}\right]_{z=h} \tag{6.58}$$

Weak diffusion

Alternately, in the limit of weak diffusion, we substitute $Pe \approx \varepsilon^{-}2$ into eqs. (6.55) and (6.56) to obtain,

$$\left[\frac{\partial \chi_A}{\partial z}\right]_{z=0} = 0 \tag{6.59}$$

$$\left[\frac{\partial \chi_A}{\partial z}\right]_{z=h} = E(\chi_A J - J_A) \tag{6.60}$$

To facilitate further simplification of eq. (6.60), we differentiate eq. (6.40) w.r.t. z, giving,

$$\frac{\partial \chi_A}{\partial z} = \left(\frac{\chi_{A2}}{h^2}\right)2z \tag{6.61}$$

Applying $z = h$ yields,

$$\left[\frac{\partial \chi_A}{\partial z}\right]_h = \frac{2\chi_{A2}}{h} \tag{6.62}$$

Substituting eq. (6.62) is into eq. (6.60) and rearranging constructs an expression for χ_A in terms of χ_{A2},

$$\chi_A = \frac{2\chi_{A2}}{EJh} + \frac{J_A}{J} \tag{6.63}$$

By evaluating eq. (6.40) at $z = h$, substituting our expression for χ_A in eq. (6.63), and re-arranging, we obtain the following expression for χ_{A2} independent of χ_A,

$$\chi_{A2} = \frac{(J_A - J\chi_{A0})}{2\left(\dfrac{J}{3} - \dfrac{1}{Pe'Eh}\right)} \tag{6.64}$$

Substituting eq. (6.64) into eq. (6.62), we arrive at the final form of the concentration balance over the interface in the limit of weak diffusion,

$$\left[\frac{\partial \chi_A}{\partial z}\right]_{z=h} = \frac{(J_A - J\chi_{A0})}{h\left(\dfrac{J}{3} - \dfrac{1}{Pe'Eh}\right)} \tag{6.65}$$

6.4.4 Precursor layer

To conclude our description of the dimensionless problem, we derive an expression for the height of the precursor layer, h_∞, upon which the drop is released. In the precursor region, we assume the fluid to be a flat film with zero mean curvature. Additionally, we assume there is no evaporation, meaning $J = J_A = J_B = 0$, and that the mixture is at an equilibrium concentration which we will call $\chi_{A0,\infty}$. In order to derive an expression for the thickness of the precursor film unique to the binary fluid, we take the expression for total mass flux given in eq. (6.50) and apply the normal stress BC (eq. (6.47)) for zero mean curvature when $h = h_\infty$. This yields,

$$h_\infty = \left(\frac{\mathscr{A}\delta}{\delta p_{sat,A}\chi_{A0,\infty}(1-\alpha) + \Lambda T_w}\right)^{1/3} \tag{6.66}$$

where $\chi_{A0,\infty}$ is the concentration of component A in the liquid at thickness h_∞ (i.e. within the precursor layer region). Since component A is the MVC and evaporates on a shorter time scale to component B, we assume that by the time the precursor layer has formed, component A has completely evaporated and so, $\chi_{A0,\infty} = 0$. Hence the precursor region consists solely of the LVC (component B) and eq. (6.66) reduces to,

$$h_\infty = \left(\frac{\mathscr{A}\delta}{\Lambda T_w}\right)^{1/3} \tag{6.67}$$

6.4.5 Summary of dimensionless groups

In summary, by applying the expression for thermocapillary velocity ($\hat{U}^* = \varepsilon\hat{\gamma}_A \varDelta\hat{T}/\hat{\mu}_A$), the following dimensionless groups have arisen,

$$\begin{array}{lll}
\varepsilon = \dfrac{\hat{H}_0}{\hat{R}_0} & Re = \dfrac{\hat{\rho}\hat{\gamma}_A \varDelta\hat{T}\hat{H}_0}{\hat{\mu}_A^2} & Pr = \dfrac{\hat{\mu}_A \hat{c}_{p,A}}{\hat{k}_A} \\[2ex]
Ma = \dfrac{\hat{\gamma}_A \varDelta\hat{T}}{\hat{\sigma}_{A,0}} & E = \dfrac{\hat{k}_A \hat{\mu}_A}{\varepsilon^2 \hat{\rho}\hat{\gamma}_A \hat{H}_o \hat{L}_{v,A}} & K = \dfrac{\hat{k}_A (2\pi \hat{R}_g^3 \hat{T}_g^5)^{\frac{1}{2}}}{\hat{H}_0 \hat{L}_{v,A}^2 \hat{p}_{sat,A} \hat{M}_A^{\frac{3}{2}}} \\[2ex]
\mathscr{A} = \dfrac{\hat{\mathscr{A}}}{6\pi\hat{\gamma}_A \varDelta\hat{T}\hat{H}_0^2} & \delta = \dfrac{\hat{T}_g \hat{\gamma}_A}{\rho\hat{H}_0 \hat{L}_{v,A}} & Pe = \dfrac{\hat{\gamma}_A \varDelta\hat{T}\hat{H}_0}{\hat{\mu}_A \hat{\mathcal{D}}_A} \\[2ex]
\sigma_R = \dfrac{\hat{\sigma}_{B,r}}{\hat{\sigma}_{A,r}} & \gamma_R = \dfrac{\hat{\gamma}_{T,B}}{\hat{\gamma}_{T,A}} & \alpha = \dfrac{\hat{p}_{sat,B}}{\hat{p}_{sat,A}} \\[2ex]
k_R = \dfrac{\hat{k}_B}{\hat{k}_A} & \mu_R = \dfrac{\hat{\mu}_B}{\hat{\mu}_A} & c_{pR} = \dfrac{\hat{c}_{p,B}}{\hat{c}_{p,A}} \\[2ex]
M_R = \dfrac{\hat{M}_B}{\hat{M}_A} & \varLambda = \dfrac{\hat{L}_{v,B}}{\hat{L}_{v,A}} &
\end{array} \tag{6.68}$$

6.5. Kármán-Pohlhausen approximation

We now apply the Kármán-Pohlhausen integral approximation whereby we integrate eqs. (6.29) to (6.35) over z from 0 to h. Doing this removes any multiple variable differentials while retaining the inertia and advection terms in the momentum and energy balance equations. First, let us define the integrated forms of f, g and $\varTheta$ as,

$$f = \int_0^h u\,dz, \qquad g = \int_0^h v\,dz, \qquad \varTheta = \int_0^h T\,dz. \tag{6.69}$$

Given these new expressions, we must now find alternate forms of u, v, and T to aid in our solution, known as closure approximations. We assume that each variable takes the form $c_1 + c_2 z + c_3 z^2$ and use boundary conditions given in eqs. (6.51), (6.52), (6.54) and (6.69) to find c_1, c_2 and c_3. We arrive at the following expressions for u, v and T,

$$u = \left(\frac{3f}{h^2} - \frac{\partial\sigma}{\partial r}\frac{1}{2\mu Ma}\right)z - \left(\frac{3f}{2h^3} - \frac{\partial\sigma}{\partial r}\frac{3}{4h\mu Ma}\right)z^2 \tag{6.70}$$

$$v = \left(\frac{3g}{h^2} - \frac{\partial\sigma}{\partial\theta}\frac{1}{2r\mu Ma}\right)z - \left(\frac{3g}{2h^3} - \frac{\partial\sigma}{\partial\theta}\frac{3}{4rh\mu Ma}\right)z^2 \tag{6.71}$$

$$\begin{aligned} T = T_w &+ \left(\frac{(J_A + \Lambda J_B)}{2k} + \frac{3\Theta}{h^2} - \frac{3T_w}{h}\right) z \\ &+ \left(-\frac{3(J_A + \Lambda J_B)}{4hk} - \frac{3\Theta}{2h^3} + \frac{3T_w}{2h^2}\right) z^2 \end{aligned} \tag{6.72}$$

Substitution into the governing equations yields,

$$\frac{\partial h}{\partial t} = -EJ - \frac{\partial r}{\partial r} - \frac{f}{r} - \frac{1}{r}\frac{\partial g}{\partial \theta} \tag{6.73}$$

$$\begin{aligned} \varepsilon Re \Bigg(\frac{\partial f}{\partial t} + \frac{1}{r}\frac{\partial}{\partial r}\left(r \int_0^h u^2 \, dz\right) + \frac{1}{r}\frac{\partial}{\partial \theta}\left(\int_0^h uv \, dz\right) - \frac{1}{r}\int_0^h v^2 \, dz \\ + u|_h EJ \Bigg) = -h\frac{\partial p}{\partial r} + \left[\mu \frac{\partial u}{\partial z}\right]_0^h \end{aligned} \tag{6.74}$$

$$\begin{aligned} \varepsilon Re \Bigg(\frac{\partial g}{\partial t} + \frac{1}{r}\frac{\partial}{\partial r}\left(r \int_0^h uv \, dz\right) + \frac{1}{r}\frac{\partial}{\partial \theta}\left(\int_0^h v^2 \, dz\right) - \frac{2}{r}\int_0^h uv \, dz \\ + v|_h EJ \Bigg) = -\frac{h}{r}\frac{\partial p}{\partial \theta} + \left[\mu \frac{\partial v}{\partial z}\right]_0^h \end{aligned} \tag{6.75}$$

$$\begin{aligned} \varepsilon Re Pr c_p \Bigg(\frac{\partial \Theta}{\partial t} + \frac{1}{r}\frac{\partial}{\partial r}\left(r \int_0^h uT \, dz\right) + \frac{1}{r}\frac{\partial}{\partial \theta}\left(\int_0^h vT \, dz\right) \\ + T|_h EJ \Bigg) = \left[k \frac{\partial T}{\partial z}\right]_0^h \end{aligned} \tag{6.76}$$

$$\begin{aligned} \frac{\partial \chi_{A0}}{\partial t} + \frac{f}{h}\frac{\partial \chi_{A0}}{\partial r} + \frac{g}{rh}\frac{\partial \chi_{A0}}{\partial \theta} - \frac{E}{h}(\chi_{A0} J - J_A) \\ = \frac{1}{hPe}\left(\frac{\partial h}{\partial r}\frac{\partial \chi_{A0}}{\partial r} + \frac{1}{r^2}\frac{\partial h}{\partial \theta}\frac{\partial \chi_{A0}}{\partial \theta}\right) \end{aligned} \tag{6.77}$$

$$\frac{\partial \chi_{A0}}{\partial t} + \frac{f}{h}\frac{\partial \chi_{A0}}{\partial r} + \frac{g}{hr}\frac{\partial \chi_{A0}}{\partial \theta} = \frac{(J_A - J\chi_{A0})}{Pe' h^2 \left(\frac{J}{3} - \frac{1}{Pe' E h}\right)} \tag{6.78}$$

Eqs. (6.77) and (6.78) are the integrated concentration equation in the limits of rapid vertical diffusion and weak diffusion respectively.

In what follows, the equations are restricted to those of what we call a transient base state along r. This means we restrict our equations to only deal with the r-direction, disregarding the azimuthal θ direction for the moment. Film height is handled via the kinematic boundary condition and so we need only to solve on a 1D mesh along r—this will be described further in Section 6.9. For now we note that going forward, all rates of change and velocity pertaining to θ (meaning g, $\partial h/\partial \theta$, etc.) are set to zero in calculation of the base state. We will consider θ once more when accessing the stability of the base state in Chapter 8.

6.6. Initial and boundary conditions in r

For $0 \leq r \leq 1$ we apply the following initial conditions for h, f, and Θ,

$$h(r,0) = h_{\infty} + 1 - r^2, \qquad f(r,0) = 0, \qquad \Theta(r,0) = h(r,0)T_0. \tag{6.79}$$

Depending on the desired composition of the drop, the initial concentration, $\chi_A(r,0)$, within this region is set anywhere between 0 and 1. Beyond the drop profile and into the precursor region where $r > 1$, the initial conditions are,

$$h(r,0) = h_{\infty}, \qquad f(r,0) = 0, \qquad \Theta(r,0) = h_{\infty}, \qquad \chi_A(r,0) = 0. \tag{6.80}$$

The value of χ_A within the drop will vary depending on the desired initial concentration of the MVC. With $\chi_A = 0$ corresponding to pure LVC and $\chi_A = 1$ pure MVC. Note that when $\chi_A = 1$ within the drop, $\chi_A = 1$ in the precursor layer also. Considering now the boundary conditions in r, we apply,

$$\begin{gathered}
\frac{\partial h}{\partial r}(0,t) = 0, \quad f(0,t) = 0, \quad \frac{\partial \Theta}{\partial r}(0,t) = 0, \quad \frac{\partial \chi_A}{\partial r}(0,t) = 0. \\
h(r_{\infty},t) = h_{\infty}, \quad \frac{\partial h}{\partial r}(r_{\infty},t) = 0, \quad f(r_{\infty},t) = 0, \quad \Theta(r_{\infty},0) = h_{\infty}, \\
\chi_A(r_{\infty},t) = 0.
\end{gathered} \tag{6.81}$$

r_{∞} being the length of the domain.

6.7. Discussion of the penalty function

Due to our modelling approach, the drop is deposited onto a thin precursor film. This sufficiently thin for van der Waals interactions in the liquid to dominate and suppress further evaporation. It is then logical to assume that the precursor layer consists solely of the LVC since any MVC will have evaporated before the film forms. When testing the model, we noticed that artificial behaviour can occur in the precursor film resulting from the added complexity of a second component. Diffusion of the MVC into the precursor film from to the bulk drop is possible as is condensation of MVC from the gas phase into the film region. To circumvent this problem, we incorporate a forcing-type penalty function (P) with which we can control the composition of the precursor film. This ensures that the inert precursor region does not interfere with the evaporation of the drop or induce any artificial behaviour.

The penalty function itself is applied to the advection-diffusion equation and forces the precursor film to solely consist of the LVC, preventing any evaporation or condensation

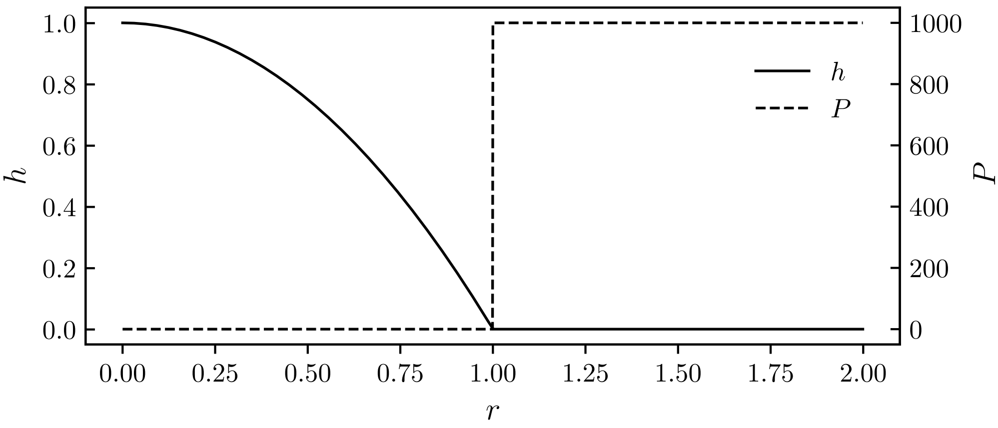

Fig. 6.2 Initial drop height (solid line, left axis) and resulting penalty function (dashed line, right axis) along r. When $h > h_\infty$, penalty is zero and has no effect on the solution. When $h = h_\infty$, penalty tends to $M = 1.00 \times 10^{-3}$ meaning χ_{A0} is forced to zero to satisfy the weak form of the advection-diffusion equation—eq. (6.93) or eq. (6.94).

from occurring. It takes the form,

$$P = \mathcal{M}\chi_{A0}\left(1 - \tanh\left[\mathcal{B}\left(\frac{h}{h_\infty} - 1\right)\right]\right) = 0 \tag{6.82}$$

where $\mathcal{M} = 10^3$ is its magnitude and $\mathcal{B} = 5$. When $h > h_\infty$, as is the case in the bulk drop, P is zero regardless of the value of χ_{A0} and so has no effect on the solution. The penalty function begins to influence the solution when drop height approaches the height of the precursor. If $h = h_\infty$, P tends towards $\mathcal{M}$. Added to the advection-diffusion equation, we are seeking values of χ_{A0} which satisfy the equation when equal to zero. In the precursor layer where P is large, the only option available to the solver to satisfy the advection-diffusion expression is to force χ_{A0} to zero. The physical effects of this restriction are twofold. First, it is ensured that there is no artificial condensation of the MVC into the precursor layer. Second, any diffusion of MVC from the bulk drop to the precursor layer is arrested.

6.8. Finite element and Galerkin method

From our definitions above, we have 8 unknown variables; h, p, f, g, Θ, J_A, J_B, χ_A along with 8 independent equations, these being eqs. (6.29) to (6.31), (6.33), (6.35), (6.47), (6.49) and (6.50). These equations are discretised using the finite element method (FEM) applied to a uniform mesh. Fundamentally, solutions to the system of equations are obtained using the Newton-Raphson method. Initial solutions are provided (via initial conditions) and progressively more accurate values are iterated to over each time step.

In line with FEM, in order to solve our equations we must convert our equations to be solved into a discrete problem. For this we use the Galerkin method of weighted residuals, the particulars of which will not be discussed here, rather, the reader is referred to the excellent book by David Burnett [227]. The method centres on the assumption that the differential governing equations are well approximated by a finite sum of a series of test functions, ϕ_i, located between grid points. In order to do this, the differential equations which we seek solutions to must be brought into their weak forms. Given a generic PDE with second order derivatives, such as,

$$\frac{\partial y}{\partial t}+y\frac{\partial y}{\partial x}=\frac{\partial^2 y}{\partial x^2} \tag{6.83}$$

the strong form is given as,

$$R=\frac{\partial y}{\partial t}+y\frac{\partial y}{\partial x}-\frac{\partial^2 y}{\partial x^2} \tag{6.84}$$

where is a solution is reached when R tends to zero. To bring into the weak form we multiply eq. (6.84) by the test function and integrate with respect to x,

$$R=\int\left(\frac{\partial y}{\partial t}+y\frac{\partial y}{\partial x}-\frac{\partial^2 y}{\partial x^2}\right)\phi_i\,dx \tag{6.85}$$

This simplifies to,

$$R=\int\left(\frac{\partial y}{\partial t}\phi_i+y\frac{\partial y}{\partial x}\phi_i+\frac{\partial y}{\partial x}\frac{\partial \phi_i}{\partial x}\right)dx-\left[\frac{\partial y}{\partial x}\phi_i\right]_a^b \tag{6.86}$$

where the last term on the RHS is referred to as the boundary residual with a and b referring here to the limits of the domain. Applying the weak formulation to eqs. (6.47), (6.49), (6.50), (6.73), (6.74) and (6.76) to (6.78), along with appropriate application of the boundary conditions and simplification yields,

$$\int\left[\left(\frac{\partial h}{\partial t}+EJ+\frac{f}{r}\right)\phi_i-f\frac{\partial \phi_i}{\partial r}\right]r\,dr+\big[rf\phi_i\big]_0^{r_\infty}=0 \tag{6.87}$$

$$\int\left[\left(p+\frac{A}{h^3}\right)\frac{Ma}{\sigma\varepsilon^2}\phi_i-\frac{\partial h}{\partial r}\frac{\partial \phi_i}{\partial r}\right]r\,dr+\left[\frac{\partial h}{\partial r}\right]_0^{r_\infty}\phi_i=0 \tag{6.88}$$

$$\begin{aligned}\int\Bigg[\varepsilon Re\Big(\frac{\partial f}{\partial t}\phi_i+u|_h EJ\phi_i-\Big(\int_0^h u^2\,dz\Big)\frac{\partial \phi_i}{\partial r}\Big)-\left[\mu\frac{\partial u}{\partial z}\right]_0^h\phi_i\\ +h\frac{\partial p}{\partial r}\phi_i\Bigg]r\,dr+\left[\varepsilon Re\Big(\int_0^h u^2\,dz\Big)\phi_i\right]_0^{r_\infty}=0\end{aligned} \tag{6.89}$$

$$\begin{aligned}\int \Bigg[\varepsilon RePrc_p\Big(\frac{\partial \Theta}{\partial t}\phi_i + T|_h EJ\phi_i - \Big(\int_0^h uT\,dz\Big)\frac{\partial \phi_i}{\partial r}\Big) \\ - \Big[rk\frac{\partial T}{\partial z}\Big]_0^h \phi_i\Bigg] r\,dr + \Big[\varepsilon RePrc_p\Big(\int_0^h uT\,dz\Big)\phi_i\Big]_0^{r_\infty} = 0\end{aligned} \tag{6.90}$$

$$\int \Big[KJ_A\phi_i - \chi_A\Big(\delta p + T|_h\Big)\phi_i\Big] r\,dr = 0 \tag{6.91}$$

$$\int \Big[KJ_B\phi_i - (1-\chi_A)\alpha M_R^{3/2}\Big(\delta p + \Lambda T|_h\Big)\phi_i\Big] r\,dr = 0 \tag{6.92}$$

$$\begin{aligned}\int \Big[h\frac{\partial \chi_{A0}}{\partial t}\phi_i + f\frac{\partial \chi_{A0}}{\partial r}\phi_i - E(J\chi_{A0} - J_A)\phi_i + \frac{h}{Pe}\frac{\partial \chi_{A0}}{\partial r}\frac{\partial \phi_i}{\partial r}\Big] r\,dr \\ -\frac{1}{Pe}\Big[r\,h\frac{\partial \chi_{A0}}{\partial r}\phi_i\Big]_0^{r_\infty} + P = 0\end{aligned} \tag{6.93}$$

$$\int \left[h\frac{\partial \chi_{A0}}{\partial t}\phi_i + f\frac{\partial \chi_{A0}}{\partial r}\phi_i - \frac{(J_A - J\chi_{A0})}{Pe'h^2\Big(\frac{J}{3} - \frac{1}{Pe'Eh}\Big)}\phi_i\right] r\,dr + P = 0 \tag{6.94}$$

Note that although two advection-diffusion equations are presented - eqs. (6.93) and (6.94), only one is chosen in the model depending on the value of Pe investigated. These then form our seven independent equations solved by the code to obtain solutions for the seven unknown independent variables h, p, f, Θ, J_A, J_B, and χ_A.

6.9. Solution method

The domain is discretised along r from 0 to r_∞ into equally spaced nodes, the total being $N_{r,tot}$. Fig. 6.3 shows the case of $r_\infty = 3$ and $N_{r,tot} = 300$. Imposing the initial conditions yields profiles of the variables in the governing equations along r, see Fig. 6.3 showing the height profile. The governing equations are solved using FEM whereby the Newton-Raphson scheme is employed to find the solutions to the system of equations. The iterative program is written in Fortran90 programming language. A transient base state is formed by evolving the simulation forward in time by use of an adaptive time step, dt. The time step is increased or decreased based on the largest residual error of the governing equations from the previous time step. The base state can be frozen at any time step (in order to perform a stability analysis—see Chapter 8) or continued until dry out, upon which drop mass reaches zero.

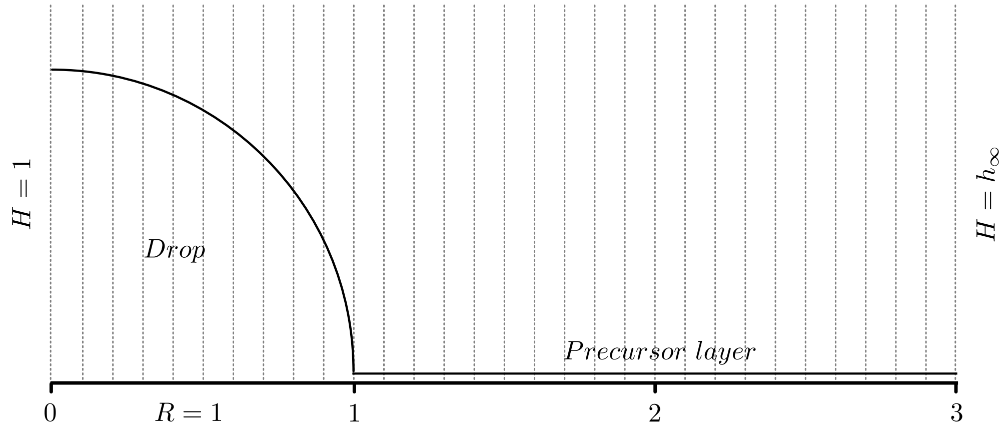

Fig. 6.3 Illustration of the height, h, variable under initial conditions in a domain where $r_\infty = 3$. The one dimensional domain consists of equally spaced N_r nodes, here, the vertical dotted lines represent every tenth node where the total number of nodes, $N_{r,tot} = 300$. The value of height is stored at every node point and is reconstructed to form the drop profile over the domain. The drop is initialised as a quarter circle in dimensionless space for $0 \leq r \leq 1$, with the precursor layer height, h_∞, imposed for $r > 1$. Similar profiles along r are used as initial conditions for the other variables.

7. Transient results

7.1. Validation with single component model

We begin our investigation by comparing the results from our model to the single component model by Karapetsas et al. [203] on which it was based. This provides our first source of validation and we later go on to also validate with experimental data. To approximate a single component mixture, all property ratios are set to 1 and the initial mass fraction, $\chi_{A0,i}$ to 0.5. This way we effectively have an equal mixture of two identical components. Tab. 7.1 shows the values of the parameters investigated. A domain length of $r_\infty = 2$ is used with total number of nodes set to $N_{r,tot} = 200$. Grid convergence is obtained when the total number of nodes is refined to $N_{r,tot} = 250$, with the same independent solutions obtained using both meshes.

Using the properties in Tab. 7.1, Fig. 7.1 shows the contact line position, r_c, and apex height, $h(0,t)$, for two values of the Knudsen number; $K = 10^{-3}$ and $K = 10^{-1}$. As expected, results from our pseudo-single component model matches perfectly with the solutions of Karapetsas et al. [203]. Oscillations at the apex are observed at early times when $t < 10^{-1}$ due to inertia introduced by non-zero Re. K can be thought of as an inverse Biot number, controlling heat transfer over the interface [168]. It is calculated as $K \approx 10^{-3}$ from dimensional properties in Tab. 6.1, however, the evaporation rate can be controlled by increasing K which effectively decreases the heat transfer rate and evaporation across the interface. With our one-sided model not accounting for the gas phase, increasing K can be used as a tool to enhance the resistance of air to heat transfer. Fig. 7.1 shows that increasing K from 10^{-3} to 10^{-1} prolongs the drop life time, resulting in a longer spreading time and maximum drop radius before evaporation takes over and the contact line begins to recede.

7.2. Dimensionless base parameters

We now introduce the parameters used in modelling an ethanol-water drop. We begin by assuming a temperature difference between the substrate and air, $\Delta\hat{T}$, of 45 °C.

Tab. 7.1 Dimensionless parameters used for the comparison of our model with Karapetsas et al. [203].

ε	0.20	δ	1×10^{-5}	k_R	1.00
Re	10	$\mathscr{A}$	1×10^{-4}	μ_R	1.00
Pr	1.00	Pe	100	$c_{p,R}$	1.00
Ma	1×10^{-2}	σ_R	1.00	M_R	1.00
E	1×10^{-4}	γ_R	1.00	Λ	1.00
K	1×10^{-3}	α	1.00	$\chi_{A0,i}$	0.50

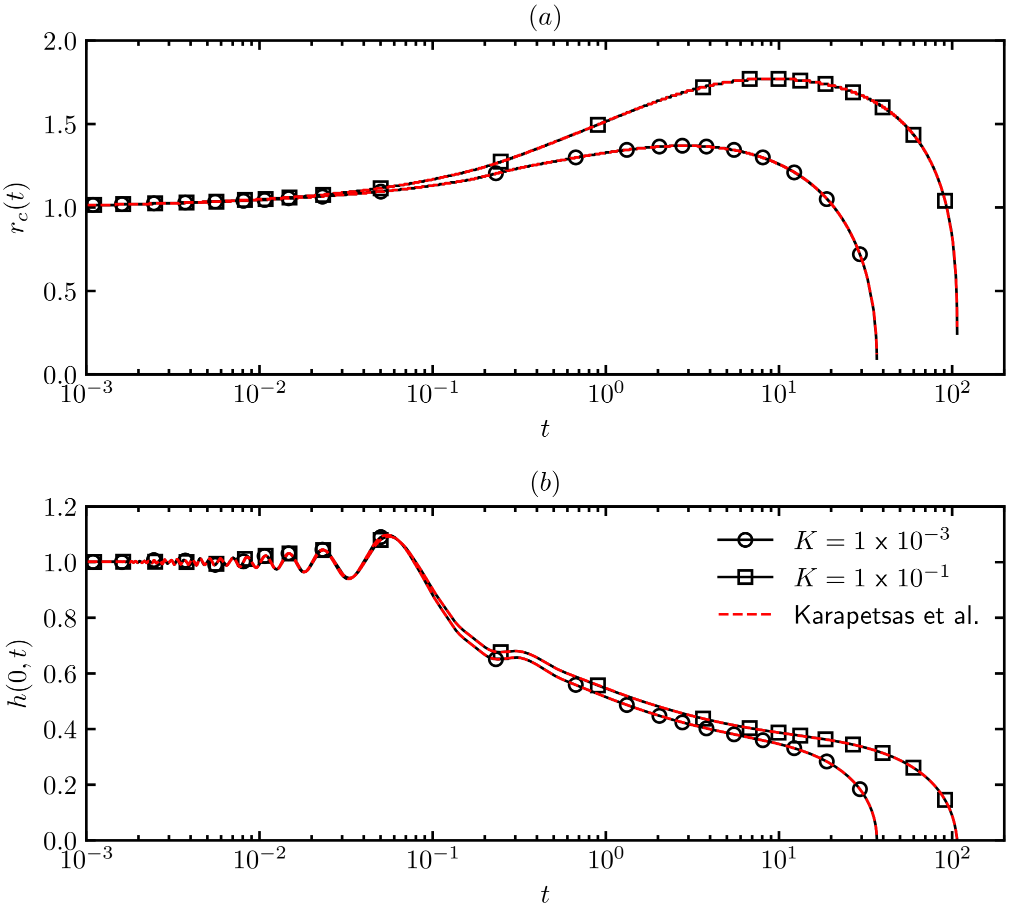

Fig. 7.1 Comparison of our model for the parameters given in Tab. 7.1 with the single component model of Karapetsas et al. [203]. (a) shows contact line position and (b) apex height throughout drop lifetime. Unless otherwise stated, parameters take the values given in Tab. 7.1.

Tab. 7.2 Dimensionless base parameters for an ethanol-water mixture

ε	0.20	δ	1×10^{-5}	k_R	1.00
Re	0.00	$\mathscr{A}$	1×10^{-4}	μ_R	0.84
Pr	16.1	Pe	20	$c_{p,R}$	1.74
Ma	1.64×10^{-1}	σ_R	3.20	M_R	0.39
E	2.66×10^{-4}	γ_R	1.81	$\mathit{\Lambda}$	1.00
K	8.85×10^{-4}	α	0.40	$\chi_{A0,i}$	0–0.75

All drops have an initial volume of 1 µl and an initial aspect ratio of 0.2. This means that the initial diameter of a drop is ten times larger than its height. Dimensionless numbers and property ratios are calculated from the dimensional physical properties of each component given in Tab. 6.1. A complete list of these base parameters is given in Tab. 7.2. Due to modelling limitations, we are forced to modify some of these calculated values slightly. The drops we consider are assumed to be small and very thin, meaning, surface tension is the dominating force meaning the Reynolds number will be small. For both simplicity and the suppression of the interfacial oscillations shown in Fig. 7.1, we set $Re = 0$ for most cases. The Péclet number indicates the rate of mass diffusion in the drop; high numbers indicate slow diffusive component transport. Mass transport is intimately tied to the rate of evaporation, something that is relatively fast in our one-sided model due to the assumption of a phase-transition limited evaporation over a diffusion limited approach. We begin by restricting Pe to 20 and examine its influence in more detail later on in Section 7.5.4.

$\mathscr{A}$ and δ are both used in defining the thickness of the precursor layer. If either take small values, the result in a thin precursor layer and vice versa for large values. While the experimentally observed precursor layer is very thin, imposing too thin of a layer in our simulations can cause severe numerical difficulties. An overly thin precursor layer ($h_\infty < 10^{-4}$) will cause a very large disjoining pressure, $\mathit{\Pi}$, making our problem numerically stiff and convergence hard to achieve. We therefore increase $\mathscr{A}$ and δ several orders of magnitude above their calculated values to 10^{-4} and 10^{-5} respectively. This sets the precursor thickness to around 10^{-3} with equal latent heats ($\mathit{\Lambda} = 1$) assumed also for this reason. It is worth noting that decreasing either $\mathscr{A}$ and δ individually by an order of magnitude does not affect the solution by a significant amount. Lastly, for simplicity, we also assume a uniform thermal conductivity throughout the drop, meaning $k_R = 1$. The remaining dimensionless number and property ratios are left as the directly calculated quantities from the liquid component properties given in Tab. 6.1.

7.3. Pure water drop

Before considering a binary ethanol-water drop, we first document the spreading and evaporation behaviour of a pure water drop to serve as a reference case. A pure water drop corresponds to the dimensionless properties in Tab. 7.2, with $\chi_{A0,i} = 0$. Fig. 7.2 details the evolution of the interface profile, surface tension, and total evaporative flux along r via snapshots in time as the drop evaporates. The LV interface begins with a scaled dimensionless height and radius of 1. At early times, the drop spreads outwards as the forces at the contact line come into balance. By $t = 5.00$, evaporation takes over and the contact line slowly recedes with the drop retaining a spherical cap shape over the remaining lifetime until dry-out at $t \approx 50$. The heated substrate causes the drop to always be warmest at the contact line due to the reduced thickness of the liquid. It is evident that throughout the drop lifetime, maximum evaporation occurs at the warm contact line—see Fig. 7.2(c), where the vapour pressure is highest. The minimum liquid temperature is always located at the drop apex. In the absence of solutal Marangoni effects, this is also the location of highest surface tension. Fig. 7.2(b) shows that a positive surface tension gradient between the contact line and apex is maintained throughout the drop lifetime. Thermal Marangoni stresses therefore drive the liquid from the contact line towards the apex, limiting spreading in the early stages and causing the spherical cap to be retained as evaporation takes over and the contact line recedes. This behaviour is in line with the findings in other similar theoretical and experimental works [158, 159], and with the mechanisms described by Deegan et al. [129] and Hu and Larson [133].

7.4. Ethanol-water binary drops

7.4.1 Influence of initial ethanol concentration

We now gradually increase the initial mass fraction of ethanol ($\chi_{A0,i}$) in the drop and examine the effects this has on the spreading behaviour and total lifetime. The parameters used are again those in Tab. 7.2. Specifically, we look at five cases: $\chi_{A0,i} = 0.00, 0.10, 0.25, 0.50, 0.75$. Fig. 7.3 shows the position of the contact line, apex height along with the total evaporative flux and mass fraction of ethanol at the apex versus time. Beginning by again considering a pure water drop, Fig. 7.3(a) shows that pure water sees a modest initial spreading followed by a steady recession. After the initial stages, the height also decreases steadily—see Fig. 7.3(b)—and evaporation from the apex is modest until the final stages before dry-out—Fig. 7.3(c). Introducing ethanol into the drop, we see that increasing $\chi_{A0,i}$ enhances the drop spreading and increases

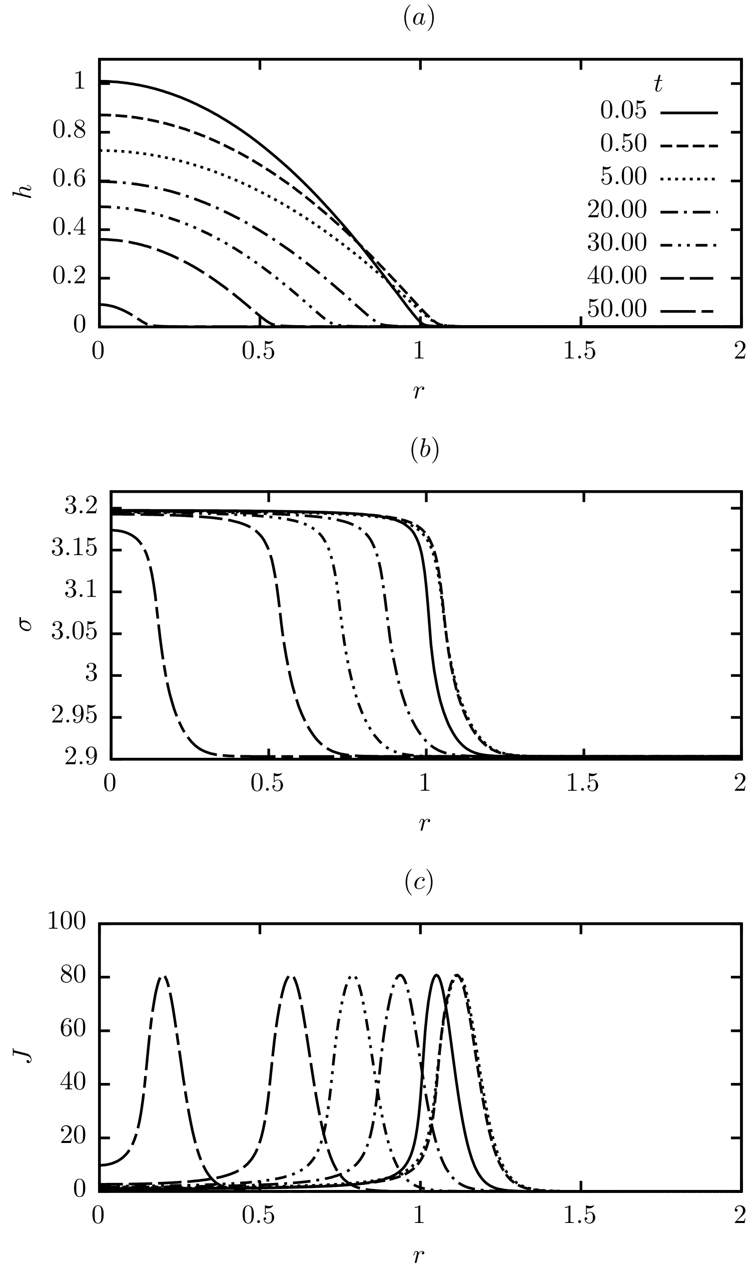

Fig. 7.2 Snapshots of (a) interface profile, h, (b) surface tension, σ, and (c) total evaporative flux, J, of a pure water drop over its lifetime. Dimensionless parameters are those given in Tab. 7.2 with $\chi_{A0,i} = 0$.

the maximum position of the contact line. In all cases, the enhanced spreading is accompanied with a rapid drop in apex height. Drop lifetime is reduced as $\chi_{A0,i}$ increases owing both to the increased volatility of the mixture and the decreased drop thickness due to enhanced spreading.

For $\chi_{A0,i} = 0.10$, we see that once maximum radius is reached, the drop begins to retract, accompanied by a regain in apex height to a position similar to the pure water drop. Closer inspection of Fig. 7.3(d) reveals that contact line retraction coincides with depletion of χ_{A0} at the apex, and hence in the rest of the drop. A similar behaviour is displayed by $\chi_{A0,i} = 0.25$, with a greater initial spreading and maximum radius followed by a smaller retracted radius due to the larger proportion of evaporated ethanol leaving less drop mass once depleted. Beyond this, with drops constituting mainly water, evaporation then proceeds in the same way as the pure water drop until dry-out.

In both of these cases, enhanced spreading is driven by the preferential evaporation of ethanol from the contact line. This leaves an ethanol depleted (water rich) region at the contact line with higher surface tension than the bulk drop. Induced by solutal Marangoni stresses, liquid flows towards the freely moving contact line, causing it to spread further outwards. Spreading continues until ethanol is depleted at which point solutal Marangoni stresses are eliminated. With the absence of ethanol, the surface tension gradient is reversed. Surface tension now highest in the coldest region of the drop. On our heated substrate this corresponds to the thickest area of liquid, in these cases the apex. Flow is now directed away from the contact line towards the apex, driven now by thermal Marangoni stresses. The further the drop has spread and deformed from a spherical cap shape, the further it must contract to regain this profile. With greater spreading at higher initial ethanol concentrations, this explains the rapid recession of the contact line and increase in height for $\chi_{A0,i} = 0.25$ over $\chi_{A0,i} = 0.10$. It is clear that thermal and solutal Marangoni stresses are in completion against each other with solutal effects dominating the initial stages and thermal effects the latter. We will look at these in more detail to follow.

In the concentrations discussed previously, a significant amount of water remains after ethanol depletion, causing retraction and return to spherical cap shape. With higher initial ethanol, this is not the case and drops remain in a flattened shape throughout their lifetime. Contact line recession in these binary mixtures is caused by both the inward driven Marangoni flow and mass loss from the drop as it evaporates. Increasing initial ethanol from $\chi_{A0,i} = 0.50$ to $\chi_{A0,i} = 0.75$, the drop spreads by a greater amount—reaching a larger maximum radius. This is explained by the increased maximum surface tension gradient between the apex and the contact line for larger $\chi_{A0,i}$. Fig. 7.4 shows the rate of change of surface tension along r at the early time of $t = 0.25$ for full range of concentrations considered. A positive surface tension gradient between the apex and contact line is clearly seen to increase with $\chi_{A0,i}$. A greater maximum spreading radius also results in a thinner drop which is subject to higher temperatures and hence more rapid evaporation rate. Fig. 7.3(c) shows that there is always higher evaporative flux from the apex for higher initial ethanol concentration. This is due in part to the increased proportion of volatile ethanol but also to the decreased thickness causing a warmer interface and greater evaporation rate for any given mixture as well as the larger radius leading to an increased effective interfacial area for evaporation.

Taking a closer look at the influence of initial ethanol concentration on spreading rate, Fig. 7.5 plots radius growth versus time in the common logarithmic domain for the data shown in Fig. 7.3. As we know, the spreading behaviour of wetting drops tends to obey a power law growth of radius in time, $r \propto t^n$, where n is the spreading exponent. Therefore, the gradient of the radii plotted in Fig. 7.5 will give the spreading exponents of for each $\chi_{A0,i}$. Note that similar values of n can be found for the retraction rate. In the case of a pure drop, spreading will obey Tanner's law whereby $n \approx 0.1$ [134]. We can see from Fig. 7.3 that as we increase initial ethanol concentration, the line growth gradients and hence spreading exponents approach values of 1, moving into the realms of superspreading liquids such as trisiloxane surfactants [156]. Precise values for the linear fit are given in Tab. 7.3. n_1 gives the first spreading coefficient until the first breakpoint in time, b_1, where the gradient shifts to n_2 until time b_2 and so on and so forth until dry-out.

In Tab. 7.3, we see that for pure water, $\chi_{A0,i} = 0.00$, there is an initial contact line adjustment with rapid spreading at early times where $n_1 = 0.6$. This corresponds to the inertial spreading phase, expected to be $n \approx 0.5$ for pure liquids [147]. The spreading exponent soon slows and settles at $n_2 = 0.11$, close to Tanner's law as expected for pure liquids [65, 136, 142]. After time $b_3 = 0.78$, an exponent close to zero, $n_3 = 0.02$, shows a region where forces at the contact line are largely balanced and is effectively stationary before evaporation taking over and the drop receding at increasing rates from n_4 to n_8. For the majority of the recession time, $t = 20.83$–34.24, is conducted at exponent $n_6 = -0.50$. This is similar to recession rates found reported by Cachile and co-workers [150, 134] as well as Poulard et al. [151]. The increasing recession rate is explained by the shrinkage in drop height from mass loss as it evaporates. As previously discussed, the reduced drop thickness gives rise to greater evaporation rates since the drop is heated more by the substrate.

Increasing to $\chi_{A0,i} = 0.10$ sees n_2 rise to 0.15 with the increased spreading rate lasting for longer times until $b_2 = 1.03$. $\chi_{A0,i} = 0.25$ continues the trend with $n_2 = 0.19$ until $b_2 = 1.90$. This trend was also seen by Guéna et al. [154] when increasing concentration of the more volatile alkane. If we compare the breakpoint time b_2 signifying the end of the spreading regime with Fig. 7.3(d) showing apex ethanol mass fraction, we see

Tab. 7.3 Spreading coefficients, n, and corresponding breakpoints in time, b, for increasing initial concentrations of ethanol. Physical properties are those given in Tab. 7.2.

	$\chi_{A0,i} = 0.00$	$\chi_{A0,i} = 0.10$	$\chi_{A0,i} = 0.25$	$\chi_{A0,i} = 0.50$	$\chi_{A0,i} = 0.75$
n_1	0.60	0.45	0.50	1.12	1.47
b_1	0.11	0.26	0.54	0.15	0.12
n_2	**0.11**	**0.15**	**0.19**	**0.67**	**0.89**
b_2	0.78	1.03	1.90	0.51	0.35
n_3	0.02	0.05	−0.02	**0.36**	**0.51**
b_3	2.44	2.18	3.66	1.21	0.80
n_4	−0.05	−0.12	−0.23	**0.16**	**0.27**
b_4	8.75	13.93	5.68	2.31	1.64
n_5	−0.17	−0.24	−0.39	0.00	**0.11**
b_5	20.83	21.86	8.12	3.44	2.72
n_6	−0.50	−0.46	−0.65	−0.15	−0.07
b_6	34.24	30.62	10.12	4.61	3.85
n_7	−1.39	−0.93	−0.30	−0.31	−0.30
b_7	43.88	38.99	26.48	6.11	5.11
n_8	−4.18	−2.14	−1.22	−0.45	−0.60

that ethanol is not totally depleted within the drop until $t = 10$ in both cases. This suggests that a residual amount of ethanol remains in the drop well into the recession regime.

Increasing initial ethanol higher still to $\chi_{A0,i} = 0.50$ displays a slightly different spreading behaviour. The first spreading exponent n_2 is now significantly higher at 0.67 with the rate progressively decreasing to $n_3 = 0.36$ and $n_4 = 0.16$ before the contact line retracts. This is due to the decreasing concentration gradient between the contact line and apex as ethanol evaporates and solutal Marangoni stresses weaken. As maximum radius is approached, spreading rate decreases towards a Tanner's law value. $\chi_{A0,i} = 0.75$ also exhibits this behaviour with a greater initial rate of $n_2 = 0.89$ and the emergence of three further distinct linear spreading regimes: $n_3 = 0.51$, $n_4 = 0.27$, and $n_5 = 0.11$. Overall retraction exponents decrease with increasing $\chi_{A0,i}$. As will be explained later, this is owing to the increased solutal Marangoni outward force acting against inward thermal Marangoni stresses.

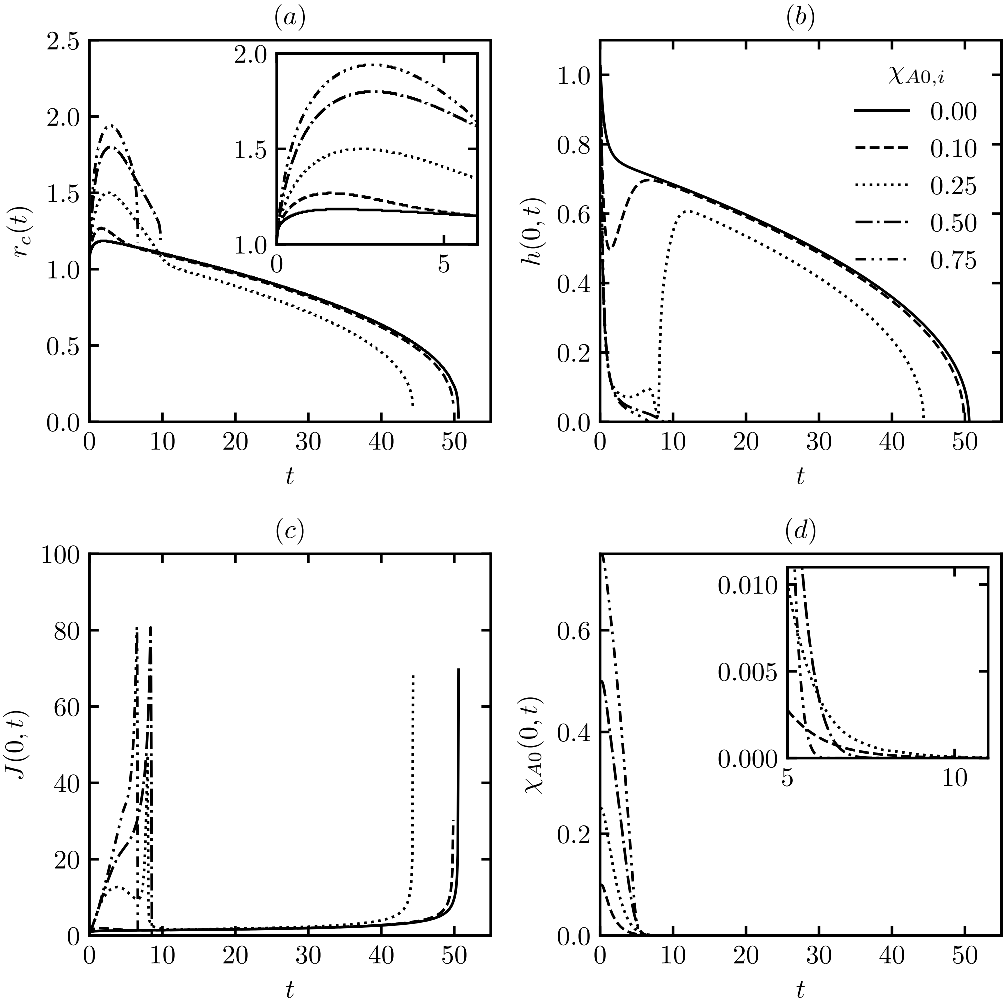

Fig. 7.3 Profiles of (a) contact line position, (b) apex height, (c) apex mass flux, and (d) apex mass fraction throughout drop lifetime for varying initial mass fraction of MVC, $\chi_{A0,i}$. Dimensionless parameters are given in Tab. 7.2 with only $\chi_{A0,i}$ altered in each dataset.

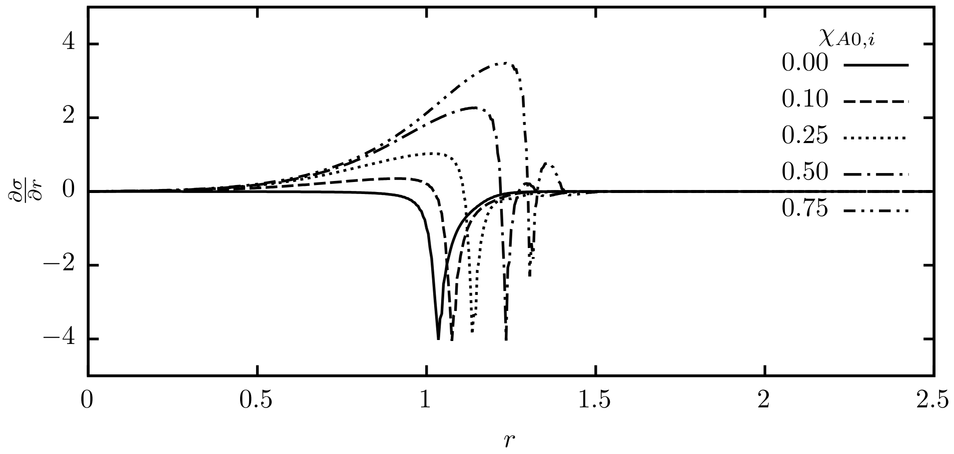

Fig. 7.4 Rate of change of surface tension along r for all initial ethanol concentrations considered at $t = 0.25$. Unless otherwise stated, dimensionless parameters are those given in Tab. 7.2.

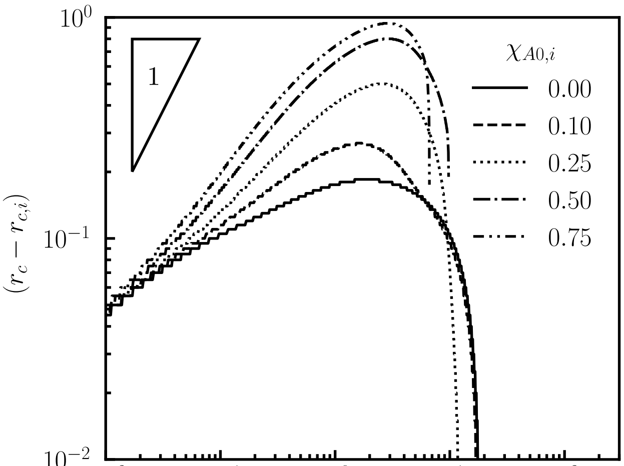

Fig. 7.5 Contact line position versus time on a logarithmic scale for increasing initial ethanol concentrations. Corresponding spreading coefficients and breakpoints in time are shown in Tab. 7.3. Dimensionless parameters are those given in Tab. 7.2.

7.4.2 Decomposed interface velocities

It is clear at this stage that binary mixture drops exhibit distinctly different spreading and evaporation behaviours from their pure component counterparts. Spreading rates and durations are increased which then cause interesting recession behaviour. We have also seen that, depending on the initial concentration of the second component, two typical scenarios emerge. For lower concentrations, the MVC (component A) totally evaporates, leaving a substantial amount of the LVC (component B). For higher initial concentrations of MVC, both components are depleted at approximately the same time. In both cases there is a delicate balance of solutal and thermal Marangoni stresses governing the behaviour. We now look in more detail at the lower concentrations for each of these scenarios: $\chi_{A0,i} = 0.10$ and $\chi_{A0,i} = 0.50$.

To reveal more information about the flow field, the averaged velocity at the interface, u, can be decomposed into three distinct components,

$$u = u_{tg} + u_{cg} + u_{ca} \tag{7.1}$$

These are the three mechanisms that can drive movement and spreading of the contact line. u_{tg} is the thermocapillary velocity, where surface tension gradients arising from temperature variations drive the fluid motion. u_{cg} is the solutocapillary velocity, where flow is driven by a surface tension gradient sustained by an uneven mixture concentration. u_{ca} is the capillary velocity, sustained by the capillary pressure over the interface. By decomposing the bulk velocity into these three contributions, we can gain insight into the driving forces governing the spreading behaviour. We have already defined an expression for the bulk velocity—its closure approximation from eq. (6.70). Using this, it can be shown that the decomposed velocities at the interface simplify to,

$$u_{ca} = -\frac{h^2}{2\mu}\frac{\partial p}{\partial r} \tag{7.2}$$

$$u_{cg} = \left[\frac{\partial \chi_{A0}}{\partial r} - \sigma_R\frac{\partial \chi_{A0}}{\partial r} - MaT_s\frac{\partial \chi_{A0}}{\partial r}(1-\gamma_R)\right]\frac{h}{\mu Ma} \tag{7.3}$$

$$u_{tg} = \left[-\frac{\partial T_s}{\partial r}\chi_{A0} - \frac{\partial T_s}{\partial r}\gamma_R(1-\chi_{A0})\right]\frac{h}{\mu} \tag{7.4}$$

7.4.3 10 wt.% initial ethanol concentration

Fig. 7.6 shows the evolution of interface position, surface tension and ethanol mass fraction along r for an ethanol-water drop with $\chi_{A0,i} = 0.10$. The interface profile, Fig. 7.6(a), indicates that the drop spreads significantly between $t = 0.05$ and $t = 0.35$

with a significant drop in apex height of 0.3. Fig. 7.6(b) reveals that the surface tension gradient between the apex and contact line increases during with Fig. 7.6(c) showing increased depletion of ethanol closer to the contact line. Spreading continues until $t = 1$ and by $t = 3$, the drop begins to recede as thermal Marangoni effects start to dominate. The apex height increases from $t = 1$ as thermal Marangoni stress pulls liquid towards the centre. Inspection of Fig. 7.6(c) shows that ethanol is still present within the drop in small amounts ($\chi_{A0} < 0.02$). By the next snapshot at $t = 20$, ethanol is totally depleted in the drop and evaporation now proceeds relatively slowly with the interface retaining a spherical cap shape. We can see in Fig. 7.6(b) that surface tension at later times is always higher at the apex, however, the magnitude of the surface tension gradient is significantly smaller than the reverse gradient present at early times due to concentration effects.

We now examine the decomposed interface velocities of these time snapshots in Fig. 7.7. A positive value indicates velocity directed towards the contact line while a negative value shows velocity directed towards the centre. Capillary velocity, u_{ca}, resulting from interface curvature is predictably large and positive at the contact line as the drop profile transitions into the precursor layer while becoming negative towards the centre due to reverse curvature. Fig. 7.7(a) shows the movement of u_{ca} over time with the spreading and recession of the contact line. The solutocapillary velocity, u_{cg}, in Fig. 7.7(b) displays a clear trend. It is positive at all times, driving liquid towards the contact line and decays over time. u_{cg} is largest at the earliest time of $t = 0.05$ when the concentration gradient between the apex and contact line is also at its greatest. The strength of the outward solutocapillary velocity gradually decreases as χ_{A0} evaporates until beyond $t = 3.00$ where it dies out completely—coinciding with total depletion of χ_{A0}. Fig. 7.7(c) tracks the development of theromocapillary velocity, u_{tg}, which is negative at all times. Again, this is in line with intuitive ideas of Ajaev [95] and Ehrhard and Davis [158] by demonstrating that fluid is forced inwards towards the centre under thermocapillary forces. The largest magnitude of u_{tg} is always located at the contact line, becoming more negative the thinner the interface becomes—corresponding to a warmer region.

Examining further the balance between thermal and solutal Marangoni stresses, we turn out attention to Fig. 7.8 which illustrates the combined Marangoni velocity profiles at times $t = 1$, $t = 3$, and $t = 20$, along with the interface profile. The drop radius is largest at $t = 1$ before beginning to recede at $t = 3$. Fig. 7.8(a) shows a net negative (inward) Marangoni velocity in the vicinity of the contact line with a net positive (outward) velocity in the drop interior. We know as time proceeds, u_{cg} diminishes in strength and so this action combined with the constant inward flow of u_{tg} halts the movement of the contact line. By $t = 3$, χ_{A0} is sufficiently depleted that there is only a weak outward combined Marangoni velocity in the bulk drop with the overwhelming velocity directed inwards from the contact line. By $t = 20$, combined Marangoni velocity throughout the whole drop profile is negative and directed inwards with the absence of any solutal effects.

7.4.4 50 wt.% initial ethanol concentration

When initial ethanol concentration is increased to $\chi_{A0,i} = 0.50$, the evolution of the drop profile becomes more complex. In Fig. 7.9 we again examine the evolution of the interface position, surface tension and mass fraction of ethanol. With Figs. 7.10 and 7.11 exploring the decomposed velocities in more detail. It is clear from Fig. 7.9(a) that evolution of the interface is radically different from the Fig. 7.6. From $t = 0.05$ to $t = 3.00$, the drop spreads rapidly to a pancake shape with the formation of a ridge of liquid preceding the contact line. This is similar to the ridge formed in the spreading of trisiloxane-laden surfactant drops [85, 156]and results from the rapid rate of spreading. Fig. 7.9 reveals that before $t = 3$, surface tension is always largest towards the contact line, specifically at the apex of the ridge. The contact line can be seen retracting from $t = 5.00$ onwards while the flat plane in the drop interior trapped by the ridge gradually decreases in height. Notice that at $t = 9.00$, the drop centre has reached dry-out, however the ridge at the contact line still remains. Extrapolated in the azimuthal plane to three dimensions, film dry-out leaves a torus shaped ring of liquid. This is analogous to ring observed in the experiments conducted by Guéna et al. [154] on drops of alkane mixtures evaporating from isothermal substrates. Fig. 7.9(c) confirms that all ethanol (component A) is depleted from the drop by $t = 7.00$ and so it can be concluded that the ridge consists entirely of water (component B).

In Fig. 7.10(a) we see that u_{ca} is larger than the $\chi_{A0,i} = 0.10$ case at early times. u_{ca} is largest at the contact line at all times, even during ridge formation. A similar trend is displayed in solutocapillary velocity as before, the key difference being that the magnitude of u_{cg} is around four times larger when $\chi_{A0,i} = 0.50$ over $\chi_{A0,i} = 0.10$. This is expected due to the higher concentration gradient between the apex and contact line. It also appears from Fig. 7.10(b) that outward flow from u_{cg} is negligible at $t = 3.00$ and this is the time at which recession begins. The thermocapillary velocities in Fig. 7.10 show an altogether more interesting trend. Before ridge formation, u_{tg} is of the same direction and magnitude as the $\chi_{A0,i} = 0.10$ case—around 0.5 directed inwards toward the drop centre. However, as the drop flattens and the ridge forms, a positive u_{tg} begins to emerge on the LHS of the ridge. This velocity pushes fluid from the bulk drop outwards toward the ridge while there is simultaneously a negative u_{tg} on the RHS of the ridge pushing fluid inward. Physically, this means that liquid from both sides is flowing towards the ridge, sustaining its formation. As liquid flows from the thin plane on the LHS to feed the ridge, the removal of liquid from the thin layer

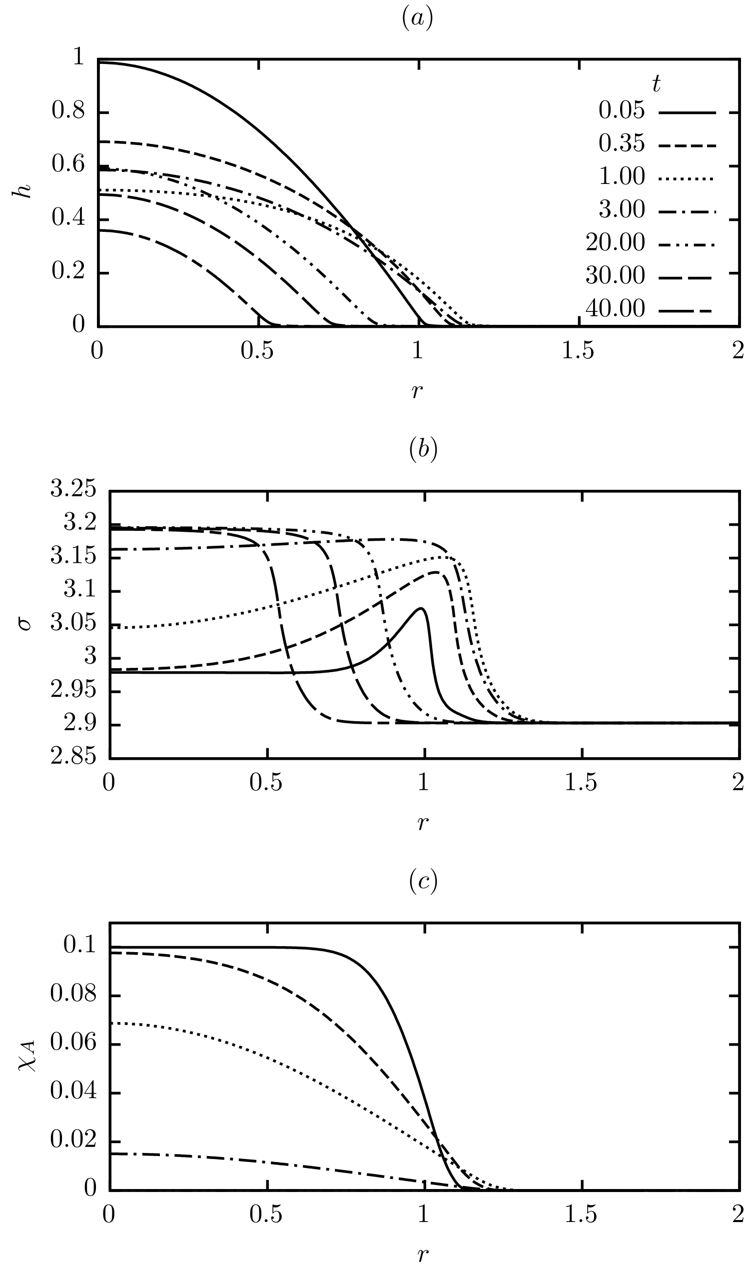

Fig. 7.6 Snapshots of (a) interface profile, (b) surface tension, and (c) concentration of component A for an ethanol-water drop with $\chi_{A0,i} = 0.10$. Dimensionless parameters are those given in Tab. 7.2.

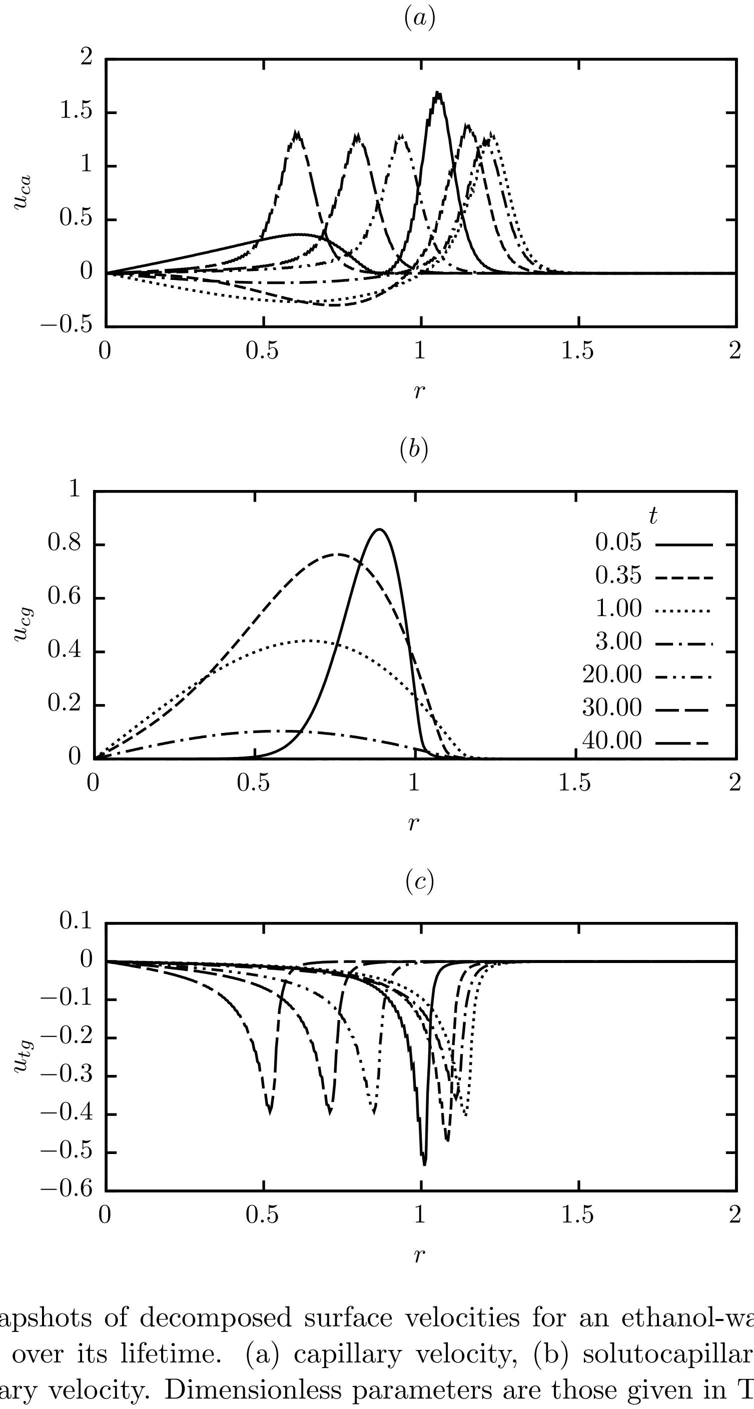

Fig. 7.7 Snapshots of decomposed surface velocities for an ethanol-water drop with $\chi_{A0,i} = 0.10$ over its lifetime. (a) capillary velocity, (b) solutocapillary velocity, (c) thermocapillary velocity. Dimensionless parameters are those given in Tab. 7.2.

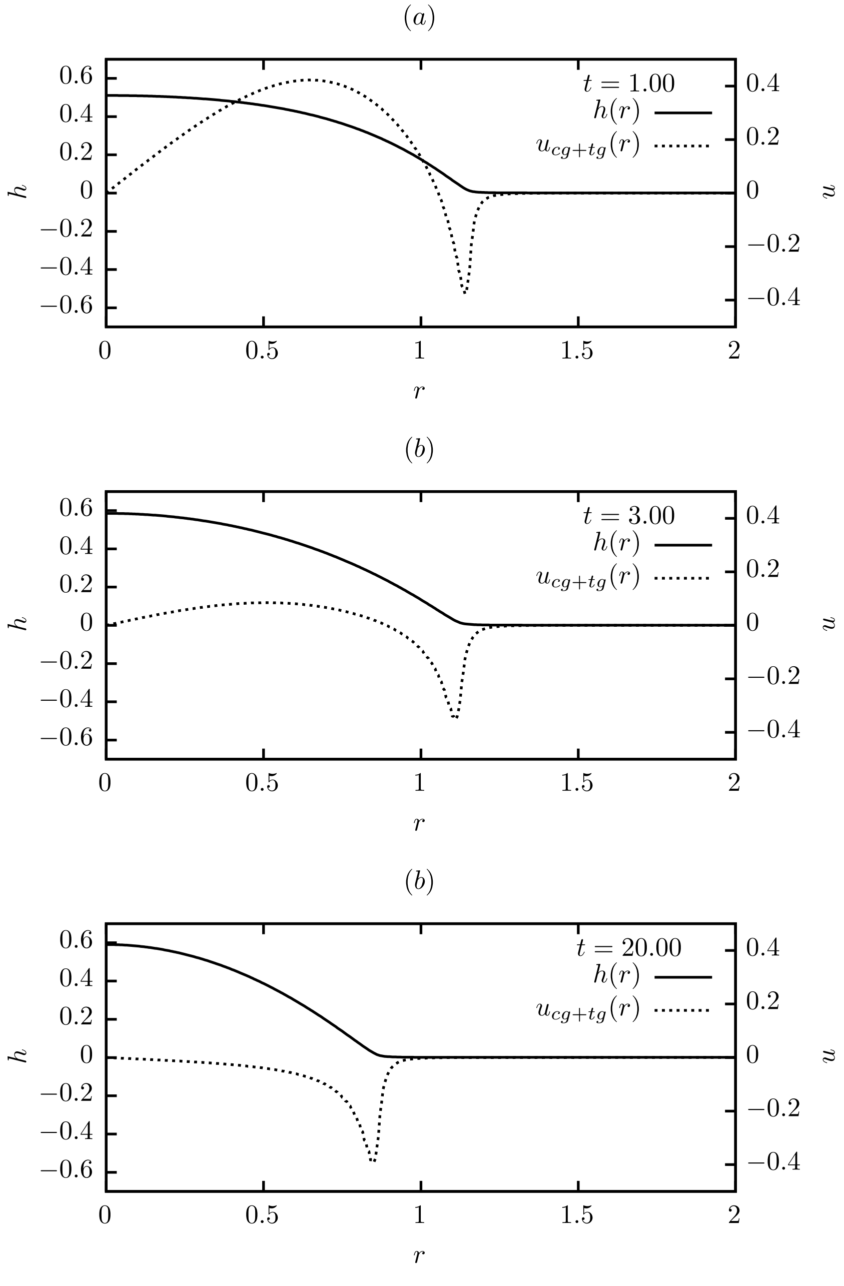

Fig. 7.8 Interface profile and corresponding combined Marangoni velocity (solutal and thermal) for an ethanol-water drop with $\chi_{A0,i} = 0.10$. Other dimensionless parameters are those given in Tab. 7.2. (a)$t = 1.00$, (b) $t = 3.00$, (c) $t = 20.00$

causes a dimple in the interface profile to form adjacent to the ridge. This can be seen by examining h in Fig. 7.9(a) from $t = 5.00$ to $t = 7.00$ to $t = 9.00$ where the ridge is shown steadily receding while the interior dries out. The reduced thickness of the interface in this region causes the liquid to be heated to a greater temperature and hence produces a larger surface tension gradient between the bottom of the dimple and the apex of the ridge. This then results in a stronger thermocapillary velocity from the dimple to the ridge which can be seen clearly in Fig. 7.10(c). Therefore, it appears that the initial ridge is formed due to solutocapillarity inducing very rapid spreading of the contact line. Once formed, the ridge is sustained by thermocapillarity providing a steady flow of fluid to the apex.

Finally, let us consider the combined actions of the solutal and thermal Marangoni velocities at key points in the $\chi_{A0,i} = 0.50$ drop lifetime. Fig. 7.11(a) shows the interface profile and combined Marangoni velocity at $t = 1$ while the drop is still firmly in the spreading regime. Fig. 7.11(b) considers $t = 3.00$ when maximum radius is reached and (c) shows the drop well into the recession regime at $t = 7.00$, with the liquid film on the LHS of the ridge still present but close to dry-out. At $t = 1$, velocity is overwhelmingly directed towards the contact line with a small inward velocity at the contact line itself where liquid is warmest. Inward velocity at the contact line grows by $t = 3$ while outward velocity declines as ethanol evaporates. By $t = 7.00$, there is a clear inward Marangoni velocity from the RHS of the ridge as the drop contact line recedes. The dimple in the interface profile on the LHS of the ridge is also visible. At the minimum point of the dimple, there is a positive and negative velocity on either side (the RHS and LHS respectively). This means that fluid from the dimple is driven both outwards towards the ridge at the contact line and inward towards the centre. The mechanism sustains ridge formation even after spreading has finished and only water remains in the drop. The simultaneously decreasing dimple depth increases the strength of the Marangoni flow while intimately leading to dry-out in the interior before the contact line ridge completely evaporates.

7.5. Other factors influencing binary drop spreading

As reported by Guéna et al. [154], the spreading of small binary mixture sessile drops is a complex process governed by a delicate interplay between evaporation, surface tension gradients, mass diffusion, hydrodynamic flow, and capillary forces. An explicit advantage of our model over experiments is the ability to alter specific dimensionless numbers while keeping other properties constant, allowing us to assess the impact of each mechanism individually. We now briefly examine the effect changing the magnitude of E, Ma, σ_R, Pe, and Re on the solution on for $\chi_{A0,i} = 0.50$.

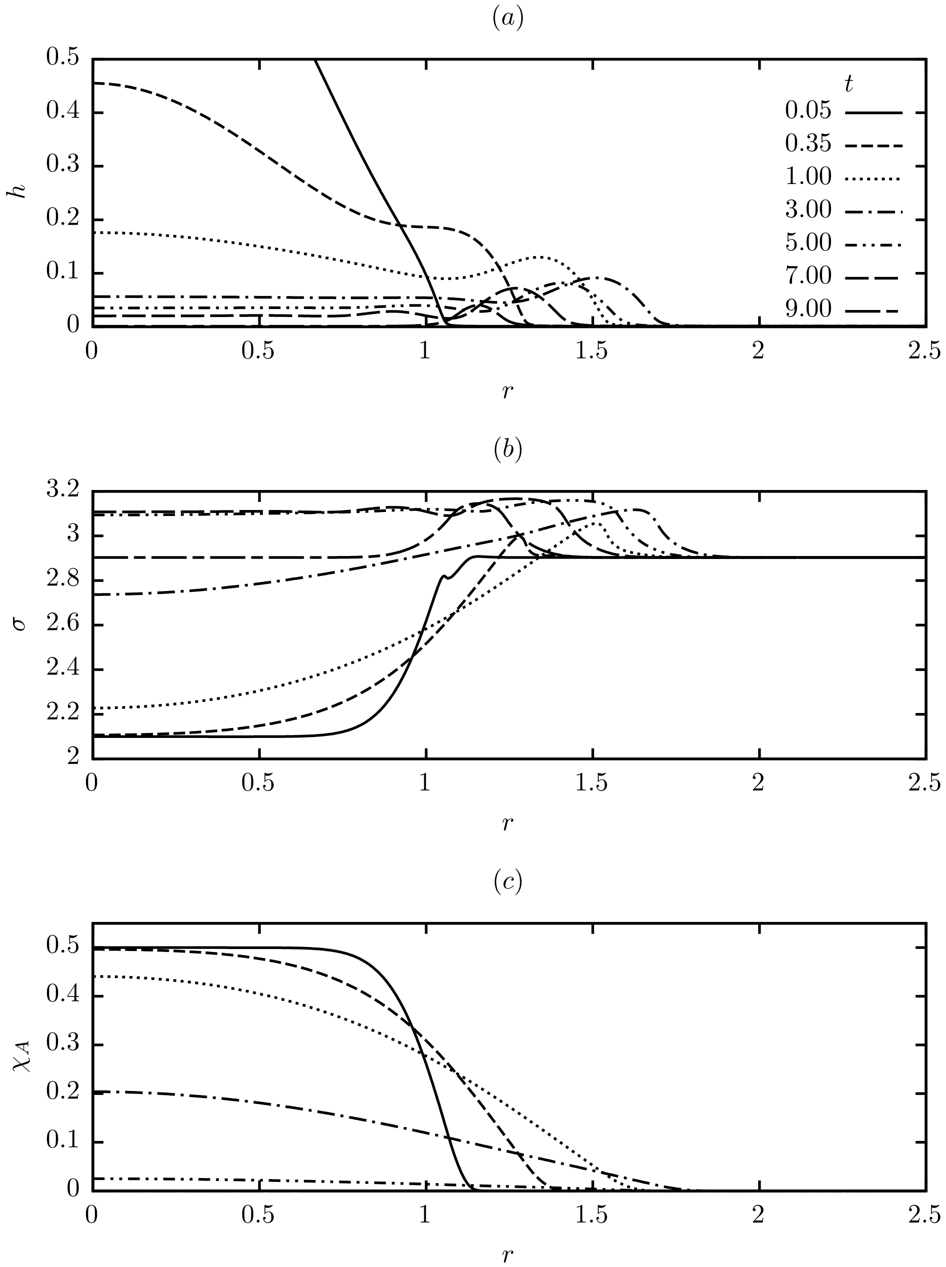

Fig. 7.9 Snapshots of (a) interface profile, (b) surface tension, and (c) concentration of component A along the interface for an ethanol-water drop with $\chi_{A0,i} = 0.50$. Dimensionless parameters are those given in Tab. 7.2.

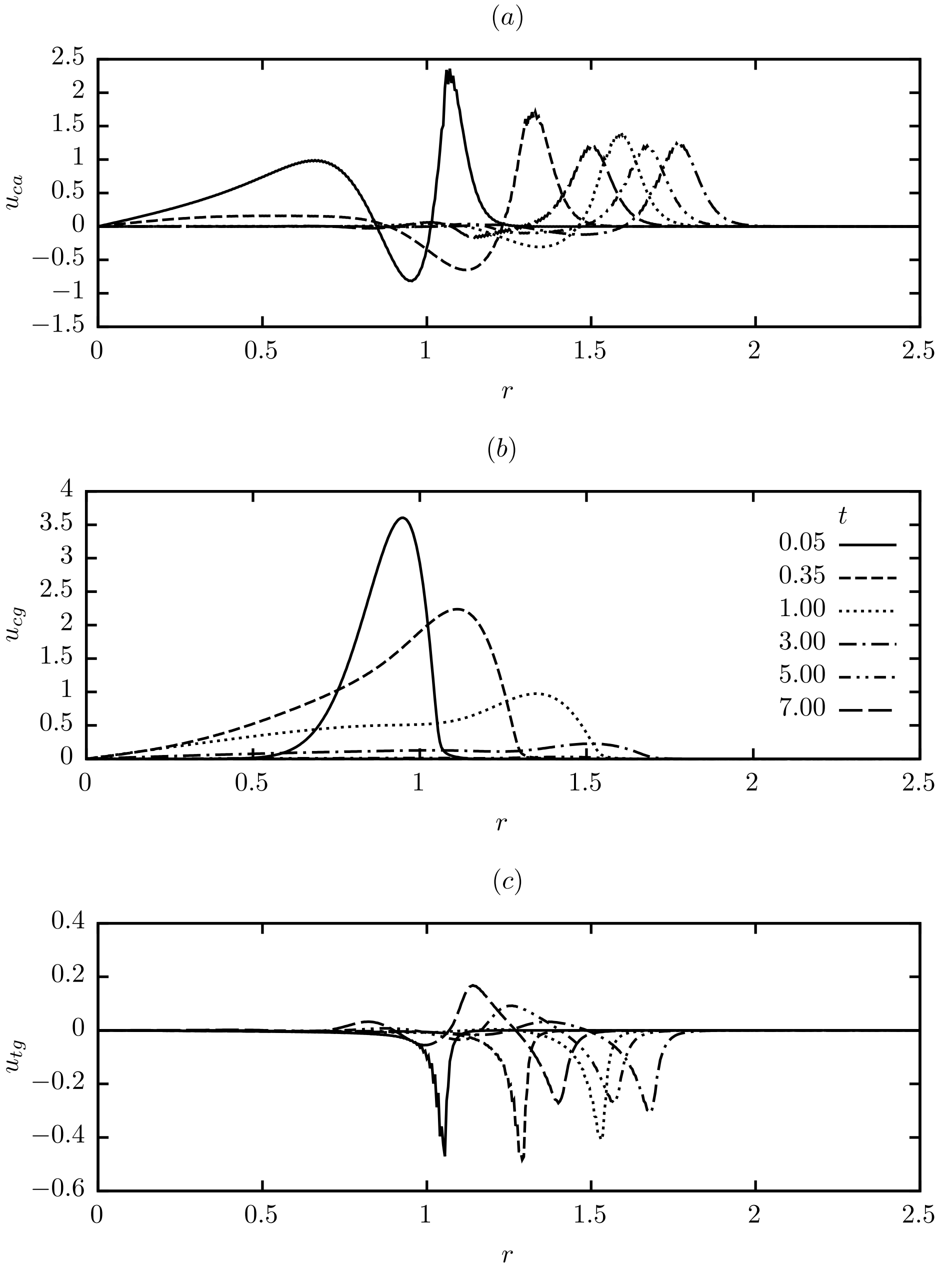

Fig. 7.10 Snapshots of decomposed surface velocities for an ethanol-water drop with $\chi_{A0,i} = 0.50$ over its lifetime. (a) capillary velocity, (b) solutocapillary velocity, (c) thermocapillary velocity. Dimensionless parameters are those given in Tab. 7.2.

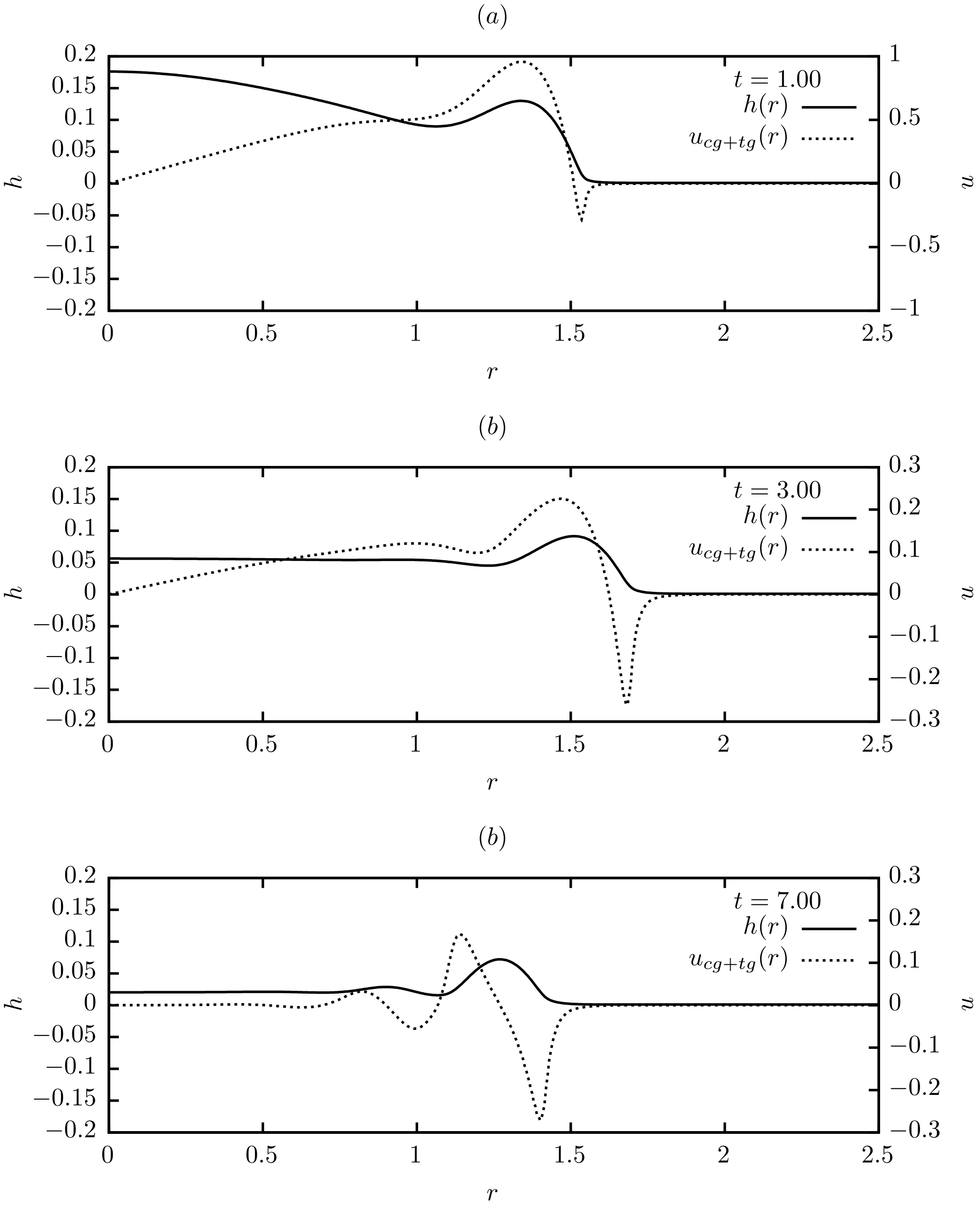

Fig. 7.11 Interface profile and corresponding combined Marangoni velocity (solutal and thermal) for an ethanol-water drop with $\chi_{A0,i} = 0.50$. Other dimensionless parameters are those given in Tab. 7.2. (a)$t = 1.00$, (b) $t = 3.00$, (c) $t = 7.00$

7.5.1 Evaporation number

Increasing the evaporation number increases the volatility of both components in the mixture and vice versa for decreasing E. In Fig. 7.12, we examine the effect of increasing and then decreasing E by one order of magnitude over the base case value of $E = 2.66 \times 10^{-4}$ given in Tab. 7.2. Increasing E to 2.66×10^{-3} simultaneously reduces spreading extent and drop lifetime as evaporation rate of both liquids becomes larger. Decreasing E to 2.66×10^{-5} has the opposite effect. With evaporation now weaker, the drop spreads to a larger maximum radius where it remains stationary for a period before recession. These trends are similarly reflected in the profiles of apex evaporative flux and ethanol mass fraction in Fig. 7.12(c) and (d) respectively. In an experimental scenario, increasing E is analogous to increasing the substrate temperature. We see a similar trend here as we do in our experiments conducted in Chapter 9.

7.5.2 Marangoni number

The Marangoni number controls the strength of thermal Marangoni forces and hence the thermocapillary velocity, u_{tg}. We progressively decrease the base case value of $Ma = 1.64 \times 10^{-1}$ to 9.12×10^{-2} and then 1.84×10^{-2}, gradually weakening the thermal Marangoni stress. We see from Fig. 7.13 that reducing Ma increases the spreading rate and maximum drop radius. This can is explained by the reduction of inward velocity u_{tg} which provides opposition to spreading. Drop that spread further then possess thinner interface profiles which leads to greater evaporative flux—see Fig. 7.13(b) and (c). This ultimately leads to a shorter drop lifetime at lower Ma.

7.5.3 Surface tension ratio

By increasing the surface tension ratio, σ_R, we can strengthen solutal Marangoni forces in the drop. Larger σ_R means the surface tension of the LVC is increased relative to the MVC. When $\chi_{A0,i} = 0.50$, as in Fig. 7.14, the concentration induced surface tension gradient becomes larger as σ_R increases. The larger surface tension gradient will amplify the outward solutocapillary velocity, u_{cg}, with liquid being more strongly drawn toward the contact line. Similar to cases with lowered Marangoni numbers, the increased spreading results in a thinner drop subject to higher evaporative fluxes, hence resulting in shorter lifetimes.

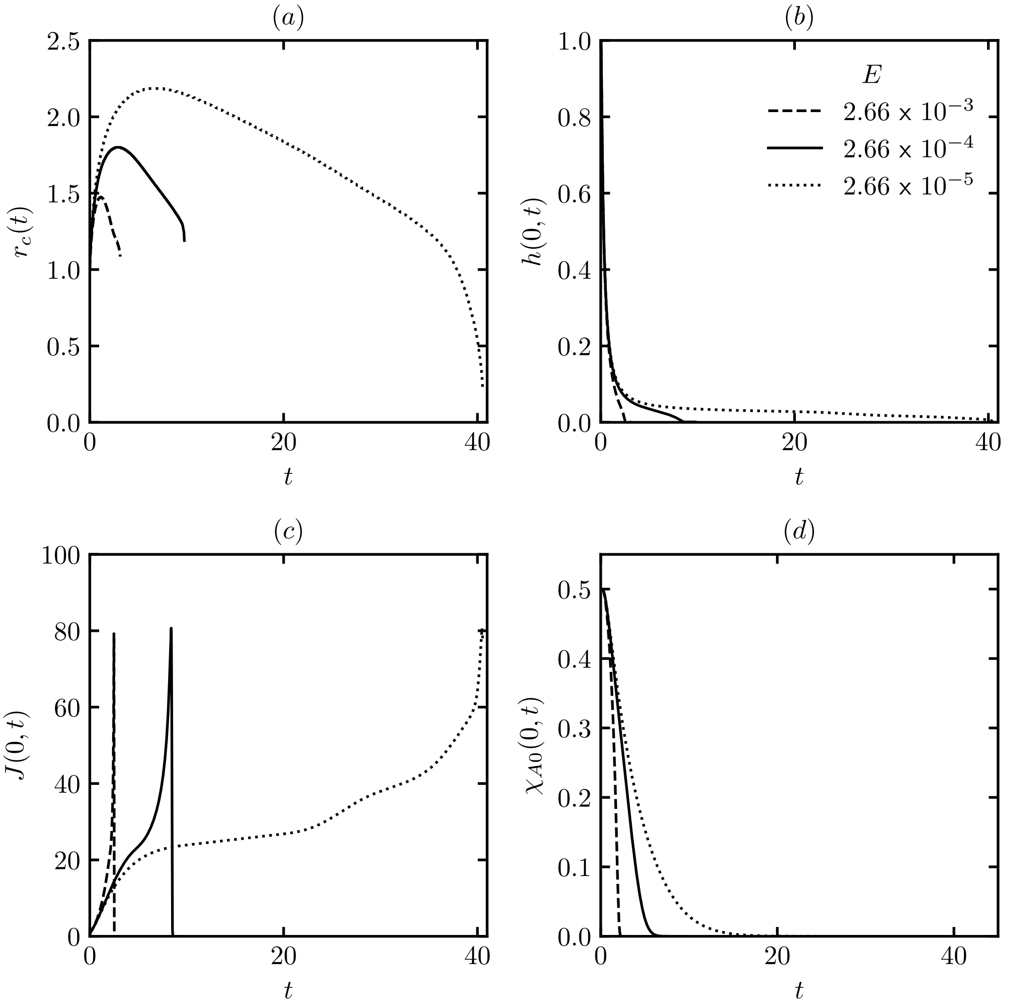

Fig. 7.12 Profiles of (a) contact line position, (b) apex height, (c) apex mass flux, and (d) apex mass fraction throughout the lifetime of a $\chi_{A0,i} = 0.50$ drop with varying Evaporation numbers, E. Unless otherwise stated, dimensionless parameters are those given in Tab. 7.2.

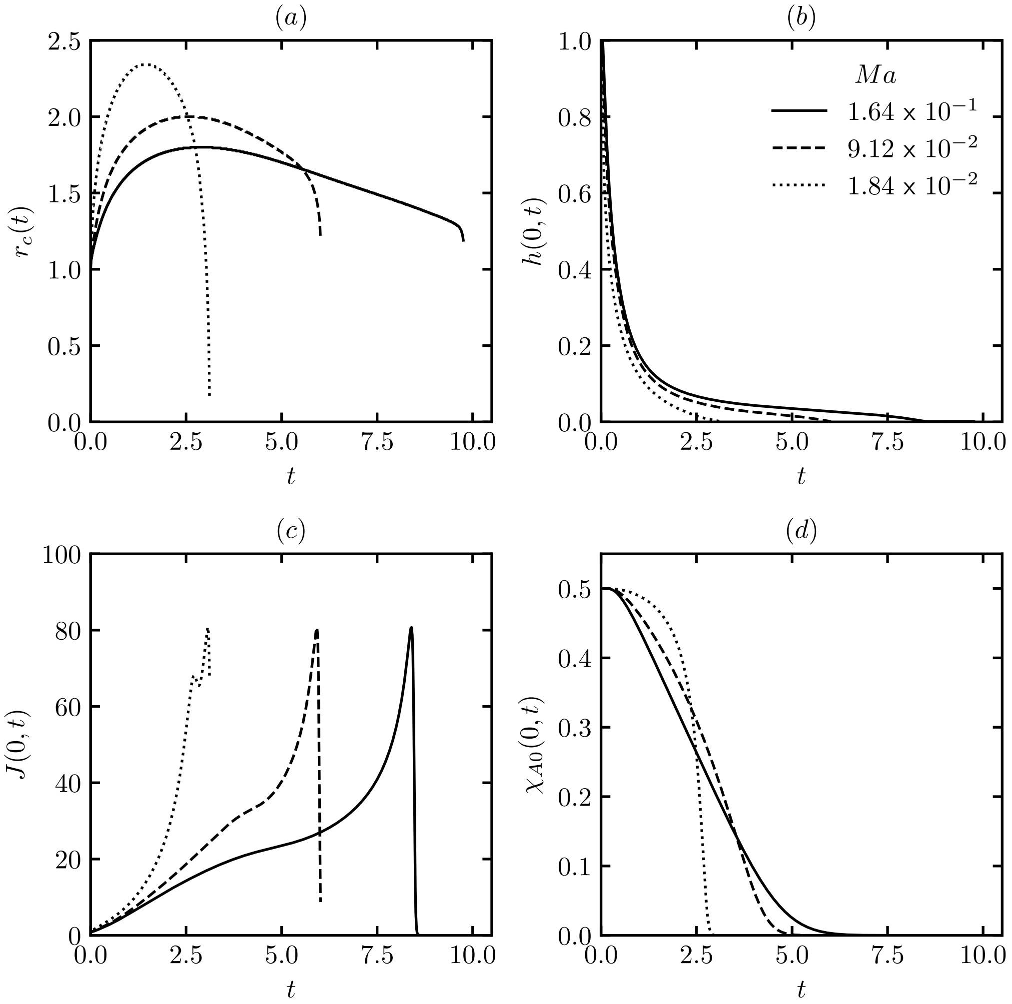

Fig. 7.13 Profiles of (a) contact line position, (b) apex height, (c) apex mass flux, and (d) apex mass fraction throughout the lifetime of a $\chi_{A0,i} = 0.50$ drop with varying Marangoni numbers, Ma. Unless otherwise stated, dimensionless parameters are those given in Tab. 7.2.

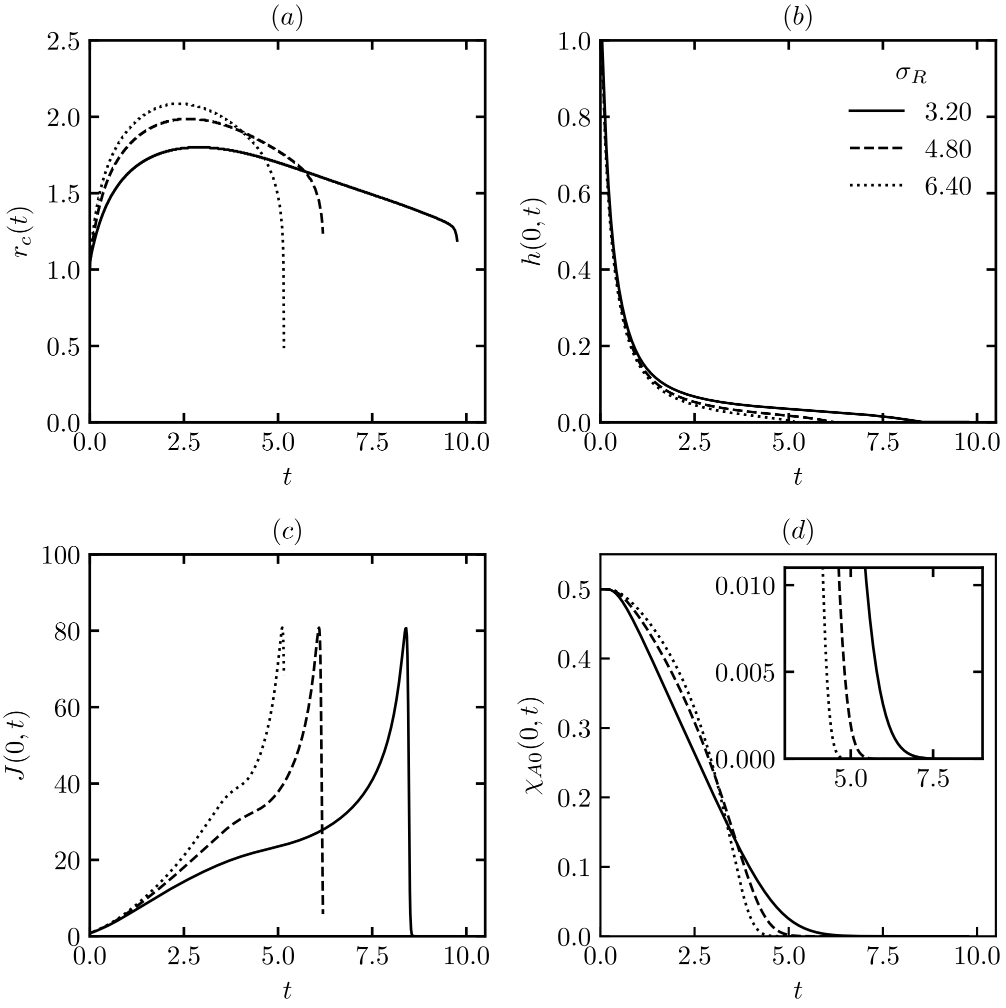

Fig. 7.14 Profiles of (a) contact line position, (b) apex height, (c) apex mass flux, and (d) apex mass fraction throughout the lifetime of a $\chi_{A0,i} = 0.50$ drop with varying surface tension ratio, σ_R. Unless otherwise stated, dimensionless parameters are those given in Tab. 7.2.

7.5.4 Péclet number

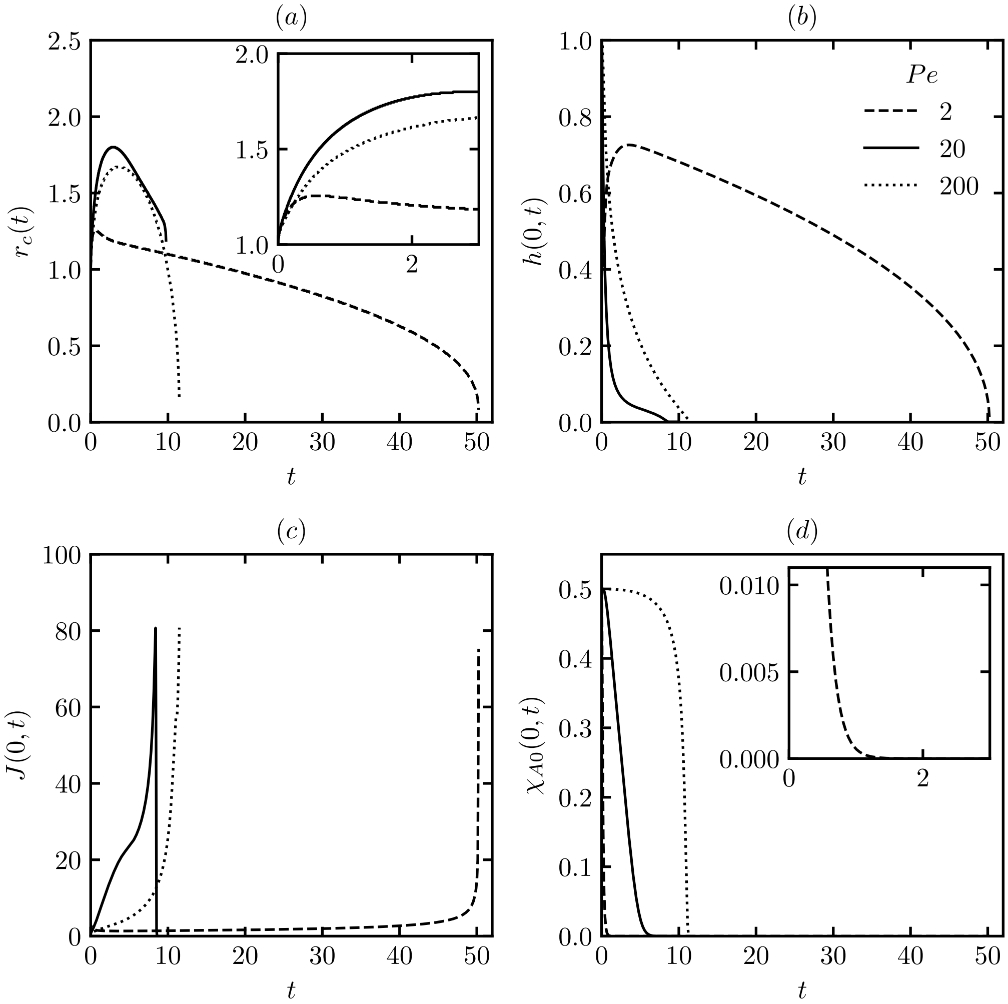

Fig. 7.15 Profiles of (a) contact line position, (b) apex height, (c) apex mass flux, and (d) apex mass fraction throughout the lifetime of a $\chi_{A0,i} = 0.50$ drop with varying Pélet numbers Pe. Unless otherwise stated, dimensionless parameters are those given in Tab. 7.2.

The mass diffusion is controlled by the Péclet number, with smaller values signifying more rapid diffusion of the MVC, ethanol in our case. By default, the base value in Tab. 7.2 is set to $Pe = 20$. In Fig. 7.15 we increase and decrease this by an order of magnitude. Decreasing to $Pe = 2$ causes ethanol to rapidly diffuse out of the drop, being depleted by $t = 2$—see Fig. 7.15(d). Contact line spreading is abruptly halted as solutal Marangoni stresses cease and the drop begins to retract. With limited spreading, the drop remains relatively thick with a spherical cap profile. Only water is present after $t = 2$ and so evaporation is predictably slow compared to superspreading cases. Increasing Pe to 200 means ethanol is retained in the drop for longer times. In this

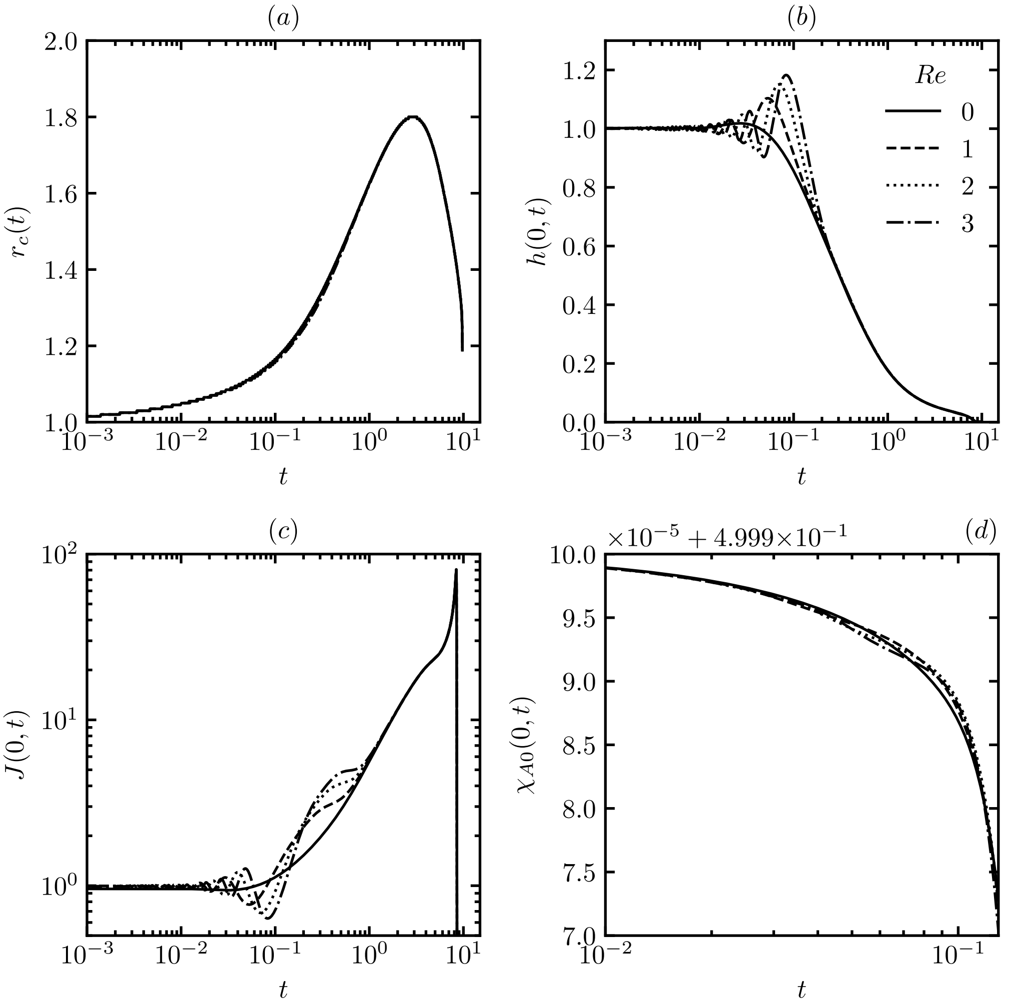

Fig. 7.16 Profiles of (a) contact line position, (b) apex height, (c) apex mass flux, and (d) apex mass fraction throughout the lifetime of a $\chi_{A0,i} = 0.50$ drop with varying Reynolds numbers, *Re*. Unless otherwise stated, dimensionless parameters are those given in Tab. 7.2.

case it has the effect of maintaining the surface tension gradient from apex to contact line as well as the volatility of the mixture. We can see from Fig. 7.15(d) that ethanol is present in large concentrations at the apex until dry-out, suggesting it is also present in large concentration throughout the rest of the drop. It is the retention of ethanol that results in higher evaporation rates over the interface and ultimately leads to faster evaporation and a shorter lifetime than the base case of $Pe = 20$.

7.5.5 Reynolds number

Finally, we consider the effect of hydrodynamic flow by introducing inertia via the Reynolds number. As we have already shown in Fig. 7.1, a non-zero *Re* introduces oscillations in the interface profile near the apex at early times. The effect is found to be more dramatic in the binary ethanol-water drop. In Fig. 7.16, the Reynolds number is increased from $Re = 0$ to $Re = 3$. Fig. 7.16(a) indicates that this has little effect on the position of the contact line, however, the stronger hydrodynamic flow increases both the amplitude and frequency of the apex interface oscillations seen in Fig. 7.16(b). Closer inspection of the evaporative flux and mass fraction in Fig. 7.16(c) and (d) respectively reveal similar oscillations in these fields, also increasing in amplitude and frequency with Re.

7.6. Conclusions

We have developed a one-sided model under the lubrication approximation to study the spreading and subsequent evaporation of volatile binary drops consisting of an ethanol-water type mixture deposited on a heated substrate. The contact line was allowed to move freely with the drops assumed to be very thin such that their radius is much larger than their height.

We validated our model against a similar model used to study pure single component drops before examining the effect of increasing initial ethanol mass fraction in a binary ethanol-water drop. We showed that increasing the strength of solutal Marangoni stress gives rise to superspreading. We demonstrated the delicate interplay between solutal effects driving the drop outwards and the competing thermal Marangoni stress encouraging the contact line to contract inward. If the concentration induced surface tension gradient is large enough, we showed spreading can be so fast that a ridge rich in the LVC (water) can form at the contact line with the drop centre subsequently drying out before the ridge.

We also investigated the effects of other important parameters significantly affecting the behaviour. These included the evaporation rate (via E), thermal Marangoni stress (via Ma), solutal Marangoni stress (via σ_R), mass diffusion (via Pe), and inertial effects (via Re).

We now use this numerical solution, frozen at an instantaneous time, as the base state around which to perform our stability analysis. Discussion is continued in Chapter 8.

8. Quasi-steady-state linear stability analysis

8.1. Explanation and derivation of the stability equations

We examine the stability of the flow by introducing infinitesimally small disturbances to the flow and conducting a quasi-steady state linear stability analysis. The evolution of the base state is time dependant so we freeze the transient solution examined in Chapter 7 at a discrete time instant and use this as the base state around which to perform the stability analysis. We assume the quasi-steady state approximation, meaning the growth rate of the base state is assumed to be much slower than those of the disturbances introduced. At the chosen frozen time, we compute the eigenvalues of the system for various values of the wavenumber, k. Note that we are interested in azimuthal disturbances in the θ-direction, so contrary to the base state, we re-introduce θ-based expressions into our stability equations.

The process begins by perturbing the frozen base state solution and hence we write all variables in the form of the base state solution plus a disturbance,

$$a(r,\theta,z,t) = a_o(r,z) + \zeta a_1(r,z)e^{ik\theta+\omega t} \tag{8.1}$$

The generic variable, a, is split where the first term, a_o, represents the instantaneous base state and the second, a_1, a perturbation. ζ is an infinitesimally small number, indicating that the magnitude of the perturbation is small compared to the instantaneous base state. Given we are considering the temporal stability of the system here, k is the real wavenumber in the azimuthal direction and $\omega = \omega_R + i\omega_I$ denotes the complex growth rate with temporal growth, ω_R, at frequency, ω_I.

Since the base state solution if fixed, the derivative in time is equal to zero and since the magnitude of the perturbation, ζ, is small, higher order terms in the linear expansion (ζ^2 and above) are regarded as infinitesimally small and hence ignored. By then substituting eq. (8.1) into the governing equations for each variable, we obtain the linear stability equations. Simplifications to these are made using the following expressions for the rate of change of a with time, t, and the azimuthal direction, θ,

$$\frac{\partial a}{\partial t} = \omega\zeta a_1 e^{ik\theta+\omega t} \tag{8.2}$$

$$\frac{\partial a}{\partial \theta} = ik\zeta a_1 e^{ik\theta+\omega t} \tag{8.3}$$

Applying these to each governing equation, we arrive at an eigenvalue problem of generic form:

$$\mathbf{J}\mathbf{v} = \omega\mathbf{M}\mathbf{v} \tag{8.4}$$

Where $\mathbf{J}$ is the Jacobian matrix, $\mathbf{M}$ is the mass matrix, ω are the eigenvalues and $\mathbf{v}$ the corresponding eigenvectors. The stability of the flow and its temporal growth rate is determined by the real part of the eigenvalues, ω_R, while the imaginary part, ω_I, determines the frequency. When all the eigenvalues have a negative real part, the corresponding eigenmodes will decay. However, if at least one eigenvalue has a positive real part, the corresponding eigenmode can be defined as linearly unstable. Let us also define k_d as the wavenumber associated with the most unstable mode.

To derive the stability equations, the base state governing equations given by eqs. (6.47), (6.49), (6.50), (6.73) to (6.76) and (6.78) are expanded according to eq. (8.1) before removing the base state and higher order terms. By then performing a Galerkin expansion, as described in Section 6.8, the stability equations are derived as follows,

$$\int_0^h \left[EJ_1\phi_i + \frac{f_1}{r}\phi_i + \frac{ik}{r}g_1\phi_i - f_1\frac{\partial \phi_i}{\partial r}\right] r\,dr = \int_0^h -(\omega h_1\phi_i)\, r\,dr \tag{8.5}$$

$$\int \left[MC_1\phi_i + \left(\frac{\partial h}{\partial r}\right)_1 \frac{\partial \phi_i}{\partial r} + \frac{k^2}{r^2}h_1\phi_i\right] r\,dr = 0 \tag{8.6}$$

$$\begin{aligned}\int \Bigg[\varepsilon Re\Bigg(&- \left(\int_0^h u^2\,dz\right)_1 \frac{\partial \phi_i}{\partial r} + \frac{ik}{r}\left(\int_0^h uv\,dz\right)_1 \phi_i - \frac{1}{r}\left(\int_0^h v^2\,dz\right)_1 \phi_i \\ &+E\Big(u|_h J_1 + (u|_h)_1 J\Big)\phi_i\Bigg) + \left(h\left(\frac{\partial p}{\partial r}\right)_1 + h_1\frac{\partial p}{\partial r}\right)\phi_i \\ &-\mu\left(\left.\frac{\partial u}{\partial z}\right|_0^h\right)_1 \phi_i\Bigg] r\,dr = \int_0^h -\big(\varepsilon Re\omega f_1\phi_i\big) r\,dr\end{aligned} \tag{8.7}$$

$$\begin{aligned}\int \Bigg[\varepsilon RePrc_p\Bigg(&\left(-\int_0^h uT\,dz\right)_1 \frac{\partial \phi_i}{\partial r} + \frac{ik}{r}\left(\int_0^h vT\,dz\right)_1 \phi_i \\ &+E\big(T|_h J_1 + (T|_h)_1 J\big)\phi_i\Bigg) - k\left(\left.\frac{\partial T}{\partial z}\right|_0^h\right)_1 \phi_i\Bigg] r\,dr \\ &= \int_0^h -\big(\varepsilon RePrc_p\omega\Theta_1\phi_i\big)\, r\,dr\end{aligned} \tag{8.8}$$

$$\int \Big[K(J_A)_1\phi_i - \delta\Big(\chi_{A0}p_1 + (\chi_{A0})_1 p\Big)\phi_i - \Big(\chi_{A0}(T|_h)_1 + (\chi_{A0})_1 T|_h\Big)\phi_i\Big]\, r\,dr = 0 \tag{8.9}$$

$$\begin{aligned}\int \Big[K(J_B)_1\phi_i - \alpha M_R^{3/2}\Big(&\delta p_1\phi_i + \Lambda(T|_h)_1\phi_i - \delta\Big(\chi_{A0}p_1 + (\chi_{A0})_1 p\Big)\phi_i \\ &-\Lambda\Big(\chi_{A0}(T|_h)_1 + (\chi_{A0})_1 T|_h\Big)\phi_i\Big)\Big]\, r\,dr = 0\end{aligned} \tag{8.10}$$

$$\begin{aligned}\int \Bigg[\bigg(\frac{\partial\chi_{A0}}{\partial r}f_1 + \left(\frac{\partial\chi_{A0}}{\partial r}\right)_1 f\bigg)\frac{\phi_i}{h} + \frac{\partial\chi_{A0}}{\partial r}f\frac{\phi_i}{h_1} + \frac{ik}{r}(\chi_{A0})_1 g\frac{\phi_i}{h} \\ - \frac{(J_A)_1 - (J(\chi_{A0})_1 + J_1\chi_{A0})}{Pe'h\left(\dfrac{2h_1J}{3} + \dfrac{hJ_1}{3} + \dfrac{h_1}{Pe'Eh}\right)}\phi_i\Bigg]\, r\,dr \\ = \int_0^h -\big(\omega(\chi_{A0})_1\phi_i\big)\, r\,dr\end{aligned} \tag{8.11}$$

$$\begin{aligned}\int \Bigg[\varepsilon Re\Bigg(-\left(\int_0^h uv\,dz\right)_1 \frac{\partial\phi_i}{\partial r} + \frac{ik}{r}\left(\int_0^h v^2 dz\right)_1\phi_i + \frac{2}{r}\left(\int_0^h uvdz\right)_1\phi_i \\ + E\big(v|_h J_1 + (v|_h)_1 J\big)\phi_i\Bigg) + \frac{ik}{r}hp_1\phi_i - \mu\left(\frac{\partial v}{\partial z}\bigg|_0^h\right)_1\phi_i\Bigg]\, r\,dr + P_1 \\ = \int_0^h -\big(\varepsilon Re\omega g_1\phi_i\big)\, r\,dr\end{aligned} \tag{8.12}$$

Where ϕ_i is the test function, a finite series of which is used to approximate differential equations on FEM. Additionally, the perturbed penalty function to be added to eq. (8.12) takes the form:

$$P_1 = \frac{\mathcal{M}}{h_\infty}\left(1 + \tanh\left[\mathcal{B}\left(1 - \frac{h}{h_\infty}\right)\right]\right)\left(\mathcal{B}h_1\chi_{A0}\left(\tanh\left[\mathcal{B}\left(1 - \frac{h}{h_\infty}\right)\right] - 1\right) + h_\infty(\chi_{A0})_1\right) \tag{8.13}$$

The stability equations above give the eigenvalue problem and are solved in the same Fortran90 program used to resolve the transient base state. When solving the base state, a discrete time step is chosen at which to halt iterative time-stepping, causing the solution to become frozen in time. The frozen solution is then taken as the constant base state value to which the perturbation is applied—generic variable a_o in eq. (8.1). The stability equations are then solved for a discrete set of perturbing wavenumbers in the azimuthal direction (k) using the Newton-Raphson method. The values of k to be solved for are specified in ascending order in the initial conditions. Solution yields a series of eigenvalues (ω) and corresponding eigenvectors ($\mathbf{v}$) for each wavenumber, giving the temporal growth rates and frequencies, hence revealing the most dangerous and unstable modes. The eigenvalue problem is first solved for the smallest value of k, before subsequently progressing in ascending order to the largest k. The program terminates once the eigenvalues and corresponding eigenvectors are obtained for the largest and final wavenumber.

Tab. 8.1 Dimensionless parameters used for the stability analysis comparison of our model with Karapetsas et al. [203].

ε	0.20	δ	1×10^{-5}	k_R	1.00
Re	0.00	$\mathscr{A}$	1×10^{-4}	μ_R	1.00
Pr	1.00	Pe	100	$c_{p,R}$	1.00
Ma	1×10^{-2}	σ_R	1.00	M_R	1.00
E	1×10^{-4}	γ_R	1.00	Λ	1.00
K	1×10^{-3}	α	1.00	$\chi_{A0,i}$	0.50

We now go on to validate these newly derived stability equations before examining the stability of a binary system.

8.2. Validation

For validation purposes, we return to the single component model used by Karapetsas et al. [203]. Similar to the comparison presented in Section 7.1, we set all property rations equal to 1, achieving again a pseudo-single component mixture with equal initial concentrations of each component. The values of all dimensionless numbers and property ratios are reprinted in Tab. 8.1. Since our interest is in instabilities caused by solutal Marangoni stress, we keep the Reynolds number at zero to minimise instabilities sustained by inertia.

For this analysis we begin by freezing the time-stepped base-state solution at the early time of $t = 0.1$ and perform a stability analysis using the equations above. The dispersion curve comparing the results from our model against Karapetsas et al. [203] is shown in Fig. 8.1. This plots the real part of the most unstable eigenvalue, ω_R, at each wavenumber, $k = 0$–10. A reasonably good agreement is achieved between the two models, with only a small variation in ω_R at each value of k considered. Resultant examination of the eigenvectors will reveal the reason for not achieving exact agreement. The value of ω_R at $k = 0$ in both cases is just above zero. This corresponds to the transient process of evaporation and as we expect, this is only weakly positive, confirming our quasi-steady state assumption to be valid. If ω_R at $k = 0$ was very large, for example, it would suggest that the rate of evaporation is faster than the growth rate of any disturbances.

Beyond $k = 0$, the eigenvalues decay, suggesting that at $t = 0.1$, the pseudo-single component drop is stable to our perturbations. Although with slightly different dimensionless properties, the pseudo-single component drop is analogous to a pure water drop. Considering our experimental observations of pure water drops in Chapter 9, as well as those reported by other researchers [70, 154], we note that this single component

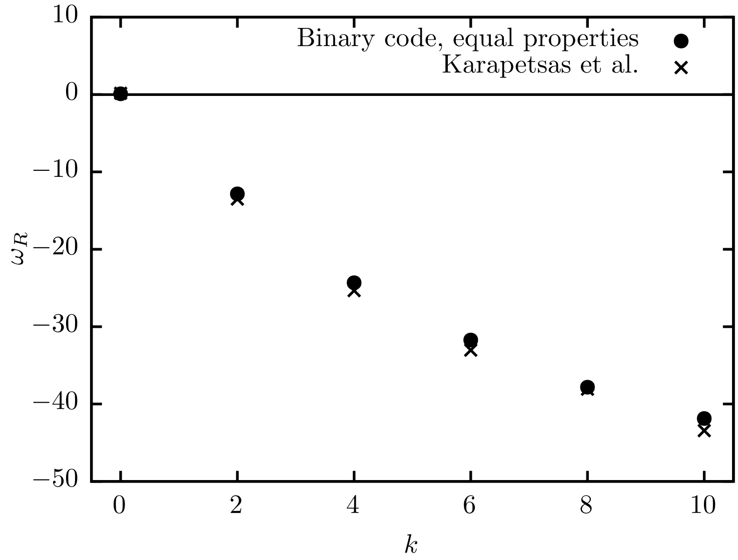

Fig. 8.1 Dispersion curves for the pseudo-single component mixture and the model of Karapetsas et al. [203] with the base state frozen at $t = 0.1$. All dimensionless properties are given in Tab. 8.1.

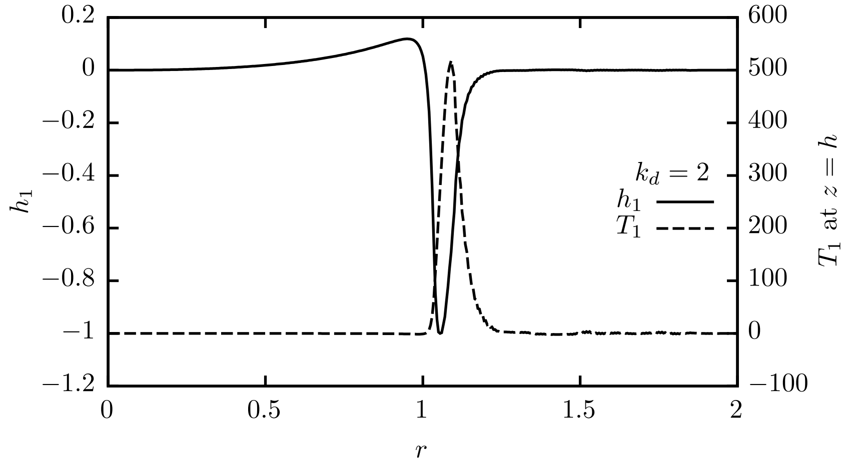

Fig. 8.2 Eigenvectors in h_1 and T_1 associated with the most unstable eigenmode, $k_d = 2$, for Karapetsas et al. [203].

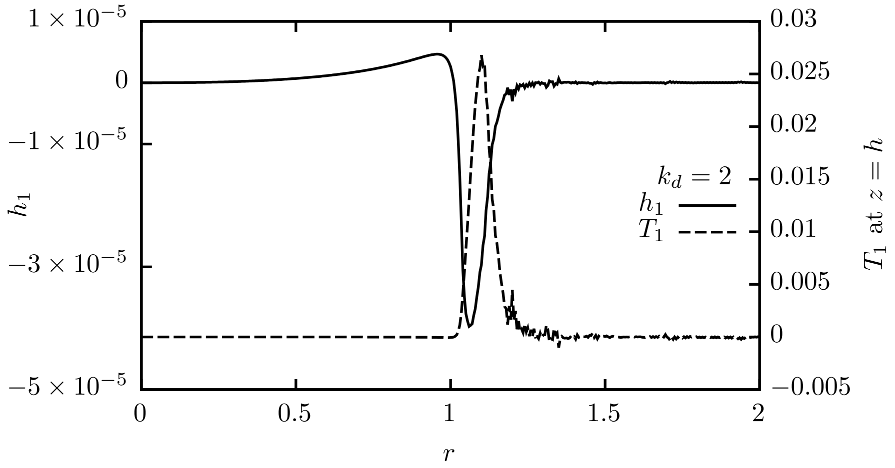

Fig. 8.3 Eigenvectors in h_1 and T_1 associated with the most unstable eigenmode, $k_d = 2$ for the binary code with equal component properties given in Tab. 8.1.

configuration with weak evaporation is stable.

The corresponding eigenvectors in interface height and temperature, h_1 and T_1, associated with the most unstable eigenmode, $k_d = 2$, are given in Fig. 8.2 for Karapetsas et al. [203] and in Fig. 8.3 for our pseudo-single binary model. Both Figs. 8.2 and 8.3 show that each eigenvector deviates from zero in the vicinity of the contact line, suggesting that if ω_R was positive, the instability would grow from here. Comparing Figs. 8.2 and 8.3 more closely, however, there are measurable differences in magnitude between the two, our model yielding both eigenvectors $O(4)$ smaller then Karapetsas et al. [203].

Additionally, in the results from our model shown in Fig. 8.3, there is a larger amount of noise in both eigenvectors towards the RHS of the contact line. This corresponds to the beginning of the precursor film region. Since this noise is not present in the model of Karapetsas et al. [203], we believe its origin results from our application of the penalty function to the precursor layer. Another important distinction we noticed is that the penalty function also adds to the number of spurious eigenvalues detected at each wavenumber. These were identified by the significant amount of noise present in the eigenvectors over the whole precursor region. These spurious eigenvalues are not detected using the model of Karapetsas et al. [203] under the same conditions and neither is any noise along the precursor film.

Upon applying ethanol-water properties such as those given in Tab. 7.2, the number of spurious eigenvalues caused by noise in the precursor film increased dramatically. These effects become so prominent the quasi-steady assumption can become violated and the ensuing stability analysis is rendered invalid. It is clear from our transient results and experimental investigation in Chapter 9 that increasing solutal Marangoni

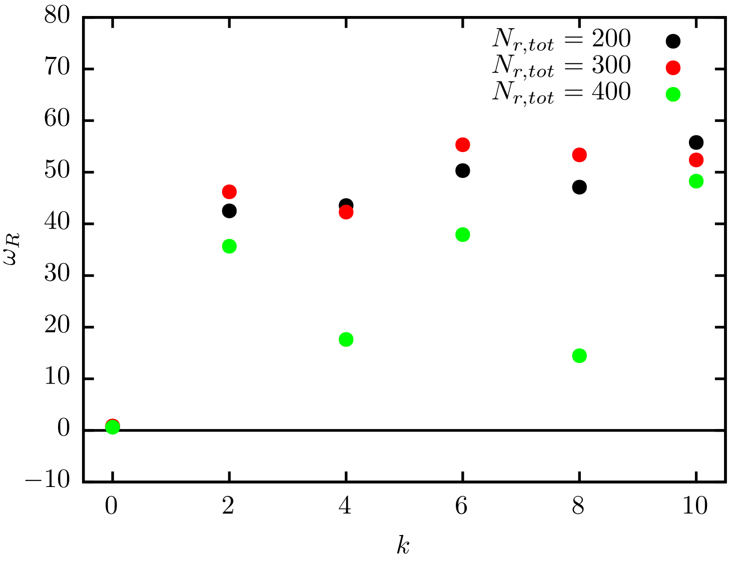

Fig. 8.4 Dispersion curves for mesh refinements $N_{r,tot} = 200$,300 and 400 when $\sigma_R = 1.10$ and $p_R = 0.90$ with the remaining dimensionless properties are given in Tab. 8.1. The base state frozen at $t = 0.1$.

stresses drives behaviour not seen in pure single component drops (e.g, the formation of a contact line ridge in 1D and fingers in 3D). We therefore move forward by retaining the dimensionless numbers of the pseudo-single component mixture given in Tab. 8.1 with the exception of the surface tension ratio and the relative volatility, which we set as $\alpha = 1.10$ and $\sigma_R = 0.90$. By doing this we are able to stimulate some uneven evaporation between components and introduce solutal Marangoni stresses into our stability analysis while keeping noise from the penalty function under control.

8.3. Binary droplet stability

As described above, we now assess the stability of a binary component drop with the dimensionless properties given in Tab. 8.1 with the exception of $\sigma_R = 1.10$ and $\alpha = 0.90$ to introduce some solutal Marangoni stress. Whilst noise in the precursor layer is minimised by adopting these modest property ratios, it is still present and causes difficulties in our analysis. As a method of verification, ensuring we are reporting non-spurious eigenvalues, we consider three mesh densities, the original being $N_{r,tot} = 200$, the second refined by a factor of 1.5 giving, $N_{r,tot} = 300$, and the third refined by a factor of 2 resulting in $N_{r,tot} = 400$.

The dispersion curves for $k = 0$–10 at all three mesh refinements are shown in Fig. 8.4. Similar to the pseudo-single component case, ω_R at $k = 0$ is weakly positive indicating that evaporation rate is sufficiently slow compared to growth rate of the distur-

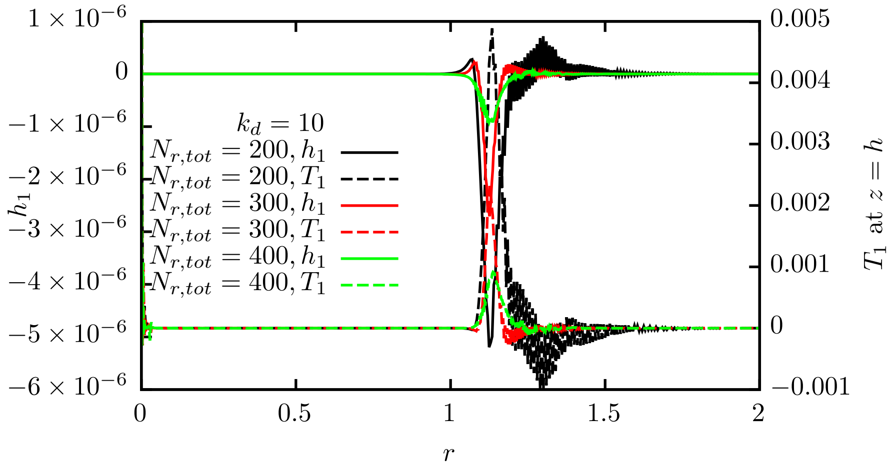

Fig. 8.5 Eigenvectors in h_1 and T_1 associated with the most unstable eigenmode, $k_d = 10$ for $\sigma_R = 1.10$, $p_R = 0.90$, $\chi_{A0,i} = 0.50$ at all three mesh refinements, $N_{r,tot} = 200$ (black), $N_{r,tot} = 300$ (red) and $N_{r,tot} = 400$ (green). All other dimensionless properties are given in equal prop parameters stability.

bances for quasi-steady state to be assumed. With increasing wavenumber, however, the eigenvalues become positive suggesting that the drop is now linearly unstable at these wavenumbers. In general, the magnitude of ω_R increases similarly to k with the most unstable eigenmode occurring at $k = 10$ for both $N_{r,tot} = 200$ and 400 and at $k = 6$ for $N_{r,tot} = 300$.

There is clear variation in predicted values of ω_R between mesh refinements. We again turn to the eigenvectors to explain this. Fig. 8.5 shows the eigenvectors associated with the most unstable eigenvalue at $k = 10$ for $N_{r,tot} = 200$ (black lines), $N_{r,tot} = 300$ (red lines), and $N_{r,tot} = 400$ (green lines). Large amounts of noise are visible in both the eigenvectors of h_1 and T_1 at $N_{r,tot} = 200$ in the precursor region. Refining the mesh to $N_{r,tot} = 300$ and 400 is effective in progressively reducing the noise around the precursor region, with increased refinement also reducing the magnitude of each eigenvector around the contact line (indicating the location of the disturbance). Ultimately, the changing shape of the eigenvector is responsible of difference in the corresponding eigenvalues at each wavenumber between mesh refinements in dispersion curve SR=110 poR=090. However, ω_R at each wavenumber continues to remain positive between cases, strongly suggesting instability which is independent of mesh density.

8.4. Conclusions

Here, a first attempt on the stability analysis of an evaporating sessile drop comprising of a binary miscible mixture has been presented. Under the quasi-steady state approximation, we introduced infinitesimally small disturbances to a numerical solution frozen in time. Albeit challenging, the system demonstrates a rich interplay of thermal and solutal Marangoni phenomena coupled to species, thermal and hydrodynamic transport in the drop. Regardless, our preliminary results suggest that introducing solutal Marangoni stress does have a strong destabilising effect on the evaporating drop. This destabilising effect is also clearly visible in our numerical modelling solution presented in Chapter 7 and also through our experimental investigations into ethanol-water drops presented in Chapter 9.

Part IV

Binary droplet experiments

9. Experiments on spreading binary sessile droplets

9.1. Experimental scope and aims

The experiments conducted in this chapter aim to provide a source of validation for our one-sided spreading drop model presented in Part III. The intention is to shown that despite its simplicity and limitations, the model is capable of predicting the defining behaviours of wetting sessile drops. As an overview of the experiments, drops are deposited on a heated hydrophilic substrate that has been chemically treated to ensure that as close to complete wetting as possible is achieved. The drops spread on the smooth surface and consequently evaporate into the ambient atmosphere. Varying concentrations of ethanol-water mixtures are investigated along with several substrate temperatures. As we know, drops close to complete wetting take a flat pancake shape with a very low contact angle between the liquid and substrate. We confirmed that the drops considered here have a contact angle of below 10° since the equilibrium contact angles (however brief) in all cases were below the detection limits of DSA contact angle analysis software. As such, we record from above in an aerial view using an optical CMOS camera to capture the total lifetime from deposition to dry-out. This allows us to track the movement of the contact line as drops spread and retract under evaporation. For comparison with our simulation results we look at the trends in a few easily measured quantities. The rate of spreading is obtained along with the maximum spreading radius. Drop lifetime is also recorded, although this is not expected to quantitatively match our simulation results due to simplifications made in the one-sided model. As previously discussed, our model is not meant to account for diffusion limited evaporation, taking a kinetic approach. It is for this reason we chose to experiment on heated substrates, increasing the rate of evaporation over isothermal cases and moving it away from a diffusion dominated regime. Nevertheless, limitations of our modelling and experimental approaches mean we are often restricted to comparing trends rather than absolute measurements.

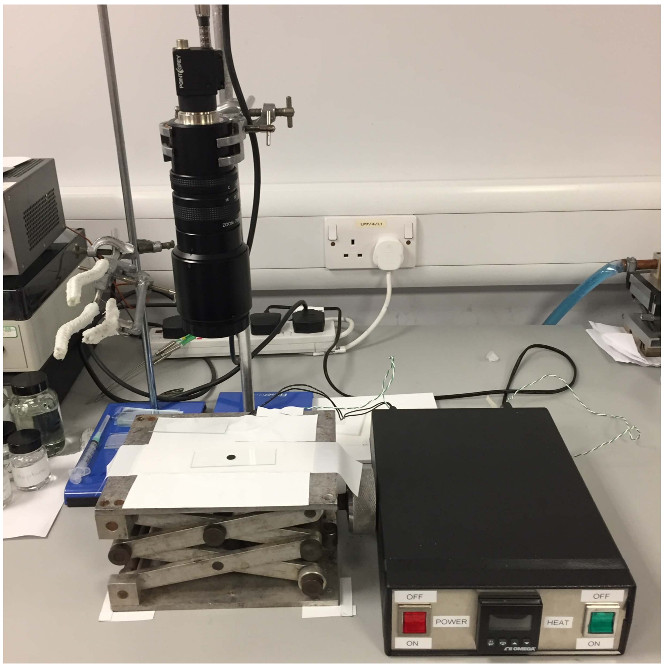

Fig. 9.1 Photograph of the experimental apparatus. The flat drop is recorded from above with a Point Grey CMOS camera. The light source, a smart phone, missing from this image is affixed via the clamp on the left. The silicon heater is fixed in place below the white tape. Heater temperature is maintained via a PID controller on the right.

9.2. Experimental apparatus and method

Fig. 9.1 provides a photograph of the experimental apparatus, and Fig. 9.2 a schematic diagram. The apparatus centres around a flexible silicone heating pad (Omega SRFR-4/5-P-230V) providing a heat flux of 0.775 $\mathrm{W\,cm^{-2}}$. This sits atop an aluminium mechanical scissor lift platform and is held in place with heavy duty white duct (Gorilla) tape. The temperature of the heater is controlled with a PID controller in a feedback loop; the controller maintains the desired set point measured by a thermocouple attached to the heating pad. The CMOS camera is held in place above the scissor lift platform using a laboratory stand and clamp with liberal amounts of duct tape securing it to the desk. The CMOS camera used is a Point Grey Research Flea3 (FL3-U3-13E4M) with a 18 mm–108 mm/2.5–16 Navigator Zoom 7000 zoom lens. The camera is connected to a PC via USB3 and is controlled through FlyCapture2 software. Optical recording is conducted at 60 fps. The drop is illuminated from the side using a smart phone touch mounted on a large 3 prong clamp as the light source. To ensure a clear image is captured by the camera, Diall PVC repairing tape, possessing a smooth white surface, is layered on top of the duct tape. Borosilicate glass microscope slides manufactured by RC Components are used for the substrate. These are simply placed on top of the tape holding down the heating pad with the friction between the two materials sufficient to prevent movement. The factory treatment of the glass results

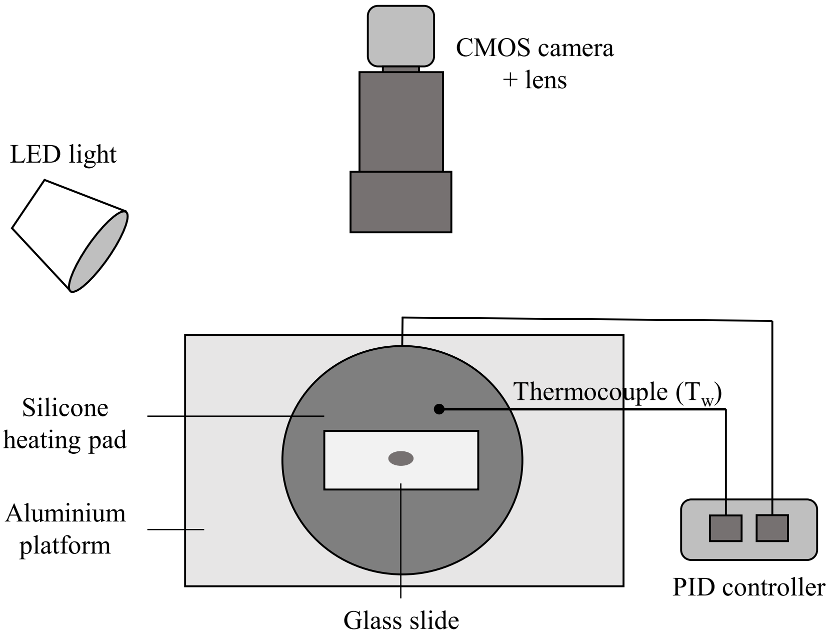

Fig. 9.2 Schematic diagram of the experimental apparatus.

in a low equilibrium contact angle for all fluids tested. High wettability was verified by treating the slides with “piranha” solution—a volatile mixture of sulfuric acid and hydrogen peroxide. Piranha solution is a strong oxidiser and so removes organic matter whilst additionally hydroxylating the surface. The drops are deposited on the substrate manually using a microliter syringe (Hamilton 701N 10 µl) with reading increments of 0.2 µl.

In the study presented here, we consider ethanol-water mixture drops of initial volume (1.0 ± 0.2) µl. Mixtures ranging from 11 wt.% to 50 wt.% initial ethanol concentration are considered at three substrate temperatures (T_w); 30 °C, 50 °C and 70 °C. Solutions are prepared in 25 mm volumes and stored in 25 mm jars. Separate syringes of volume (2.50 ± 0.05) ml were used to collect samples of each pure component for mixing. The mixing volumes of each fluid as well as the initial ethanol concentrations investigated are given in Tab. 9.1. Once the solutions are prepared, evaporation of the mixtures was kept to a minimum by covering the mouth of the jar with a plastic paraffin film (Parafilm); this allowed the seal to be retained with the lid removed. A sample was taken by piercing the film with the micro-syringe, leaving only a small hole and suppressing unwanted evaporation as much as possible. The lid was returned after obtaining each sample. For each mixture concentration deposited at each substrate temperature, a minimum of five experimental runs were conducted to ensure the results are replicable. Of these multiple runs, typically only the most representative single run is presented.

The results are processed by tracking the drops radius over time, both the initial spread-

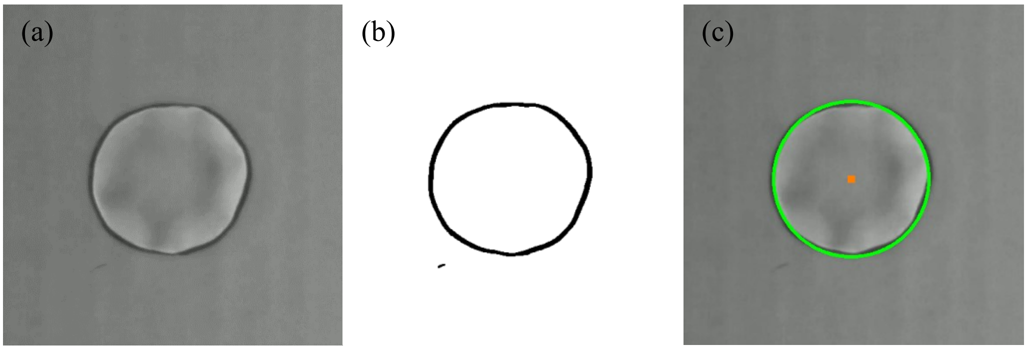

Fig. 9.3 Aerial snapshots of a 1 µl ethanol-water drop comprising 25 wt.% initial ethanol deposited on a 70 °C substrate at $t = 0.6\,\mathrm{s}$. (a) shows the original greyscale image captured by the camera, (b) shows the binary image after passing through imaging filters, and (c) shows the best-fit circle (green) to the contact line (black) along with the corresponding centre point (orange) overlaid on (a).

ing followed by contact line recession as evaporation takes over. The radius is tracked frame to frame using an in-house algorithm written in python, making use of NumPy and OpenCV repositories. The basic overview is to convert each frame to a high contrast image using in-built OpenCV image processing tools and then detect the circular shape of the drop using the OpenCV Hough Circles Transform. Image processing begins by removing noise from the greyscale images captured by the camera—an example being Fig. 9.3(a)—by passing through the GuassianBlur and medianBlur filters. After this, the sharp edges of the image corresponding to the contact line are detected using the adaptiveThreshold filter and converted to a binary black and white image using the binary threshold filter—Fig. 9.3(b). It is to this image that the Hough Circles Transform is applied which determines the best fit circle to the circular-shaped drop outline and calculates the corresponding centre point and radius, as shown in Fig. 9.3(c). To set the scale, a circular black sticker of diameter 0.8 mm is affixed to a sample glass slide. With the scale set, the expanding and contracting radius of the drop as it spreads and recedes is measured directly. A clear limitation of this method is that the drop must close to circular to obtain meaningful results. In our case, this is already a requirement since we are comparing to a 1D axis-symmetric model where the drop is perfectly circular. Contact line radius against time for each drop can then be plotted. The spreading and retraction rates are obtained by analysing the radius-time graphs in the common logarithmic domain using R statistical software [228] (available free and open source under the GNU General Public Licence). This method allows linear fits along with breakpoints to be determined in a statistically significant and consistent manner.

9.3. Errors and uncertainty

We now turn to a brief discussion to sources of error in the experiment, some more difficult to quantify than others. First, there is the error in measuring the volumes of ethanol and water when preparing the binary mixtures for storage in jars. These are given in Tab. 9.1. Second, due to the small volumes of the drops considered and the relatively large reading increments on the micro-syringe, there is a large uncertainty in the deposited drop volume—typically 20 % relative error. The uncertainly from the PID feedback loop can be assumed as ±1 K. However, with the heater and thermocouple buried beneath insulating plastic tape along with inherently low thermal conductivity of the glass substrate, it is likely that the surface the drop is deposited onto will be slightly cooler than the advertised value by the controller.

Considering imaging errors, the drops are clearly captured by the camera due to the angled light source casting a shadow around the contact line. This causes the contact line to appear thicker than in reality. In addition, the formation of a ridge at the contact line in drops with higher initial ethanol concentration causes this region to appear thicker still. Contact line instabilities also arise in ethanol rich drops, making accurate resolution even more difficult. Measuring the pixel width of the drop at its thickest point in the final images provides a reasonable estimate of this error. Perhaps the largest source of error is also the most difficult to quantify. Our radius detection method relies on the idealistic assumption that drops are always perfectly circular throughout spreading and recession. In the absence of perfectly consistent curvature around the whole circumference, the algorithm will fit a circle that best fits the largest portion of the drop circumference. Practically, this results in fluctuation of the radius measurement as the algorithm searches for the optimum curvature. Whilst this is unavoidable in our automatic detection method, under or over prediction of the drop radius remains a persistent problem. The best estimation of this uncertainty comes from the standard error of the linear fit determined by R.

To minimise this error for each run, we took several measures to maximise the chances of even spreading. These include ensuring a completely level surface, the selection of small drop volumes and the gentle deposition of the drops from the micro syringe. Another limitation worth mentioning is that, particularly for higher concentrations of ethanol, drops do not dry out in a circular shape meaning the exact point of dry out cannot be measured by our algorithm. Rather, we rely on the visual disappearance of the drop from the original video footage for this.

Tab. 9.1 Mixing volumes of ethanol and water used to prepare the mixtures and the corresponding initial volume and weight percentages of ethanol.

Ethanol (ml)	Water (ml)	initial ethanol vol.%	initial ethanol wt.%
0.00	25.00 ± 0.50	0.0	**0.0**
3.5 ± 0.10	21.50 ± 0.45	14.0 ± 0.7	$\mathbf{11.4 \pm 0.6}$
7.5 ± 0.15	17.50 ± 0.35	30.0 ± 1.2	$\mathbf{25.3 \pm 1.0}$
14.0 ± 0.30	11.00 ± 0.25	56.0 ± 3.0	$\mathbf{50.0 \pm 2.7}$

9.4. Results and discussion

9.4.1 Typical evaporation process

As previously mentioned, we consider only drops of pure water and water-ethanol mixtures consisting of 11 wt.%, 25 wt.%, and 50 wt.% initial ethanol at substrate temperatures of 30 °C, 50 °C, and 70 °C. In order to maximise the evaporation rate for comparison with our simulations, we restrict our investigations into the effect of concentration variation for a substrate at temperature $T_w = 70\,^\circ\mathrm{C}$ only, while effects of temperature variation are restricted to the most volatile binary mixture—50 wt.% initial ethanol. Higher ethanol concentrations, extending to pure ethanol are not included due to difficulties in capturing a sharp contact line using our imaging method.

After a drop is deposited carefully with the microsyringe, the typical evaporation process for all concentrations and temperatures can be split into two main stages: a rapid spreading stage followed by a slower retraction stage. These stages are to be expected with wetting drop and has been observed extensively in the literature [107]. The length of each stage depends on the drop composition and substrate temperature. Additionally, for lower volatility cases, a third stationary phase can appear between spreading and retraction whereby the drop remains at maximum radius for a time before retraction begins. Such behaviour is also expected for lower volatility liquids [134] and is observed in our modelling results for low evaporation numbers—see, for example Fig. 7.12.

Immediately after depositions, the drops spread to their maximum radii. The very initial stages are dominated by inertial spreading, similar to pure and other binary mixture drops [147, 188]. Tab. 9.3 gives the spreading coefficients, n (where $R \propto t^n$), for each linear regime and their corresponding breakpoints in time, b, to the next linear regime. In the case of pure water, the inertial spreading exponent, n_1, is 0.36 ± 0.07, rising with initial ethanol concentration. Spreading rate then decreases to a viscous regime, characterised by spreading exponents close to Tanner's law in the case of pure water and higher for binary compositions. After maximum radius is reached, drops possessing lower volatilities and those on cooler substrates remain stationary for a period of time before retraction. In the case of binary drops, retraction tends to happen in two stages; first there is a rapid retraction followed by a slower contact line recession at later times. We now go on to examine these processes in more detail for a 25 wt.% and 50 wt.% ethanol-water drop on a 70 °C substrate.

9.4.2 25 wt.% ethanol-water droplet

Fig. 9.4 presents snapshots taken with the CMOS camera over the lifetime of a 25 wt.% ethanol-water drop on a 70 °C substrate. The third column of Tab. 9.3 gives the spreading exponents and their transition points in time for this concentration. After deposition at $t = 0\,\mathrm{s}$, the drop begins to spread rapidly with $n_1 = 1.61 \pm 0.11$ up until $t = 0.87 \pm 0.14\,\mathrm{s}$, considered to be firmly within the inertial regime. Faint interface ripples appear near the contact line at $t = 0.4\,\mathrm{s}$, subsequently dying down by $t = 0.8\,\mathrm{s}$ as the spreading rate slows slightly to $n_2 = 1.15 \pm 0.45$. The lighter rim near the drop edge indicates a thicker area of liquid near the contact line, presumably formed from strong currents pulling the fluid outwards. The drop continues to spread until $t \approx 2.0\,\mathrm{s}$ while at the same time the light rim decreases in thickness. A maximum drop radius of $r = 4.47 \pm 0.12\,\mathrm{mm}$ is reached, given in Tab. 9.2. The drop then proceeds to recede in two main regimes. A period of rapid recession comes first with an exponent, $n_5 = -2.06 \pm 0.24$, terminating at $t = 3.69 \pm 0.04\,\mathrm{s}$. The second regime is slower and characterised by an exponent of $n_8 = -0.86 \pm 0.06$. Our simulations indicate that the first rapid recession is owing to the sudden reversal of surface tension gradient as ethanol becomes sufficiently depleted within the drop. The drop then continues to evaporate and recede until dry-out at $t \approx 25.0\,\mathrm{s}$.

9.4.3 50 wt.% ethanol-water droplet

Upon increasing the initial concentration of ethanol from 25 wt.% to 50 wt.%, radically different behaviour emerges. Fig. 9.5 shows camera stills taken over the drop lifetime and the corresponding spreading exponents are given in the fourth column of Tab. 9.3. It is immediately clear when comparing with the lower concentration drop in Fig. 9.4 that the initial spreading rate when $\chi_{A,i} = 0.50$ is noticeably faster. Beginning at $n_1 = 3.66 \pm 0.33$ until $t_1 = 0.24 \pm 0.01\,\mathrm{s}$ and continuing at the slightly reduced rate of $n_1 = 1.36 \pm 0.15$ until $t_1 = 0.65 \pm 0.03\,\mathrm{s}$. Spreading then proceeds at a rate of $n_3 = 0.59 \pm 0.06$ until the maximum radius of $5.35 \pm 0.30\,\mathrm{mm}$ is reached at $t_3 = 1.68 \pm 0.04\,\mathrm{s}$. From $t = 0.2\,\mathrm{s}$ in Fig. 9.5, two distinct instabilities can be seen forming in the drop.

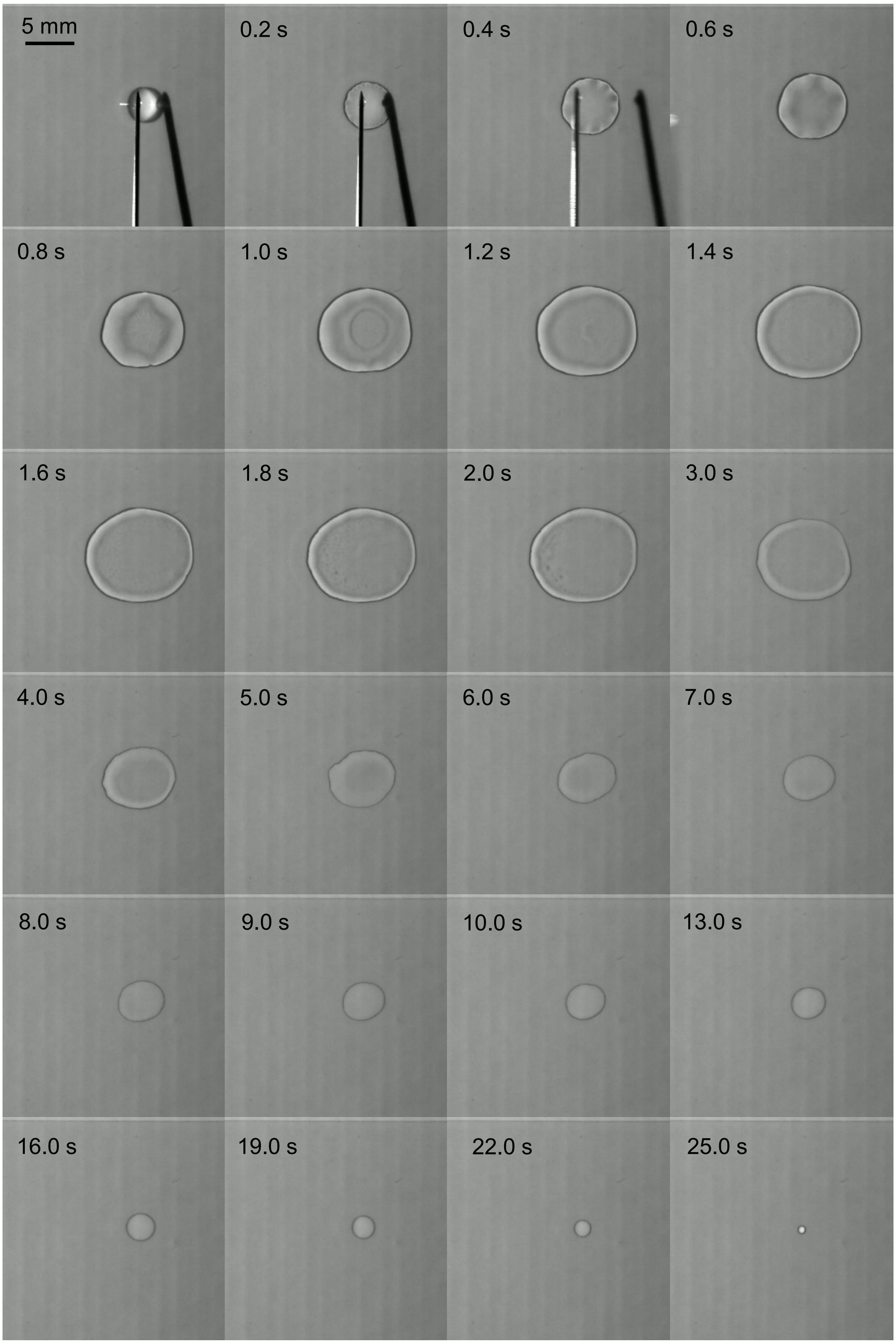

Fig. 9.4 Aerial snapshots of a 1 µl ethanol-water drop comprising 25 wt.% initial ethanol deposited on a 70 °C substrate.

The first is a contact line instability whereby the contact line breaks up into fingers that grow with time. The second instability appears to occur over the interface, equidistant between the drop centre and contact line. It takes the form of spoke-like patterns arranged radially around the drop centre.

The fingering instability at the contact line resembles the "octopi" instability observed by Gotkis et al. [172] and is similar to the drop ejection phenomena seen by Keiser et al. [177] in ethanol-water drops. Since the emergence of both instabilities only occurs at high initial ethanol concentrations, the clear indication is that they arise due to solutal Marangoni stresses. As the drop is deposited on the 70 °C substrate, ethanol, being more volatile, evaporates preferentially over water. As the drop is initially deposited as a spherical cap, evaporation will be particularly strongest at the contact line—as we have predicted with our model. With high ethanol concentration within the drop, this causes a large surface tension gradient between the apex and contact line, driving rapid spreading. It is this rapid spreading that causes the fingering contact line instability. The spoke-line patterns on the interface appear to be resulting from the strong outward flow within the drop towards the contact line.

As time proceeds from $t = 0.2\,\mathrm{s}$ to $t = 1.8\,\mathrm{s}$, Fig. 9.5 clearly shows the contact line fingers growing in volume while the number stays constant at 21–24 fingers. The fingers appearing white to the camera indicate their thickness compared to the drop interior. Our base state model seems to predict this phenomena in 1D by the formation of a thicker ridge of liquid ahead of the contact line. By $t = 2.0\,\mathrm{s}$ finger growth ceases and the radial interface patterns decay to leave a smooth interface. The drop then begins to retract, although this could not be recorded by out detection algorithm due to the contact line not being sharp enough after passing through imaging filters. This sudden retraction, resulting from the reversal of the surface tension gradient as ethanol is depleted, causes the fingering patters to also decay as the contact line is drawn inwards. At this point, the drop is likely to constitute entirely water. At around $t = 3.2\,\mathrm{s}$, the drop centre appears to dry out as it recedes and we see a third instability forming in the form of fingers appearing at this newly formed inner contact line. We are now essentially left with a ring of liquid similar to that observed by Guéna et al. [154], with our numerical model also predicting dry-out of the interior before the contact line ridge.

9.4.4 Variation in concentration

Fig. 9.6 plots the drop radii measured by our detection algorithm for $\chi_{A,i} = 0.00$, 0.11, 0.25, and 0.50 versus time for $T_w = 70\,^\circ\mathrm{C}$. This clearly illustrates the increased spreading (both rate and maximum radius) exhibited as initial ethanol concentration is in-

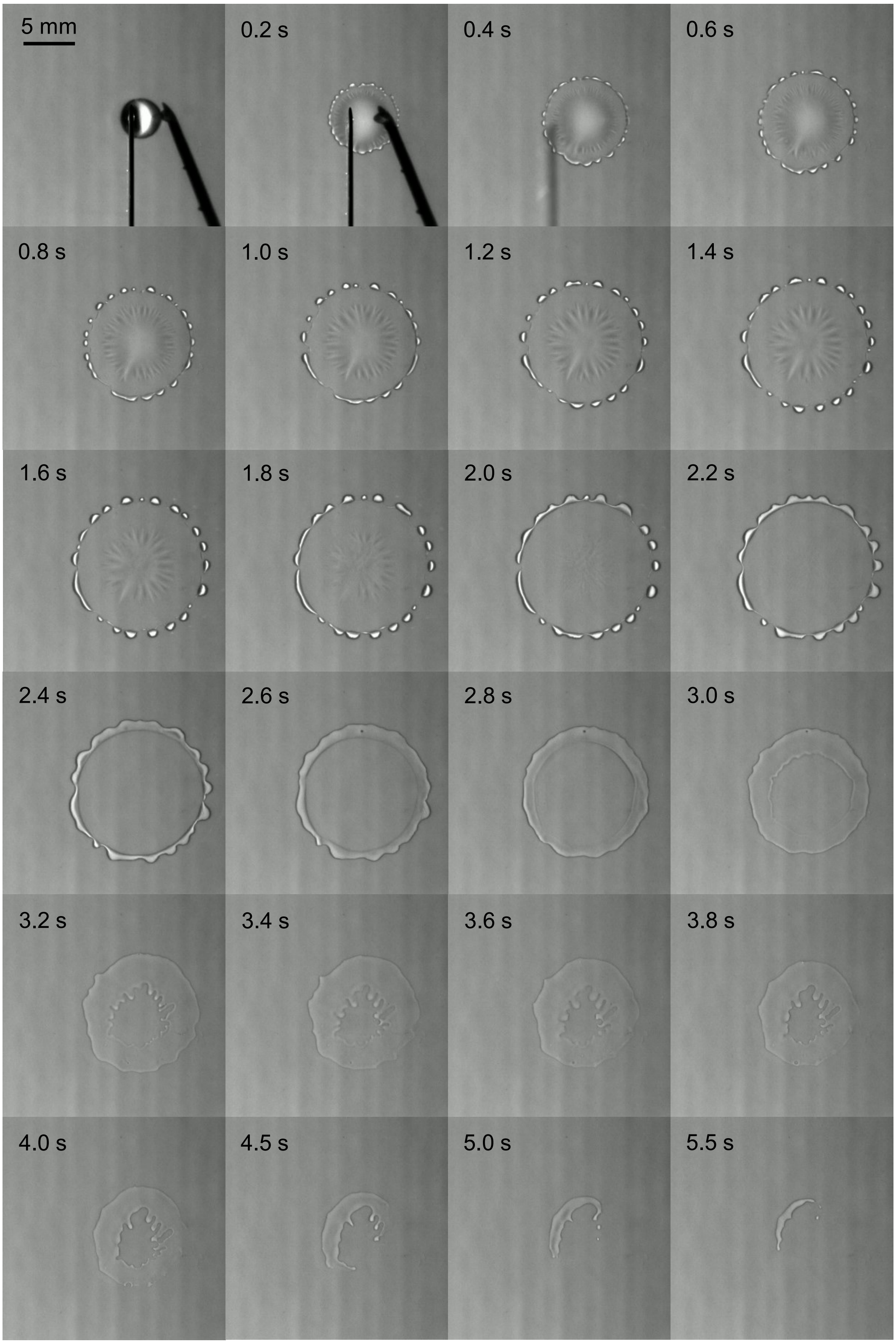

Fig. 9.5 Aerial snapshots of a 1 µl ethanol-water drop comprising 50 wt.% initial ethanol deposited on a 70 °C substrate.

Tab. 9.2 Maximum radii of drops deposited on a substrate of temperature $T_w = 70\,°\mathrm{C}$.

$\chi_{A,i}$	r_{max} (mm)
0.00	2.33 ± 0.11
0.11	3.01 ± 0.14
0.25	4.47 ± 0.12
0.50	5.35 ± 0.30

creased. As expected, drop lifetime decreases with increasing ethanol concentration, owing part to increased mixture volatility and part to a larger effective area for evaporation as spreading increases. Tab. 9.2 gives the maximum radii, r_{max}, achieved by the drops in these plots. Compared to the 1 µl pure water drop, where $r_{max} = 2.33 \pm 0.11\,\mathrm{mm}$, maximum radius is increased by 29 % for a $\chi_{A,i} = 0.11$ drop of the same volume and then by 92 % and 130 % for drops of $\chi_{A,i} = 0.25$ and $\chi_{A,i} = 0.50$ respectively. The rapid recession regimes are also seen clearly for $\chi_{A,i} = 0.11$ and $\chi_{A,i} = 0.25$, whereas recession is slow and steady for pure water.

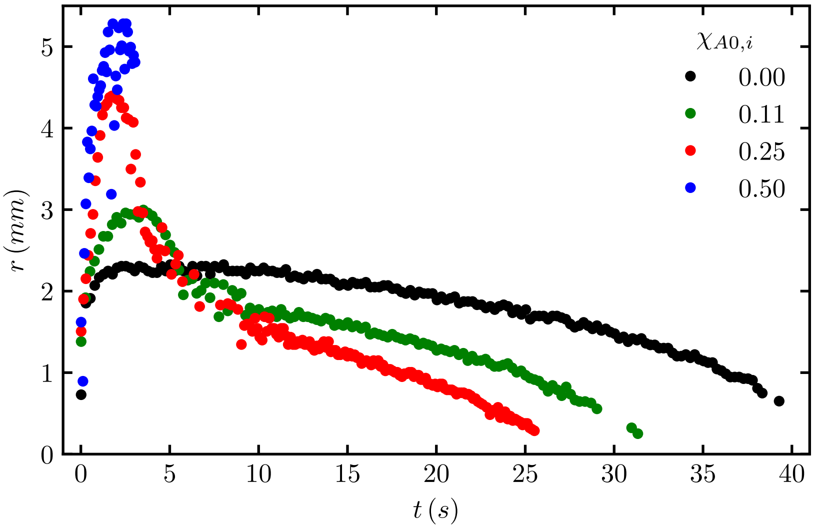

Fig. 9.6 Drop radius versus time at a constant substrate temperature of 70 °C for initial ethanol concentrations of 0.00 wt.%–0.50 wt.%.

9.4.5 Variation in temperature

We consider briefly the effects of varying the substrate temperature, T_w, restricting ourselves to only the most volatile ethanol-water mixture, $\chi_{A,i} = 0.50$. Fig. 9.7 plots radius over time for $T_w = 30\,°\mathrm{C}$, $50\,°\mathrm{C}$, and $70\,°\mathrm{C}$ with maximum radii achieved shown in Tab. 9.4. As we would expect, lower T_w results in prolonged drop lifetimes with the

Tab. 9.3 Spreading coefficients, n, and corresponding breakpoints in time, b, for increasing initial concentrations of ethanol with substrate temperature $T_w = 70\,°\mathrm{C}$.

	$\chi_{A,i} = 0.00$	$\chi_{A,i} = 0.11$	$\chi_{A,i} = 0.25$	$\chi_{A,i} = 0.50$
n_1	0.36(7)	0.74(16)	1.61(11)	3.66(33)
$b_1\,(s)$	0.65(17)	0.63(20)	0.87(14)	0.24(1)
n_2	0.23(3)	0.54(13)	1.15(45)	1.36(15)
$b_2\,(s)$	1.29(10)	1.30(17)	1.20(12)	0.65(3)
n_3	0.09(4)	0.30(11)	0.45(37)	0.59(6)
$b_3\,(s)$	2.14(14)	2.13(14)	1.63(9)	1.68(4)
n_4	0.00()	0.02(4)	−0.34(12)	−0.03(6)
$b_4\,(s)$	7.49(59)	4.87(8)	2.73(4)	
n_5	−0.23(2)	−0.71(27)	−2.06(24)	
$b_5\,(s)$	21.87(3)	5.87(4)	3.69(4)	
n_6	−0.78(4)	−2.31(32)	0.07(30)	
$b_6\,(s)$	33.16(1)	5.77(3)	4.47(6)	
n_7	−2.74(16)	−0.37(3)	−1.34(14)	
$b_7\,(s)$		14.87(9)	6.81(19)	
n_8		−0.93(9)	−0.86(6)	
$b_8\,(s)$		20.33(5)	14.42(7)	
n_9		−2.14(16)	−1.98(14)	

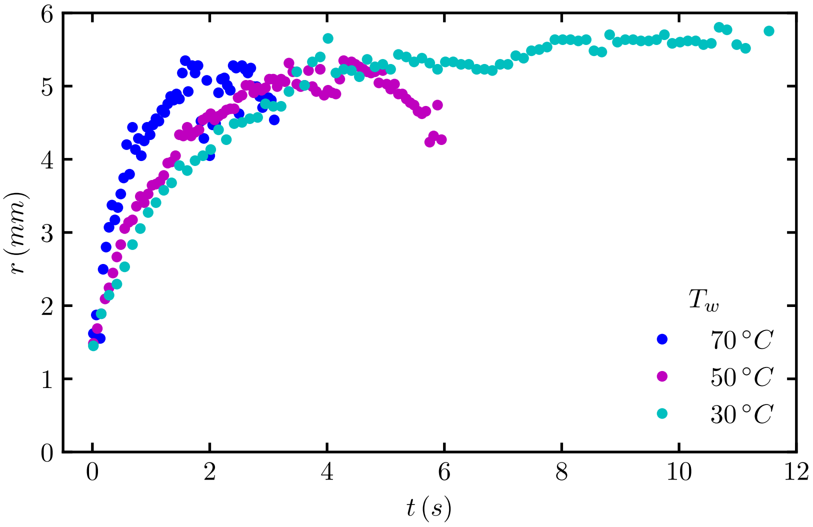

Fig. 9.7 Drop radii versus time at constant initial ethanol concentration of 50 wt.% for substrate temperatures of 30, 50, and 70 °C.

Tab. 9.4 Maximum radii of $\chi_{A,i} = 0.50$ ethanol-water drops deposited on each substrate temperature, T_w.

T_w (°C)	r_{max} (mm)
30	5.85 ± 0.41
50	5.40 ± 0.24
70	5.35 ± 0.30

mixture volatility decreasing with temperature. Lower temperature drops are therefore able to spread for longer times, achieving a larger r_{max}. It is also clear from Fig. 9.7 that although drops spread further overall, the rate of spreading is reduced as the substrate temperature is lowered. The spreading exponents for each regime are given in Tab. 9.5. As substrate temperature is increased, the spreading exponent for each regime increases while the corresponding break point in time signifying transition to the next regime occurs earlier. This is likely due to the more rapid development of a concentration gradient when the drop touches the substrate as ethanol evaporates more vigorously at the higher temperatures. Mamalis et al. [188] also saw an increase in the spreading exponents with substrate temperature in their experiments with self-rewetting drops. Additionally, when the temperature is increased, the number of fingers produced at the contact line also increases with approximately 18 seen at $T_w = 30\,°C$, 20 at $T_w = 50\,°C$ and 21–24 see at $T_w = 70\,°C$. The length of the fingers also increases with substrate temperature as higher evaporation rate drives the instability. A similar trend was seen by Sefiane et al. [167], where the wavenumber of interfacial HTWs increased with increasing substrate temperature for FC-72 drops.

Tab. 9.5 Spreading coefficients, n, and corresponding breakpoints in time, b, for initial ethanol concentration of $\chi_{A,i} = 0.50$ and increasing substrate temperatures 30 °C, 50 °C, 70 °C.

	$T_w = 30\,°\mathrm{C}$	$T_w = 50\,°\mathrm{C}$	$T_w = 70\,°\mathrm{C}$
n_1	1.29(10)	2.01(15)	3.66(33)
$b_1\,(s)$	0.96(1)	0.50(1)	0.24(1)
n_2	0.64(6)	0.82(6)	1.36(15)
$b_2\,(s)$	2.15(4)	1.53(3)	0.65(3)
n_3	0.39(4)	0.41(4)	0.59(6)
$b_3\,(s)$	4.51(14)	3.06(3)	1.68(4)
n_4	−0.01(1)	−0.13(5)	−0.03(6)

9.5. Comparison to modelling

Given the nature of our one-sided model presented in Part III, we do not attempt a direct comparison to our experimental results. The lifetimes of experimental drops are several orders of magnitude longer than our one-sided model predicts once a re-dimensionalisation is performed. This is not unexpected considering our experiments are performed under atmospheric air where even at high substrate temperatures diffusion of the vapour will play some role, although we could mitigate this somewhat by controlling the Knundsen number (K) in our modelling. There are also additional effects of evaporative cooling and poor conductivity from the glass substrate in our experiments not accounted for in the model. Regardless, in their respective time frames, similar spreading rates (the same order of magnitude or closer) are predicted between the model and experiments, indicating that our one-sided model is sufficient to capture the main flow phenomena. The formation of a contact line ridge by our model at $\chi_{A0} = 0.50$ is very likely indicative of the beginning of the "octopi" patterns observed in the experiments as the same initial ethanol concentration. What's more, the results from our preliminary stability analysis in Chapter 8 indicate that the addition of a second component, thereby introducing solutal Marangoni stress, is strongly destabilising on the drop. This unstable nature is clear from our experimental results.

9.6. Conclusions

We have conducted an experimental investigation into the spreading and evaporation behaviour of sessile drops comprising various concentrations of ethanol-water mixtures. The drops were deposited on heated borosilicate glass substrates with a hydrophilic coating to encourage spreading. An apparatus was designed to capture the drops from above in an aerial viewpoint and a detection algorithm written to measure position of the contact line during spreading and recession. Specifically, 1 µl ethanol-water drops with 11 wt.%, 25 wt.%, and 50 wt.% initial ethanol concentration we investigated and compared to a pure water drop of the same volume. The effect of increasing substrate temperature for 30 °C to 50 °C to 70 °C on drops comprising 50 wt.% initial ethanol was also considered. We found that in all cases increasing initial ethanol concentration, and hence the magnitude of solutal Marangoni stresses, enhanced drop spreading. This led to faster spreading rates while reducing the length of the spreading phase, resulting in a slightly reduced maximum drop radius and shorter overall drop lifetime. When initial ethanol concentration reached 50 wt.%, a contact line instability emerges in the form of advancing fingers in an "octopi" arrangement accompanied by a second instability showing spoke-like patters arranged radially over the interface. Instabilities persist at all substrate temperatures for initial ethanol concentration of 50 wt.%. The enhanced spreading rates cause the drop interior to dry out before the contact line, leaving a ring where the contact line instability was previously present. The measured spreading rates closely match those predicted by our one-sided model in their respective time frames. The formation of the contact line ridge we observed in 50 wt.% initial ethanol drops preceding instability is also predicted by our model at the same concentration. Our stability analysis also indicates that the addition of solutal Marangoni stress also has a destabilising effect on the drop, which is clearly demonstrated here.

Part V

Conclusion and outlook

10. Conclusions and future work

10.1. Conclusions

In surface tension dominated flows, whether they be planar layers of sessile drops, addition of a second miscible component introduces solutal Marangoni stress which can compete with or enhance the already present thermal Marangoni stress. With liquids comprising binary mixtures being a promising candidate for many modern micro cooling systems, it is essential these influences are understood. This thesis has focused on the development of numerical models to investigate the solutally-induced phenomena in binary fluids, first in laterally heated liquid layers and then in sessile drops spreading on heated substrates. In both cases, models of the past have overwhelmingly focused on pure fluids with examples for liquid layers including Smith and Davis [3], Riley and Neitzel [19] and Sáenz et al. [31, 41]. Notable examples for sessile drops include Hu and Larson [130, 131], Dunn and co-workers [69, 115], Karapetsas et al. [168] and Sáenz et al. [78]. Only recently have advances been made to model multicomponent mixtures by researches such as Yu and co-workers [49, 50, 51, 52, 53] and Diddens and coworkers [90, 192, 193].

The recent advances made in the field of binary liquid layers by Yu and co-workers [49, 50, 51, 52, 53] have neglected the presence of deformable liquid-vapour interface as well as evaporation and the effects of the bounding gas phase above. We addressed this in Part II where we developed a new two-phase direct numerical simulation framework for modelling laterally heated liquid layers comprising of two miscible components, both with and without evaporation. We fully considered both phases and accounted for the deformable interface by using the Volume-of-Fluid method. The effects of thermally induced Soret diffusion in the liquid mixture along with standard Fick's diffusion were also included. For binary liquid layers under saturated environments, we found that the mild effect of Soret diffusion causes component segregation in the liquid phase which can go on to impact the nature of hydrothermal wave instabilities on the interface. In addition, concentration waves double the wavelength of the hydrothermal waves were observed on the interface similar to Yu et al. [50]. In the presence of evaporation, the more volatile component becomes depleted in the liquid while the layer remains well mixed due the strong return flow maintained by thermal Marangoni stress. Removal of the surface tension dependence on temperature causes the return flow to be reversed, owing to solutal Marangoni stress coupled with preferential evaporation from the hot wall reversing the surface tension gradient.

We continued in Part III to develop a one-sided model under the lubrication approximation to study the spreading and subsequent evaporation of volatile binary sessile drops deposited on heated substrates. We considered specifically flat (low contact angle) drops residing on a precursor film with a freely moving effective contact line. We found that increasing the influence of solutal Marangoni stress increased both the spreading rate and maximum wetted radius of deposited drops. Spreading rates in some cases were compatible to those of superspreading surfactants such as trisiloxanes. In these cases, a ridge in the interface profile is formed ahead of the contact line, causing a thicker rim of liquid at the drop edge rich in the less volatile component. This results in the drop interior drying out before the edge, leaving the ridge to remain in the final stages of evaporation. This behaviour is similar to that seen in the alkane mixtures studied by Guéna et al. [154]. We observed the same qualitative behaviour as our experimental investigation—presented in Part IV—with quantitatively similar spreading rates achieved between model and experiment. This suggests that our novel one-sided model is sufficient to capture the key underlying behaviour governing volatile wetting binary mixture drops deposited on heated substrates.

In Chapter 8 of Part III, we assessed the stability of the solutions obtained by our one-sided model by freezing the transient base state profile solved in Chapter 7 and conducting a novel linear stability analysis under the quasi-steady state approximation. Although challenging, our initial results indicate that the addition of a second component, thereby introducing solutal Marangoni stress, has a strong destabilising effect on the drop. This reflected the trends seen in our transient modelling in Chapter 7 and the experiments in Chapter 9.

We finished this thesis in Part IV with a series of experiments on ethanol-water mixture drops of various concentrations deposited on hydrophilic glass substrates heated to varying temperatures. These were selected to be close to the properties and conditions of our model in order to serve as a form of validation. An experimental apparatus was constructed and an algorithm written to track the contact line development from an aerial perspective. Similar to our modelling results in Chapter 7, we found that increasing the initial concentration of ethanol (the more volatile component with lower surface tension) enhanced both the spreading rate and total wetted area, with good agreement achieved between our model. Additionally, for an initial ethanol concentration of 50 wt.%, we observed a visibly thicker contact line region with the emergence of contact line fingering instabilities, among others, culminating in the drop centre drying out before the contact line and leaving a torus shaped ring. The fingering patterns resembled the "octopi" drop reported by Gotkis et al. [172] and are predicted by our model from the formation of the contact line ridge. Our stability analysis in Chapter 8 also points to this unstable behaviour.

10.2. Future work

With the total field of capillary driven fluid flows being vast and the specific interest of multiple component liquids being relatively young, there are ample avenues for future research—both concerning the work presented here and beyond. In terms of our two-phase liquid layer model, a more detailed investigation of component separation caused by the Soret effect is required, along with more detailed analysis on the resultant transient phenomena. A study where the Soret coefficient is increased significantly while suppressing evaporation would accomplish this. In the evaporating case, we still need to explore the interface stability impacted by the addition of the second component. A next step will be to introduce perturbations to the 3D base states to induce hydrothermal wave instabilities.

In terms of our one-sided drop model, a richer parametric study including mixtures of a different nature (e.g. those such as water-glycerol where the more volatile component has the higher surface tension of the pair) would be worthwhile. Additionally, a closer investigation into the specific effects of component latent heat and thermal conductivity would also be interesting. With the vast amount literature documenting the powerful effects of substrate properties such as thermal conductivity [68, 69] and roughness [65, 66, 67], it seems apt to incorporate this into a future version of our model. Treating the contact line with a slip condition or introducing a physical dimple in the substrate ahead of the contact line to restrict spreading would be a good starting point for this. Restricting contact line movement would extend the model to consider low contact angle drops with pinned contact lines. Further extension of our model to the gas phase by way of a 1.5-sided approach would achieve better quantitative agreement with experiments as well as being able to introduce evaporative cooling effects. Inclusion of the gas phase would also open the door to modelling the very interesting scenario of binary drops interacting thorough their vapour atmospheres, as observed in the experiments of Cira et al. [190]. With our stability analysis on binary drops being very preliminary, further work is required first by extending our analysis to larger wavenumbers and later timesteps. This will allow tracking of the most unstable mode (most dangerous wavenumber to the flow) over the drop lifetime.

Despite the work presented here, among others, demonstrating the significant impact of solutally driven Marangoni flow in binary liquids, a fully 3D two-sided model for an evaporating binary sessile drop still remains elusive. Therefore, a direct numerical simulation type approach, accounting fully for both liquid and gas phases in all three dimensions presents itself the next obvious challenge in binary drop research.

Part VI

Appendix

11. Appendix A: Pertaining to sessile droplets

11.1. Description of solution method

11.1.1 Time stepping procedure

The base state solution is marched forward in time by use of an adaptive time step, dt. Here we describe the procedure for selecting the time step size over the course of the simulation. Initially at $t = 0$, a minimum time step dt_{min} $=1 \times 10^{-7}$ and maximum time step dt_{max} $=5 \times 10^{-2}$ are specified and the time step set to the minimum, $dt = dt_{min}$. As time is advanced, at the end of each time step, the function $\mathcal{F}$ is computed,

$$\mathcal{F} = \sqrt{\frac{ER_T}{ER_{MAX}}} \tag{11.1}$$

where ER_{MAX} is the maximum residual error from the calculated variables in the governing equations and $ER_T = 1 \times 10^-3$ is the target residual value. If $ER_{MAX} \geq ER_T$ then $\mathcal{F} \leq 1$ where as if the residual error become sufficiently small, $ER_{MAX} < ER_T$, then $\mathcal{F} > 1$. The $\mathcal{F}$ function acts as a multiplying factor for dt, such that,

$$dt_{t+dt} = dt_t \mathcal{F} \tag{11.2}$$

where dt_t is the time step at current time and dt_{t+dt} is the value at the next time step. Using this procedure, dt is increased or decreased based on the magnitude of the largest residual. $\mathcal{F}$ is never allow to exceed 2 so the dt is at most doubled over one time step.

11.1.2 Solving with Jacobian

Let $\boldsymbol{f}(\boldsymbol{x})$ be a vector-valued function consisting of both component vectors x_i and component functions $f_i(\boldsymbol{x})$. $i = 1, 2, ..., n$, where n is the number of unknown variables corresponding with the number independent equations. We define a system of equations by setting the vector function equal to zero:

$$\boldsymbol{f}(\boldsymbol{x}) = 0 \tag{11.3}$$

We now seek a value for $\boldsymbol{x}$ which satisfies the above condition, allowing $\boldsymbol{f}(\boldsymbol{x})$ to equal zero. Initial values for the unknown variables x_i are given as initial conditions, providing an initial guess for the vector, $\boldsymbol{x}_0$. A linear approximation to $\boldsymbol{f}(\boldsymbol{x})$ is found using the first order Taylor expansion for each function in the vector, leading to:

$$\boldsymbol{f}(\boldsymbol{x}) \approx \boldsymbol{f}(\boldsymbol{x}_0) + \boldsymbol{J}(\boldsymbol{x}_0)(\boldsymbol{x} - \boldsymbol{x}_0) \tag{11.4}$$

Where $\boldsymbol{J}(\boldsymbol{x})$ is a square matrix of the first partial derivatives of the component functions of $\boldsymbol{f}(\boldsymbol{x})$, known as the Jacobian matrix. If $\boldsymbol{x}_0$ is the initial guess then let $\boldsymbol{x}_1$ be the first iterate towards our desired solution. In order to calculate a value of $\boldsymbol{x}_1$ which satisfies $\boldsymbol{f}(\boldsymbol{x}) = 0$, we apply:

$$\boldsymbol{f}(\boldsymbol{x}_0) + \boldsymbol{J}(\boldsymbol{x}_0)(\boldsymbol{x}_1 - \boldsymbol{x}_0) = 0 \tag{11.5}$$

Re-arranging to give:

$$\boldsymbol{x}_1 = \boldsymbol{x}_0 - (\boldsymbol{J}(\boldsymbol{x}_0))^{-1}\boldsymbol{f}(\boldsymbol{x}_0) \tag{11.6}$$

We can generalise this expression for any number of iteration, k:

$$\boldsymbol{x}_{k+1} = \boldsymbol{x}_k - (\boldsymbol{J}(\boldsymbol{x}_k))^{-1}\boldsymbol{f}(\boldsymbol{x}_k) \tag{11.7}$$

$(\boldsymbol{J}(\boldsymbol{x}))^{-1}$ is the inverse of the Jacobian matrix which in practice proves too computationally expensive to calculate. To circumvent this problem we define the difference in the solutions from iteration $k+1$ and k as:

$$(\boldsymbol{x}_{k+1} - \boldsymbol{x}_k) = \Delta\boldsymbol{x} \tag{11.8}$$

Where $\Delta\boldsymbol{x}$ is known as the solution vector. Substituting into eq. (11.7) and rearranging, we obtain:

$$\boldsymbol{J}(\boldsymbol{x}_k)\Delta\boldsymbol{x} = -\boldsymbol{f}(\boldsymbol{x}_k) \tag{11.9}$$

Applying to the code, $\boldsymbol{f}(\boldsymbol{x}_k)$ is a known vector with its components calculated in the previous iteration, from this we can compute the Jacobian, $\boldsymbol{J}(\boldsymbol{x}_k$. Now we have a system of linear equations to be solved for the solution vector, $\Delta\boldsymbol{x}$. Once the solution vector is calculated, we obtain the improved estimate for our vector of unknown variables, $\boldsymbol{x}_{k+1}$:

$$\boldsymbol{x}_{k+1} = \boldsymbol{x}_k + \Delta\boldsymbol{x} \tag{11.10}$$

A more accurate approximation, $\boldsymbol{x}_{k+2}$ is then obtained by updating the vector function to $\boldsymbol{f}(\boldsymbol{x}_{k+1})$ and repeating the process summarised below.

1. Compute the Jacobian, $\boldsymbol{J}(\boldsymbol{x}_{k+1})$.

2. Solve the linear system, $\boldsymbol{J}(\boldsymbol{x}_k)\varDelta\boldsymbol{x} = -\boldsymbol{f}(\boldsymbol{x}_k$, for $\varDelta\boldsymbol{x}$.

3. Update solution with improved estimate, $\boldsymbol{x}_{k+2} = \boldsymbol{x}_{k+1} + \varDelta\boldsymbol{x}$

11.2. Derivation of decomposed velocities

The bulk average velocity, u, can be decomposed into three distinct components:

$$u = u_{tg} + u_{cg} + u_{ca} \tag{11.11}$$

These are the three mechanisms that can drive movement and spreading of the contact line. u_{tg} is the thermocapillary velocity, where surface tension gradients arising from temperature variations drive the fluid motion. u_{cg} is the solutocapillary velocity where flow is driven by a surface tension gradient sustained by an uneven mixture concentration. u_{ca} is the capillary velocity which is sustained by the capillary pressure over the interface.

By decomposing the bulk velocity into these three contributions, we can gain insight into the driving forces governing the spreading behaviour. We have already defined an expression for the bulk velocity , u, given by its closure approximation in eq. (6.70). Setting $z = h$, we arrive at the expression for the bulk average velocity on the interface:

$$u = \frac{3f}{2h} + \frac{\partial \sigma}{\partial r}\frac{h}{4\mu Ma} \tag{11.12}$$

As defined elsewhere, $f = \int_0^h u\,dz$, it contains contributions from both capillary and surface tension forces. We now seek to find an analytic expression for f devoid of dependence on surface tension and hence temperature and concentration gradients. First let us differentiate eq. (6.70) with respect to z to give:

$$\frac{\partial u}{\partial z} = \left(\frac{3f}{h^2} - \frac{\partial \sigma}{\partial r}\frac{1}{2\mu Ma}\right) - \left(\frac{3f}{h^3} - \frac{\partial \sigma}{\partial r}\frac{3}{2h\mu Ma}\right)z \tag{11.13}$$

Substitution of $z = h$ and the $z = 0$ yields the following:

$$\begin{gathered}\frac{\partial u}{\partial z}|_h = \frac{\partial \sigma}{\partial r}\frac{1}{\mu Ma}\\ \frac{\partial u}{\partial z}|_0 = \frac{3f}{h^2} - \frac{\partial \sigma}{\partial r}\frac{1}{2\mu Ma}\end{gathered} \tag{11.14}$$

Now let us recall the dimensionless form of the r-momentum equation given in eq. (6.30).

Setting the Reynolds number to zero and integrating over z, we obtain:

$$\mu\left(\frac{\partial u}{\partial z}|_h - \frac{\partial u}{\partial z}|_0\right) = h\frac{\partial p}{\partial r} \tag{11.15}$$

Substituting eq. (11.14) into eq. (11.15), we obtain a new expression for f:

$$f = -\frac{h^3}{3\mu}\frac{\partial p}{\partial r} + \frac{h^2}{2\mu Ma}\frac{\partial \sigma}{\partial r} \tag{11.16}$$

The first term on the RHS in eq. (11.16) holds the capillary contribution for f and the second term gives the surface tension contribution, dependent on both temperature and concentration gradients. Substitution of eq. (11.16) into eq. (11.12) yields a new expression for u independent of f:

$$u = -\frac{h^2}{2\mu}\frac{\partial p}{\partial r} + \frac{h}{\mu Ma}\frac{\partial \sigma}{\partial r} \tag{11.17}$$

Eq. (6.28) defines the dimensionless form of surface tension which is re-arranged to give:

$$\sigma = \chi_A + \sigma_R(1-\chi_A) + MaT_s\big(\gamma_R(\chi_A - 1) - \chi_A\big) \tag{11.18}$$

Differentiating σ with respect to r, we arrive at the following expression:

$$\frac{\partial \sigma}{\partial r} = \frac{\partial \chi_A}{\partial r} - \sigma_R\frac{\partial \chi_A}{\partial r} + Ma\frac{\partial T_s}{\partial r}\Big(\gamma_R(\chi_A - 1) - \chi_A\Big) + MaT_s\left(\gamma_R\frac{\partial \chi_A}{\partial r} - \frac{\partial \chi_A}{\partial r}\right) \tag{11.19}$$

We then substitute eq. (11.19) into eq. (11.17) and arrive at the expressions for the decomposed bulk surface velocity:

$$\begin{aligned} u = \left[-\frac{h^2}{2\mu}\frac{\partial p}{\partial r}\right] + \left[\frac{\partial \chi_A}{\partial r} - \sigma_R\frac{\partial \chi_A}{\partial r} - MaT_s\left(\gamma_R\frac{\partial \chi_A}{\partial r} + \frac{\partial \chi_A}{\partial r}\right)\right]\frac{h}{\mu Ma} \\ + \left[-\frac{\partial T_s}{\partial r}\Big(\chi_A + \gamma(1-\chi_A)\Big)\right]\frac{h}{\mu} \end{aligned} \tag{11.20}$$

The first squared bracket term is dependent on the rate of change of capillary pressure with r and so gives our expression for the capillary velocity, u_{ca}. See eq. (6.47) for the definition of p. The second term defines the solutocapillary velocity, u_{cg}, given it depends on concentration gradients along r. The final term, being dependent on temperature gradient, gives the thermocapillary velocity, u_{tg}. These are summarised as follows:

$$u_{ca} = -\frac{h^2}{2\mu}\frac{\partial p}{\partial r} \tag{11.21}$$

$$u_{cg} = \left[\frac{\partial \chi_A}{\partial r} - \sigma_R \frac{\partial \chi_A}{\partial r} - MaT_s \frac{\partial \chi_A}{\partial r}(1-\gamma_R)\right]\frac{h}{\mu Ma} \tag{11.22}$$

$$u_{tg} = \left[-\frac{\partial T_s}{\partial r}\chi_A - \frac{\partial T_s}{\partial r}\gamma(1-\chi_A)\right]\frac{h}{\mu} \tag{11.23}$$

12. Acronyms

AFM atomic force microscopy

CCA constant contact angle

CCR constant contact radius

CMOS complementary metal oxide semiconductor

CSF continuum surface force

DNS direct numerical simulations

DSA Drop Shape Analyzer

FEM finite element method

HC heavier component

HMDSO hexamethyldisiloxane

HTWs hydrothermal waves

IPA isopropyl alcohol

LC lighter component

LHS left hand side

LV liquid-vapour

LVC less volatile component

MVC more volatile component

NEOS non-equilibrium one-sided

NSBC normal stress boundary condition

PDE partial differential equation

PDEs partial differential equations

PG propylene glycol

PID proportional integral derivative

PIV particle image velocimetry

PMMA poly(methyl methacrylate)

PTFE polytetrafluoroethylene

PVC polyvinyl chloride

QSSA quasi-steady-state approximation

RHS right hand side

RMS root mean squared

SL solid-liquid

SS stick-slip

SV solid-vapour

TBLs thermal boundary layers

TCL triple contact line

VOF volume of fluid

13. Dimensional symbols: Liquid layers

$\hat{A}$, $\hat{B}$, $\hat{C}$ Antoine coefficients (K)

$\hat{\mathcal{C}}$ mass of vapour per unit volume of gas phase ($\mathrm{kg\,m^{-3}}$)

$\hat{\mathcal{D}}_T$ thermal diffusion coefficient ($\mathrm{m^2\,s^{-1}\,K^{-1}}$)

$\hat{\mathcal{D}}_l$ mass diffusion coefficient of component A in the liquid phase ($\mathrm{m^2\,s^{-1}}$)

$\hat{\mathcal{D}}_g$ mass diffusion coefficient of component A in the gas phase ($\mathrm{m^2\,s^{-1}}$)

$\hat{H}$ height of domain (y-direction) (m)

$\hat{\mathcal{J}}_{A,x}$ mass flux of component A in the x-direction ($\mathrm{kg\,m^{-2}\,s^{-1}}$)

$\hat{L}$ length of domain (z-direction) (m)

$\hat{L}_v$ specific latent heat of vaporisation ($\mathrm{kJ\,kg^{-1}}$)

$\hat{M}_A$ molecular weight of component A ($\mathrm{kg\,mol^{-1}}$)

$\hat{M}_{g1}$ molecular weight of inert gas ($\mathrm{kg\,mol^{-1}}$)

$\hat{S}$ volumetric mass transfer across the interface ($\mathrm{kg\,m^{-3}}$)

$\hat{\mathscr{S}}$ volumetric mass flux across the interface ($\mathrm{kg\,m^{-3}\,s^{-1}}$)

$\hat{S}_T$ Soret coefficient ($= \hat{D}_T/\hat{D}_l$) ($\mathrm{K^{-1}}$)

$\hat{T}_c$ cold wall temperature (K)

$\hat{T}_h$ hot wall temperature (K)

$\hat{T}_r$ reference temperature (K)

$\Delta\hat{T}$ temperature difference (K)

$\hat{V}_C$ infinitesimal control volume ($\mathrm{m^3}$)

$\hat{W}$ width of domain (x-direction) (m)

$\hat{b}_i$ effective temperature gradient (K)

$\hat{c}_{p,g}$ specific heat capacity of gas phase ($\mathrm{kJ\,kg^{-1}\,K^{-1}}$)

$\hat{c}_{p,l}$ specific heat capacity of liquid phase ($\mathrm{kJ\,kg^{-1}\,K^{-1}}$)

$\hat{d}$ liquid layer depth (m)

$\hat{\boldsymbol{f}}_{\boldsymbol{b}}$ buoyancy force ($\mathrm{N\,m^{-3}}$)

$\hat{\boldsymbol{f}}_{\boldsymbol{sv}}$ surface force resulting from surface tension ($\mathrm{N\,m^{-3}}$)

$\hat{g}$ gravitational acceleration ($\mathrm{m\,s^{-2}}$)

$\hat{k}_g$ thermal conductivity of gas phase ($\mathrm{W\,m^{-1}\,K^{-1}}$)

$\hat{k}_l$ thermal conductivity of liquid phase ($\mathrm{W\,m^{-1}\,K^{-1}}$)

$\hat{m}_g$ some mass of gas (kg)

$\hat{m}_{gA,sat}$ mass of component A vapour in gas phase at saturation (kg)

$\hat{m}_l$ some mass of liquid (kg)

$\hat{p}$ pressure ($\mathrm{N\,m^{-2}}$)

$\hat{p}_r$ reference pressure ($\mathrm{N\,m^{-2}}$)

$\hat{p}_{sat,A}$ saturation pressure of component A ($\mathrm{N\,m^{-2}}$)

$\hat{t}_s$ marching time step (s)

$\hat{\boldsymbol{u}}$ velocity vector ($\mathrm{m\,s^{-1}}$)

$\hat{\alpha}_l$ thermal diffusivity of the liquid ($\mathrm{m^2\,s^{-1}}$)

$\hat{\beta}_{T,g}$ coefficient of thermal expansion for the gas phase ($\mathrm{K^{-1}}$)

$\hat{\beta}_{T,g1}$ coefficient of thermal expansion for the inert gas (air) ($\mathrm{K^{-1}}$)

$\hat{\beta}_{T,l}$ coefficient of thermal expansion for the liquid phase ($\mathrm{K^{-1}}$)

$\hat{\gamma}_T$ temperature coefficient of surface tension ($\mathrm{N\,m^{-1}\,K^{-1}}$)

$\hat{\gamma}_\chi$ concentration coefficient of surface tension ($\mathrm{N\,m^{-1}}$)

$\hat{\kappa}$ mean curvature of the interface ($\mathrm{m^{-1}}$)

$\hat{\mu}_g$ dynamic viscosity of gas phase ($\mathrm{Pa\,s^{-1}}$)

$\hat{\mu}_l$ dynamic viscosity of liquid phase ($\mathrm{Pa\,s^{-1}}$)

$\hat{\nu}_l$ momentum diffusivity of the liquid ($\mathrm{m^2\,s^{-1}}$)

$\hat{\rho}_g$ density of gas phase ($\mathrm{kg\,m^{-3}}$)

$\hat{\rho}_{r,g}$ density of gas phase at reference temperature and concentration ($\mathrm{kg\,m^{-3}}$)

$\hat{\rho}_{r,gA}$ density of pure component A vapour at reference temperature ($\mathrm{kg\,m^{-3}}$)

$\hat{\rho}_{r,g1}$ density of the inert gas (air) at reference temperature ($\mathrm{kg\,m^{-3}}$)

$\hat{\rho}_l$ density of liquid phase ($\mathrm{kg\,m^{-3}}$)

$\hat{\rho}_{r,l}$ density of liquid phase at reference temperature and concentration ($\mathrm{kg\,m^{-3}}$)

$\hat{\sigma}_r$ surface tension at reference temperature and concentration ($\mathrm{N\,m^{-1}}$)

$\hat{\nabla}_s$ gradient operator tangential to the interface ($\mathrm{m^{-1}}$)

$\hat{\nabla}$ dimensional gradient operator ($\mathrm{m^{-1}}$)

14. Dimensionless symbols: Liquid layers

Bo_d dynamic Bond number

Ca_T thermal Capillary number

Ca_χ solutal Capillary number

Fr Froude number

Gr_T thermal Grashof number

Gr_χ solutal Grashof number

Ja Jakob number

K overall wavenumber

Ma_L thermal Marangoni number

Ma_{crit} critical Marangoni number

Ma_E effective Marangoni number

$\mathcal{M}$ ratio of molecular weights of component A to inert gas $g1$

Pr Prandtl number

R_σ capillary ratio

Re_{crit} critical Reynolds number

Re_T thermocapillary Reynolds number

Re_χ solutocapillary Reynolds number

S_T dimensionless Soret coefficient

Sc_g Schmidt number for the gas phase

Sc_l Schmidt number for the liquid phase

We Weber number

$X_{A,sat}$ saturated mole fraction of component A in the gas phase

$\varGamma_\vartheta$ ratio liquid to component A vapour for generic property ς

$\varUpsilon_A$ mass fraction of component A in the gas phase

$\mathit{\Upsilon}_{A,sat}$ saturated mass fraction of component A in the gas phase

$\mathit{\Upsilon}_{g1}$ mass fraction of inert gas $g1$ in the gas phase

$\mathit{\Psi}_{\vartheta}$ ratio liquid to component A vapour for generic property ς

$\mathit{\Omega}_{\vartheta}$ ratio liquid to inert gas $g1$ for generic property ς

c volume fraction (colour function)

$\boldsymbol{e}_z$ unit vector in z-direction

k_x perturbation wavenumber in x direction

k_z perturbation wavenumber in z direction

$\boldsymbol{n}$ unit vector normal to the interface

$\beta_{\chi,l}$ coefficient of solutal expansion for the liquid phase

ϑ generic variable

ϑ_1 perturbation of generic variable

ϑ' fluctuation of generic variable from the base state

$\tilde{\vartheta}$ amplitude of generic variable perturbation

χ_A mass fraction of component A in the liquid phase

$\chi_{A,0}$ initial mass fraction of component A in liquid phase

χ_B mass fraction of component B in the liquid phase

χ' difference in mass fraction between components B and A $(= \chi_B - \chi_B)$

$\mathit{\Delta}\chi_A$ mass fraction gradient of component A

ψ angle of propagation (°)

15. Dimensional symbols: Sessile droplets

$\hat{\mathscr{A}}$ dimensional Hamaker constant (N m)

$\hat{\mathcal{D}}_A$ mass diffusion coefficient of component A ($\mathrm{m^2\,s^{-1}}$)

$\hat{H}_0$ initial height of droplet at apex(m)

$\hat{J}$ evaporative mass flux ($\mathrm{kg\,m^{-2}\,s^{-1}}$)

$\hat{M}$ molecular weight ($\mathrm{kg\,mol^{-1}}$)

$\hat{R}_g$ Universal Gas Constant ($\mathrm{J\,K^{-1}\,mol^{-1}}$)

$\hat{R}_0$ initial droplet radius (m)

$\hat{T}$ temperature (K)

$\hat{T}|_h$ temperature of the interface (K)

$\hat{T}_g$ gas phase temperature (K)

$\hat{T}_w$ substrate (bottom wall) temperature (K)

$\hat{U}^*$ characteristic velocity ($\mathrm{m\,s^{-1}}$)

$\hat{\mathit{\Pi}}$ disjoining pressure ($\mathrm{N\,m^{-2}}$)

$\hat{c}_p$ specific heat capacity ($\mathrm{kJ\,kg^{-1}\,K^{-1}}$)

$\hat{k}$ thermal conductivity ($\mathrm{W\,m^{-1}\,K^{-1}}$)

$\hat{p}_{sat,i}$ saturation vapour pressure of pure component i ($\mathrm{N\,m^{-2}}$)

$\hat{p}_v$ total pressure of the gas phase ($\mathrm{N\,m^{-2}}$)

$\hat{p}_{v,i}$ partial vapour pressure of component i ($\mathrm{N\,m^{-2}}$)

$\hat{p}_{v,e,i}$ equilibrium vapour pressure of component i ($\mathrm{N\,m^{-2}}$)

r_{max} maximum radius of drop (mm)

$\hat{\boldsymbol{u}}_s$ interface velocity ($\mathrm{m\,s^{-1}}$)

$\hat{\mu}$ dynamic viscosity ($\mathrm{Pa\,s^{-1}}$)

$\hat{\rho}$ density ($\mathrm{kg\,m^{-3}}$)

$\hat{\sigma}$ surface tension ($\mathrm{N\,m^{-1}}$)

$\hat{\sigma}_{i,r}$ surface tension of component i at reference temperature T_r ($\mathrm{N\,m^{-1}}$)

$\hat{\gamma}_{T,i}$ temperature coefficient of surface tension of component i ($\mathrm{N\,m^{-1}\,K^{-1}}$)

$\hat{\boldsymbol{\tau}}$ dimensional total stress tensor ($\mathrm{N\,m^{-2}}$)

$\hat{\upsilon}_i$ molar volume of component i ($\mathrm{m^3\,mol^{-1}}$)

16. Dimensionless symbols: Sessile droplets

$\mathscr{A}$ Hamaker constant

Bi Biot number

Bo Bond number

E evaporation number

Gr Grashof number

$\mathbf{I}$ identity tensor

$\mathbf{J}$ Jacobian matrix

K Knudsen number

$\mathbf{M}$ mass matrix

$\mathcal{M}$ magnitude of penalty function P

M_R molar weight ratio

Ma Marangoni number

$N_{r,tot}$ total number of nodes in r

P penalty function

Pe Péclet number

Pe' modified Péclet number for weak diffusion

Ra Rayleigh number

Re Reynolds number

$\mathit{\Lambda}$ latent heat ratio

$\mathit{\Theta}$ integral of temperature T between $z = 0$ and $z = h$

a generic variable

a_o base state of generic variable a

a_1 perturbation of generic variable a

c_{pR} specific heat ratio

dt adaptive time step

$\boldsymbol{e}_r$ unit vector in r-direction

$\boldsymbol{e}_\theta$ unit vector in θ-direction

f integral of u velocity between $z = 0$ and $z = h$

g integral of v velocity between $z = 0$ and $z = h$

$h(0, t)$ apex height at time t

h_∞ precursor layer thickness

k_R thermal conductivity ratio

k_d wavenumber associated with the most unstable eigenmode

$\boldsymbol{n}$ unit vector normal to the interface

p total pressure

$p_{sat,A}$ saturation vapour pressure of component A

p_v vapour pressure

r_c contact line position

r_∞ length of domain

$\boldsymbol{t}$ unit vector tangential to the interface

$\mathbf{v}$ eigenvector

α relative volatility

$\alpha_{v,i}$ accommodation coefficient for evaporation

$\beta_{v,i}$ accommodation coefficient for condensation

γ_R temperature coefficient of surface tension ratio

δ dimensionless number accounting for pressure effects on the interface

ε aspect ratio

ζ small number determining the magnitude of perturbation a_1

μ_R viscosity ratio

σ_R surface tension ratio

ϕ_i test function

χ_A mass fraction of component A in the liquid phase

χ_{A0} mean mass fraction of component A independent of z

$\chi_{A0,i}$ initial mass fraction of component A

$\chi_{A0,\infty}$ mass fraction of component A (independent of z) within precursor region

χ_{A1} mass fraction of component A retaining z dependence

χ_{A2} modified mass fraction of component A

ω eigenvalue (consisting of real and imaginary parts)

ω_I eigenvalue imaginary part

ω_R eigenvalue real part

Bibliography

[1] A. Bar-Cohen, M. Arik, and M. Ohadi. Direct Liquid Cooling of High Flux Micro and Nano Electronic Components. *Proc. IEEE*, 94(8):1549–1570, 2006.

[2] M. Lappa. Review : Thermal convection and related instabilities in models of crystal growth from the melt on earth and in microgravity : Past history and current status. *Cryst. Res. Technol.*, 40(6):531–549, 2005.

[3] M. K. Smith and S. H. Davis. Instabilities of dynamic thermocapillary liquid layers. Part 1. Convective Instabilities. *J. Fluid Mech.*, 132:119–144, 1983.

[4] M. Lappa. Hydrothermal waves in two-dimesnional liquid layers with sudden changes in available cross-section. *Int. J. Numer. Methods Heat Fluid Flow*, 27(11):2629 – 2649, 2017.

[5] D. Yang, M. Krasowska, C. Priest, M. N. Popescu, and J. Ralston. Dynamics of Capillary-Driven Flow in Open Microchannels. *J. Phys. Chem. C*, 115(38):18761–18769, 2011.

[6] M. F. Schatz and G. P. Neitzel. Experiments on Thermocapillary Instabilities. *Annu. Rev. Fluid Mech.*, 33:93–127, 2001.

[7] J. Pearson. On convection cells induced by surface tension. *J. Fluid Mech.*, 4(05):489–1120, 1958.

[8] S. Davis. Thermocapillary Instabilities. *Annu. Rev. Fluid Mech.*, 19(1):403–435, 1987.

[9] L. E. Scriven and C. V. Sternling. On cellular convection driven by surface-tension gradients: Effects of mean surface tension and surface viscosity. *J. Fluid Mech.*, 19(3):321–340, 1964.

[10] J. A. Maroto, V. Perez-Munuzuri, and M. S. Romero_Cano. Introductory analysis of Bénard – Marangoni convection B enard – Marangoni. *Eur. J. Phys.*, 26:311–320, 2007.

[11] M. K. Smith and S. H. Davis. Instabilities of dynamic thermocapillary liquid layers. Part 2. Surface-wave instabilities. *J. Fluid Mech.*, 132:145–162, apr 1983.

[12] D. Schwabe and A. Scharmann. Some evidence for the existence and magnitude of a critical marangoni number for the onset of oscillatory flow in crystal growth melts. *J. Cryst. Growth*, 46(1):125–131, 1979.

[13] M. K. Smith. Instability mechanisms in dynamic thermocapillary liquid layers. *Phys. Fluids*, 29(10):3182, 1986.

[14] J. M. Garr-Peters. The neutral stability of surface-tension driven cavity flows subject to buoyant forces- I.Transverse and longitudinal disturbances. *Chem. Eng. Sci.*, 47(5):1247–1264, 1992.

[15] J. M. Garr-Peters. The neutral stability of surface-tension driven cavity flows subject to buoyant forces-II. Oblique disturbances. *Chem. Eng. Sci.*, 47(5):1265–1276, 1992.

[16] P. M. Parmentier, V. C. Regnier, and G. Lebon. Buoyant-thermocapillary instabilities in medium-Prandtl-number fluid layers subject to a horizontal temperature gradient. *Int. J. Heat Mass Transf.*, 36(9):2417–2427, 1993.

[17] J. F. Mercier and C. Normand. Buoyant-thermocapillary instabilities of differentially heated liquid layers. *Phys. Fluids*, 8(6):1433–1445, 1996.

[18] C. L. Chan and C. F. Chen. Effect of gravity on the stability of thermocapillary convection in a horizontal fluid layer. *J. Fluid Mech.*, 647:91–103, 2010.

[19] R. J. Riley and G. P. Neitzel. Instability of thermocapillary-buoyancy convection in shallow layers. Part 1. Characterization of steady and oscillatory instabilities. *J. Fluid Mech.*, 359:143–164, 1998.

[20] D. Villers and J. K. Platten. Coupled buoyancy and Marangoni convection in acetone experiments and comparison with numerical simulations. *J. Fluid Mech.*, 234:487–510, 1992.

[21] D. Schwabe, U. Moller, J. Schneider, and A. Scharmann. Instabilities of shallow dynamic thermocapillary liquid layers. *Phys. Fluids A Fluid Dyn.*, 4(11):2368, 1992.

[22] J. Burguete, N. Mukolobwiez, F. Daviaud, N. Garnier, and A. Chiffaudel. Buoyant-thermocapillary instabilities in extended liquid layers subjected to a horizontal temperature gradient. *Phys. Fluids*, 13(10):2773–2787, 2001.

[23] D. Schwabe and S. Benz. Thermocapillary flow instabilities in an annulus under microgravity - results of the experiment magia. *Adv. Sp. Res.*, 29(4):629–638, 2002.

[24] D. Schwabe, A. Zebib, and B. C. Sim. Oscillatory thermocapillary convection in open cylindrical annuli. Part 1. Experiments under microgravity. *J. Fluid Mech.*, 491(491):239–258, 2003.

[25] N. Garnier, A. Chiffaudel, and F. Daviaud. Hydrothermal waves in a disk of fluid. *Dyn. Spat. Cell. Struct. Henri Benard Centen. Rev.*, 207:147–161, 2006.

[26] L. Peng, Y.-R. Li, W.-Y. Shi, and N. Imaishi. Three-dimensional thermocapillary–buoyancy flow of silicone oil in a differentially heated annular pool. *Int. J. Heat Mass Transf.*, 50(5-6):872–880, mar 2007.

[27] H. C. Kuhlmann and S. Albensoeder. Three-dimensional flow instabilities in a thermocapillary-driven cavity. *Phys. Rev. E*, 77(3):036303, mar 2008.

[28] J. Xu and A. Zebib. Oscillatory two- and three-dimensional thermocapillary convection. *J. Fluid Mech.*, 364:187–209, 1998.

[29] B.-C. Sim, A. Zebib, and D. Schwabe. Oscillatory thermocapillary convection in open cylindrical annuli. Part 2. Simulations. *J. Fluid Mech.*, 491:259–274, 2003.

[30] E. Bucchignani. Numerical characterization of hydrothermal waves in a laterally heated shallow layer. *Phys. Fluids*, 16(11):3839–3849, 2004.

[31] P. J. Sáenz, P. Valluri, K. Sefiane, G. Karapetsas, and O. K. Matar. Linear and nonlinear stability of hydrothermal waves in planar liquid layers driven by thermocapillarity. *Phys. Fluids*, 25(9):094101, 2013.

[32] D. Merkt and M. Bestehorn. Bénard-Marangoni convection in a strongly evaporating fluid. *Phys. D Nonlinear Phenom.*, 185(3-4):196–208, 2003.

[33] H. Mancini and D. Maza. Pattern formation without heating in an evaporative convection experiment. *Europhys. Lett.*, 66(6):812–818, jun 2004.

[34] J. P. Burelbach, S. G. Bankoff, and S. H. Davis. Nonlinear Stability of Evaporating Condensing Liquid-Films. *J. Fluid Mech.*, 195:463–494, 1988.

[35] H. J. Palmer. The hydrodynamic stability of rapidly evaporating liquids at reduced pressure. *J. Fluid Mech.*, 75(3):487 – 511, 1976.

[36] E. Sultan, A. Boudaoud, and M. Ben Amar. Evaporation of a thin film: diffusion of the vapour and Marangoni instabilities. *J. Fluid Mech.*, 543(1966):183–202, 2005.

[37] W. Guo and R. Narayanan. Interfacial instability due to evaporation and convection: linear and nonlinear analyses. *J. Fluid Mech.*, 650:363, mar 2010.

[38] O. Ozen and R. Narayanan. The physics of evaporative and convective instabilities in bilayer systems: Linear theory. *Phys. Fluids*, 16(12):4644–4652, 2004.

[39] G. B. McFadden, S. R. Coriell, K. F. Gurski, and D. L. Cotrell. Onset of convection in two liquid layers. *Phys. Fluids*, 112(2007):271–281, 2007.

[40] K. Kanatani and A. Oron. Nonlinear dynamics of confined thin liquid-vapor bilayer systems with phase change. *Phys. Fluids*, 23(3):032102, 2011.

[41] P. J. Sáenz, P. Valluri, K. Sefiane, G. Karapetsas, and O. K. Matar. On phase change in Marangoni-driven flows and its effects on the hydrothermal-wave instabilities. *Phys. Fluids*, 26(2):024114, feb 2014.

[42] J.-J. Yu, D.-F. Ruan, Y.-R. Li, and J.-C. Chen. Experimental study on thermocapillary convection of binary mixture in a shallow annular pool with radial temperature gradient. *Exp. Therm. Fluid Sci.*, 61:79–86, feb 2015.

[43] O. Ecenarro, J. A. Madariaga, J. Navarro, C. M. Santamaria, J. A. Carrion, and J. M. Saviron. Non-steady-state density effects in liquid thermal diffusion columns. *J. Phys. Condens. Matter*, 1:9741–9750, 1989.

[44] C. Soret. Sur l'état d'équilibre que prend au point de vue de sa concentration une dissolution saline primitivement homohéne dont deux parties sont portées à des températures différentes. *Arch. Sci. Phys. Nat*, 2:48–61, 1879.

[45] J. K. Platten. The Soret Effect: A Review of Recent Experimental Results. *J. Appl. Mech.*, 73:5, 2006.

[46] Y. Kamotani, L. Wang, S. Ostrach, and H. Jiang. Experimental study of natural convection in shallow enclosures with horizontal temperature and concentration gradients. *Int. J. Heat Mass Transf.*, 28(1):165–173, 1985.

[47] T. L. Bergman. Numerical simulation of double-diffusive Marangoni convection. *Phys. Fluids*, 29(7):2103, 1986.

[48] A. Bergeon and E. Knobloch. Oscillatory Marangoni convection in binary mixtures in square and nearly square containers. *Phys. Fluids*, 16(2):360–372, 2004.

[49] J.-J. Yu, Y.-R. Li, C.-M. Wu, and J.-C. Chen. Three-dimensional thermocapillary – buoyancy flow of a binary mixture with Soret effect in a shallow annular pool. *Int. J. Heat Mass Transf.*, 90:1071–1081, 2015.

[50] J.-J. Yu, L. Zhang, Y.-R. Li, and J.-C. Chen. Numerical Simulations of Thermocapillary Flow of a Binary Mixture with the Soret Effect in a Shallow Annular Pool. *Microgravity Sci. Technol.*, 28(1):1–10, 2016.

[51] J.-C. Chen, Y.-R. Li, J.-J. Yu, L. Zhang, and C.-M. Wu. Flow pattern transition of thermal - solutal capillary convection with the capillary ratio of -1 in a shallow annular pool. *Int. J. Heat Mass Transf.*, 95:1–6, 2016.

[52] J.-J. Yu, C.-M. Wu, Y.-R. Li, and J.-C. Chen. Thermal-solutal capillary-buoyancy flow of a low Prandtl number binary mixture with a -1 capillary ratio in an annular pool. *Phys. Fluids*, 28(8):084102, 2016.

[53] J.-J. Yu, Y.-R. Li, J.-C. Chen, Y. Zhang, and C.-M. Wu. Thermal-solutal capillary-buoyancy flow of a low Prandtl number binary mixture with various capillary ratios in an annular pool. *Int. J. Heat Mass Transf.*, 113:40–52, 2017.

[54] R. O. Grigoriev and T. Qin. The effect of phase change on stability of convective flow in a layer of volatile liquid driven by a horizontal temperature gradient. *J. Fluid Mech.*, 838:248–283, 2018.

[55] S. Rieks and E. Y. Kenig. Modelling and numerical simulation of coupled transport phenomena with phase change: Layer evaporation of a binary mixture. *Chem. Eng. Sci.*, 176:367–376, 2018.

[56] J. Kim. Spray cooling heat transfer: The state of the art. *Int. J. Heat Fluid Flow*, 28(4):753–767, 2007.

[57] W. Deng and A. Gomez. Electrospray cooling for microelectronics. *Int. J. Heat Mass Transf.*, 54(11-12):2270–2275, 2011.

[58] P. Calvert. Inkjet Printing for Materials and Devices. *Chem. Mater.*, 13(10):3299–3305, 2001.

[59] M. Singh, H. M. Haverinen, P. Dhagat, and G. E. Jabbour. Inkjet Printing — Process and Its Applications. *Adv. Mater.*, 22(6):673–685, 2010.

[60] Y. Yu, H. Zhu, J. M. Frantz, M. E. Reding, K. C. Chan, and H. E. Ozkan. Evaporation and coverage area of pesticide droplets on hairy and waxy leaves. *Biosyst. Eng.*, 104(3):324–334, 2009.

[61] M. Damak, S. R. Mahmoudi, N. Hyder, and K. K. Varanasi. Enhancing droplet deposition through in-situ precipitation. *Nat. Commun.*, 7:12560, 2016.

[62] K. Sefiane. On the Formation of Regular Patterns from Drying Droplets and Their Potential Use for Bio-Medical Applications. *J. Bionic Eng.*, 7:S82–S93, 2010.

[63] D. Brutin, B. Sobac, B. Loquet, and J. Sampol. Pattern formation in drying drops of blood. *J. Fluid Mech.*, 667:85–95, 2011.

[64] R. Chen, L. Zhang, D. Zang, and W. Shen. Blood drop patterns: Formation and applications. *Adv. Colloid Interface Sci.*, 231:1–14, 2016.

[65] A. M. Cazabat and M. A. Cohen Stuart. Dynamics of Wettlng: Effects of Surface Roughness. *J. Phys. Chem.*, 90(22):5845–5849, 1986.

[66] H. Nakae, R. Inui, Y. Hirata, and H. Saito. Effects of surface roughness on wettability. *Acta Mater.*, 46(7):2313–2318, 1998.

[67] Y. Chen, B. He, J. Lee, and N. A. Patankar. Anisotropy in the wetting of rough surfaces. *J. Colloid Interface Sci.*, 281(2):458–464, 2005.

[68] W. D. Ristenpart, P. G. Kim, C. Domingues, J. Wan, and H. A. Stone. Influence of Substrate Conductivity on Circulation Reversal in Evaporating Drops. *Phys. Rev. Lett.*, 99(23):234502, 2007.

[69] G. J. Dunn, S. K. Wilson, B. R. Duffy, S. David, and K. Sefiane. The strong influence of substrate conductivity on droplet evaporation. *J. Fluid Mech.*, 623:329–351, 2009.

[70] K. Sefiane, J. R. Moffat, O. K. Matar, and R. V. Craster. Self-excited hydrothermal waves in evaporating sessile drops. *Appl. Phys. Lett.*, 93(7):074103, 2008.

[71] V. Starov and K. Sefiane. On evaporation rate and interfacial temperature of volatile sessile drops. *Colloids Surfaces A Physicochem. Eng. Asp.*, 333(1-3):170–174, 2009.

[72] K. Sefiane, S. K. Wilson, S. David, G. J. Dunn, and B. R. Duffy. On the Effect of the Atmosphere on the Evaporation of Sessile Droplets of Water. *Phys. Fluids*, 21(6):062101, 2009.

[73] Y. Fukatani, D. Orejon, Y. Kita, Y. Takata, J. Kim, and K. Sefiane. Effect of ambient temperature and relative humidity on interfacial temperature during early stages of drop evaporation. *Phys. Rev. E*, 93(4):043103, 2016.

[74] N. Shahidzadeh-Bonn, S. Rafaï, A. Azouni, and D. Bonn. Evaporating droplets. *J. Fluid Mech.*, 549:307–313, 2006.

[75] F. Girard and M. Antoni. Influence of Substrate Heating on the Evaporation Dynamics of Pinned Water Droplets. *Langmuir*, 24(20):11342–11345, 2008.

[76] B. Sobac and D. Brutin. Thermal effects of the substrate on water droplet evaporation. *Phys. Rev. E*, 86:021602, 2012.

[77] M. Parsa, S. Harmand, K. Sefiane, M. Bigerelle, and R. Deltombe. Effect of Substrate Temperature on Pattern Formation of Nanoparticles from Volatile Drops. *Langmuir*, 31(11):3354–3367, 2015.

[78] P. J. Sáenz, K. Sefiane, J. Kim, O. K. Matar, and P. Valluri. Evaporation of sessile drops: a three-dimensional approach. *J. Fluid Mech.*, 772:705–739, 2015.

[79] C. W. Extrand and S. I. Moon. When Sessile Drops Are No Longer Small: Transitions from Spherical to Fully Flattened. *Langmuir*, 76(23):11815–11822, 2010.

[80] S. Srinivasan, G. H. Mckinley, and R. E. Cohen. Assessing the Accuracy of Contact Angle Measurements for Sessile Drops on Liquid-Repellent Surfaces. *Langmuir*, 27(22):13582–13589, 2011.

[81] V. Bergeron, D. Bonn, J. Y. Martin, and L. Vovelle. Controlling droplet deposition with polymer additives. *Nature*, 405(6788):772–775, 2000.

[82] D. Orejon, K. Sefiane, and M. E. R. Shanahan. Stick-Slip of Evaporating Droplets : Substrate Hydrophobicity and Nanoparticle Concentration. *Langmuir*, 27(21):12834–12843, 2011.

[83] G. Karapetsas, K. C. Sahu, and O. K. Matar. Evaporation of Sessile Droplets Laden with Particles and Insoluble Surfactants. *Langmuir*, 32(27):6871–6881, 2016.

[84] V. X. Nguyen and K. J. Stebe. Patterning of Small Particles by a Surfactant-Enhanced Marangoni-Bénard Instability. *Phys. Rev. Lett.*, 88(14):164501, 2002.

[85] G. Karapetsas, R. V. Craster, and O. K. Matar. On surfactant-enhanced spreading and superspreading of liquid drops on solid surfaces. *J. Fluid Mech.*, 670:5–37, 2011.

[86] N. Shahidzadeh-Bonn, S. Rafaï, D. Bonn, and G. Wegdam. Salt crystallization during evaporation: Impact of interfacial properties. *Langmuir*, 24(16):8599–8605, 2008.

[87] N. Shahidzadeh, M. F. Schut, J. Desarnaud, M. Prat, and D. Bonn. Salt stains from evaporating droplets. *Sci. Rep.*, 5:1–9, 2015.

[88] J. R. E. Christy, Y. Hamamoto, and K. Sefiane. Flow Transition within an Evaporating Binary Mixture Sessile Drop. *Phys. Rev. Lett.*, 106(20):205701, 2011.

[89] R. Bennacer and K. Sefiane. Vortices, dissipation and flow transition in volatile binary drops. *J. Fluid Mech.*, 749:649–665, may 2014.

[90] H. Tan, C. Diddens, P. Lv, J. G. M. Kuerten, X. Zhang, and D. Lohse. Evaporation-triggered microdroplet nucleation and the four life phases of an evaporating Ouzo drop. *Proc. Natl. Acad. Sci.*, 113(31):8642–8647, 2016.

[91] A. W. Wray, D. T. Papageorgiou, R. V. Craster, K. Sefiane, and O. K. Matar. Electrostatic Suppression of the “Coffee Stain Effect”. *Langmuir*, 30:5849–5858, 2014.

[92] C. Bourges-Monnier and M. E. R. Shanahan. Influence of Evaporation on Contact Angle. *Langmuir*, 11(7):2820–2829, 1995.

[93] H. Hu and R. G. Larson. Evaporation of a Sessile Droplet on a Substrate. *J. Phys. Chem. B*, 106(6):1334–1344, feb 2002.

[94] D. M. Anderson and S. H. Davis. The spreading of volatile liquid droplets on heated surfaces. *Phys. Fluids*, 7:248–265, 1995.

[95] V. S. Ajaev. Spreading of thin volatile liquid droplets on uniformly heated surfaces. *J. Fluid Mech.*, 528:279–296, 2005.

[96] T. Young. An Essay on the Cohesion of Fluids. *Philos. Trans. R. Soc. London*, 95:65–87, 1805.

[97] P. G. de Gennes. Wetting: statics and dynamics. *Rev. Mod. Phys.*, 57(3):827–863, 1985.

[98] P. S. Laplace. *Traité de Mécanique Céleste: Tome Quatriéme.* J.B.M. Duprat, 1805.

[99] P. G. de Gennes, F. Brochard-Wyart, and D. Quere. *Capillarity and Wetting Phenomena: Drops, Bubbles, Pearls, Waves.* Springer New York, 2003.

[100] L. E. Scriven and C. V. Sternling. The Marangoni Effects. *Nature*, 187(4733):186 – 188, 1960.

[101] J. Thomson. XLII. On certain curious motions observable at the surfaces of wine and other alcoholic liquors. *London, Edinburgh, Dublin Philos. Mag. J. Sci.*, 10(67):330–333, nov 1855.

[102] D. Bonn, J. Eggers, J. Indekeu, J. Meunier, and E. Rolley. Wetting and spreading. *Rev. Mod. Phys.*, 81(2):739–805, 2009.

[103] L. Courbin, J. C. Bird, M. Reyssat, and H. A. Stone. Dynamics of wetting: From inertial spreading to viscous imbibition. *J. Phys. Condens. Matter*, 21:464127, 2009.

[104] A.-m. Cazabat and G. Guena. Evaporation of macroscopic sessile droplets. *Soft Matter*, 6:2591–2612, 2010.

[105] H. Y. Erbil. Evaporation of pure liquid sessile and spherical suspended drops: A review. *Adv. Colloid Interface Sci.*, 170(1-2):67–86, jan 2012.

[106] K. Sefiane. Patterns from drying drops. *Adv. Colloid Interface Sci.*, 206:372–381, 2014.

[107] S. Semenov, A. Trybala, R. G. Rubio, N. Kovalchuk, V. Starov, and M. G. Velarde. Simultaneous spreading and evaporation: Recent developments. *Adv. Colloid Interface Sci.*, 206:382–398, 2014.

[108] D. Brutin and V. Starov. Recent advances in droplet wetting and evaporation. *Chem. Soc. Rev.*, 47(V):558–585, 2018.

[109] R. G. Picknett and R. Bexton. The Evaporation of Sessile or Pendant Drops in Still Air. *J. Colloid Interface Sci.*, 61(2):336–350, 1977.

[110] C. Poulard, G. Guena, and A. M. Cazabat. Diffusion-driven evaporation of sessile drops. *J. Phys. Condens. Matter*, 17:S4213–S4227, 2005.

[111] P. L. Kelly-Zion, C. J. Pursell, N. Hasbamrer, B. Cardozo, K. Gaughan, and K. Nickels. Vapor distribution above an evaporating sessile drop. *Int. J. Heat Mass Transf.*, 65:165–172, 2013.

[112] P. L. Kelly-Zion, C. J. Pursell, S. Vaidya, and J. Batra. Evaporation of sessile drops under combined diffusion and natural convection. *Colloids Surfaces A Physicochem. Eng. Asp.*, 381(1-3):31–36, 2011.

[113] F. Carle, B. Sobac, and D. Brutin. Experimental evidence of the atmospheric convective transport contribution to sessile droplet evaporation. *Appl. Phys. Lett.*, 102(6), 2013.

[114] X. Xu and L. Ma. Analysis of the effects of evaporative cooling on the evaporation of liquid droplets using a combined field approach. *Sci. Rep.*, 5:8614, 2015.

[115] G. Dunn, S. Wilson, B. Duffy, S. David, and K. Sefiane. A mathematical model for the evaporation of a thin sessile liquid droplet: Comparison between experiment and theory. *Colloids Surfaces A Physicochem. Eng. Asp.*, 323(1-3):50–55, jun 2008.

[116] H. V. Tran, T. A. H. Nguyen, S. R. Biggs, and A. V. Nguyen. On the predictions for diffusion-driven evaporation of sessile droplets with interface cooling. *Chem. Eng. Sci.*, 177:417–421, 2018.

[117] P. Kavehpour, B. Ovryn, and G. H. McKinley. Evaporatively-driven Marangoni instabilities of volatile liquid films spreading on thermally conductive substrates. *Colloids Surfaces A Physicochem. Eng. Asp.*, 206(1-3):409–423, 2002.

[118] V. S. Ajaev and O. A. Kabov. Heat and mass transfer near contact lines on heated surfaces. *Int. J. Heat Mass Transf.*, 108:918–932, 2017.

[119] C. Sodtke, V. S. Ajaev, and P. Stephan. Evaporation of thin liquid droplets on heated surfaces. *Heat Mass Transf.*, 43(7):649–657, 2007.

[120] C. Sodtke, V. S. Ajaev, and P. Stephan. Dynamics of volatile liquid droplets on heated surfaces: theory versus experiment. *J. Fluid Mech.*, 610:343–362, aug 2008.

[121] K. Sefiane, Y. Fukatani, Y. Takata, and J. Kim. Thermal Patterns and Hydrothermal Waves (HTWs) in Volatile Drops. *Langmuir*, 29:9750–9760, 2013.

[122] S. Semenov, V. M. Starov, M. G. Velarde, and R. G. Rubio. Droplets evaporation: Problems and solutions. *Eur. Phys. J. Spec. Top.*, 197(1):265–278, 2011.

[123] S. Semenov, V. M. Starov, R. G. Rubio, and M. G. Velarde. Computer simulations of evaporation of pinned sessile droplets: Influence of kinetic effects. *Langmuir*, 28(43):15203–15211, 2012.

[124] K. S. Birdi, D. T. Vu, and A. Winter. A Study of the Evaporation Rates of Small Water Drops Placed on a Solid Surface. *J. Phys. Chem.*, 93(9):3702–3703, may 1989.

[125] S. M. Rowan, M. I. Newton, and G. McHale. Evaporation of Microdroplets and the Wetting of Solid Surfaces. *J. Phys. Chem.*, 99(35):13268–13271, aug 1995.

[126] K. Sefiane and L. Tadrist. Experimental investigation of the de-pinning phenomenon on rough surfaces of volatile drops. *Int. Commun. Heat Mass Transf.*, 33(4):482–490, apr 2006.

[127] J. R. Moffat, K. Sefiane, and M. E. R. Shanahan. Effect of TiO2 Nanoparticles on Contact Line Stick-Slip Behavior of Volatile Drops. *J. Phys. Chem. B*, 113(26):8860–8866, 2009.

[128] R. D. Deegan, O. Bakajin, T. F. Dupont, G. Huber, S. R. Nagel, and T. A. Witten. Capillary flow as the cause of ring stains from dried liquid drops. *Nature*, 389(6653):827–829, 1997.

[129] R. D. Deegan, O. Bakajin, T. F. Dupont, G. Huber, S. R. Nagel, and T. A. Witten. Contact line deposits in an evaporating drop. *Phys. Rev. E*, 62(1):756–765, jul 2000.

[130] H. Hu and R. G. Larson. Analysis of the Effects of Marangoni Stresses on the Microflow in an Evaporating Sessile Droplet. *Langmuir*, 21(9):3972–3980, 2005.

[131] H. Hu and R. G. Larson. Analysis of the Microfluid Flow in an Evaporating Sessile Droplet. *Langmuir*, 21(9):3963–3971, 2005.

[132] Y. O. Popov. Evaporative deposition patterns: Spatial dimensions of the deposit. *Phys. Rev. E - Stat. Nonlinear, Soft Matter Phys.*, 71:036313, 2005.

[133] H. Hu and R. G. Larson. Marangoni Effect Reverses Coffee-Ring Depositions. *J. Phys. Chem. B*, 110(14):7090–7094, apr 2006.

[134] M. Cachile, O. Be, and A. M. Cazabat. Evaporating Droplets of Completely Wetting Liquids. *Langmuir*, 18(15):7985–7990, 2002.

[135] D. Bonn and D. Ross. Wetting transitions. *Reports Prog. Phys.*, 64:1085–1163, 2001.

[136] J. D. Chen and N. Wada. Wetting Dynamics of the Edge of a Spreading Drop. *Phys. Rev. Lett.*, 62(26):3050–3054, 1989.

[137] N. Churaev, V. Starov, and B. Derjaguin. The shape of the transition zone between a thin film and bulk liquid and the line tension. *J. Colloid Interface Sci.*, 89(1):16–24, 1982.

[138] J. Berthier. Theory of Wetting. In *Micro-Drops Digit. Microfluid.*, pages 7–73. William Andrew, second edition, 2013.

[139] W. Fyen, F. Holsteyns, T. Bearda, S. Arnauts, J. Van Steenbergen, G. Doumen, K. Kenis, and P. W. Mertens. A Detailed Study of Semiconductor Wafer Drying. In *Dev. Surf. Contam. Clean. Second Ed.*, volume 1, pages 795–854. Elsevier Inc., 2 edition, 2015.

[140] J. N. Israelachvili. Chapter 13 – Van der Waals Forces between Particles and Surfaces. In *Intermol. Surf. Forces*, pages 253–289. Academic Press, third edition, 2011.

[141] L. H. Tanner. The spreading of silicone oil drops on horizontal surfaces. *J. Phys. D. Appl. Phys.*, 12:1473–1484, 1979.

[142] J. D. Chen. Experiments on a spreading drop and its contact angle on a solid. *J. Colloid Interface Sci.*, 122(1):60–72, 1988.

[143] W. B. Hardy. III. The spreading of fluids on glass. *London, Edinburgh, Dublin Philos. Mag. J. Sci.*, 38(223):49–55, jul 1919.

[144] W. Radigan, H. Ghiradella, H. L. Frisch, H. Schonhorn, and T. K. Kwei. Kinetics of Spreading of Glass on Fernico Metal. *J. Colloid Interface Sci.*, 49(2):241–248, 1974.

[145] C. Iwamoto and S. ichiro Tanaka. Atomic morphology and chemical reactions of the reactive wetting front. *Acta Mater.*, 50(4):749–755, 2002.

[146] A. A. Mehrizi and H. Wang. Evaporation-induced receding contact lines in partial-wetting regime on a heated substrate. *Int. J. Heat Mass Transf.*, 124:279–287, 2018.

[147] K. G. Winkels, J. H. Weijs, A. Eddi, and J. H. Snoeijer. Initial spreading of low-viscosity drops on partially wetting surfaces. *Phys. Rev. E*, 85:055301, 2012.

[148] M. Elbaum and S. G. Lipson. How does a thin wetted film dry up? *Phys. Rev. Lett.*, 72(22):3562–3565, 1994.

[149] M. Elbaum, S. G. Lipson, and J. S. Wettlaufer. Evaporation Preempts Complete Wetting. *Europhys. Lett.*, 29(6):457–462, 1995.

[150] M. Cachile, O. Benichou, C. Poulard, and A. M. Cazabat. Evaporating Droplets. *Langmuir*, 18(21):8070–8078, 2002.

[151] C. Poulard, O. Bénichou, and A. M. Cazabat. Freely Receding Evaporating Droplets. *Langmuir*, 19(21):8828–8834, 2003.

[152] C. Poulard, G. Gue, A. M. Cazabat, A. Boudaoud, and M. B. Amar. Rescaling the Dynamics of Evaporating Drops. *Langmuir*, 21(18):8226–8233, 2005.

[153] E. Jambon-Puillet, O. Carrier, N. Shahidzadeh, D. Brutin, J. Eggers, and D. Bonn. Spreading dynamics and contact angle of completely wetting volatile drops. *J. Fluid Mech.*, 844:817–830, 2018.

[154] G. Guéna, C. Poulard, and A. M. Cazabat. Evaporating drops of alkane mixtures. *Colloids Surfaces A Physicochem. Eng. Asp.*, 298(1-2):2–11, 2007.

[155] P. E. Theodorakis, E. A. Müller, R. V. Craster, and O. K. Matar. Insights into surfactant-assisted superspreading. *Curr. Opin. Colloid Interface Sci.*, 19(4):283–289, 2014.

[156] S. Rafaï, D. Sarker, V. Bergeron, J. Meunier, and D. Bonn. Superspreading: Aqueous surfactant drops spreading on hydrophobic surfaces. *Langmuir*, 18(26):10486–10488, 2002.

[157] A. Oron, S. H. Davis, and S. G. Bankoff. Long-scale evolution of thin liquid films. *Rev. Mod. Phys.*, 69(3):931–980, 1997.

[158] P. Ehrhard and S. H. Davis. Non-isothermal spreading of liquid drops on horizontal plates. *J. Fluid Mech.*, 229:365–388, 1991.

[159] P. Ehrhard. Experiments on Isothermal and Non-Isothermal Spreading. *J. Fluid Mech.*, 257:463–483, 1993.

[160] R. Mollaret, K. Sefiane, J. R. E. Christy, and D. Veyret. Experimental and numerical investigation of the evaporation into air of a drop on a heated surface. *Chem. Eng. Res. Des.*, 82(4):471–480, 2004.

[161] F. Girard, M. Antoni, S. Faure, and A. Steinchen. Evaporation and Marangoni driven convection in small heated water droplets. *Langmuir*, 22(26):11085–11091, 2006.

[162] F. Girard, M. Antoni, and K. Sefiane. On the effect of Marangoni flow on evaporation rates of heated water drops. *Langmuir*, 24(17):9207–9210, 2008.

[163] S. David, K. Sefiane, and L. Tadrist. Experimental investigation of the effect of thermal properties of the substrate in the wetting and evaporation of sessile drops. *Colloids Surfaces A Physicochem. Eng. Asp.*, 298(1-2):108–114, apr 2007.

[164] G. J. Dunn, S. K. Wilson, B. R. Duffy, and K. Sefiane. Evaporation of a thin droplet on a thin substrate with a high thermal resistance. *Phys. Fluids*, 21(5):052101, 2009.

[165] K. Sefiane and R. Bennacer. An expression for droplet evaporation incorporating thermal effects. *J. Fluid Mech.*, 667:260–271, 2011.

[166] P. J. Sáenz, A. W. Wray, Z. Che, O. K. Matar, P. Valluri, J. Kim, and K. Sefiane. Dynamics and universal scaling law in geometrically-controlled sessile drop evaporation. *Nat. Commun.*, 8:14783, 2017.

[167] K. Sefiane, A. Steinchen, and R. Moffat. On hydrothermal waves observed during evaporation of sessile droplets. *Colloids Surfaces A Physicochem. Eng. Asp.*, 365(1-3):95–108, aug 2010.

[168] G. Karapetsas, O. K. Matar, P. Valluri, and K. Sefiane. Convective Rolls and Hydrothermal Waves in Evaporating Sessile Drops. *Langmuir*, 28:11433–11439, aug 2012.

[169] D. Brutin, B. Sobac, F. Rigollet, and C. Le Niliot. Infrared visualization of thermal motion inside a sessile drop deposited onto a heated surface. *Exp. Therm. Fluid Sci.*, 35(3):521–530, 2011.

[170] B. Sobac and D. Brutin. Thermocapillary instabilities in an evaporating drop deposited onto a heated substrate. *Phys. Fluids*, 24:032103, 2012.

[171] F. Carle, B. Sobac, and D. Brutin. Hydrothermal waves on ethanol droplets evaporating under terrestrial and reduced gravity levels. *J. Fluid Mech.*, 712:614–623, 2012.

[172] Y. Gotkis, I. Ivanov, N. Murisic, and L. Kondic. Dynamic structure formation at the fronts of volatile liquid drops. *Phys. Rev. Lett.*, 97(18):1–4, 2006.

[173] A. M. Cazabat, F. Heslot, S. M. Troian, and P. Carles. Fingering instability of thin spreading films driven by temperature gradients. *Nature*, 346(6287):824–826, 1990.

[174] O. K. Matar and R. V. Craster. Dynamics of surfactant-assisted spreading. *Soft Matter*, 5(20):3801, 2009.

[175] C. Redon, F. Brochard-Wyart, and F. Rondelez. Festoon instabilities of slightly volatile liquids during spreading. *J. Phys. II*, 2:1671–1676, 1992.

[176] F. Wodlei, J. Sebilleau, J. Magnaudet, and V. Pimienta. evaporating drop spreading on a liquid substrate. *Nat. Commun.*, 9:820, 2018.

[177] L. Keiser, H. Bense, P. Colinet, J. Bico, and E. Reyssat. Marangoni Bursting: Evaporation-Induced Emulsification of Binary Mixtures on a Liquid Layer. *Phys. Rev. Lett.*, 118(7):1–5, 2017.

[178] S. M. Rowan, M. I. Newton, F. W. Driewer, and G. Mchale. Evaporation of Microdroplets of Azeotropic Liquids. *J. Phys. Chem. B*, 104(34):8217–8220, 2000.

[179] K. Sefiane, L. Tadrist, and M. Douglas. Experimental study of evaporating water-ethanol mixture sessile drop: Influence of concentration. *Int. J. Heat Mass Transf.*, 46(23):4527–4534, 2003.

[180] A. K. H. Cheng, D. M. Soolaman, and H.-z. Yu. Evaporation of Microdroplets of Ethanol - Water Mixtures on Gold Surfaces Modified with Self-Assembled Monolayers. *J. Phys. Chem. B*, 110:11267–11271, 2006.

[181] Z. Wang, X.-f. Peng, A. S. Mujumdar, A. Su, and D.-j. Lee. Evaporation of Ethanol-Water Mixture Drop on Horizontal Substrate. *Dry. Technol.*, 26(6):806–810, 2008.

[182] L. Shi, P. Shen, D. Zhang, Q. Lin, and Q. Jiang. Wetting and evaporation behaviors of water-ethanol sessile drops on PTFE surfaces. *Surf. Interface Anal.*, 41(12-13):951–955, 2009.

[183] K. Sefiane, S. David, and M. E. R. Shanahan. Wetting and Evaporation of Binary Mixture Drops. *J. Phys. Chem. B*, 112(36):11317–11323, 2008.

[184] C. Liu, E. Bonaccurso, and H. ü. Butt. Evaporation of sessile water/ethanol drops in a controlled environment. *Phys. Chem. Chem. Phys.*, 10(47):7150–7157, 2008.

[185] J. R. Christy, K. Sefiane, and E. Munro. A Study of the Velocity Field during Evaporation of Sessile Water and Water/Ethanol Drops. *J. Bionic Eng.*, 7(4):321–328, dec 2010.

[186] X. Zhong and F. Duan. Flow regime and deposition pattern of evaporating binary mixture droplet suspended with particles. *Eur. Phys. J. E*, 39(2):18, 2016.

[187] Y. Abe. Self-rewetting fluids: beneficial aqueous solutions. *Ann. N. Y. Acad. Sci.*, 1077:650–67, sep 2006.

[188] D. Mamalis, V. Koutsos, and K. Sefiane. Nonisothermal Spreading Dynamics of Self-Rewetting Droplets. *Langmuir*, 34:1916–1931, 2018.

[189] P. Chen, S. Harmand, S. Ouenzerfi, and J. Schiffler. Marangoni Flow Induced Evaporation Enhancement on Binary Sessile Drops. *J. Phys. Chem. B*, 121(23):5824–5834, 2017.

[190] N. J. Cira, a. Benusiglio, and M. Prakash. Vapour-mediated sensing and motility in two-component droplets. *Nature*, 519(7544):446–450, 2015.

[191] D. Pesach and A. Marmur. Marangoni Effects in the Spreading of Liquid Mixtures on a Solid. *Langmuir*, 3(4):519–524, 1987.

[192] C. Diddens, J. G. M. Kuerten, C. W. M. van der Geld, and H. M. A. Wijshoff. Modeling the evaporation of sessile multi-component droplets. *J. Colloid Interface Sci.*, 487:426–436, 2017.

[193] C. Diddens. Detailed finite element method modeling of evaporating multi-component droplets. *J. Comput. Phys.*, 340:670–687, 2017.

[194] H. Tan, C. Diddens, M. Versluis, H.-J. Butt, D. Lohse, and X. Zhang. Self-wrapping of an ouzo drop induced by evaporation on a superamphiphobic surface. *Soft Matter*, 13(15):2749–2759, 2017.

[195] Y. Li, P. Lv, C. Diddens, H. Tan, H. Wijshoff, M. Versluis, and D. Lohse. Evaporation-triggered segregation of sessile binary droplets. *Phys. Rev. Lett.*, 120(22):224501, 2018.

[196] N. Murisic and L. Kondic. On evaporation of sessile drops with moving contact lines. *J. Fluid Mech.*, 679:219–246, 2011.

[197] M. A. Saxton, D. Vella, J. P. Whiteley, and J. M. Oliver. Kinetic effects regularize the mass-flux singularity at the contact line of a thin evaporating drop. *J. Eng. Math.*, 106(1):47–73, 2017.

[198] A. H. Persad and C. A. Ward. Expressions for the Evaporation and Condensation Coefficients in the Hertz-Knudsen Relation. *Chem. Rev.*, 116(14):7727–7767, 2016.

[199] C. Huh and L. E. Scriven. Hydrodynamic model of steady movement of a solid/liquid/fluid contact line. *J. Colloid Interface Sci.*, 35(1):85–101, 1971.

[200] M. A. Saxton, J. P. Whiteley, D. Vella, and J. M. Oliver. On thin evaporating drops: When is the d2-law valid? *J. Fluid Mech.*, 792:134–167, 2016.

[201] M. Potash and P. C. Wayner. Evaporation from a two-dimensional extended meniscus. *Int. J. Heat Mass Transf.*, 15(10):1851–1863, 1972.

[202] S. Moosman and G. M. Homsy. Evaporating Menisci of Wetting Fluids. *J. Colloid Interface Sci.*, 73(1):212–223, 1980.

[203] G. Karapetsas, P. J. Saenz, K. Sefiane, P. Valluri, and O. K. Matar. Numerical study of the evaporation of sessile drops: formation of hydrothermal waves. In *63nd Annu. Meet. APS Div. fluid Dyn.*, page 65, Long Beach, California, USA, 2010.

[204] ANSYS Inc. *ANSYS CFX-Solver Theory Guide, Release 15.0.* 2014.

[205] C. B. Kretschmer and R. Wiebe. Liquid-Vapor Equilibrium of Ethanol-Toluene Solutions. *J. Am. Chem. Soc.*, 71(5):1793–1797, 1949.

[206] O. C. Bridgeman and E. W. Aldrich. Vapor Pressure Tables for Water. *J. Heat Transfer*, 86(2):279–286, 1964.

[207] C. Willingham, W. Taylor, J. Pignocco, and F. Rossini. Vapor pressures and boiling points of some paraffin, alkylcyclopentane, alkylcyclohexane, and alkylbenzene hydrocarbons. *J. Res. Natl. Bur. Stand. (1934).*, 35(3):219, 1945.

[208] G. F. Carruth and R. Kobayashi. Vapor Pressure of Normal Paraffins Ethane Through n-Decane from Their Triple Points to About 10 Mm Hg. *J. Chem. Eng.*, 18(2):115–126, 1973.

[209] J. Brackbill, D. Kothe, and C. Zemach. A continuum method for modeling surface tension. *J. Comput. Phys.*, 100:335–354, 1992.

[210] ANSYS Inc. ANSYS CFX, Release 15.0, 2014.

[211] R. V. Craster, O. K. Matar, and K. Sefiane. Pinning, Retraction, and Terracing of Evaporating Droplets Containing Nanoparticles. *Langmuir*, 25(6):3601–3609, 2009.

[212] R. G. Larson. Transport and deposition patterns in drying sessile droplets. *AIChE J.*, 60:1538–1571, may 2014.

[213] M. S. Plesset and A. Prosperetti. Flow of vapour in a liquid enclosure. *J. Fluid Mech.*, 78(3):433–444, 1976.

[214] P. Jafari, A. Masoudi, P. Irajizad, M. Nazari, V. Kashyap, B. Eslami, and H. Ghasemi. Evaporation Mass Flux: A Predictive Model and Experiments. *Langmuir*, 34(1):11676–11684, 2018.

[215] J. D. Smith, C. D. Cappa, W. S. Drisdell, R. C. Cohen, and R. J. Saykally. Raman Thermometry Measurements of Free Evaporation from Liquid Water Droplets. *J. Am. Chem. Soc.*, 128:12892–12898, 2006.

[216] Y. Q. Li, P. Davidovits, Q. Shi, J. T. Jayne, C. E. Kolb, and D. R. Worsnop. Mass and Thermal Accommodation Coefficients of H2O(g) on Liquid Water as a Function of Temperature. *J. Phys. Chem. A*, 105(47):10627–10634, 2001.

[217] W. S. Drisdell, R. J. Saykally, and R. C. Cohen. On the evaporation of ammonium sulfate solution. *Proc. Natl. Acad. Sci.*, 106(45):18897–18901, 2009.

[218] K. C. Duffey, O. Shih, N. L. Wong, W. S. Drisdell, R. J. Saykally, and R. C. Cohen. Evaporation kinetics of aqueous acetic acid droplets : mechanism of water evaporation. *Phys. Chem. Chem. Phys.*, 15:11634, 2013.

[219] J. Julin, M. Shiraiwa, R. E. H. Miles, J. P. Reid, and U. Po. Mass Accommodation of Water : Bridging the Gap Between Molecular Dynamics Simulations and Kinetic Condensation Models. *J. Phys. Chem. A*, 117:410–420, 2013.

[220] J. F. Davies, R. E. H. Miles, A. E. Haddrell, and J. P. Peid. Temperature dependence of the vapor pressure and evaporation coefficient of supercooled water. *J. Geophys. Res. Atmos.*, 119:10,931–10,940, 2014.

[221] V. S. Ajaev and G. M. Homsy. Steady Vapor Bubbles in Rectangular Microchannels. *J. Colloid Interface Sci.*, 240(1):259–271, 2001.

[222] J. L. Plawsky, A. G. Fedorov, S. V. Garimella, H. B. Ma, S. C. Maroo, L. Chen, and Y. Nam. Nano- and Microstructures for Thin-Film Evaporation - A Review. *Nanoscale Microscale Thermophys. Eng.*, 18:251–269, 2014.

[223] O. Shardt, H. Masoud, and H. A. Stone. Oscillatory Marangoni flows with inertia. *J. Fluid Mech.*, 803:94–118, 2016.

[224] O. E. Jensen and J. B. Grotberg. The spreading of heat or soluble surfactant along a thin liquid film The spreading of heat or solluble surfactant along a thin liquid film. *Phys. Fluids A Fluid Dyn.*, 5:58–68, 1993.

[225] M. R. E. Warner, R. V. Craster, and O. K. Matar. Surface patterning via evaporation of ultrathin films containing nanoparticles. *J. Colloid Interface Sci.*, 267:92–110, 2003.

[226] O. K. Matar. Nonlinear evolution of thin free viscous films in the presence of soluble surfactant. *Phys. Fluids*, 14(12):4216–4234, 2002.

[227] D. S. Burnett. *Finite Element Analysis: From Concepts to Applications.* Addison-Wesley, Reading, Massachusetts, 1987.

[228] R Core Team. R: A language and environment for statistical computing, 2013.